Numerical Simulations to Investigate Particle Dispersion in Non-Homogeneous Suspension Flows

by

Amanda A. Howard

B.Sc., Stanford University; Stanford, CA, 2012

M.Sc., Brown University; Providence, RI, 2014

A dissertation submitted in partial fulfillment of the

requirements for the degree of Doctor of Philosophy

in The Division of Applied Mathematics at Brown University

PROVIDENCE, RHODE ISLAND

May 2018

This dissertation by Amanda A. Howard is accepted in its present form
by The Division of Applied Mathematics as satisfying the
dissertation requirement for the degree of Doctor of Philosophy.

Date________________ ________________________________

Martin Maxey, Ph.D., Advisor

Recommended to the Graduate Council

Date________________ ________________________________

George Karniadakis, Ph.D., Reader

Date________________ ________________________________

Jeffrey Morris, Ph.D., Reader

Approved by the Graduate Council

Date________________ ________________________________

Andrew G. Campbell, Dean of the Graduate School

Vita

EDUCATION

Brown University, Providence, Rhode Island USA

M.S., Applied Mathematics, May 2014

Stanford University, Stanford, California USA

B.S. Applied Mathematics, June 2012

HONORS AND AWARDS

National Science Foundation Graduate Research Fellowship, 2014

PEER-REVIEWED JOURNAL ARTICLES

Amanda A. Howard, Martin R. Maxey, and Kyongmin Yeo. Settling of heavy particles in concentrated suspensions of neutrally buoyant particles under uniform shear. *Fluid Dyn. Res.*, 2018.

Francis R. Cui, Amanda A. Howard, Martin R. Maxey, and Anubhav Tripathi. Dispersion of a suspension plug in oscillatory pressure-driven flow. *Phys. Rev. Fluids*, 2(9):094303, 2017.

PAPERS UNDER REVIEW

Francis R. Cui, Amanda A. Howard, Martin R. Maxey, and Anubhav Tripathi. Simulation study of particle clouds in oscillating shear flow. *J. Fluid Mech.*. Under review.

TEACHING EXPERIENCE

Head teaching consultant, Sheridan Center for Teaching and Learning 2017-2018

Catalyst Summer Program Mathematics Instructor (online course), Summer 2015

Teaching Assistant, APMA 350: Methods of Applied Mathematics I, Spring 2015

Teaching Assistant, APMA 350: Methods of Applied Mathematics I, Spring 2014

Preface and Acknowledgments

This work is dedicated in memory of Samantha and Veronica Howard.

This thesis would not have been possible without the advice, guidance, support, and patience of my advisor, Professor Martin Maxey. He has dedicated an immense amount of time to discussions on every aspect of my work, and has offered me more opportunities than I ever imagined when I entered graduate school.

Professor George Karniadakis has been very supportive through my time at Brown, particularly welcoming me into his group meetings where I was exposed to a wide range applications of scientific computing. I also wish to thank Professor Jeffrey Morris for his time and effort serving on my committee.

I must thank with Dr. Kyongmin Yeo, for his help with the FCM simulations, and Dr. Nathaniel Trask and the Compadre team at Sandia National Laboratories, who have been invaluable in developing the GMLS code.

To all my friends in Applied Mathematics at Brown: Veronica, Alexandria, Christian, Ivana, and Steven, thank you for the many nights both doing problem sets and recovering from problem sets. Particular thanks go to Karen and Stephanie, who have spent an incredible amount of time organizing activities for the department. I cannot thank enough my husband, Antoine, for all of his support through this process. His constant encouragement has been a great resource as I wrote this thesis. Thank you for following me on our next adventure. Lastly, I must thank my parents, who have consistently emboldened me from a young age to pursue my passions. Thank you for filling my costume box as I was growing up with both princess dresses and Ph.D. robes, and for the many trips across the country for support and encouragement while I've been at Brown.

This thesis is based upon work supported by the National Science Foundation Graduate Research Fellowship under Grant No. DGE 1058262. Additional support by the U.S. Department of Energy Office of Science under Award Number DE-SC0009247 is gratefully acknowledged. The Force Coupling Method simulations were conducted using computational resources and services at the Center for Computation and Visualization, Brown University, and the Extreme Science and Engineering Discovery Environment (XSEDE), which is supported by National Science Foundation grant number ACI-1548562, through allocation TG-DMS170018 (Towns et al., 2014).

Contents

List of Tables

List of Figures

Chapter One

Introduction

Solid-fluid multiphase flows systems occur in many areas of recent interest both in nature and in industry, with applications including microfluidic systems for cell sorting and inertial focusing (Di Carlo, 2009), the microstructure that appears due to particle stresses with spherical particles at high volume fraction (Morris, 2009), and particle migration and segregation by size or density (Kanehl and Stark, 2015, Lyon and Leal, 1998, Batchelor and Van Rensburg, 1986, Chang, 1994, Pesche et al., 1998). Such flows represent a complex dynamical system due to the nonlinear coupling of the flow and the particle positions, which in turn determine the flow.

In a classical demonstration by G. I. Taylor, a small amount of dyed fluid is injected into very viscous fluid in the gap between two concentric cylinders (Taylor and Friedman, 1966). The inner cylinder is rotated for several turns, then the rotation is reversed for an equal number of turns. After the rotations the dyed fluid returns to its original position except for some fuzziness at the edges due to molecular diffusion. This experiment illustrates the reversibility of fluid motion when the fluid Reynolds number, the ratio of inertial forces to viscous forces in the fluid given by $Re = \frac{\rho U l}{\mu}$, is very small.

A similar experiment has recently been completed by Metzger and Butler (2012), with a spherical cloud of particles replacing the dyed fluid. In this case, the particles do not return to their original positions, with large particle displacements forming complex shapes forming in some cases. This experiment, and others, illustrate that in even in the zero Reynolds number Stokes flow limit, where the flow is linear and reversible, the presence of particles induces chaos and irreversibility (Pine et al., 2005, Metzger et al., 2013, Metzger and Butler, 2010, Corté et al., 2008). To understand the rheology and particle dispersion in such systems a number of works have focused on the study of spherical particles in the limit of viscous fluid, or Stokes flow. In the zero-Reynolds number Stokes flow regime the equations of motion for the particles and the fluid are symmetric with respect to time, so the hydrodynamic forces on the particles are reversible in general.

Experiments have shown, however, that this time symmetry is broken even in the case of two spherical particles in a shear flow, due to small irregularities of the particle surface or shape. This particle roughness prevents contact of the particles as they interact in a shear flow Arp and Mason (1977), Gadala-Maria and Acrivos (1980), Smart and Leighton (1989). Subsequent studies by Da Cunha and Hinch (1996) calculated the change between initial and final streamlines for two rough particles colliding in a shear flow, showing that rougher particles have a larger displacement. Further studies have shown that particle roughness is key in irreversible particle displacements for two particles of different sizes (Zarraga and Leighton, 2001) and for three particles in a shear flow (Pham et al., 2015).

The surface roughness is a critical parameter in quantifying particle dynamics because the minimum distance between two particles in a collision can be quite small, less than 10^{-4} of a particle radius (Da Cunha and Hinch, 1996). Therefore, small variations in the surface can significantly alter the particle dynamics. The inherent irreversibility due to the surface roughness causes the pair distribution function of particles in a fully seeded channel to display fore-aft asymmetry, which increases with rougher particles (Rampall et al., 1997, Blanc et al., 2011). Irreversible particle diffusion occurs even when the particles are large enough that thermal fluctuations and Brownian motion can be ignored. The major objective of this thesis is to understand the link between the forces and irreversible particle dispersion in non-Brownian suspension Stokes flows through numerical modeling.

The Péclet number, $Pe = \frac{6\pi\mu_f\dot{\gamma}a^3}{k_BT}$, is a measure of the ratio of the advection of the flow, $6\pi\mu_f\dot{\gamma}a^3$ for a particle of radius a in a fluid with viscosity μ_f and shear rate

$\dot{\gamma}$, to the thermal energy, $k_B T$. At low Pe the Brownian motion of the particles are dominant. In this work, we limit to the study of suspensions with large Pe, $Pe > 10^3$, where hydrodynamic interactions between the particles dominate the suspension dynamics. Even without Brownian motion experiments with random suspensions of hard spheres have been shown the motion to be chaotic and unpredictable. Experiments by Pine et al. (2005) of a suspension in shear flow found a critical strain amplitude, dependent on the concentration of particles, above which the suspension dynamics were irreversible and the particle self-diffusivity increased. Below this threshold strain amplitude, particles rearrange into a reversible state (Corté et al., 2008). Experiments by Guasto et al. (2010) of suspensions in Poiseuille flow, where this is non-uniform strain, confirm again a critical strain amplitude, and that the irreversibility occurred simultaneously across the channel. Further experiments and modeling by Pham et al. (2016) show that this self-diffusivity and critical strain amplitude are dependent on the particle surface roughness, with suspensions of particles with a larger surface roughness having a larger self-diffusivity and lower critical strain amplitude.

Neutrally buoyant particles in a suspension flow interact across a range of length scales. At the largest scale, each particle causes a disturbance to the fluid flow that decays as $1/r^2$, where r is the distance from the particle. This long-range hydrodynamic force represents interactions between widely separated particles. As the particles move closer together, the fluid in the gap between the particles must be displaced, resulting in lubrication forces that form between the particles due to the pressure-driven flow of fluid escaping the gap exerting a force on the particles. For spheres, analytical forms of the lubrication forces between two isolated particles in an infinite domain are known (Kim and Karilla, 1991, Jeffrey and Onishi, 1984, Jeffrey, 1992). The lubrication forces can be attractive or repulsive depending on the relative motion of the particles, either resisting the particles coming together or keeping particles from separating. With idealized fluid and smooth particles, the lubrication forces prevent the particles from touching, however, in practice, rough particles will touch, resulting in very short range forces between the particles. This can be modeled numerically through a short-range contact force between the particles, which also works to keep the particles from overlapping due to issues with discrete time stepping in numerical simulations (Yeo and Maxey, 2010, Meunier and Bossis, 2008).

To understand the source of the particle self-diffusion in a shear flow, a series of experiments and simulations have been completed studying the role of each of the three main forces between particles in a suspension flow in causing particle self-diffusion. Metzger and Butler (2010) showed that the long-range hydrodynamic interactions cannot cause, or increase, particle irreversibility. Furthermore, they showed that the lubrication interactions are too weak to cause the self-diffusivity shown in experiments (Metzger et al., 2013). It is the contacts between the rough particles that are essential to cause a significant irreversibility in oscillating shear flows (Pham et al., 2015). These studies, combined with experiments, have shown the importance of surface asperities that ensure a minimum gap width between colliding particles, altering the particle trajectories.

Early experiments by Gadala-Maria and Acrivos (1980) and later by Leighton and Acrivos (1987) showed that when a gradient exists in the fluid shear rate, suspended particles migrate to regions of lower shear, in a phenomenon called shear-induced migration. Karnis et al. (1966) found that in a Poiseuille flow in a tube the particles formed a plug at the core of the channel due to shear-induced migration. Similar results are seen in a range of experiments in a channel with both colloidal and non-colloidal particles and with monodisperse and bidisperse particle sizes (Koh et al., 1994, Hampton et al., 1998, Lyon and Leal, 1998,, Butler et al., 1999, Gao et al., 2009, Semwogerere et al., 2007, Semwogerere and Weeks, 2008). Shear-induced migration is also seen in oscillating Poiseuille flows of suspensions in a pipe (Snook et al., 2016). Results from experiments reveal that as the particles migrate to the center of the channel, they create a densely packed plug with volume fraction close to the maximum volume fraction for spheres. This high volume fraction causes a blunting or flattening of the parabolic velocity profile at the core of the channel (Lyon and Leal, 1998). Experimental results have been confirmed by simulations with the Force Coupling Method (Yeo and Maxey, 2011), lattice-Boltzmann simulations (Chun et al., 2017), and for bidisperse suspensions using the approximation of Multi-Particle Collision Dynamics (Kanehl and Stark, 2015).

Leighton and Acrivos (1987) developed a phenomenological model to explain the shear-induced migration seen in experiments, which relies on the irreversible inter-particle interactions. Later models include diffusive flux models (Phillips et al., 1992) and the Suspension Balance Model (SBM) proposed by Nott and Brady (1994), with subsequent refinements by Morris and Boulay (1999), Miller and Morris (2006), Lhuillier (2009), Nott et al. (2011), which has been successful in correlating a number of situations (Boyer et al., 2011, Snook et al., 2016, Kanehl and Stark, 2015). The SBM predicts that particle migration is due to divergence of the particle phase stress. These models are based on a mean-field, continuum representation and approximation of locally uniform gradients, particle volume fractions, and particle stresses. However, the SBM is essentially a point-particle concept with no explicit particle size. Several open issues remain, including how the presence of a wall layer, and the subsequent particle layering that builds upon the wall layer, change the dynamics, as particle stress gradients and volume fraction profiles will have sharp discontinuities at the wall layer. In addition, in the channel core of a Poiseuille flow, the shear stress drops to zero, which requires careful handling in SBM. Additionally, there can be cases where fronts occur on the scale of the particle size, which is not accounted for in SBM. An open question is what aspect of the particle stress controls the migration flux, and how to link averaged results to individual particle interactions.

The goal of this thesis is to explore the irreversible migration of particles in high volume fraction suspension flows through direct numerical simulations under controlled conditions. Motivated by this we discuss:

- Suspension flow plugs, where uniformly sized particles are seeded in half of a channel in the streamwise direction, allowing for the particles to expand out of the plug. The plugs oscillate in a Poiseuille flow, and particle fluxes are compared to those of a fully seeded channel where particles fill the entire domain.
- Suspension clouds, where a densely packed sphere or cylinder of particles is exposed to pure fluid on all sides and particles are free to expand outside the cloud as studied experimentally by Metzger and Butler (2012). The particles are placed in an oscillating Couette flow. This configuration allows for studies in the relative importance, and time to development, of hydrodynamic forces compared to those due to the particle surface roughness.
- The development of a Poiseuille flow with uniformly sized particles from a homogeneous state, in both steady and oscillating pressure gradients, comparing results to experimental results.
- Suspensions with particles of bidisperse size, where the particles may segregate by size due to the imposed flow. Simulations allow for quantification of the forces causing this segregation.

The above configurations are completed with the Force Coupling Method (FCM) for suspended, densely packed particles in Stokes flow. FCM incorporates a contact force, discussed in sec. 2.2, which accounts for the particle surface roughness. There has been a trend in recent studies to include a friction model for inter-particle contacts (Pednekar et al., 2018, Singh et al., 2018, Townsend and Wilson, 2017, Peters et al., 2016, Gallier et al., 2014). Friction models are relevant in dense suspensions, especially where jamming may occur, however, they add additional physics complicating the simulation results. They primarily affect the rheology of the suspension, including increasing the suspension viscosity. This effect is also seen through experiments where rough particles have been shown to increase both the viscosity and normal stress differences of the suspension (Tanner and Dai, 2016). The aim of this thesis is to simulate a controlled system that is physically relevant, can be simulated in detail, and for which a modeling approach can be tested. Thus, we have excluded friction forces in the present work.

The final chapter of this thesis will discuss the development of a high order Generalized Moving Least Squares (GMLS) as a new generation of meshless simulation tools for multiphase flows (Trask et al., 2018). FCM can accurately and robustly simulate dense suspensions of spheres and can be extended to ellipsoidal particles, and non-zero Reynolds numbers, however, it is an approximation, and requires careful handling of lubrication forces. GMLS allows for a full representation of the dynamics without explicitly incorporating lubrication forces. GMLS can also be used as a high-fidelity simulation or to verify lower-fidelity methods. A large advantage of GMLS over existing numerical methods is that it can simulate arbitrarily shaped particles. In addition, GMLS allows for high-order simulations of suspensions in complexly shaped or changing domains, which is increasingly important as experiments in lab-on-a-chip cell sorting devices become routine (Di Carlo, 2009). Such devices are difficult and time-consuming to simulate with existing methods due to winding, branching channels.

The remainder of the thesis is as follows. In chapter 2 the FCM simulation method is introduced, including a discussion of the particle-particle contact force. The implications of the contact force on two- and three-particle collisions is discussed, as well as the contact force chains that develop in high volume fraction suspensions. Chapters 3 and 4 discuss cases where the particles fill only one region of the domain and are free to extend outside that region: in chapter 3, the particles fill half the channel in the stream-wise direction, while in chapter 4 the particles are seeded in a spherical or cylindrical shape. Chapter 5 considers the development of particle stresses in oscillating and steady Poiseuille flows at high volume fraction. Chapter 6 discusses suspensions with bidisperse particle sizes in Couette and Poiseuille flow as well as the wall layering that occurs in a wall-bounded suspension flow. Finally, chapter 7 discusses and gives examples of GMLS for future suspension simulations.

Chapter Two

Monodisperse suspensions: Numerical methods and inter-particle forces

In this chapter, we introduce the tools used in modeling irreversible particle dispersion in monodisperse suspension flows, including an overview of the FCM numerical method in sec. 2.1. As the particle surface roughness is a key feature in particle self-diffusion in experiments, section 2.2 discusses two- and three- particle interaction in suspension flows, as well as the force chains that form as the result of the particle contact force in fully seeded shear flows.

2.1 Numerical method

In this chapter, and in chapters 2–6, the simulations are completed using the Force Coupling Method (FCM). Developed by Maxey and Patel (2001), Lomholt and Maxey (2003), the Force Coupling Method is used to simulate a large number of densely packed hard spherical particles in a wide range of applications. FCM has been used in a wide range of systems, including high volume fraction fluid flow in a channel (Yeo and Maxey, 2011, 2010), the settling of particles with bidispersed sizes (Abbas et al., 2006), and the coagulation of platelets in blood flow (Pivkin et al., 2006). Incorporation of lubrication forces allows for simulations of very densely packed particles with volume fraction $\phi > 0.2$ (Dance and Maxey, 2003). Provided here is an overview of FCM as it is implemented for the simulations discussed in this work. For more complete details, please see Yeo (2011) and Yeo and Maxey (2010).

To represent the fluid flow with FCM with N_p spherical particles we begin with the Stokes' equations,

$$\nabla p = \mathbf{f} + \mu\nabla^2\mathbf{u} + \sum_{n=1}^{N_p}\{\mathbf{F}^n\Delta_M(\mathbf{r}^n) + (G^n\cdot\nabla)\Delta_D(\mathbf{r}^n)\} \tag{2.1.1}$$

$$\nabla\cdot\mathbf{u} = 0 \tag{2.1.2}$$

In these equations p is the pressure, $\mathbf{f}$ represents any external forces, μ is the fluid viscosity, $\mathbf{u}$ is the fluid velocity, $\mathbf{F}^n$ is the force monopole moment on the nth particle, $\Delta_M(\mathbf{x})$ is the FCM force monopole, G^n is the force dipole moment, $\Delta_D(\mathbf{x})$ is the force dipole, and $\mathbf{r}^n$ is a vector representing the relative distance from the center of particle n, $\mathbf{r}^n = \mathbf{x} - \mathbf{Y}^n$.

The monopole and dipole force envelopes, Δ_M and Δ_D, are represented by Gaussians:

$$\Delta_M = \frac{1}{(2\pi\sigma_M^2)^{3/2}} \exp\left(-\frac{\mathbf{x}^2}{2\sigma_M^2}\right) \tag{2.1.3}$$

$$\Delta_D = \frac{1}{(2\pi\sigma_D^2)^{3/2}} \exp\left(-\frac{\mathbf{x}^2}{2\sigma_D^2}\right) \tag{2.1.4}$$

The scaling for the monopole force envelope is chosen such that the Stokes settling velocity matches the self-induced fluid velocity at the center of an isolated particle (Maxey and Patel, 2001), so that for a particle of radius a

$$\sigma_M = \frac{a}{\sqrt{\pi}}. \tag{2.1.5}$$

The dipole scaling is chosen to match the FCM particle angular velocity with the solution for the angular velocity from the Stokes solution (Lomholt and Maxey, 2003), giving

$$\sigma_D = \frac{a}{(6\sqrt{\pi})^{1/3}}. \tag{2.1.6}$$

The force monopole coefficient is given by the force of the particle on the fluid, which is the sum of all non-hydrodynamic forces on the particle. The force dipole moment G_{ij}^n consists of symmetric and anti-symmetric parts. The symmetric part is the stresslet S_{ij} acting on the fluid, and is found by assuming there is zero strain-rate inside the particles:

$$0 = \int \frac{1}{2}\left(\frac{\partial \mathbf{u}_i}{\partial \mathbf{x}_j} + \frac{\partial \mathbf{u}_i}{\partial \mathbf{x}_j}\right) \Delta_D(\mathbf{x})\ d^3\mathbf{x} \tag{2.1.7}$$

The anti-symmetric part T_{ij} comes from the torque the fluid exerts on the particle,

$$T_{ij} = \frac{1}{2}\epsilon_{ijk}T_k^{ext}. \tag{2.1.8}$$

Once the fluid velocity $\mathbf{u}$ is computed everywhere in the domain, the particle translational and angular velocities can be found by weighted volume integrals:

$$\mathbf{V}_i^n = \int \mathbf{u}_i(\mathbf{x})\Delta_M(\mathbf{x})\ d^3\mathbf{x} \tag{2.1.9}$$

$$\mathbf{\Omega}_i^n = \int \epsilon_{ijk}\frac{\partial \mathbf{u}_k(\mathbf{x})}{\partial \mathbf{x}_j}\Delta_D(\mathbf{x})\ d^3\mathbf{x}. \tag{2.1.10}$$

Yeo and Maxey (2010) showed that solving eqs. 2.1.1 and 2.1.2 is equivalent to the solution to the grand mobility problem, where the particle velocities and rate of strain are related to the particle forces, torques, and stresses through a matrix formulation:

$$\left(M^{FCM}\right)^{-1}\begin{bmatrix} \mathscr{V} - \mathscr{V}^{\infty} \\ -\mathbf{E}^{\infty} \end{bmatrix} = \begin{bmatrix} \mathscr{F} \\ \mathbf{S} \end{bmatrix} \tag{2.1.11}$$

$\mathscr{V}$ is a vector containing the particle angular and translational velocities, $\mathscr{V} = [\mathbf{V}^T, \Omega^T]^T$, with size $(6N_p)$, and $\mathscr{F}$ is a vector containing the monopole particle forces and torques, $\mathscr{F} = [\mathbf{F}^T, \mathbf{T}^T]^T$, also with size $(6N_p)$. $\mathbf{E}^{\infty}$ is the strain rate of the imposed fluid velocity field, and $\mathcal{V}^{\infty}$ corresponds to the translational and angular velocities of the imposed external fluid flow field. $\mathbf{S}$ is the stresslet. In implementation, it is only necessary to store a $(5N_p)$ vector containing the five independent stresslet components for each particle: $\mathbf{S}_{11}, \mathbf{S}_{12}, \mathbf{S}_{13}, \mathbf{S}_{22}, \mathbf{S}_{23}$. The stress tensor is symmetric and has zero trace, so these five components allow for computation of the entire tensor.

FCM as written above works well to resolve the long range hydrodynamics between the particles at low volume fraction Lomholt and Maxey (2003). To account for the short range inter-particle interactions, lubrication viscous forces and a short-range contact force are added. The contact force represents a finite particle surface roughness, and prevents the particles from overlapping during the discrete time steps. The contact force will be discussed in sec. 2.2. Lubrication effects are added to the grand resistance matrix and calculated as the sum of pairwise interactions between particles that have only a small separation. The exact form of the lubrication correction is covered in detail in sec. 6.2.1, so here we only describe how they are incorporated into FCM. With the full lubrication correction resistance matrix, $\mathbf{L}$, eq. 2.1.11 becomes:

$$\left((M^{FCM})^{-1} + \mathbf{L}\right) \begin{bmatrix} \mathscr{V} - \mathscr{V}^{\infty} \\ -\mathbf{E}^{\infty} \end{bmatrix} = \begin{bmatrix} \mathscr{F} \\ \mathbf{S} \end{bmatrix} \tag{2.1.12}$$

The lubrication correction matrix is given by

$$\mathbf{L} = \begin{bmatrix} \mathbf{R}^L_{\mathbf{VF}} & \mathbf{R}^L_{\mathbf{\Omega F}} & \mathbf{R}^L_{\mathbf{EF}} \\ \mathbf{R}^L_{\mathbf{VT}} & \mathbf{R}^L_{\mathbf{\Omega T}} & \mathbf{R}^L_{\mathbf{ET}} \\ \mathbf{R}^L_{\mathbf{VS}} & \mathbf{R}^L_{\mathbf{\Omega S}} & \mathbf{R}^L_{\mathbf{ES}} \end{bmatrix} \tag{2.1.13}$$

where $\mathbf{R}^L_{\alpha\beta}$ is the component of the resistance matrix relating quantities α and β: $\beta = \mathbf{R}_{\alpha\beta}\alpha$. The lubrication correction matrix is given by the difference between the exact two-body resistance matrix and the FCM two-body resistance matrix, $\mathbf{R}^L_{\alpha\beta} = \mathbf{R}_{\alpha\beta} - \mathbf{R}^{FCM}_{\alpha\beta}$.

Eq. 2.1.12 can be rearranged to give:

$$\begin{bmatrix} \mathbf{M}_{\mathscr{F}\mathscr{V}}\mathscr{F}^{tot} \\ -\mathbf{M}_{\mathscr{F}\mathbf{E}}\mathscr{F}^{tot} - \mathbf{E}^{\infty} \end{bmatrix} = \begin{bmatrix} \mathbf{I} + \mathbf{M}_{\mathscr{F}\mathscr{V}}\mathscr{R} & -\mathbf{M}_{\mathbf{S}\mathscr{V}} \\ -\mathbf{M}_{\mathscr{F}\mathbf{E}}\mathscr{R} & \mathbf{M}_{\mathbf{SE}} \end{bmatrix} \begin{bmatrix} \mathscr{V} - \mathscr{V}^{\infty} \\ \mathbf{S} + \mathbf{R}^{L}_{\mathbf{ES}}\mathbf{E}^{\infty} - \mathbf{R}^{L}_{\mathscr{V}\mathbf{S}}(\mathscr{V} - \mathscr{V}^{\infty}) \end{bmatrix} \tag{2.1.14}$$

where $\mathscr{F}^{tot} = \mathscr{F} + \mathbf{R}^{L}_{\mathbf{E}\mathscr{F}}\mathbf{E}^{\infty}$ and the resistance matrix $\mathscr{R}$ is given by

$$\mathscr{R} = \begin{bmatrix} \mathbf{R}^{L}_{\mathbf{VF}} & \mathbf{R}^{L}_{\mathbf{\Omega F}} \\ \mathbf{R}^{L}_{\mathbf{VT}} & \mathbf{R}^{L}_{\mathbf{\Omega T}} \end{bmatrix}. \tag{2.1.15}$$

To make the matrix in 2.1.16 symmetric positive definite, we solve for $\mathscr{F}^{lub} = \mathscr{R}(\mathscr{V} - \mathscr{V}^{\infty})$ instead of $\mathscr{V} - \mathscr{V}^{\infty}$.

$$\begin{bmatrix} \mathbf{M}_{\mathscr{F}\mathscr{V}}\mathscr{F}^{tot} \\ -\mathbf{M}_{\mathscr{F}\mathbf{E}}\mathscr{F}^{tot} - \mathbf{E}^{\infty} \end{bmatrix} = \begin{bmatrix} \mathscr{R}^{-1} + \mathbf{M}_{\mathscr{F}\mathscr{V}} & -\mathbf{M}_{\mathbf{S}\mathscr{V}} \\ \mathbf{M}_{\mathscr{F}\mathbf{E}} & -\mathbf{M}_{\mathbf{SE}} \end{bmatrix} \begin{bmatrix} \mathscr{F}^{lub} \\ \mathbf{S} + \mathbf{R}^{L}_{\mathbf{ES}}\mathbf{E}^{\infty} - \mathbf{R}^{L}_{\mathscr{V}\mathbf{S}}(\mathscr{V} - \mathscr{V}^{\infty}) \end{bmatrix} \tag{2.1.16}$$

In eq. 2.1.16 we are using the hydrodynamic stresslet moment, $\mathbf{S}^{FCM}$, which combines the far-field FCM component and the near-field contribution of lubrication forces. The two are related by:

$$\mathbf{S}^{FCM} = \mathbf{S} + \mathbf{R}^{L}_{\mathbf{ES}}\mathbf{E}^{\infty} - \mathbf{R}^{L}_{\mathscr{V}\mathbf{S}}(\mathscr{V} - \mathscr{V}^{\infty}). \tag{2.1.17}$$

In simulations we solve for $\mathbf{S}^{FCM}$, and $\mathbf{S}$ is computed as a post-processing step.

In practice, the FCM grand mobility matrix is not constructed, and instead eqs. 2.1.1 and 2.1.2 are solved directly. The particle velocities can either be found by eqs. 2.1.9 and 2.1.10 or by inverting the lubrication resistance matrix, $\mathscr{F} = \mathscr{R}\mathscr{V}$. For closely packed particles, the particle dynamics will be controlled by the lubrication forces, and thus calculating the particles in this way gives more robust values.

Once the particle velocities are found the particle equation of motion,

$$\frac{d\mathbf{Y}}{dt} = \mathbf{V}, \tag{2.1.18}$$

is integrated forward in time with a third order Adams-Bashforth scheme.

The particle contribution to the bulk stress is given by

$$\langle \sigma_{ij}^{p} \rangle = \frac{N_p}{V} \langle S_{ij} \rangle + \frac{N_p}{V} \langle S_{ij}^{C} \rangle \tag{2.1.19}$$

where $\langle S_{ij}^{C} \rangle$ is the contribution from the elastic contact force, $\langle S_{ij} \rangle$ is the contribution from all other terms, given in eq. 2.1.17, and V is the volume of the domain. The stress from the contact force can be found by using the dipole moment of the force distribution following Batchelor (1970):

$$\langle \sigma_{ij}^{C} \rangle = \frac{N_p}{V} \langle S_{ij}^{C} \rangle = \frac{1}{V} \sum_{i=1}^{N_p} \sum_{j=1}^{N_c^i} -\frac{1}{2} (\mathbf{r}_j - \mathbf{r}_i) \mathbf{F}_{ij}^{C} \tag{2.1.20}$$

where N_c^i is the number of particles within the contact force cutoff distance of particle i, $\mathbf{F}_{ij}^{C}$ is the contact force between particle i and j, which have centers $\mathbf{r}_i$ and $\mathbf{r}_j$. The particle pressure is defined as the trace of the stress tensor from the contact force:

$$\Pi = -\frac{1}{3} (S_{11}^{C} + S_{22}^{C} + S_{33}^{C}). \tag{2.1.21}$$

The phasic average of a variable $\mathbf{g}$ is defined as (Drew, 1983, Yeo and Maxey, 2011),

$$\langle \mathbf{g} \chi_p \rangle (y) = \frac{1}{H_x \times H_z} \left\langle \sum_{i=1}^{N_p} \mathbf{g}^i \chi_p^i(\mathbf{x}) \; dx \; dz \right\rangle, \tag{2.1.22}$$

where χ_p^i is the indicator function of the ith particle and $\mathbf{g}^i$ is the ith particle's value of $\mathbf{g}$. The particle phase average of $\mathbf{g}$ can then by found by

$$\langle \mathbf{g} \rangle(y) = \frac{\langle \mathbf{g}\chi_p \rangle(y)}{\phi_t(y)}. \tag{2.1.23}$$

In this work we will solve FCM in a channel with planar, no-slip walls separated by a distance H_y. Periodic boundary conditions are applied in the streamwise (z) and spanwise (x) or vorticity direction of the mean flow. We use a Fourier spectral method in the periodic dimensions and a spectral element method in the spanwise direction to solve eqs. 2.1.1 and 2.1.2.

2.1.1 Code scaling

The FCM code used in this work is implemented in C++ using MPI for parallelization. For implementation details, please see Yeo and Maxey (2010), Yeo (2011). Unless noted, all FCM simulations were run on the Brown University Center for Computation and Visualization cluster (CCV). The following is the result of code scaling that was completed on the CCV cluster to understand the best parameters for maximum code performance.

The code was run for 5001 time steps on CCV and the total time was recorded for each run. The volume fraction was varied while the channel remained fixed with $L_x = 30a$, $H_y = 24a$, and $L_z = 40a$, where is scaled by the particle radius, a. To limit effects from communication across cores the runs were each performed on a single node. The results are shown in table 2.1c and fig. 2.1.

While the parallelization of the FCM code is vital for efficient computational methods, there are significant changes that could be implemented to accelerate future computations. The most important of these is an efficient load balancing routine, particularly for inverting the lubrication matrix in the inner iteration of the FCM routine. When the particles are tightly clustered together, the lubrication forces are highly singular, and will be localized in one area of the domain. This can lead to inefficient work balancing if the code is parallelized by dividing the channel into equal sized regions, with each node calculating the lubrication forces for those particles located on the node. In some cases, such as the particle clouds discussed in chapter 4, this can become a significant bottle neck in the code.

(a) $\phi = 0.2$ (1376 particles)

Number of cores	Simulation time (s)	Seconds/particle	Seconds/time step
4	5213	3.7885	1.0424
8	2454	1.7834	0.4907
16	1463	1.0632	0.2925
32	2306	1.6759	0.4611

(b) $\phi = 0.3$ (2063 particles)

Number of cores	Simulation time (s)	Seconds/particle	Seconds/time step
4	6331	3.0688	1.2659
8	3034	1.4707	0.6067
16	1773	0.8594	0.3545
32	2553	1.2375	0.5105

(c) $\phi = 0.4$ (2751 particles)

Number of cores	Simulation time (s)	Seconds/particle	Seconds/time step
4	6691	2.4322	1.3379
8	3662	1.3312	0.7323
16	2047	0.7441	0.4093
32	3092	1.1240	0.6183

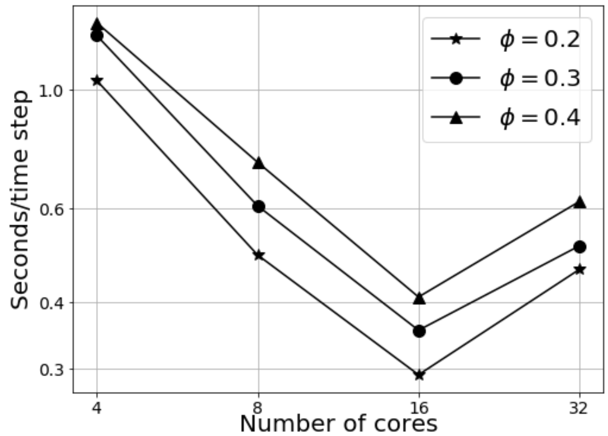

Figure 2.1: Number of seconds per time step for the FCM parallel code to run on the Brown University CCV cluster. Based on these tests, the simulations in this work were set to run on 16 cores.

2.1.2 Notation

For all simulations with the FCM code, the simulation is run in a planar channel with two channel walls at the top and bottom of the channel. The streamwise dimension is considered to be the $z-$axis, denoted by the subscript 3. The direction between the channel walls, or velocity-gradient direction, is y, denoted by 2. The third dimension is the direction of mean vorticity, denoted by x and the subscript 1. The channel is periodic in the x and z directions.

Using this notation, and denoting the ijth component of the stress tensor as σ_{ij}, the shear stress is σ_{23}, and the first and second normal stress differences are given by $N_1 = \sigma_{33} - \sigma_{22}$ and $N_2 = \sigma_{22} - \sigma_{11}$.

2.2 Force chain development: the role of the inter-particle contact force

Stokes flows are typically reversible, however, in carefully conducted experiments the particle surface roughness has been shown to break the symmetry of the flow causing the particles to be irreversibly displaced. This has been studied in great depth by Da Cunha and Hinch (1996) for two equal sized particles and by Zarraga and Leighton (2002) for particles with different sizes. In both cases, as one particle overtakes the other particle both particles are displaced across streamlines away from their original position. This displacement increases with the particle surface roughness (Da Cunha and Hinch, 1996). In simulations, the contact force models the particle surface roughness, in addition to preventing the particles from overlapping. While the lubrication forces between two spheres will theoretically prevent the particles from touching, in the simulations some form of a contact force is needed to prevent particle overlaps due to the discrete time step.

In the Force Coupling Method, the contact force between two particles is modeled by a short range force that acts along the line of the centers of the particles and depends only on the particles sizes and the distance between the two particles (Yeo and Maxey, 2010). This force is zero when the particles are separated by more than a small distance, typically a gap width of less than 0.05% of a particle radius. In the section that follows we will consider two different forms of the particle contact force, and the effects that changing the contact force has on two- and three-particle dynamics and the force chains that develop in steady suspension shear flows.

Based on the work of Yeo and Maxey (2010), the following two contact force models for the force on particle j due to particle i, with centers at $\mathbf{r}_j$ and $\mathbf{r}_i$, are

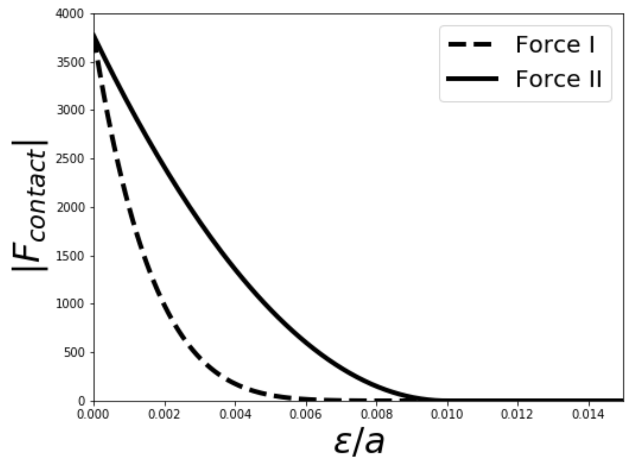

Figure 2.2: (Value of the contact forces in eqns. 2.2.1 and 2.2.2 with $F_{ref} = 200$ and $R_{ref} = 2.01a$. ϵ is the size of the gap between the two particles, $epsilon = |\mathbf{r}_i j| - 2a$

considered:

$$F_{ij}^{I} = \begin{cases} 6\pi\mu a F_{ref} \left(\frac{R_{ref}^2 - |\mathbf{r}_{ij}|^2}{R_{ref}^2 - 4a^2}\right)^6 \frac{\mathbf{r}_{ij}}{|\mathbf{r}_{ij}|}, & |\mathbf{r}_{ij}| \leq R_{ref} \\ 0, & \text{otherwise} \end{cases} \tag{2.2.1}$$

$$F_{ij}^{II} = \begin{cases} 6\pi\mu a F_{ref} \left(\frac{R_{ref}^2 - |\mathbf{r}_{ij}|^2}{R_{ref}^2 - 4a^2}\right)^2 \frac{\mathbf{r}_{ij}}{|\mathbf{r}_{ij}|}, & |\mathbf{r}_{ij}| \leq R_{ref} \\ 0, & \text{otherwise} \end{cases} \tag{2.2.2}$$

Here,$\mathbf{r}_{ij} = \mathbf{r}_j - \mathbf{r}_i$, R_{ref} is the contact force cutoff distance, and F_{ref} is a parameter chosen to control the minimum separation of the particles. These forces are shown in fig. 2.2. In the simulations considered here, $F_{ref} = 100$ for Poiseuille flows and $F_{ref} = 200$ for Couette flows, while R_{ref} varies from $2.0001a$ to $2.01a$. At values of R_{ref} higher than $2.01a$ the excluded volume from the minimum contact distance between the particles artificially inflates the particle size and thus the suspension volume fraction, which does change the suspension rheology.

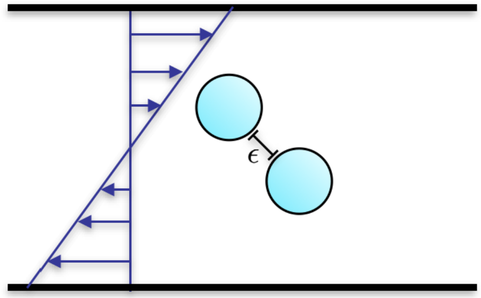

Figure 2.3: Schematic of two particle configuration for the contact force calculations.

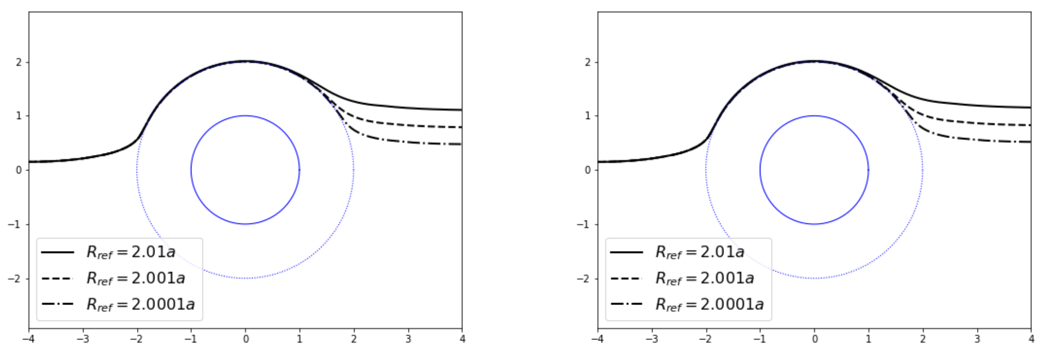

Figure 2.4: Relative trajectories of two particles in a shear flow. (Left) Force I. (Right) Force II. The blue dotted line is a circle with radius $2a$ representing the point at which the two particles are in contact.

2.2.1 Two particle contacts

In this section, we consider how the exact form of the contact force between two particles displaces the particles as they collide in a shear flow, as shown in the schematic in fig. 2.3, and what role the parameter R_{ref} has on the particle trajectories and forces. Here, we look at the effect of changing the form of the contact force as well as the cutoff value, R_{ref}, simulating smoother and rougher particles.

The relative particle trajectories are shown in fig. 2.4. The particles have an initial separation $\Delta_y(0) = 0.2$. Both contact force models show the same trend qualitatively. At higher values of R_{ref}, representing a larger surface roughness, the particles have a larger displacement from their original positions. Looking at the differences between the contact force models, if R_{ref} is fixed, simulations with force model II have a slightly large displacement of about $0.045a$. Interestingly, the maximum force reached is constant in almost all simulations, $|F_{max}| = 19.5$.

Run	Force Model	R_{ref}	ϵ_{min}	$\|F_{max}\|$	Final separation, $\Delta_y(T)$
A	I	2.01a	0.00585	19.485	1.168a
B	I	2.001a	0.000584	19.520	0.833a
C	I	2.0001a	0.0000598	15.810	0.490a
D	II	2.01a	0.00928	19.545	1.215a
E	II	2.001a	0.000928	19.723	0.875a
F	II	2.0001a	0.0000927	19.845	0.539a

Table 2.2: Contact forces between two particles in a shear flow. $F_{ref} = 200$ for all runs.

2.2.2 Three particle contacts

2.2.2.1 Triangular configuration

Here, we consider two cases with three particles arranged with their centers on a plane in the vorticity direction, again in a shear flow. The first configuration is inspired by the experiments and simulations by Pham et al. (2015), where three particles in a triangular arrangement are subjected to an oscillating shear flow. In the experiments, the three particles are displaced from their original positions after one complete oscillation, with the displacement increasing for particles with rougher surfaces. In the second case, we consider a configuration similar to the two particle configuration in sec. 2.2.1. A third particle is added far enough away from the other two particles so that it always maintains a separation larger than the contact force cutoff value, R_{ref}, from both of the other two particles, but close enough that it

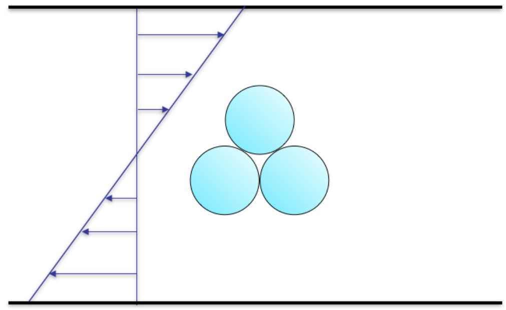

Figure 2.5: Schematic of three particle configuration.

interacts with the other particles though lubrication forces.

In the triangular configuration, shown in fig. 2.5, the particles are positioned at the vertices of an equilateral triangle with side length $R_{ref} + \frac{R_{ref}-2a}{5}$, where the second term is added so that the contact force is not activated when the particles are initially positioned. The suspended particles are then oscillated in a shear flow with period $T = 8\dot{\gamma}t$, $\dot{\gamma} = 1$, and the initial and final positions of the particles are compared along with the particle trajectories. In each case, contact force I in eqn. 2.2.1 is used with $F_{ref} = 200$ and $R_{ref} = 2.0001a, 2.001a$, or $2.01a$.

The initial and final particle positions are shown in fig. 2.6, along with the particle trajectories. Here, it is very clear that the particles with the largest value of R_{ref} have the largest displacements from their original positions. While the particles in fig. 2.6c with $R_{ref} = 2.0001a$ return close to their initial positions, the particles in fig. 2.6a with $R_{ref} = 2.01a$ are no longer in contact after one oscillation.

To quantify how are the particles are displaced from their initial trajectories, we define the mean particle displacement as:

$$D(t) = \frac{1}{3}\sum_{i=1}^{3}\left[\Big(z^i(t) - z^i(T/2-t)\Big)^2 + \Big(y^i(t) - y^i(T/2-t)\Big)^2\right]^{1/2}, \qquad (2.2.3)$$

(a) $R_{ref} = 2.01a$

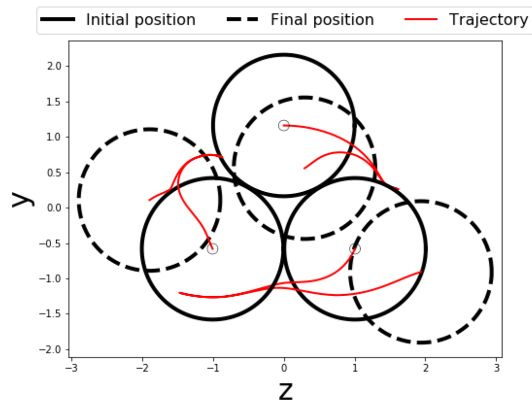

(b) $R_{ref} = 2.001a$

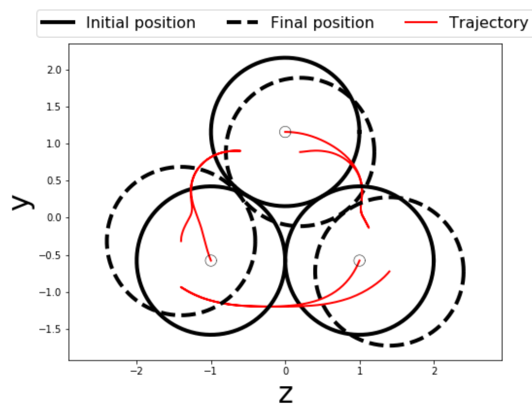

(c) $R_{ref} = 2.0001a$

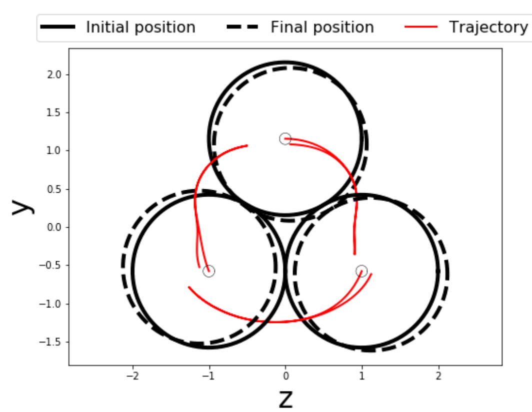

Figure 2.6: Initial (solid) and final (dashed) particle positions after one oscillation. The red solid lines show the particle trajectories, which originate in the small black circles marking the original positions of the particle centers.

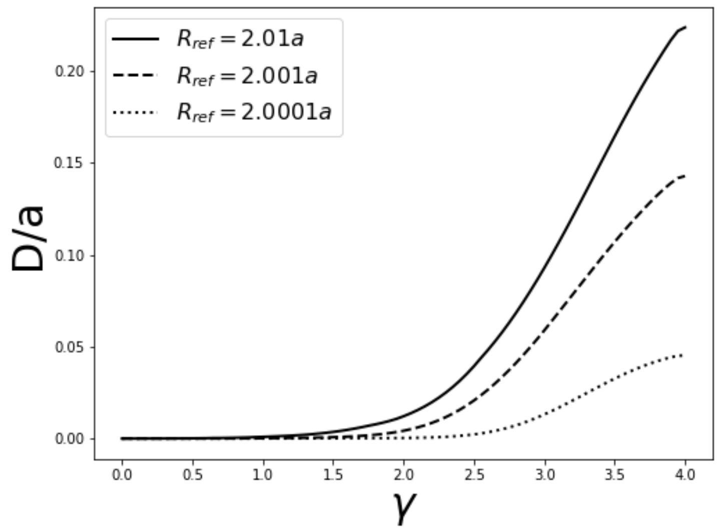

Figure 2.7: Mean particle displacement on the forward and back half cycles for each contact force cutoff value. γ is the accumulated strain on the back half cycle.

where N_p is the total number of particles and $z^i(t)$ and $y^i(t)$ are the z and y positions of the ith particle at time t (Pham et al., 2015). The mean particle displacement, plotted in fig. 2.7, gives a measure of when during an oscillation period the particles depart from their initial trajectories. The very small value of D during the first several strain units of the back half cycle indicates that the displacement occurs in the initial and final quarter periods of the oscillation, which is not surprising as that is when the particles are closest together. The values found here for the particle displacements are in the range of those found by (Pham et al., 2015), however as the particle roughness in the simulations has not been calibrated to that of the experiements it is impossible to draw an exact comparison.

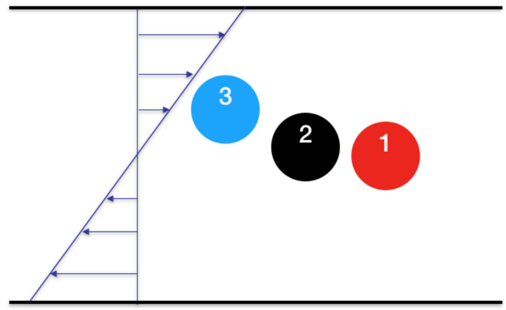

Figure 2.8: Schematic of three particle configuration.

2.2.2.2 Hydrodynamic irreversibility in three particle configurations

In this section, we fix $F_{ref} = 200$ and $R_{ref} = 2.001a$. Two particles, labeled 1 and 2 in fig. 2.8, are located close enough that they will come into contact, as in 2.2.1. The third particle, labeled 3 in fig. 2.8, is located downstream from the other two particles, and offset enough that it will not come into contact with particle 2, but close enough that they will interact through lubrication forces. The oscillation period is chosen to be long enough that no particles are in within the contact force barrier or the lubrication force barrier after half an oscillation.

The initial and final positions of the particles after a sample simulation are shown in fig. 2.9. All three particles are displaced from their original position. The minimum distances between the particles are given in table 2.3, which confirms that only particles 1 and 2 get close enough that the particle-particle contact force is activated. Particle 3 displays the smallest displacement from its original position, however, it still has a small irreversible displacement.

Repeated simulations show that the final position of particle 3 depends on the relative spacing between particles 1 and 2, and particles 2 and 3. In fig. 2.10, the positions of particles 1 and 3 are fixed, and the initial position of particle 2 is

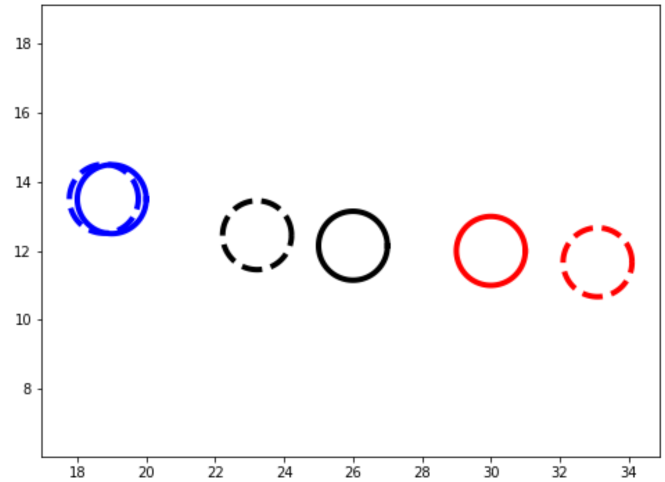

Figure 2.9: Initial (solid) and final (dashed) particle positions after one oscillation. Particle 1 is red, particle 2 is black, and particle 3 is blue.

Particles	Minimum separation
1 & 2	2.00059
1 & 3	2.00615
2 & 3	2.10701

Table 2.3: Minimum separation between the particles in the simulation in fig. 2.9. In this simulation the cutoff value for the contact force is $R_{ref} = 2.001a$, which means particles 1 & 2 are the only particles that come into contact.

varied. The exact dynamics of the particle trajectories depend on when during the oscillation cycle particle 3 moves past particle 2 relative to the interaction between particles 1 and 2, so it is impossible to draw an exact conclusion on the displacement of particle 3 without controlling when during the oscillation the particles come into contact. However, it is clear that if particle 2 is closer to particle 3, and thus further from particle 1, particle 3 has a larger displacement. This is a case where a particle that undergoes purely hydrodynamic interactions with other particles can display an irreversible displacement if it is near enough to particles that do come into contact. These third-party contact displacements may be responsible for particle self-diffusion

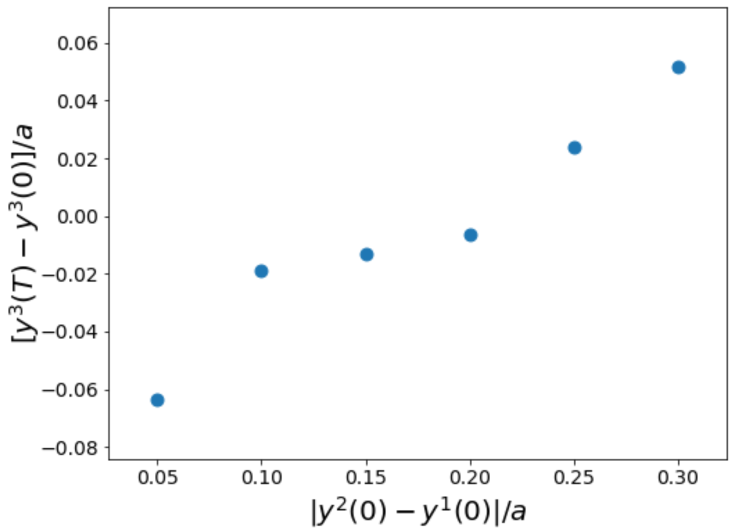

Figure 2.10: Change in the position of particle 3 based on the separation between particles 1 and 2. Particle 1 is kept fixed at $y^1(0) = 0.0$, and particle 3 is fixed at $y^3(0) = 1.5a$. Particle 2 is moved between $y^2(0) = 0.05a$ and $y^2(0) = 0.3a$.

in cases where contact between particles does not occur.

2.2.3 Full suspension particle contacts

Having studied the implications of the contact force on two-body and three-body interactions, this section discusses how those dynamics translate into many-body interactions in a fully seeded suspension. We will restrict to a Couette flow at volume fractions of $\phi = 0.3$ and 0.4, with monodispersed particles.

To understand the dynamics of the particle contact pressure as the suspension undergoes a shear flow from an initially random configuration, simulations were conducted with a range of contact force cutoff values R_{ref} at volume fractions $\phi = 0.3$ and $\phi = 0.4$ in a Couette flow. The channel size is fixed with $L_x = 30$, $L_z = 40$, and channel height $H_y = 40$, which results in 3438 particles with $\phi = 0.3$ and 4853 particles with $\phi = 0.4$. The shear rate is fixed at $\dot{\gamma} = 1$. The contact force scaling $F_{ref} = 100$, and the cutoff is varied from $R_{ref} = 2.00001a$ to $2.1a$.

The average particle contact pressure, $\langle P \rangle$, is shown in fig. 2.11c. The contact pressure is scaled by the shear stress

$$\tau = \mu_r \mu \dot{\gamma}, \tag{2.2.4}$$

where the effective viscosity is given by

$$\mu_r = 1 + \frac{1}{\mu \dot{\gamma}} \langle \sigma_{23}^P \rangle. \tag{2.2.5}$$

In both cases, the contact pressure takes several strain units to develop, and the final value of the steady contact pressure increases with the value of R_{ref}. This is possibly due to the contact force cutoff creating an excluded volume around the particles, leading to an artificially increased volume fraction. In both cases, the time to a steady constant pressure decreases with increasing R_{ref}. With smaller values of R_{ref} the particles must be more tightly confined for the contact pressure to develop, which leads to slower overall contact pressure development.

Additional simulations were completed with longer channels, to increase the number of particles in the suspension. For the following simulations, $L_z = 80$.

In fig. 2.12 we consider all particles that come into contact during a time period $T = [t_1, t_2]$, with a total elapsed time of two strain units, and look at the the average particle separation x and y directions,

$$\langle \Delta(x^i - x^j)[F_x] \rangle = \frac{1}{N_c} \sum_{k=1}^{N_c} |(x^i(t_2) - x^j(t_2)) - (x^i(t_1) - x^j(t_1))|, \tag{2.2.6}$$

(a) $\phi = 0.3$

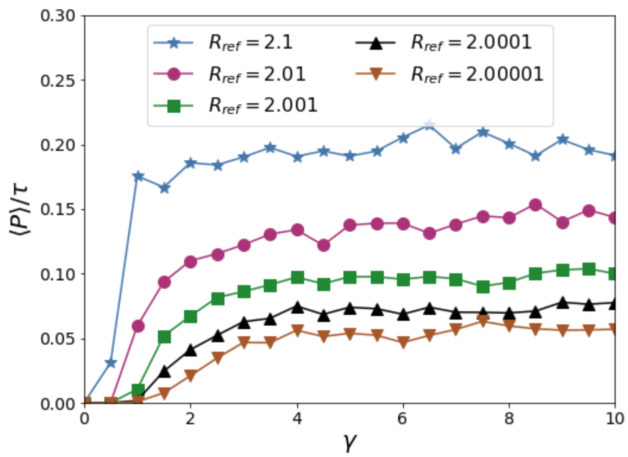

(b) $\phi = 0.4$

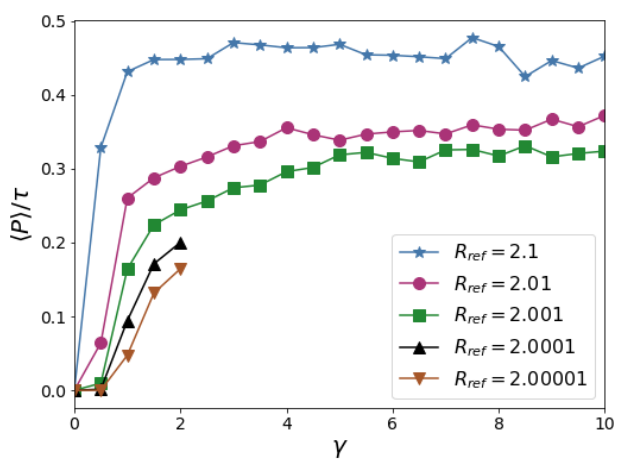

(c) Average particle contact pressure over the first ten strain units.

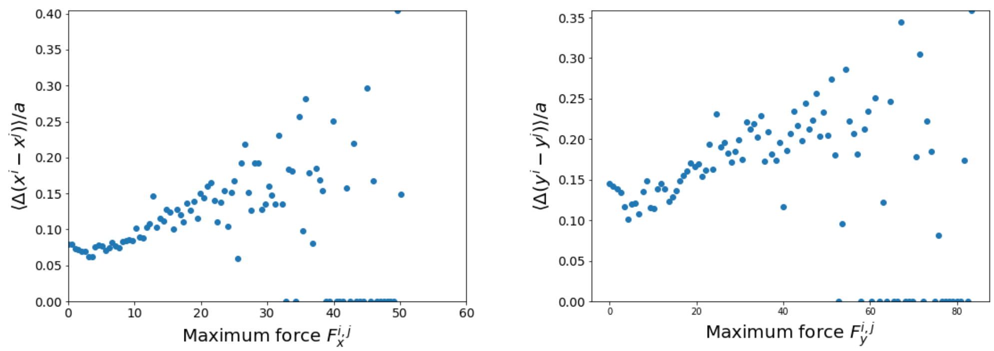

Figure 2.12: Average particle separation due to a maximum contact force of a given magnitude over four strain units in the vorticity direction (left) and cross-stream direction (right). For small contact forces the separation is relatively uniform, but for large contact forces where the particles may be tightly confined between other particles or the wall, the displacement has a large variation.

where N_c is the number of particle contacts during the time period $[t_1, t_2]$ that have a maximum contact force of $F_x^{i,j}$. The particle separation due to a contact interaction on this timescale is on the order of 5% to 30% of a particle radius. Because the force between two particles is not constant over the length of a contact interaction, fig. 2.12 considers the maximum value of the contact force over that two strain unit period. Overall, larger contact forces are associated with larger displacements, however, the largest contact forces represented by points on the far right of fig. 2.12 have a large variation in the particle separation. When a particle is tightly confined by multiple particles, it will experience a large net contact force. However, the confined particle is not free to move due to the presence of its neighbors, so it will have a small relative displacement. Thus, a large contact force is not sufficient to generate a large particle displacement.

Particles that do not experience a contact interaction can have a small displacement, as shown in 2.13. Here, particles are sorted by whether or not they experience a contact force over two strain units. The particles that experience the largest displacements typically do experience a contact force, however a smaller number of displaced

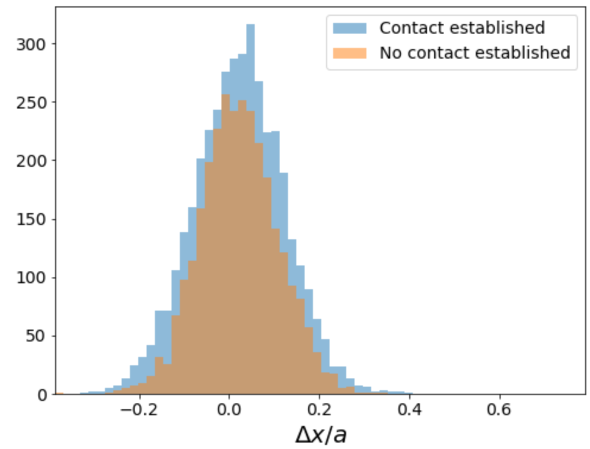

Figure 2.13: A histogram of particle displacements in the vorticity direction over two strain units. Blue bars correspond to particles that experience a contact force, orange bars correspond to particles that do not experience a contact force.

without a contact force. Of those particles that have a non-zero displacement but do not come into contact with another particle, all are within the lubrication cutoff of another particle that does experience a contact event. Thus, those particles are displaced through a similar three-particle interaction as in sec. 2.2.2.2.

One important feature that emerges in densely packed suspensions is contact force chains, or strings of particles connected by contact forces. These force chains transmit stresses within the suspension and can be quite large at high volume fraction, spanning the entire channel (De Gennes, 1979, Gallier et al., 2015). Table 2.4 contains statistics on the force chains that develop for suspensions with $\phi = 0.3$ and $\phi = 0.4$. The length of a force chain, l, is defined as the number as the number of particles that have a separation of less than R_{ref}, and consider those chains with $l > 2$ (i.e., pairs of particles within the contact force cutoff distance are excluded if they have no other contact force neighbors.) At high volume fraction, a significant proportion of particles experiences a contact force at a given time. On average, once a contact force begins it lasts for $\gamma = 1.24$ strain units when $\phi = 0.3$. After the

	$\phi = 0.3$	$\phi = 0.4$
$\langle F_{max} \rangle$	25.46	
% of particles in contact	57.33%	
Mean free path (a)	13.43	
Maximum contact force	539.3072	
Average length of contact (γ)	1.33	
Number of force chains $(l > 2)$	508	275
Maximum force chain length, $\max l$	37	5111
Mean force chain length, $\langle l \rangle$	5.56	24.88

Table 2.4: Contact force and force chain data for suspensions with $\phi = 0.3$ and $\phi = 0.4$. Data is taken at an accumulated strain of $\gamma = 200$. In both cases $R_{ref} = 2.01a$.

contact breaks, the particle has a mean free path of $z = 14.50a$ before it comes into contact with another particle.

As noted by (Gallier et al., 2015), and shown in 2.14, the contact force chains are primarily aligned along the compression axis in the shear flow.

In this chapter, we have shown the role of the contact force model in irreversible two- and three-particle contacts. Even if a particle does not come into contact with another particle, displacements from other contacts can act to alter the particle trajectory. This third-party contact force displacement can be key in explaining suspension dynamics when not all particles experience a contact force but do have a non-zero self-diffusivity. At high volume fraction, chains of particles connected by contact forces dominate the suspension dynamics. At volume fraction $\phi = 0.4$, over half the particles are connected in one giant force chain that spans the channel.

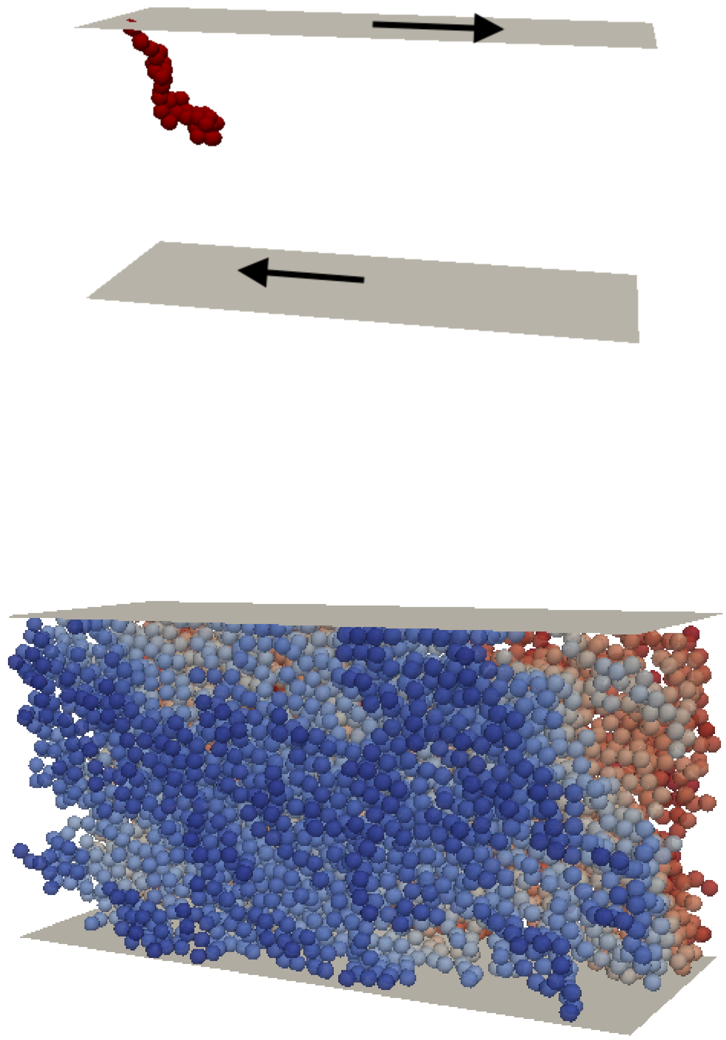

Figure 2.14: Sample contact force chain for $\phi = 0.3$ (top) and $\phi = 0.4$ (bottom). For $\phi = 0.4$ the particles are color-coded based on their x position to aid in visualization. Only particles that are in the chain are shown.

Chapter Three

Particle dispersion in suspension plugs

In this chapter, we discuss FCM simulations of a sheared, finite plug of particles in a channel, with pure fluid on either side of the plug in the streamwise direction. The FCM results are compared to experiments elucidating the particle motion in the front of the plug. The particle fluxes that develop are anomalous in comparison to results for homogeneous suspensions that fill the channel without regions of pure fluid. Results for the particle contact pressure are shown to demonstrate the importance of the contact force in the development of the plug system. The work reported in this chapter has been published in Cui et al. (2017). The experiments were carried out by Francis Cui (School of Engineering) under the supervision of Professor Anubhav Tripathi. They are included in the chapter for completeness.

******

3.1 Introduction

The field of microfluidics is rich with potential biomedical technologies in cell sorting and isolation, as well as applications involving transport of engineered micro- or nano-particles. The emergence of micro-scale transport of suspensions at low Reynolds number thus necessitates a deeper fundamental understanding of particle dispersion within these systems. For example, samples may consist of finite volumes of suspended particles that are flowed back and forth between stations in a microchannel. Motivated by this need, we consider the motion of a periodically sheared, finite plug of suspended, neutrally buoyant non-Brownian particles within a pressure-driven Stokes flow and the extent to which the motion is reversible. The plug is formed as a finite length of a concentrated suspension of particles, with a sharp front, bounded only by the pipe or channel walls and is free to disperse in the direction of flow as illustrated in Fig. 3.1. The plug is sheared in a forward flow for half a period T and then by a reversed flow. A question then is whether the plug returns to its original form or not. This question goes back to the reversibility, or not, of a Stokes suspension in shear flow. This may be posed in terms of the reversibility of individual particles or the bulk reversibility of the mean distribution of particles within the plug.

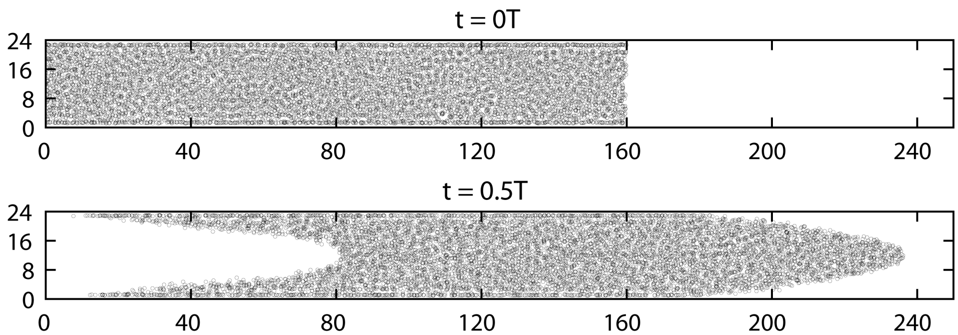

Figure 3.1: Sketch of the initial suspension plug at $t = 0$ and the plug after being sheared in a Poiseuille flow for a half-period $t = 0.5T$.

Previously, Stokesian dynamics simulations for self-diffusion of particles in a steady, uniform shear flow have shown that the particle motion is generally chaotic in the long term (Drazer et al., 2002). This leaves open the question as to the source of the chaos: whether this is result of the irreversible contact forces between non-Brownian particles or the inherently nonlinear hydrodynamic interactions of multiple particles. Experiments and simulations by Pine et al. (2005) for oscillating uniform shear flow demonstrate that the overall self-diffusion between oscillation cycles is negligible if the strain amplitude is below a threshold level, which is lower at larger volume fraction. Subsequent studies (Corté et al., 2008, Metzger and Butler, 2010, Metzger et al., 2013, Pham et al., 2015) show that this transition between reversible and irreversible dynamics can be explained largely in terms of the contact interactions. The hydrodynamic interactions, long range or short, alone do not significantly contribute to the chaotic dynamics in contrast to the context of sedimenting particles

(Jánosi et al., 1997). Experiments show that the irreversible interactions and displacements between multiple particles in a Couette flow correlate with the particle roughness (Ingber et al., 2006, Popova et al., 2007).

Consideration of how a suspension plug will develop in an oscillatory flow introduces issues regarding both the degree of reversibility in a transient flow and the effects of sharp interfaces between the suspension plug and the surrounding fluid. This configuration may be compared to the dispersion of an unbounded suspension cloud in a uniform oscillating shear flow studied by Metzger and Butler (2012). The cloud is found to extend with low strain amplitude and moderate volume fraction. At high volume fractions the cloud can form a distinct shape with "galaxy like" arms. For the oscillating plug we find that the sharp boundaries lead to anomalous cross-stream particle fluxes.

Existing theoretical models for particle fluxes within a suspension are based on the premise of small variations in the local particle concentration or in the shear-rate, and rely on local volume averaging and conditions of local equilibrium. The earliest of these assume a diffusive process (Leighton and Acrivos, 1987, Phillips et al., 1992). More recent suspension balance models for particle fluxes in a sheared suspension are based on an averaged momentum or force balance, whereby the particle flux relative to the suspension flow is related to the divergence of the averaged particle stress tensor and the effective hydrodynamic drag between the particle phase and the suspension as a whole (Nott and Brady, 1994, Morris and Boulay, 1999, Ramachandran and Leighton, 2008, Nott et al., 2011, Denn and Morris, 2014). These models give better results in representing for example the migration of particles, from regions of high shear stress towards the low shear stress near the centerline of a Poiseuille flow (Nott and Brady, 1994) as seen in experiments (Koh et al., 1994, Hampton et al., 1997) and numerical simulations (Yeo and Maxey, 2011). However, they do not take into account particle layering in the near wall region and predict close packing at the center of the channel, which is not seen in experiments for low or moderate volume fractions (Snook et al., 2016). A feature of non-Brownian suspensions is the role of particle roughness and the short-range surface repulsion that prevents direct contact of the particles as they move relative to each other in a shear flow (Arp and Mason, 1977, Gadala-Maria and Acrivos, 1980). Surface roughness introduces an inherent irreversibility for the relative motion of two particles and has been shown to modify the pair distribution function (Rampall et al., 1997, Blanc et al., 2011). This has a direct effect on the rheology and generates a resultant displacement between particles contributing to the dispersion (Da Cunha and Hinch, 1996, Zarraga and Leighton, 2002).

The present study is for a suspension plug, which has an initial particle volume fraction of 30% and is oscillated forward for half a cycle and then back in a Poiseuille flow for different strain amplitudes. We examine the extent to which the motion is reversible in the bulk and how particles are redistributed. Earlier studies by Butler et al. (1999) and by Morris (2001) of a fully seeded suspension in an oscillatory Poiseuille flow suggest that at low strain amplitudes there may be an anomalous net flux of particles towards the wall, while the more usual migration to the center is seen at larger amplitudes. More recent experiments show only a migration towards the center with increasing strain amplitude and that the onset of irreversibility, in terms of self-diffusion between oscillation cycles, occurs simultaneously across the channel even though the shear rate varies across the channel (Guasto et al., 2010).

The objective of the present work is to examine the change in shape of the plug over multiple oscillations and to characterize the flux of particles in the presence of a sharp variation in the concentration across the plug boundaries. Significant particle stresses and pressure may develop within the plug leading to a sharp transition in pressure at the plug front. Particle stresses may be transmitted from the near-wall region to the core leading to non-local effects on the dynamics at the plug front. Overall, this configuration of a suspension plug oscillating in a Poiseuille flow provides a clearly defined context in which to study the transient dynamics of shear-driven particle migration in the presence of concentration interfaces. Experimental results will be described in Sec. 3.2, and compared to two sets of simulation results in Secs. 3.3.1 and 3.3.2. The pre-sheared simulations in Sec. 3.3.1 correspond to the experimental conditions, while the simulations with a plug with a flat front in section 3.3.2 provide greater insight into the macro- and micro-scopic irreversibility of the plug.

3.2 Experimental results

Spherical monodisperse polymethylmethacrylate particles of mean diameter $d = 90\,\mu$m and density $\rho = 1.18\,\mathrm{g\,cm^{-3}}$ were suspended in a solution comprising of equal amounts by volume of poly(ethylene glycol-ran-propylene glycol) monobutyl ether (Sigma Aldrich) and water, in which potassium iodide (Sigma Aldrich) was dissolved so as to match the density of the particles. The density difference $\Delta\rho$ was controlled so that a settling velocity of $d^2 g \Delta\rho / 18\eta \approx 0.1\,\mu\mathrm{ms}^{-1}$ was achieved, thus ensuring a maximum settling distance of less than one particle diameter over the course of an experiment. The refractive index of the fluid was intentionally mismatched with that of the particles so that they were plainly visible in diffuse white light. The fluid was analyzed with a rheometer (TA Instruments) and found to be Newtonian, with a viscosity $\eta = 0.128\,\mathrm{Pa\,s}$ at 23°C. Suspensions of volume fractions 1% and 30% were prepared.

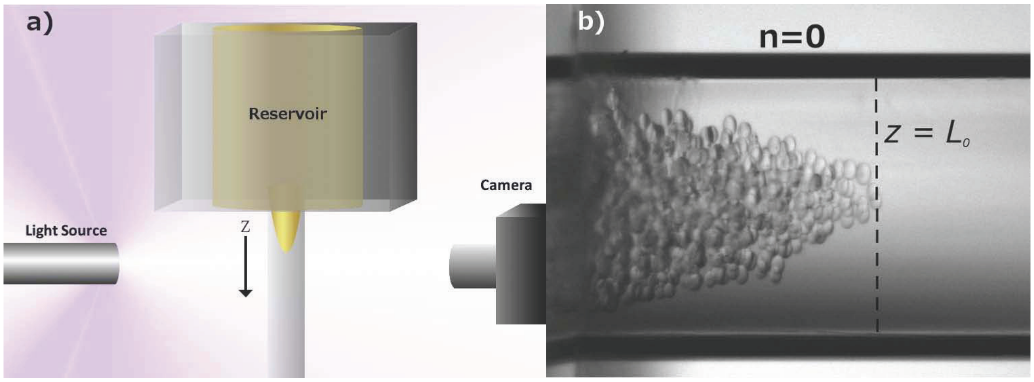

Figure 3.2: (a) Schematic diagram of the experimental setup. A glass capillary, connected to a syringe pump, is inserted into the suspension reservoir from below. (b) Suspension of concentration $\phi = 30\%$ is drawn in a distance $z = L_0$ and then repeatedly sheared.

Fig. 3.2(a) shows the experimental design that was used to observe plug dispersion in periodic flows. Approximately 400 μL of suspension was housed in a small PDMS block with an 8 mm diameter cavity open to the atmosphere. A small entry point was punched in the bottom of the block, allowing a 2 mm glass capillary with inner diameter $D = 1.16$ mm to penetrate the suspension. This setup ensured minimal interference from any air bubbles entrained during the mixing process, allowing them to rise to the surface and not into the plug. The capillary was connected to a 25 μL glass syringe (Hamilton) and fixed vertically so that the end submerged in the reservoir pointed upward. Both capillary and syringe were filled with the same fluid as in the suspension. Flow within the capillary was oscillated by a syringe pump (Harvard Apparatus) at various square-wave flow rates so as to not exceed a Reynolds number of $Re = 0.01$.

For each value of strain, the suspension was drawn in an initial distance of $L_0 \approx D$ from the opening of the capillary (Fig. 3.2(b)) and then pumped periodically for 20 cycles. For the entire range of strain amplitudes tested, the period of oscillation T remained at 10 seconds, giving flow rates that ranged from 6.0 to 39.5 μLmin^{-1}. Images were captured at the beginning of each cycle by a CCD camera (Basler), which was fitted with a high-magnification lens and mounted on a three-dimensional traversing system. The accuracy of particle location measurements depended on the quality of the image and the degree of particle overlap. House-written MATLAB scripts were then implemented for particle tracking and counting.

For both low and high concentrations the effect of strain amplitude γ_0 on the reversibility of the plug configuration was examined by measuring the dimensionless extension $E = (z - L_0)/D$ of the initial parabolic plug front, where z denotes the distance from the capillary opening. An oscillation cycle consisted of a forward motion for half a period $T/2$ followed by a reversed flow for another half period and z is measured at the end of a cycle. The strain amplitude is measured as $\gamma_0 = U_B T/D$, where U_B is the bulk velocity of the flow. This is consistent with previous studies (Butler et al., 1999, Morris, 2001) and γ_0 corresponds to the ratio of the forward excursion of the plug in a half-cycle to the tube radius $R = 0.5D$. Considering previous observations (Pine et al., 2005, Metzger and Butler, 2012, Guasto et al., 2010) on concentration thresholds for irreversibility, we anticipated minimal dispersion for dilute concentrations, regardless of applied strain. Plug extension over time for $\phi = 1\%$ at various strain amplitudes, plotted in Fig. 3.3(a), indeed indicates no significant axial particle migration, with a maximum extension of 0.07 (slightly less than one particle diameter) for all γ_0. The system retains its reversibility in the bulk in spite of large amounts of accumulated strain. At this low concentration there is a dearth of hydrodynamic interactions or contacts between particles. Moreover, there seems to be a lack of correlation between extension and amount strained; final plug front positions (measured by tracking the centerline particle farthest from the capillary opening) for $\gamma_0 = 1.4$ and 5.4 remain quite close to L_0 while those for $\gamma_0 = 0.8$, 2.8 and 4.0 stray slightly farther away. Any small deviations thus appear to be arbitrary and not significant. Fig. 3.3(a) gives then an estimate for the error

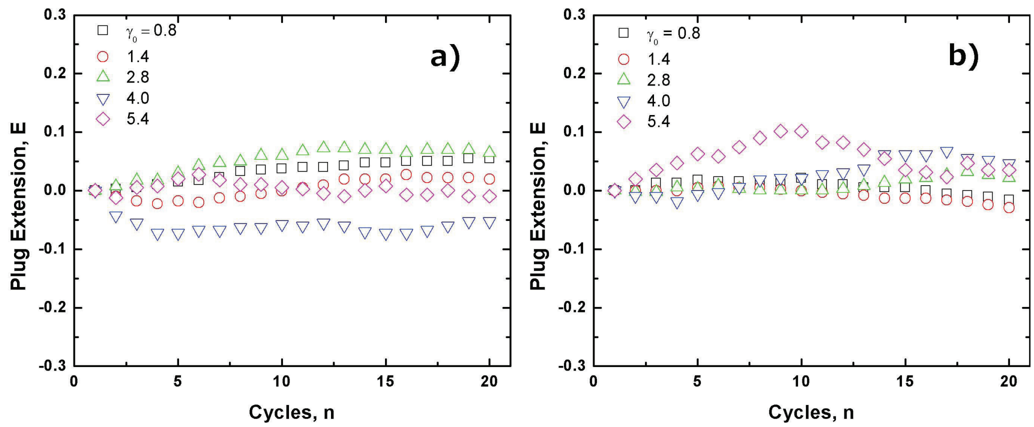

Figure 3.3: (a) Plug extension E along the capillary axis for $\phi = 1\%$. The plug tip remains close to its original position L_0 throughout the duration of shearing tested. (b) Extension values for $\phi = 30\%$ are similar in magnitude to those of dilute concentrations. Strain amplitudes: $\square, \gamma_0 = 0.8$; $\bigcirc, \gamma_0 = 1.4$; $\triangle, \gamma_0 = 2.8$; $\nabla, \gamma_0 = 4.0$; $\diamond, \gamma_0 = 5.4$.

in the experimental data as $\pm 0.07D$, as the plug with $\phi = 1\%$ should have zero net expansion.

With $\phi = 30\%$, we would anticipate that the particle motion is irreversible for strain amplitudes in for a significant portion of the range $\gamma_0 = 0.8 - 5.4$ considered here. If the suspension flow retains an approximately Poiseuille form, the shear rate at the tube wall is $4U_B/R$ and the local strain amplitude will vary linearly between zero at the centerline and $2\gamma_0$ at $r = R$. Based purely on local strain amplitudes the results for oscillating Couette flow in a fully-seeded suspension (Pine et al., 2005), the threshold for chaotic self-diffusion is a peak to peak strain amplitude of about 2. Corresponding experiments for oscillatory Poiseuille flow in a channel (Guasto et al., 2010) show that the onset of irreversibility occurs simultaneously across the channel even though the local strain may be zero at the centerline. We may further compare with the experiments for particle clouds suspended in an oscillatory shear flow (Metzger and Butler, 2012). The sharp transition in particle concentration across the leading edge of the plug would suggest that the plug expands until the concentration drops below a threshold level for a given strain amplitude.

Results for the plug extension E, near the centerline, for $\phi = 30\%$ are shown in Fig. 3.3(b). We find that the plug extension measurements are close in magnitude to those of dilute suspensions and that particles along the central axial streamline remained in high local concentration, exhibiting inappreciable net particle migration. The higher concentrated suspension does however reveal a distinguishable trend in the root mean square extension with increasing γ_0; the average distance between the plug front and L_0 over 20 cycles increases with higher strain amplitudes. These values though remain relatively small for all γ_0, with E_{rms} never exceeding 0.06 (roughly $0.75d$). Although the forward-most particles creep further away from L_0 with greater applied strain, the direction of migration along the center streamline still remains unpredictable, as the plug front seems just as likely to contract or extend. The small displacement of the plug front and its apparent impartiality towards direction of migration, even in high concentration and under high strain, suggest that the effects of particle interactions near the axis of the plug are insufficient to induce observable particle migration in the direction of flow.

Although the macroscopic bulk reversibility appears to be preserved along and near the central axis, significant particle migration near the capillary walls occurs for $\phi = 30\%$ under higher strain. At $\gamma_0 = 3.6$ to 5.4, beads at the outer radii were observed to migrate in the positive z-direction (i.e., away from the reservoir) after each successive cycle of shearing, filling the space between the parabolic plug front and walls. After 20 cycles at the highest strain, these outer beads had migrated nearly as far as $z = L_0$. Stroboscopic images reveal the chaotic nature of particle migration in the near-wall region, as beads can be displaced by several particle diameters in the streamwise direction between each period of shearing. In contrast, beads in the axial tip are never displaced by more than half a particle radius per cycle. Measurements

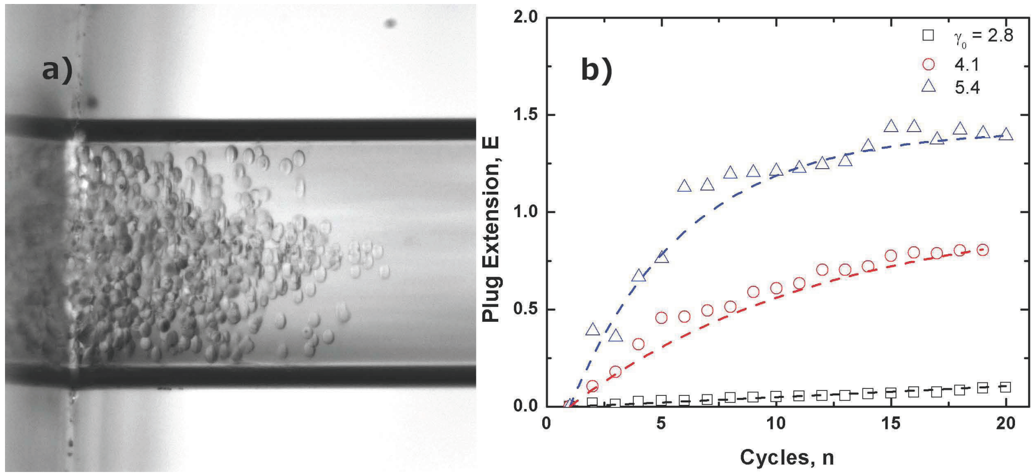

Figure 3.4: (a) For $\phi = 30\%$ and $\gamma_0 = 5.4$, significant particle migration is observed near the walls while the nose of the plug displaces little. (b) Wall extension values for various γ_0 at $\phi = 30\%$ were collected by tracking the furthest particle in the near-wall regions. Strain amplitudes: $\square, \gamma_0 = 2.8$; $\bigcirc, \gamma_0 = 4.1$; $\triangle, \gamma_0 = 5.4$.

of plug extension along the walls (shown in Fig. 3.4) convey the strong dispersive effect of utilizing high flow strain. While negligible near-wall particle migration was observed for $\gamma_0 = 2.8$ and below, particle fluxes of increasing strength were observed for periodic flows of increasing strain amplitude. Outer-plug extension develops rapidly in an initial transient phase and becomes steady with accumulated strain, with the initial rate of extension increasing with strain amplitude.

3.3 Simulation results

Further insight into the dynamics of the plug development is provided by numerical simulations. Here we employ the simulation methods of Yeo and Maxey (2011) to follow the evolution of a suspension plug in a pressure-driven Poiseuille flow for a channel formed between two parallel planar walls. The simulations use the force coupling method (Yeo and Maxey, 2010) to represent the particles and a Fourier pseudo-spectral scheme to compute the resulting Stokes flow. Each particle gives rise to a regularized, low-order force multipole expansion that captures the multi-body hydrodynamic interactions of the particles. Additional forces and torques are included to reproduce the effects of short-range viscous lubrication interactions of particles that are not otherwise represented. The distance between the two walls, H is $12d$ or $24a$, where a is the particle radius. Periodic boundary conditions are applied in the two other directions, with $L_x = 30a$ in the spanwise direction. In the direction of the flow the channel length is chosen to be long enough so that the periodic images of the plug at maximum extension do not overlap, which gives $L_z = 320a$ in all cases except the pre-sheared case with strain amplitude $\gamma_0 = 6.39$ where $L_z = 340a$. An initial plug of 8,250 particles is introduced with uniform random seeding over a length $L_P = 160a$ as illustrated in Fig. 3.1 to give a particle volume fraction of 30%. The incompressible flow is computed using a resolution of 96×1024 in the x, z periodic directions, and 12 eighth-order spectral elements in the y-direction.

A short-range repulsion force between particles is introduced to reproduce the effects of surface roughness and to prevent particle overlap. As in the earlier study (Yeo and Maxey, 2011), the potential force acts along the line of particle centers $\mathbf{Y}^\alpha$ and $\mathbf{Y}^\beta$ such that the force $\mathbf{F}_P^{\alpha\beta}$ on particle α from particle β is given as

$$\mathbf{F}_P^{\alpha\beta} = \begin{cases} -6\pi a^2 \sigma_0 F_{ref} \left(\frac{R_{ref}^2 - |\mathbf{r}|^2}{R_{ref}^2 - 4a^2} \right)^6 \frac{\mathbf{r}}{|\mathbf{r}|} & \text{if } |\mathbf{r}| < R_{ref} \\ 0 & \text{otherwise,} \end{cases} \tag{3.3.1}$$

in which $\mathbf{r} = \mathbf{Y}^\beta - \mathbf{Y}^\alpha$, R_{ref} is the cut-off distance, and F_{ref} is a constant. The force parameters are chosen to limit the force to near-contact interactions with $R_{ref} = 2.01a$ and F_{ref} is set so that minimum gap between particles is about $0.005a$. A similar force is applied for near-contact of a particle and a wall. The numerical simulations assigned unit values to a and η, with an applied pressure gradient

$-dp/dz = 0.08$ and time step $\delta t = 0.005$. The value of $\sigma_0 = -h\,dp/dz$ provides a reference scale for the fluid and particle stresses where $2h = H$.

The strain amplitude is based on the particle-averaged displacement $\langle \Delta Z \rangle_P$ during the forward half cycle with $\gamma_0 = \langle \Delta Z \rangle_P / h$. A constant pressure gradient is applied for each half cycle, but is varied smoothly to give a continuous transition over $\Delta t = 2$ for the flow reversals. Typical values of the oscillation period are $T = 30, 50$ and 70, which correspond to strain amplitudes of $\gamma_0 = 2.84, 4.64$, and 6.39, respectively.

In this section, we first provide a comparison with the experiments and then use the simulations to explore more fully the dynamics within the suspension plug. We examine the particle migration and then consider the relation to the contact forces between particles and the particle pressure that they induce.

3.3.1 Plugs with pre-shear

In the first set of simulations, the plug is given an initial shear deformation to correspond to the typical initial shape seen in the experiments. The pre-shear gives a starting strain of 4.6 and the leading front of the plug advances $75a$ from $z = 160a$ to $z = 235a$. Fig. 3.5 shows the average streamwise displacement of the particles during a forward half cycle taken from this initial pre-sheared state at $t = 0$. While the fluid satisfies a no-slip condition at the walls, the particles adjacent to the wall can advance in a quasi-rolling motion. The profiles are not exactly parabolic but the ratio of the peak displacement to the particle-averaged value is in the range $0.64 - 0.65$.

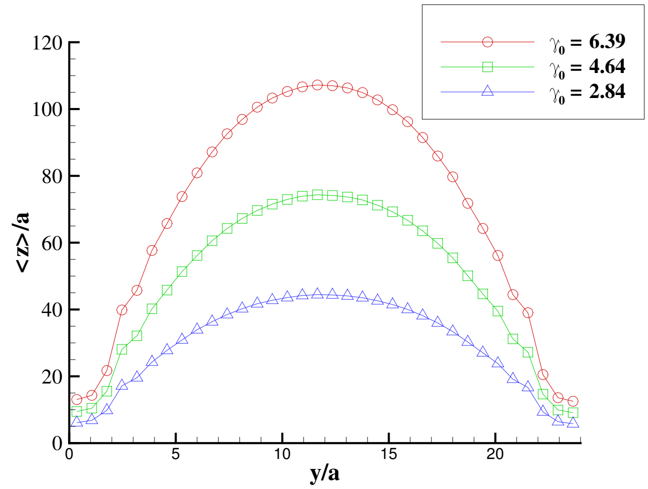

Figure 3.5: Profiles of the average particle displacement $\langle Z \rangle / a$ in the streamwise direction versus y/a for a pre-sheared plug in a forward half cycle. Results are averaged over four periods for $\gamma_0 = 2.84, 4.64, 6.39$.

Fig. 3.6 shows the development of this plug over sixteen cycles from $t = 0$ to $t = 800$ with a period $T = 50$ and strain amplitude $\gamma_0 = 4.64$. One immediate observation is that the nose of the plug does not advance from one cycle to the next as seen in the experimental observations. However, the particles near the walls show a net forward migration over several cycles, as in the experiments, blunting the shape of the plug. In Fig. 3.6 we have color coded the particles based on their final position at $t = 16T$. The particles centered in the near wall zone $0 \leq y \leq 3a$ are shown in red, in the mid-shear zone $3a \leq y \leq 6a$ are shown in green and in the core zone $6a \leq y \leq 18a$ are shown in blue. There are corresponding red and green layers near the upper wall. The core zone spans the central width h of the channel, where the mean shear-rate would be less than half of the peak value. The other two zones are layers $h/4$ thick. We can trace from these images where the particles originate in the earlier cycles. It is seen that many of the near-wall particles at $t = 16T$ originate in the mid-shear zone within the bulk of the suspension plug earlier on and then move towards to the wall and expand towards the plug front. There is no significant migration of core particles towards the wall at the plug front even though one may

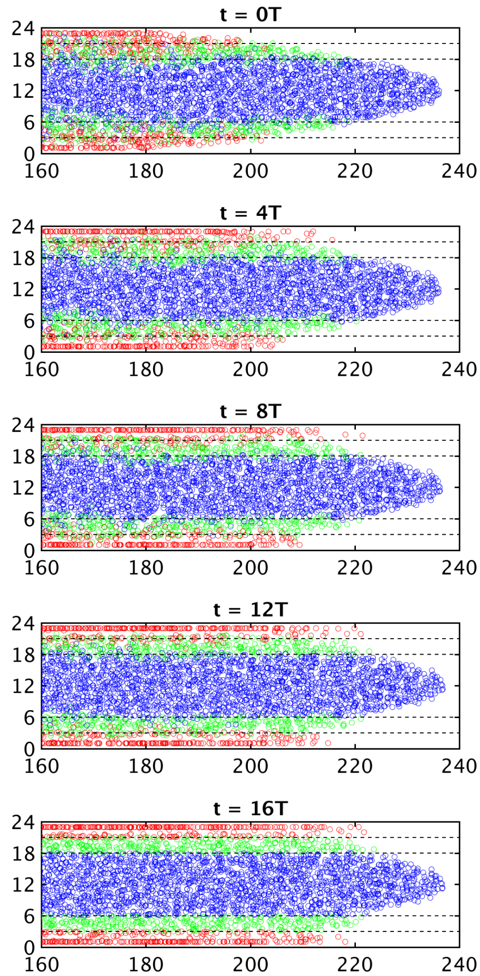

Figure 3.6: Side view of particles suspended in a 3D planar channel, showing the positions at $t = 0, 4T, 8T, 12T, 16T$, for a period of $T = 50$ and strain amplitude $\gamma_0 = 4.64$. The particles are color-coded based on their position at $t = 16T$ as described in the text, the guidelines indicate the near-wall, mid-shear and core zones.

expect this as a result of some shear-induced diffusion down a particle concentration gradient.

Fig. 3.7 provides a comparison of the near-wall forward migration E of particles at the plug front, as measured in the simulations, with the experimental results shown in Fig. 3.4. While we use standard definitions for the strain amplitude, essentially $\gamma_0 = \langle \Delta Z \rangle_P / R$ in the tube and $\gamma_0 = \langle \Delta Z \rangle_P / h$ in the channel, a direct comparison is difficult. The peak shear rate in a tube is $4U_B/R$ but $3U_B/h$ in a channel for

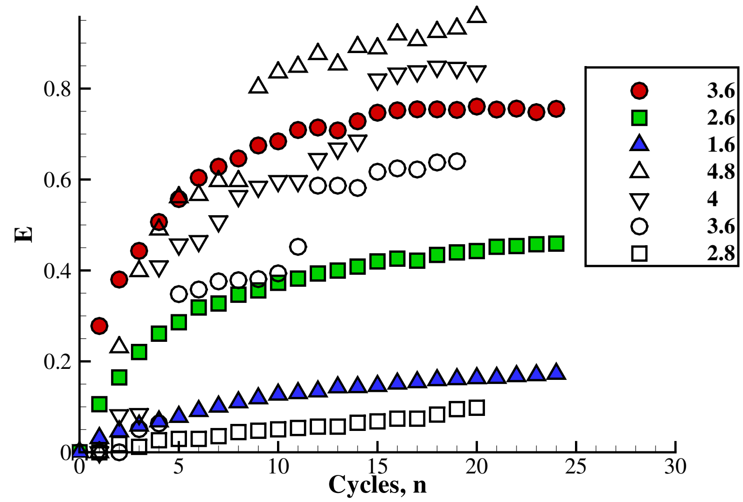

Figure 3.7: Comparison of the experimental results for the near-wall extension E of the plug in a tube (open symbols) with the simulation results in a channel (filled symbols) after n oscillation cycles. The legend shows the strain amplitudes for a tube, while the values for a channel are scaled to match the estimated particle-averaged strain amplitudes.

a corresponding Poiseuille flow. The overall particle concentration, as shown later, does not change significantly in the present time frame and one may compare the strain rate averaged over the cross-sections in the two contexts as being representative of the particle-averaged strain rate. This gives a particle-averaged strain amplitude of $8\langle \Delta Z \rangle_P / 3R$ for a tube and $1.5\langle \Delta Z \rangle_P / h$ for a channel. The results for $E = (Z - L_0)/D$ and $E = (Z - L_0)/H$, shown in Fig. 3.7, are in terms of the strain amplitude for a tube, while the amplitude for a channel is scaled by a factor of $4.5/8$ so as to match the estimated particle-averaged strain amplitudes. The simulation results fall within the range of the experimental data and indicate that they are consistent. Exact agreement is not expected due to the differences in geometry, limitations of the rescaling, and experimental error. Experimental data was also collected for $\gamma = 5.4$, where E/D was 1.4 after twenty cycles.

3.3.2 Plugs without pre-shear

The second set of simulations is based on a suspension plug without pre-shear so the plug has an initial flat profile at both the tail $z = 0$ and at the front $z = 160a$, as in the illustration in Fig. 3.1. This makes the effects of near-wall migration on the forward front, $z = 160a$, more obvious. The first results shown in Fig. 3.8 are counterparts to Fig. 3.6 and show the side view of the leading section of the plug for the region $z \geq 120a$ over eight oscillation periods for a low and a high strain amplitude. The same color coding of the particles is used with colors set here by the locations at $t = 8T$. We first note that the central region of the plug (blue) has a transient forward motion in the first cycle but then does not advance further. The front remains sharp here, with the local, sectionally averaged volume fraction in this region still varying from 30% to 0 over a distance of one particle diameter, d.

The irreversible forward migration of the near-wall particles continues to grow in time and is stronger with the larger strain amplitude. Given the differences in the periods, the accumulated strain at $t = 8T$ for the lower amplitude case is comparable to the accumulated strain at $t = 3.6T$ for the higher amplitude case. The results for the latter at $t = 4T$ shown in Fig. 3.8 (right) show a much stronger response. As can be seen in Fig. 3.6, many of the near-wall (red) particles originate earlier in the mid-shear zone. There is also an appreciable forward migration of particles ending up in the mid-shear zone for this higher amplitude.

Fig. 3.9 shows more detail of both the plug front and tail for an intermediate strain amplitude, $\gamma_0 = 4.64$ or period $T = 50$. The small initial displacement of the otherwise stationary plug front in the core is again evident, yet it remains sharply defined. The color-coding of the particles again illustrates the forward migration of particles at the wall and that they originate within the body of the plug and migrate

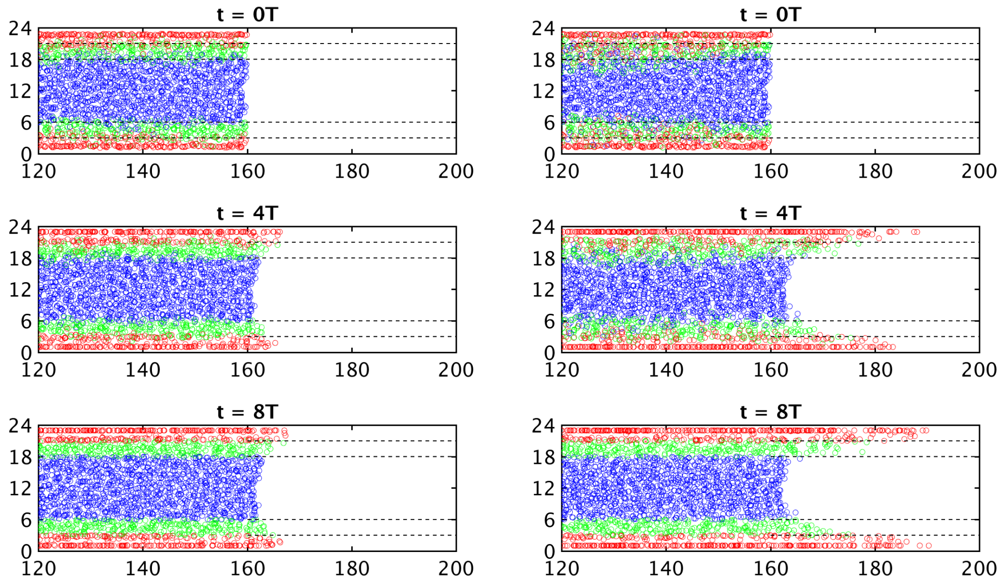

Figure 3.8: Side view of particles suspended in a 3D planar channel, showing the positions at $t = 0, 4T, 8T$: (Left) period $T = 30$ and strain amplitude $\gamma_0 = 2.84$; (Right) period $T = 70$ and strain amplitude $\gamma_0 = 6.39$. The particles are color-coded based on their position at $t = 8T$ as described for Fig. 3.6.

towards the wall, primarily from the mid-shear zone. Tracing the trajectories of particles in the mid-shear green region that migrate to the near-wall red region shows that on average the particles migrate into the near-wall region during the forward motion on the first half period, then remain with the same y-coordinate as they migrate backward on the second half-period. Because they migrate from a region with a higher streamwise velocity, the particles do not return to their initial streamwise position, causing the extension of the plug along the channel walls.

The development of the tail of the plug is more complex. A portion of the tail region is shown in Fig. 3.9 for $z \leq 20.0a$ and at the two times $t = 8T$ and $t = 16T$. Here there are 1047 particles shown, based on their initial location. Over the initial interval, $t = 0 - 8T$, there is an upstream migration of particles in the mid-shear (green) zone, with minimal upstream migration in the near-wall zone. The core zone (blue) migrates downstream. Across the channel section, there is primarily a net

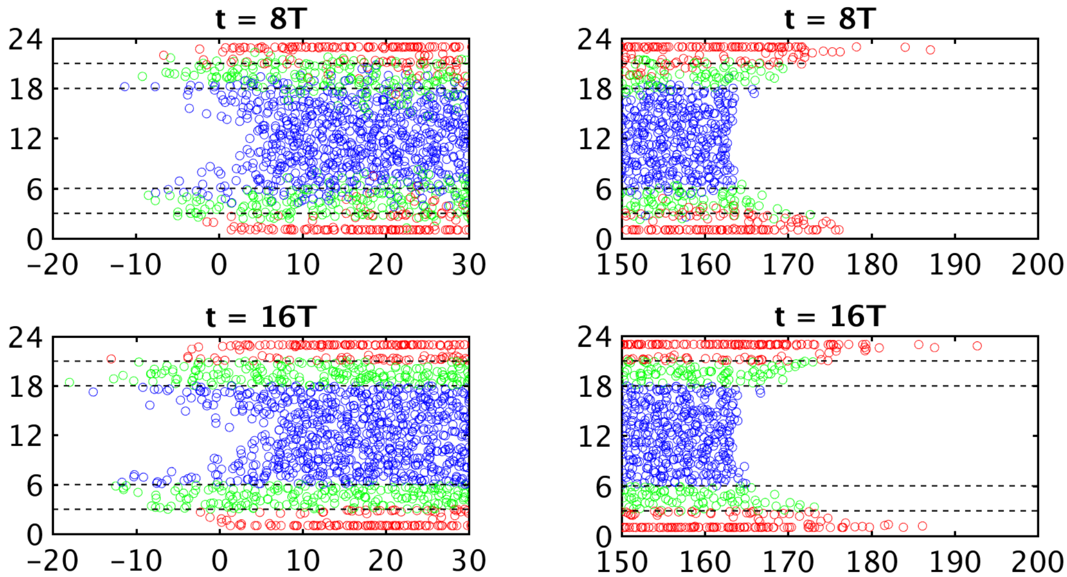

Figure 3.9: Particle locations in the tail region of the plug (left) and front region (right) for oscillation period $T = 50$ ($\gamma_0 = 4.64$). Particles are color-coded by their locations at $t = 16T$ and are shown at $t = 8T$ (top row) and $t = 16T$ (lower row).

exchange of particles from the core (blue) zone to the mid-shear (green) zone. The total number of particles in the core zone falls by 10% with increases in the number of particles in the other two zones, but mostly giving a 20% increase in the mid-shear zone. In the next interval, $t = 8T - 16T$, the trend reverses with an increase of particles in the core zone coming mostly from the mid-shear zone as particle migrate towards the centerline. The structure of the oscillation cycle implies that a particle can only substantially migrate upstream in the tail if it is initially closer to the wall in the forward half cycle than on the return half cycle. This is consistent with the net migration of near-wall particles to the mid-shear zone in the initial interval $t = 0 - 8T$.

We now consider the particles in the mid-section of the suspension plug that are removed from the direct effects of the plug front or tail. The transport in and out of these regions is quantified by a series of tables for particles originally in the mid-section, $20a \leq z \leq 140a$. As the flow is unsteady and spatially varying in two directions, plotting profiles of particle fluxes is unreliable and these tables provide a more robust overview for the exchange of particles between the different zones over the interval $t = 0$ to $t = 16T$. Table 3.1a covers the low strain amplitude $\gamma_0 = 2.84$ or $T = 30$ and Table 3.1b is for $\gamma_0 = 6.39$ or $T = 70$. The rows give the number of particles initially in each zone and the columns give the number in a zone at $t = 16T$. For the oscillating suspension plugs there is a systematic increase in the number of near-wall particles (red) and this is more pronounced at higher strain amplitude. There is a corresponding decrease in the number of particles in both the mid-shear (green) and core (blue) zones. The off-diagonal entries show the two-way exchange of particles between zones. For example, in Table 3.1b, there is migration of 226 particles from the wall zone to the mid-shear zone with a counterbalancing migration of 551 particles in the other direction leading to a net transfer to the wall zone. There is also a smaller net transfer of particles from the core (blue) zone to the near-wall zone. Other choices for the division of the channel into zones were evaluated and found to give similar conclusions. There was no special effect from selecting the boundary of the near-wall zone at $y/a = 3$ versus 3.25 or 3.5,

There is then a clear indication of a net transfer of particles from the mid-shear and core zones towards the walls. This is contrary to the usual expectation for developing Poiseuille flows under a constant pressure gradient where the particles migrate towards the core leaving a reduced particle concentration closer to the walls. With any Poiseuille flow, steady or oscillating, there is a brief transient flux of particles towards the wall if there is an initial random seeding of the particles in the channel. At the outset, there is no structure to the particle distribution near the wall and as a shear flow develops the particles form an organized layer adjacent to the wall, with a first peak in the particle void fraction occurring at $y/a = 1$ or 23 (Yeo and Maxey, 2011). Examination of a fully-seeded flow with a homogeneous pressure gradient shows that 50% of the total transfer of particles to the near-wall zone occurs within $t = 0 - 50$ and this flux then diminishes quickly. For the oscillating plugs such a transient adjustment occurs within the first one or two oscillation cycles, however the net migration to the wall continues as the streamwise extent of the wall layer expands. Additional flux tables for $T = 50$, $\gamma_0 = 4.64$, and figures demonstrating the particle fluxes are available in sec. 3.4.

Table 3.1: Number of particles in each of three zones, near-wall (red), mid-shear (green) and core zones (blue); values show numbers of particles moving from row location to column location, with corresponding totals at $t = 0$ and $t = 16T$ for T = 30 (3.1a) and T = 70 (3.1b). Particles are in the central section with initial stream-wise coordinate $20a \leq z \leq 140a$. Tables for T = 50 and homogeneous fully seeded flow are available in the 3.4.

(a) T = 30.

	Blue	Green	Red	Total, $t = 0$
Blue	2822	419	14	3255
Green	206	981	512	1699
Red	3	123	1104	1230
Total, $t = 16T$	3031	1523	1630	6184

(b) T = 70.

	Blue	Green	Red	Total, $t = 0$
Blue	2465	584	206	3255
Green	482	666	551	1699
Red	87	226	917	1230
Total, $t = 16T$	3034	1476	1674	6184

We now consider factors linked to the redistribution of particles within the suspension plug. First, the development of the particle void fraction profile after $t = 16T$ is given in Fig. 3.10 for both oscillating plugs and for a developing flow under a steady pressure gradient. The latter is taken at $t = 800$, which corresponds to the same time as the $\gamma_0 = 4.64$ flow after $t = 16T$. While the average particle volume fraction is 30%, there are peaks in the particle concentration adjacent to each wall in a layering effect, already noted. The peak values are greatest for the two oscillating flows with strain amplitudes $\gamma_0 = 4.64, 6.39$ and least for the steady pressure gradi-

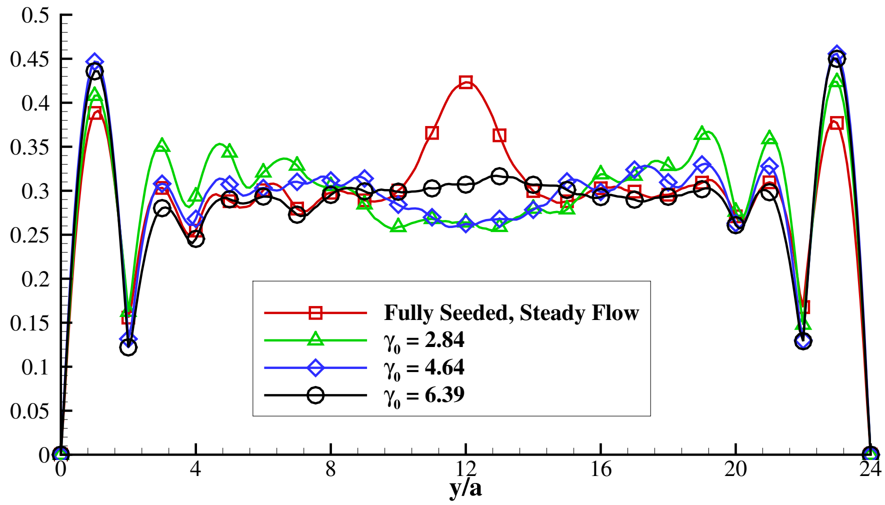

Figure 3.10: Volume fraction profile for oscillating plug flows at strain amplitudes $\gamma_0 = 2.84, 4.64, 6.39$ at $t = 16T$ and a fully seeded steady flow at $t = 800$ or strain $\gamma = 150$.

ent flow. Further layering of the particles is evident near the walls, at $y/a = 3$ and 21, most noticeably for the lowest amplitude oscillating flow. By $t = 800$ or a total strain of $\gamma = 150$, the flow with the steady pressure gradient has already developed a significant peak close to the centerline, while the oscillating flows have a more nearly uniform value over the core region.

Fig. 3.11 shows the profiles for per cycle fluctuating mean-square displacement in the streamwise and cross-stream directions averaged over the eight cycles from 8T to 16T for the three different oscillation amplitudes. These profiles reflect the self-diffusivity of the particles. In the direction of shear, the mean square displacement $\langle \Delta Y^2 \rangle / a^2$ increases with strain amplitude and is strongest at distances of $4a - 7a$ from each wall. Particles are less influenced by confining effect of the wall at these locations and fall mostly within the mid-shear (green) zone. The values for the two larger amplitudes are consistent with a scaling based on strain amplitude. The results for the mean square displacement in the streamwise direction are similar but

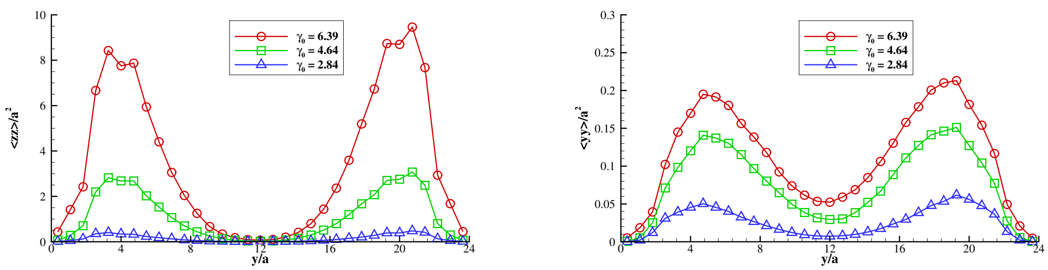

Figure 3.11: Per cycle, means square displacements in the streamwise (left) and cross-stream (right) directions shown as a profile. The results are averaged over all particles in the plug, for strain amplitudes $\gamma_0 = 2.84, 4.64, 6.39$.

magnified by the dispersion effect of the mean shear flow.

A key factor in the description of particle migration by suspension balance models (Nott and Brady, 1994, Morris and Boulay, 1999, Nott et al., 2011) is the role of particle stresses and specifically the role of contact forces due to particle roughness (Metzger and Butler, 2010, Metzger et al., 2013, Pham et al., 2015). Here we have computed the particle pressure due to the contact forces between particles as set by (6.2.8). The contact forces are generated as equal and opposite pairs between particles along the line of centers giving rise to a force dipole for each pair. These are summed and averaged to obtain the pressure from the trace. In an earlier study of steady Poiseuille flow (Yeo and Maxey, 2011) this pressure was found to be nearly uniform across most of the channel once the flow is fully developed.

Fig. 3.12 shows this particle pressure, averaged across the whole flow, in a simple Poiseuille flow as the strain develops under a steady pressure gradient. The pressure is scaled by σ_0 and the results are shown for time $t = 0 - 200$, corresponding to strains $0 - 37$. The average particle pressure reaches the peak value by about $t = 25$ and levels off for $t > 40$ to a value consistent with previous results for this volume fraction of 30% (Yeo and Maxey, 2011). This indicates the time scale for the initial development of particle contacts. Also shown is the particle pressure for the

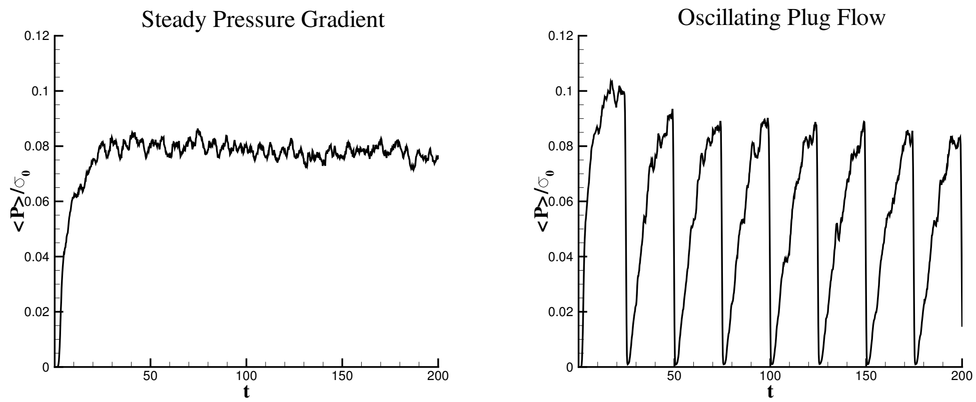

Figure 3.12: (Left) Development of particle contact pressure averaged over all particles for a simple initially uniform suspension in a steady Poiseuille flow. (Right) Particle averaged contact pressure in a plug for $T = 50$ over four cycles.

oscillating suspension plug with period $T = 50$ as it varies over several cycles. The pressure grows during the forward half cycle, $0 < t < 25$, drops to zero as the flow is reversed and then grows again on the reverse half cycle. The initial half cycle has a somewhat higher peak pressure as the particles rearrange from the random seeding. The peak pressure then settles to an ambient level for later cycles. When the shear flow goes to zero, any non-zero contact forces between particles will soon create the small displacements needed to reduce this force to zero.

The average profiles of the particle contact pressure, taken over the mid-section of the plug, are shown in Fig. 3.13 just prior to the flow reversal at several instances for the three strain amplitudes. Because of the intermittent nature of displacement and contact events observed within the front of the plug, the pressure profiles are averaged over four periods, with data taken from one time unit before the end of the period. The pressure profiles are found by:

$$\langle P\rangle(y) = \frac{1}{L_x \times L_z}\left\langle \sum_{i=1}^{N_p} \int\int P^i \chi_p^i(\mathbf{x})\, dx\, dz \right\rangle,$$

in which P^i is the value of the particle contact pressure and χ_p^i is the indicator function of particle i.

Also shown in Fig. 3.13, as a reference, are profiles for particle contact pressure in the fully-seeded flow driven by a steady pressure gradient. This may be compared to the results for the intermediate strain amplitude. In general terms for this steadily driven flow, the particle contact pressure is greater near the wall and decreases towards the centerline reflecting the corresponding change in mean shear. The highest peaks signify the wall layer and the second layer of particles adjacent to the wall layer, which represent the red and green particles respectively. The relative heights of the two peaks are nearly balanced in the first interval shown, averaged at $t = 250, 300, 350$ and 400 labeled as $5T - 8T$, and thereafter the peak at $y/a \sim 1$ is slightly larger. By $t = 250$ the particle layer adjacent to the wall is already formed and filled, remaining little changed later on while the next layer and particles further out are more mobile. Once the wall layer is formed, the particles on average migrate towards the center of the channel.

In the first plot at $t = 5T - 8T$, the particle pressure for each oscillatory flow has a larger peak value at $y/a \sim 3$ than at $y/a \sim 1$. This is consistent with the observed migration of particles towards the wall (red zone). At $t = 13T - 16T$, the near-wall peak is higher than the mid-shear region peaks for the highest strain amplitude. This comes at a transition from the migration towards the walls to beginning a net migration to the zero shear region in the center of the channel. The peak is still greater at $y/a \sim 3$ for the two lower strain amplitude cases. These observations can be compared to the volume fraction profile in Fig. 3.10 taken at $t = 16T$. Finally, at $t = 21T - 24T$, the peaks are nearly balanced for the intermediate strain amplitude $\gamma_0 = 4.64$, while the pressure at the lowest and highest strain amplitudes are still greatest at $y/a \sim 3$ and $y/a \sim 1$, respectively. We can relate these changes to the results of Fig. 3.7 which show that there is no increase in near-wall extension for

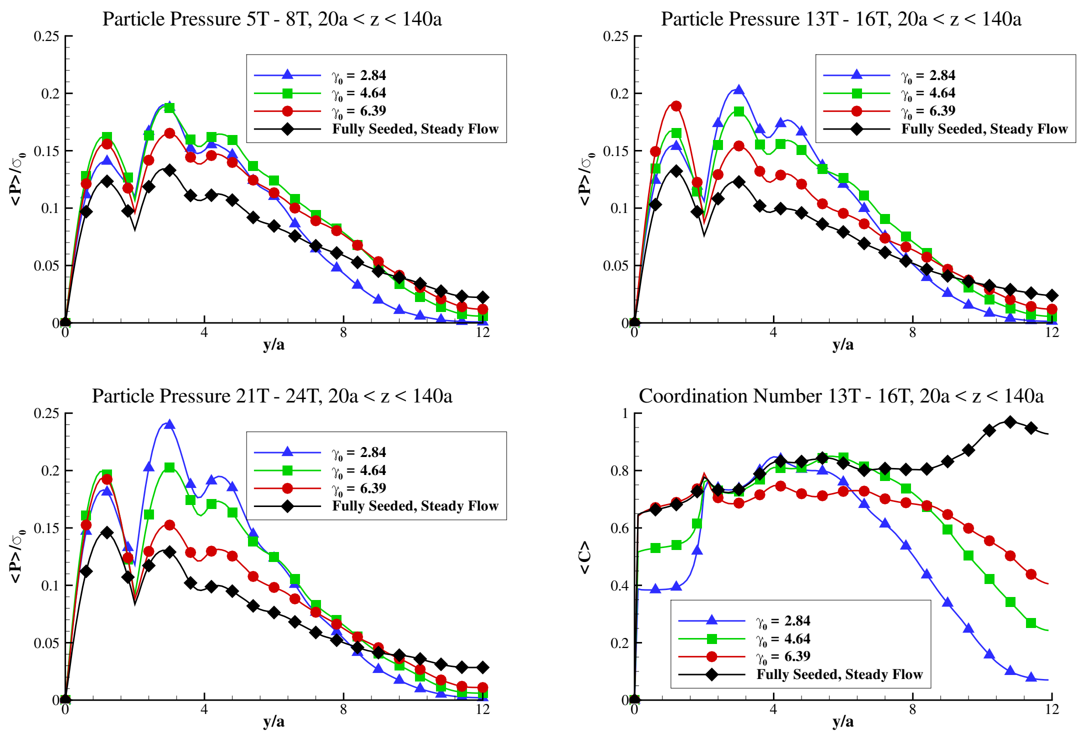

Figure 3.13: Profiles of particle pressure and coordination number formed over the mid-section of the plug just before flow reversal in oscillating flow (oscillatory) or for corresponding time intervals for an initially uniform suspension with a constant pressure gradient (steady). Top left: Particle pressure at $t = 5T - 8T$ (oscillatory) and $t = 250 - 400$ (steady); top right: Particle pressure at $t = 13T - 16T$ (oscillatory) and $t = 650 - 800$ (steady); bottom left: Particle pressure at $t = 21T - 24T$ (oscillatory) and $t = 1050 - 1200$ (steady); bottom right: coordination number at $t = 13T - 16T$ (oscillatory) and $t = 650 - 800$ (steady).

$\gamma_0 = 6.39$ after $t = 16T$, while $\gamma_0 = 4.64$ is only slowly increasing from $t = 16T$ to $t = 24T$. At all three intervals, the pressure at the centerline is largest for the steady case and lower for the oscillating flows. The pressure profile for the fully-seeded flow is quite similar at $t = 650 - 800$ and $t = 1050 - 1200$, and the $\langle P \rangle / \sigma_0$ drops to a value of 0.027 at the centerline.

While we may associate a difference in contact pressure as an indicator for the net particle flux, the duration for which this pressure difference exists is equally as important in the oscillating flows. The accumulated strain at $24T$ for the lowest strain amplitude is substantially lower than for the other two. Even though the contact pressure has the greatest difference in the near-wall peaks for the lowest strain amplitude, the net migration of particles is the least. This reflects the time for the pressure to develop within a half-cycle, a more disordered state in the near-wall layers, and the time (or strain) needed for significant migration to occur within the half-cycle. Since the reversal of the flow results in an instantaneous drop in the contact pressure, the flows with higher strain amplitude, and thus more time for the contact pressure to form and act, demonstrate larger particle migrations.

Further information is provided in Fig. 3.13, where the profile for the coordination number is shown for the particles just prior to $t = 13T - 16T$. This measures the fraction of particles in near-contact, as determined by whether two particles are close enough to generate a contact force (6.2.8) even though the magnitude of the contact force is low. This is given by:

$$\langle C \rangle (y) = \frac{1}{\phi(y)} \frac{1}{L_x \times L_z} \left\langle \sum_{i=1}^{N_p} \int \int C^i \chi_p^i(\mathbf{x}) \, dx \, dz \right\rangle,$$

in which C^i the number of particles within a distance R_{ref} of particle i and χ_p^i is the indicator function of particle i. For the flow driven by a steady pressure gradient the coordination number is highest near the centerline where particles are migrating. For the oscillating flows it is generally greater in the mid-shear zone. In the near-wall layer, the coordination number increases with the strain amplitude, with the value for the highest strain amplitude case matching that of the constant pressure gradient. This is consistent with the wall layer reaching a fully populated equilibrium and this match of coordination number for the cases of constant pressure gradient and for $\gamma_0 = 6.39$ persists.

3.4 Extended discussion of particle fluxes

In addition to the results in Table 3.1 and Figs. 3.8 and 3.9, we provide further results for the particles in the mid-section of the suspension plug that are removed from the direct effects of the plug front or tail. Fig. 3.14 (left) shows the initial position of particles that fall within the mid-section, covering $20a \leq z \leq 140a$, for $\gamma_0 = 4.64$. The particles are color coded based on their positions at $t = 16T$ so that the figure shows in which region each group of particles originated. The top image shows the initial locations for particles that end up in the near-wall zone. There is a clear indication of a net transfer of particles from the mid-shear and core zones towards the walls, contrary to the usual expectation for developing Poiseuille flows. The middle image shows that there is an active exchange of particles into the mid-shear zone from both adjacent zones. The lower image indicates that some particles do migrate from the mid-shear zone to the core in the normal manner. Fig. 3.14 (right) shows the corresponding images for the front section of the plug, where particles are initially in the interval $140a \leq z \leq 160a$. The general trends are the same as in the mid-section with particles migrating from the mid-shear zone towards the walls.

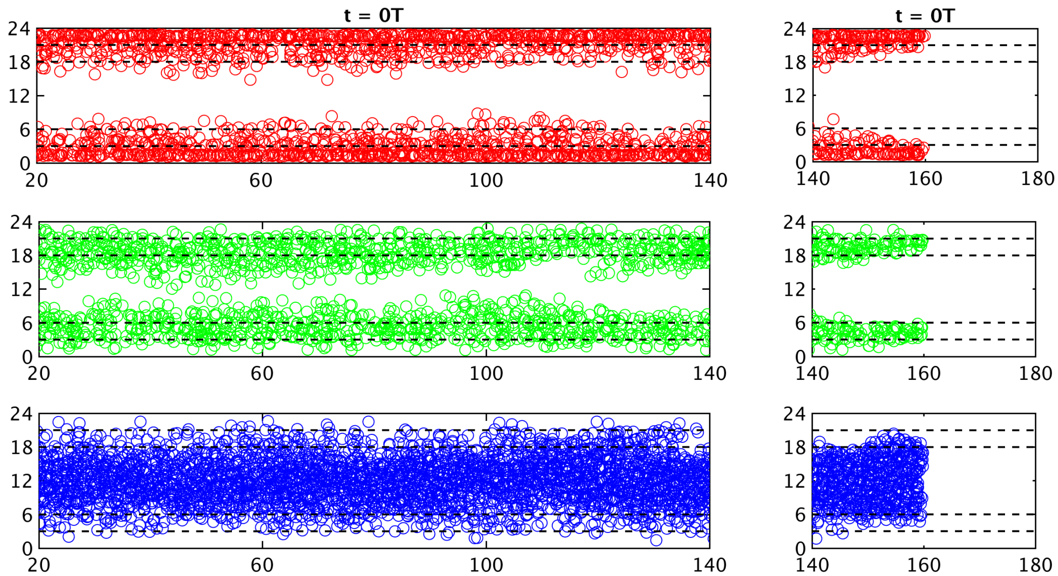

Figure 3.14: (Left) Initial particle positions, at $t = 0$, based on zone locations at $t = 16T$ for $T = 50$ within the mid-section of the plug, $20 \leq z/a \leq 140$. Top image - particles in (red) near-wall zone; middle - particles in (green) mid-shear zone; bottom - particles in (blue) core zone. (Right) Similar initial particle positions for the front section of the plug, where $140 \leq z/a \leq 160$ at $t = 0$.

Table 3.2 gives results for $\gamma_0 = 4.64$ ($T = 50$) based on two different simulations. The two sets of data indicate the level of statistical variation in the relative numbers of particles in each zone. The results show the same trends as at the higher strain amplitude, with a systematic increase in the number of particles in the near-wall zone. As a comparison, Table 3.2c gives results from a simple, steadily evolving Poiseuille flow at $t = 800$. The particles in this case fully populate the channel $L_z = 160a$, are uniformly seeded at $t = 0$ and are sampled for the same mid-section. The accumulated strain is approximately $\gamma = 150$ and this example may be compared to the results in Table 3.2a for the intermediate strain amplitude at $t = 16T$. In this instance there is a more modest transfer of particles from the mid-shear zone to the near-wall zone, that tends to equilibrate the number of particles in each of these zones, which may be expected as they are of the same width. The number of particles in the core zone shows a small net decrease.

Table 3.2: Number of particles in each of three zones, near-wall (red), mid-shear (green) and core zones (blue); values show numbers of particles moving from row location to column location, with corresponding totals at $t = 0$ and $t = 16T$ for T = 50 (3.2a and 3.2b) and a fully seeded homogeneous flow from $t = 0$ to $t = 800$ (3.2c). Particles are in the central section with initial stream-wise coordinate $20a \leq z \leq 140a$.

(a) T = 50, Run 1.

	Blue	Green	Red	Total, $t = 0$
Blue	2564	565	126	3255
Green	410	737	552	1699
Red	44	180	1006	1230
Total, $t = 16T$	3018	1482	1684	6184

(b) T = 50, Run 2.

	Blue	Green	Red	Total, $t = 0$
Blue	2710	475	79	3264
Green	376	780	545	1701
Red	27	203	1019	1249
Total, $t = 16T$	3113	1458	1643	6214

(c) $t = 800$, $\gamma \approx 150$, homogeneous fully seeded flow.

	Blue	Green	Red	Total, $t = 0$
Blue	2620	492	143	3255
Green	563	698	438	1699
Red	102	247	881	1230
Total, $t = 800$	3285	1437	1462	6184

Similar tables were compiled for the migration of particles within the front of the suspension plug to provide further information on the results shown in Fig. 3.14 (right). Results were compared for two different simulations with a strain amplitude $\gamma_0 = 4.64$ for particles initially in the region $140 \leq z/a \leq 160$. The total number of particles in the front for the two simulations is 1019 and 1042. After $t = 16T$, the number of particles in near-wall (red) zone for the two runs increased, with the increase coming from particles in the mid-shear (green) zone. While the initial random seeding of the near-wall zone results in fewer particles than in the mid-shear zone, this is reversed by $t = 16T$. The relative increase of particles in the near-wall zone was lower than in the mid-section in Tables 3.2a and 3.2b. There was a small increase of particles in the core (blue) zone in the front of the plug, again linked to particles migrating from the mid-shear zone.

3.5 Conclusions

In this study, we have investigated the development of a concentrated plug of suspended non-Brownian particles when subjected to oscillating, pressure-driven Stokes flow. A primary question is whether the motion of the plug, in either a circular tube or a channel, is reversible in the bulk for the plug as a whole. Both the experiments and numerical simulations demonstrate the same features. The plug front shows minimal change or net displacement in the region near the centerline even after many oscillation cycles and over a range of strain amplitudes. In the region adjacent to the walls the particles in the plug front advance, with this being greater for larger strain amplitudes. There is an apparent minimum strain amplitude for this irreversible response in the bulk motion. The experiments and the simulations indicate that the rate of forward extension of near wall particles in the plug front becomes slower after the first $10 - 15$ cycles, and shows negligible increase after 16 cycles at the high strain amplitude $\gamma_0 = 6.39$.

This system highlights the practical issues of how samples of suspended material may be handled in microfluidic systems. A suspension plug with bulk concentration of 30% can be moved with a good degree of bulk reversibility over short distances. These results apply to the early development and dispersion of a suspension plug in unsteady flow. Due to the time scale, the long term Taylor dispersion of a suspension having gradual streamwise variations in particle concentration has not been established (Griffiths and Stone, 2012, Ramachandran, 2013).

The system also illustrates the fundamental questions posed for particle transport and particle fluxes in unsteady, inhomogeneous suspension shear flow. The interface between the suspended particles in the plug and the clear fluid outside remains sharp at the plug front in the core zone. The observed net migration of particles towards the near-wall zone for the oscillating plugs, while anomalous, appears to be consistent with the effects of particle stresses and supports the general concepts behind the suspension balance model. It is clear though that the details of how the particle stresses, and the contact forces in particular, govern the particle fluxes requires further investigation. This is especially true for the interactions between the confined near-wall zone and the more mobile mid-shear zone adjacent to it.

Several general features emerge. Noticeably for individual particles at the leading edge of the plug, movement in the cross-stream direction is observed to be associated with contact with other particles, leading to intermittent displacement events instead of a continual migration. Within the central section of the plug, away the leading and trailing edges, the particles are fully immersed in the suspension and contacts between particles can be characterized by the particle contact pressure. As the strain increases during a half-cycle the micro-structure of the sheared suspension develops and the particle pressure builds to an equilibrium level. Only if the contact pressure is sustained at this level before the flow reverses is there significant cross-stream migration of particles.

These observations of the particle pressure indicate the important role of the particle contact forces in generating a net flux. It is clear too that this is only part of the story and further study is needed. One issue is the relative mobility of particles in the near-wall region where the finite size of the particles and the confining effects of the wall are important. Further we do not have sufficient data at this point to determine the variation of the particle stresses along the length of the plug and the extent to which the fronts at the leading and trailing ends of the plug relieve the particle stress.

******

Chapter Four

Particle dispersion in suspension clouds

4.1 Introduction

In this chapter, we investigate the particle migration in cylindrical and spherical clouds of suspended non-Brownian spherical particles when subjected to an oscillating Couette flow. Motivated by experiments by Metzger and Butler (2012), where they tracked a spherical cloud of particles in an oscillating Couette flow, we consider a periodic cylinder of particles that is initially circular in the plane of shear flow, as shown in fig. 4.1. The particles are sheared forward for half a period T, and then the flow is reversed so the cylinder approaches its original position. The particles are free to disperse in all directions outside of the cylinder.

The cloud has an initial volume fraction $\phi_i = 40\% - 55\%$ and a cylinder radius R. Metzger and Butler (2012) showed two different regimes for spherical clouds. At lower volume fractions, if the strain amplitude was higher than the critical strain amplitude in Pine et al. (2005), the clouds extended along the channel centerline after several oscillations resulting in an elliptical cross section. When the volume fraction approached close packing, the clouds began to rotate. "Galaxy"-like arms emerged when the radius of the cloud was much larger than the particle radius, e.g. $R/a = 20$. In this chapter we discuss the first case in section 4.3 and the second case in section 4.4. Some results with spherical, instead of cylindrical, clouds are discussed in 4.3.2 to provide a comparison to the experiments in Metzger and Butler (2012). The range of parameters and cloud behavior considered allows for examination of the forces leading to macroscopic irreversibility of the cloud shape in both regimes, and the simulations give complementary data to the previous experiments.The goal of the present chapter is to give further insight into the relative significance of the particle contacts and long-range hydrodynamic forces in the irreversible particle displacements in a suspension flow.

4.2 Simulation Parameters

The simulations are completed using the Force Coupling Method (FCM) to represent the particles and a Fourier pseudo-spectral scheme to solve for the resulting fluid flow in the zero-Reynold's number Stokes' regime (Yeo and Maxey, 2011). In FCM, each particle is represented by a low-order force multipole expansion that captures the hydrodynamic interactions of the particles. When the particles are close together viscous lubrication forces and a short-range contact force barrier are employed to include the forces not captured by the force multipole expansions. Cylindrical clouds of densely packed, neutrally buoyant, non-Brownian spherical particles with radius a are initially placed in a channel with height H_y, where H_y is varied to study the effects of the spacing between the channel walls, using a and the strain rate $\dot{\gamma}$ as the scale. The flow in the channel is periodic in the spanwise direction, x, and the streamwise direction, z, using the notation velocity $\mathbf{u} = (u, v, w)$ and vorticity $\boldsymbol{\omega} = (\omega_x, \omega_y, \omega_z)$. The channel length in the stream-wise direction, L_z, is chosen to be long enough so that the periodic image of the sheared cloud does not overlap with itself. The channel walls move to create a Couette flow in the channel, with shear rate $\dot{\gamma} = 1$. After $\dot{\gamma}t = T/2$ the shear rate is reversed so $\dot{\gamma} = -1$, as illustrated in Fig. 4.1. The actual shear rate $\dot{\gamma}$ is adjusted continuously during a short interval at each reversal to ensure a smooth variation in the particle velocities. The initial volume fraction of the clouds, $\phi = \frac{\frac{4}{3}\pi a^3 N}{\pi R^2 L_x}$, where R is the radius of the circular cross section of the cloud and L_x is the channel length in the vorticity direction, is varied between $\phi = 40\%$ and $\phi = 55\%$.

A short range repulsion force between the particles acts to prevent particle overlap and physically represents the roughness of the particles. The contact force between particles α and β, with centers $\mathbf{Y}^\alpha$ and $\mathbf{Y}^\beta$, acts along the line of centers of the particles and is given by

$$\mathbf{F}_P^{\alpha\beta} = \begin{cases} -6\pi a^2 \eta \dot{\gamma} F_{ref} \left(\dfrac{R_{ref}^2 - |\mathbf{r}|^2}{R_{ref}^2 - 4a^2} \right)^6 \dfrac{\mathbf{r}}{|\mathbf{r}|} & \text{if} \quad |\mathbf{r}| < R_{ref}, \\ 0 \quad \text{otherwise} & \end{cases} \tag{4.2.1}$$

in which $\mathbf{r} = \mathbf{Y}^\beta - \mathbf{Y}^\alpha$, η is the fluid viscosity, and R_{ref} is the cut-off distance and F_{ref} is a constant chosen so that the minimum gap between the particles is $0.005a$ when $R_{ref} = 2.01a$ (Yeo and Maxey, 2011). The contact force breaks the irreversibility of two particle interactions, causing the particles to migrate across streamlines, as shown for two-particles in a Couette flow in fig. 4.2, which can be compared to Da Cunha and Hinch (1996) and Blanc et al. (2011). For two-particle interactions the maximum contact force attained by the simulation is in the range $|F_{max}| = 15.50 - 20.15$, and the minimum gap between the particles varies so that the maximum force is attained. For $R_{ref} = 2.01a, 2.001a$, and $2.0001a$, the minimum gap widths are $0.00531a$, $0.000534a$, and $0.000055a$, respectively. Unless mentioned otherwise, the contact force cutoff for all simulations $R_{ref} = 2.01a$.

The particles interact with the channel walls through a short range repulsion force similar to eqn. 6.2.8 and through viscous lubrication forces. However, the channel height is chosen to be large enough so that particles are isolated from the walls and do not enter the cut-off distances for these forces.

The particles are randomly seeded in two stages to create a compact, high volume fraction cloud without effects from confining the particles during seeding. In the first stage, particles with radius $a_i = 0.85a$ are randomly placed in a cylinder with radius Ra. Once all the particles are placed a molecular dynamics simulation with a repulsive potential is preformed while the particle size is slowly increased so that particles have a final radius of a. If the particles are confined during this second

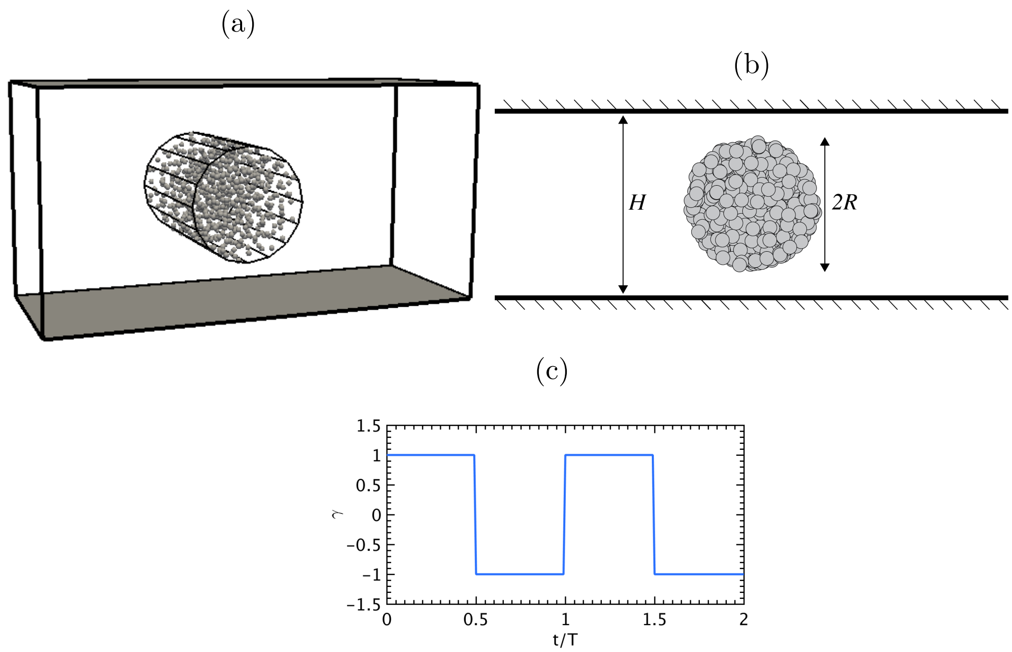

Figure 4.1: (a) and (b): Simulation initial condition for a periodic cylindrical cloud with channel height $H = 24$ and $R/a = 8$. The channel is periodic in the streamwise and vorticity directions. (c): Strain profile over t/T for an oscillating Couette flow.

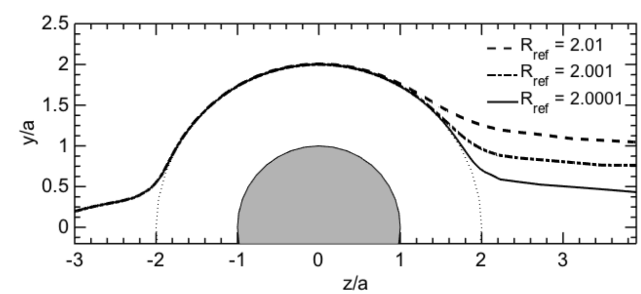

Figure 4.2: Relative trajectories of two particles with initial separation $\Delta y = 0.2a$ with different values of R_{ref}. The final location of the overtaking particle depends on R_{ref}, and the separation from the initial streamline increases with R_{ref}.

stage they form layers along the edge of the cylinder, analogous to particle layering along a channel wall in a fully seeded suspension flow in a channel. To prevent this, the particles are not confined to the cylinder during the inflation stage. This causes a slight increase in the cloud radius, and the change to the volume fraction is less than 15% when $\phi = 40\%$ and 25% when $\phi = 55\%$. Allowing the particles to expand out of the initial cylinder confinement during the inflation step may give a better comparison to the experiments, where the particles are injected into the flow using a syringe but are not confined to a prescribed volume (Metzger and Butler, 2012).

The macroscopic irreversibility of the cloud (i.e., the final shape of the cross section of the cylindrical cloud after many oscillations) is related to the size of the cloud, volume fraction of the particles, and the strain amplitude, as defined by

$$\gamma_0 = \dot{\gamma}\frac{T}{2},$$

where T is the period of one oscillation. This definition of the strain amplitude corresponds to twice that of Pine et al. (2005). The current study uses a square wave where the flow is reversed after half a cycle, while the experiments by Pine et al. (2005) used a sine wave where the flow was reversed after the first quarter period. For the volume fraction $\phi_i = 40\%$, the study by Pine et al. (2005) found the threshold for microscopic irreversibility to be $\gamma_0 = 0.8$, corresponding to $\gamma_0 \approx 1.6$ using the current definition. Previous studies, however, have looked at a fully seeded flow with a homogenous volume fraction across the sample and do not consider the effects of gradients in the particle volume fraction. In the current simulations we consider γ_0 between 0.5 and 12.5, extending the results of Metzger and Butler (2012), where $\gamma_0 \leq 8$.

The simulations reveal four distinct regimes distinguished by the final configuration of particles in reference to the initial cross-section of the cloud: macroscopic reversible states, extensional states, parallelogram states, and rotational or "galaxy-like" states with arms extending from the cloud. The last case occurs in large clouds with a high initial volume fraction, while the former three states form in lower volume fraction clouds, with the final particle migration determined by the strain amplitude. Section 4.3 focuses on lower volume fraction clouds, $\phi = 40\%$, while section 4.4 will discuss the formation of rotational states with $\phi = 55\%$.

4.3 Lower volume fraction clouds, $\phi = 40\%$

First, we will address the dispersion of particles in small spherical and cylindrical clouds, where $\frac{R}{a} \leq 10$ and $\phi = 40\%$, where the particle migration is demonstrated to be determined by the strain amplitude. In comparison to the spherical clouds used in experiments, cylinders allow for a more detailed analysis of the cloud structure. The number of particles in a periodic cylinder depends on length of the periodic domain along the axis of the cylinder. By extending the domain in the span-wise direction the number of particles can be increased to improve statistical averages. In contrast, at $\frac{R}{a} \leq 10$ and $\phi = 40\%$, the maximum number of particles in a spherical cloud is approximately 400. Because of this, we will predominately focus on the migration of particles in cylindrical clouds, discussed in sec. 4.3.1. In sec. 4.3.2 basic results from spherical clouds are provided as a direct comparison to the experiments in Metzger and Butler (2012).

4.3.1 Cylindrical clouds

In this section we consider the particle migration for cylindrical clouds with an initial circular cross section of radius R. Two channel heights and initial cloud sizes are considered to study the influence of the channel walls on the migration of the particles, $H = 24a$ with cloud size $R = 8a$ and $H = 40a$ with cloud size $R = 9a$. Observations of the cloud are made after sixteen oscillations by comparing the initial and final positions of the particles, shown in Fig. 4.3. Compared to the initial particle locations, simulations with strain amplitude $3 \leq \gamma_0 \leq 5$ show expansion of the cloud in the streamwise direction and a slight compression in the wall-normal direction at $\dot{\gamma}t = 16T$, consistent with the observations of Metzger and Butler (2012). In contrast, simulations with $\gamma_0 \geq 10$ also show expansion in the streamwise direction, but along the top and bottom of the cloud instead of the channel centerline. The transition between these regimes occurs between $5 \leq \gamma_0 \leq 10$. Additional simulations were done with $\gamma_0 = 0.5, 1.25$, and 2, which demonstrated no qualitative difference between the initial and final cloud shapes, consistent with the threshold for irreversibility from Pine et al. (2005) and Pham et al. (2016) for homogeneous shear flow.

Irreversibility in fully seeded homogeneous suspension flows and in two- and three-particle interactions increases with the particle roughness (Da Cunha and Hinch, 1996, Zarraga and Leighton, 2002, Pham et al., 2015), and increasing the particle roughness increases the self-diffusivity of the system (Da Cunha and Hinch, 1996, Pham et al., 2016). With this in mind, we now look at the role of two-particle interactions in the shapes of the clouds at $\dot{\gamma}t = 8T$ through varying the cutoff distance of the contact force, R_{ref}, for the cases of $\gamma_0 = 5$ and $\gamma_0 = 10$. As shown in Fig. 4.4, changing R_{ref} does not produce a large qualitative difference for the lower strain amplitude. In contrast, for the higher strain amplitude, lower values of R_{ref}

(a) $H = 24a$

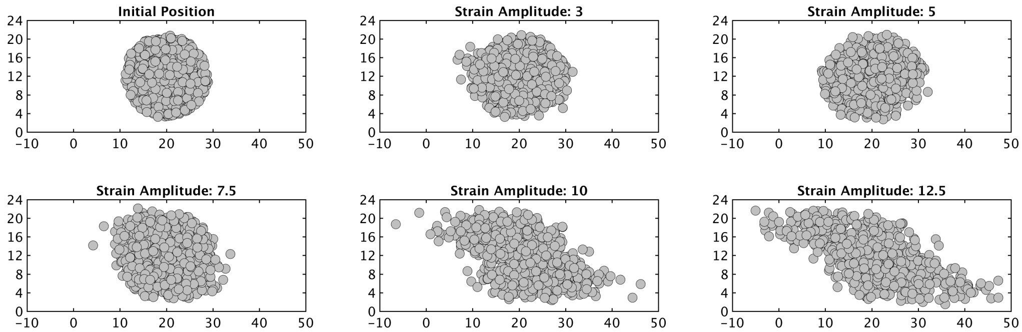

(b) $H = 40a$

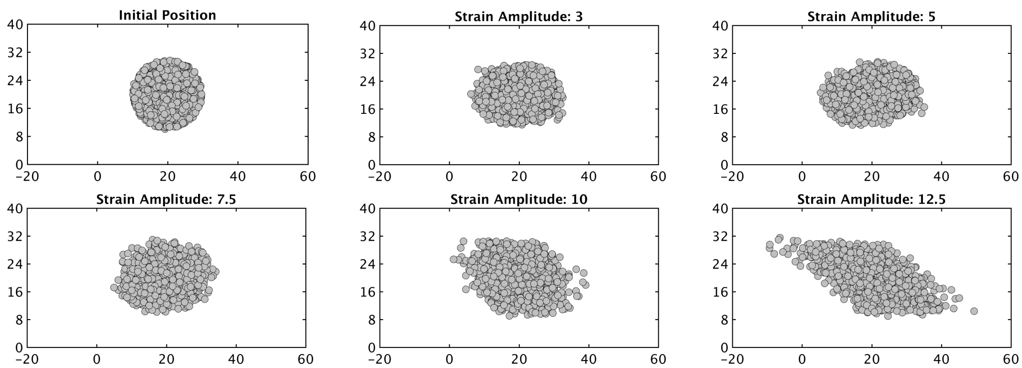

Figure 4.3: Initial particle positions (top left) and positions after sixteen oscillations for varying strain amplitudes for channel heights $H = 24a$ (top) and $H = 40a$ (bottom). Particles are actual size and are projected onto the yz-plane. $R_{ref} = 2.01a$

(a) $\gamma_0 = 5$

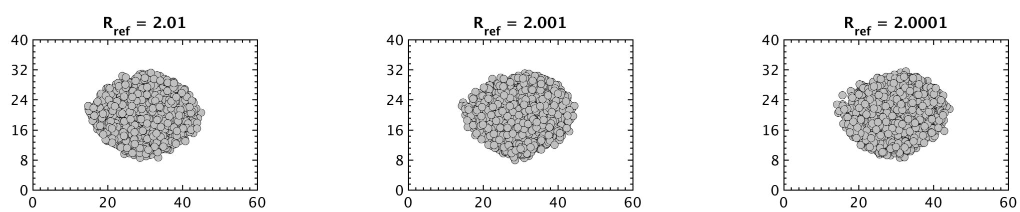

(b) $\gamma_0 = 10$

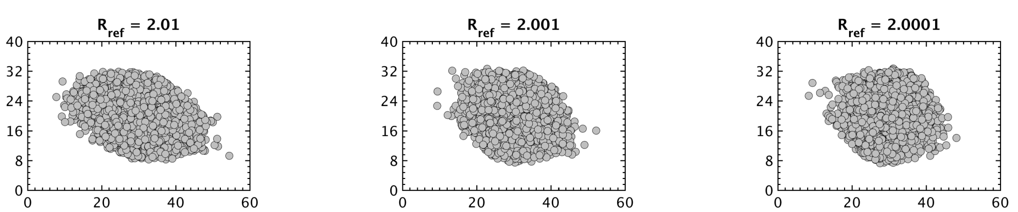

Figure 4.4: Particle positions of the cloud after eight oscillations with $R_{ref} = 2.01$ (left), $R_{ref} = 2.001$ (middle), and $R_{ref} = 2.0001$ (right). Decreasing R_{ref} decreases the irreversibility for $\gamma_0 = 10$ (bottom) but not for $\gamma_0 = 5$ (top). Particles are actual size and $H/a = 40$.

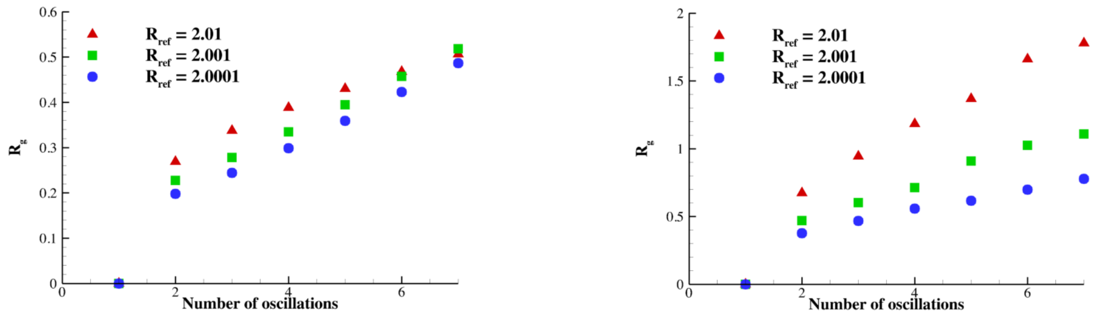

Figure 4.5: Change in radius of gyration, $R_g(t) - R_g(T)$ for eight periods of oscillation. $L_x = 60$ and $H/a = 40$ (a): $\gamma_0 = 5$. (b): $\gamma_0 = 10$

reduce the near-wall extension of the cloud. This suggests that near-wall extension is the result of two-particle contact interactions while the cloud is being sheared in each oscillation.

To quantify the macroscopic irreversibility of the clouds we introduce the radius of gyration, shown in Fig. 4.5. The radius of gyration measures the average squared distance between each particle and the center of mass of the cloud in the yz-plane, $\mathbf{r}^m = (y_{cm}, z_{cm})$, given by

$$R_g^2(t) = \frac{1}{N} \sum_{i=1}^{N} \left[y_i(t) - y_{cm}(t)\right]^2 + \left[z_i(t) - z_{cm}(t)\right]^2. \tag{4.3.1}$$

Here, $y_{cm}(t) = \frac{1}{N}\sum_{i=1}^{N} y_i(t)$, $z_{cm}(t) = \frac{1}{N}\sum_{i=1}^{N} z_i(t)$, and (x_i, y_i, z_i) is the position vector of particle i. Motion due to the first oscillation is not included in measurements to avoid the initial transient caused by particle seeding. Only small differences in radius of gyration are observed for $\gamma_0 = 5$. However, the radius of gyration increases with R_{ref} for $\gamma_0 = 10$.

The footprints of the simulation clouds can be further quantified in terms of the average particle displacements in the velocity gradient direction, $\langle \Delta y \rangle$, plotted in

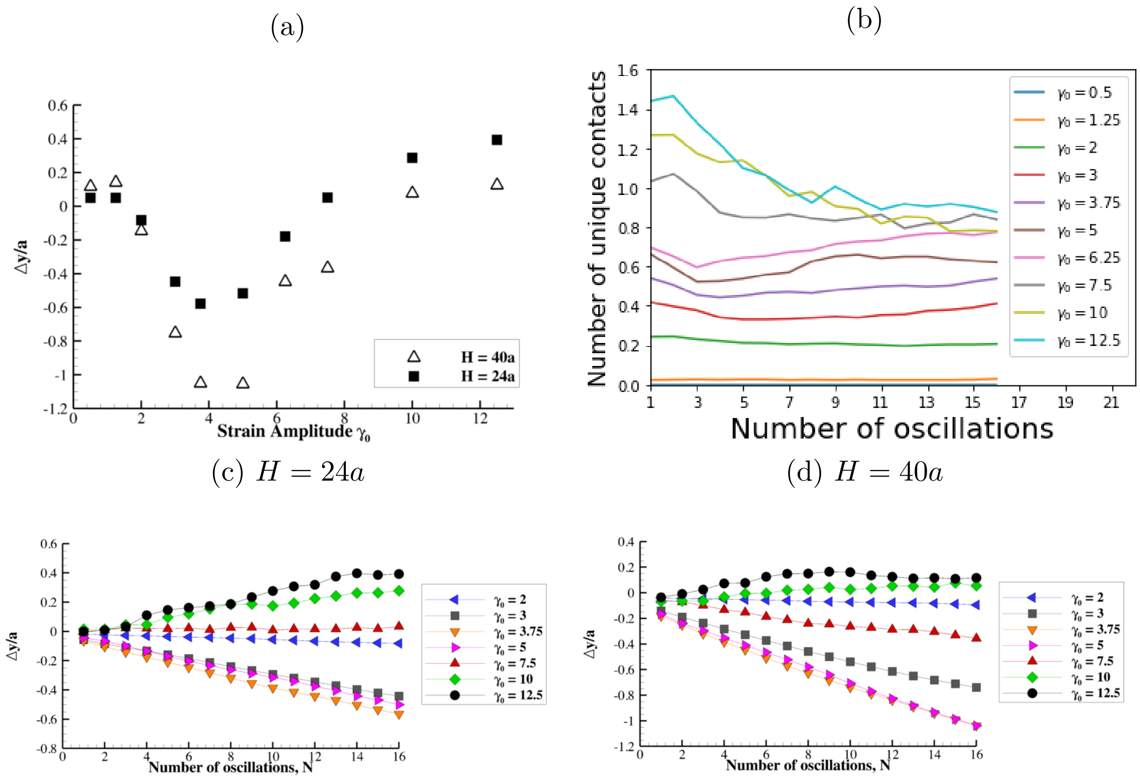

Figure 4.6: (a) Net displacement in the wall-normal direction after 16 periods. A positive displacement means that the particles are on average moving towards the channel wall. (b) Number of unique contacts per particle during each oscillation for $H = 40a$. (c) Displacement after each period for $H = 24a$. (d) Displacement after each period for $H = 40a$. In both (c) and (d), the net displacement for $\gamma_0 \leq 2$ is negligible. For $3 \leq \gamma_0 \leq 5$ there is a strong negative displacement, with a larger displacement in the wider channel. In all cases, the displacement is roughly linear with respect to time.

Fig. 4.6. The particle displacement Δy_i is defined by

$$\Delta y_i = \begin{cases} \dfrac{y_i(16T) - y_i(0)}{a} & \text{if} \quad y_i(0) \geq \dfrac{H}{2}, \\ -\dfrac{y_i(16T) - y_i(0)}{a} & \text{if} \quad y_i(0) < \dfrac{H}{2}. \end{cases} \tag{4.3.2}$$

Using this definition, particles with $\Delta y_i > 0$ are displaced closer to the wall, while particles with $\Delta y_i < 0$ are displaced towards the center of the channel. Very low strain amplitudes, $\gamma_0 < 2$, show only a small displacement of less than $0.1a$, consistent with the threshold strain amplitude for irreversibility found by experiments in homogeneous flow. When the strain amplitude is low, $2 < \gamma_0 < 7$, the particles display an average displacement towards the centerline of the channel, $\langle \Delta y \rangle < 0$. From fig. 4.6, this displacement is linear with time, with a small average cross-stream displacement of $0.02 - 0.05a$ per oscillation. At high strain amplitude, $\gamma_0 \geq 10$, the particles have a small average positive displacement, $\langle \Delta y \rangle > 0$. Particles in a Couette flow that migrate closer to the walls have a larger stream-wise velocity, and thus return and move past their initial steam-wise position by the end of the period. The resulting stream-wise particle displacement corresponds to the parallelogram extension in clouds subject to a high strain amplitude Couette flow, shown in fig. 4.3. Fig. 4.6 also shows the average number of unique particle contacts per oscillation. Here, there are three distinct regimes. For $\gamma_0 < 2$, there are close to zero contacts per oscillation. For $2 \leq \gamma_0 \leq 6.25$, the number of contacts per oscillation is approximately constant. At larger strain amplitudes, $\gamma_0 \geq 7.5$, the number of contacts starts higher initially, and decreases over the first several oscillations to reach a constant value.

Several features are observed for the clouds at lower strain amplitudes during the course of an oscillation cycle. First is the rotation of the cloud in the shear flow while the cloud retains a compact form, followed by a near-return to the initial cloud shape. Over many oscillations there is a net development into an elliptic shape, aligned and elongated in the streamwise direction but slightly compressed in the direction of shear. Overall there is a net increase in the volume of the cloud and dilution of the particle volume fraction. In summary, the height of the cloud in the wall-normal direction decreases after many oscillations, while the cloud extends along the channel centerline.

Further insight comes from looking at the mean volumetric flow field, averaged in the spanwise direction. This flow $(\langle v \rangle, \langle w \rangle)$ is incompressible and is given by the FCM scheme. A short time into the forward half cycle, $\dot{\gamma}t = 0.75$, the presence of the cloud induces a flow in the wall-normal direction, $\langle v \rangle$, as shown in fig. 4.7a, along with the vorticity in the spanwise direction, $\langle \omega_x \rangle$, in fig. 4.7b. The vorticity within the cloud is noise due to averaging and the random particle positions. While the cloud is porous and deformable, not solid, in this more compact state it significantly blocks the flow. This causes a recirculation of the fluid from the shear flow, and induces a rotational velocity inside the cloud. The induced flow is symmetric with respect to the background Couette flow.

At $\dot{\gamma}t = 2.5$, the induced wall normal flow is still essentially symmetric, as shown in fig. 4.8a. The direct rotation of the cloud is weaker but the bulk stresslet of the cloud and the associated vorticity distribution are still significant. The net effect is for a compression of the cloud towards the centerline. While this is reversed on the return half-cycle, there is an asymmetry since the particle contact forces (on each oscillation) break the symmetry of the flow. This asymmetry creates a mismatch between the forward and reverse sweeps of the cloud as the cloud first expands to a sheared cross section and then contracts, resulting in a net displacement towards the centerline over many periods, for $2 < \gamma_0 < 7$. The mechanism of particle migration is similar to that described in fig. 2.5 in chapter 5. While the particles may not directly

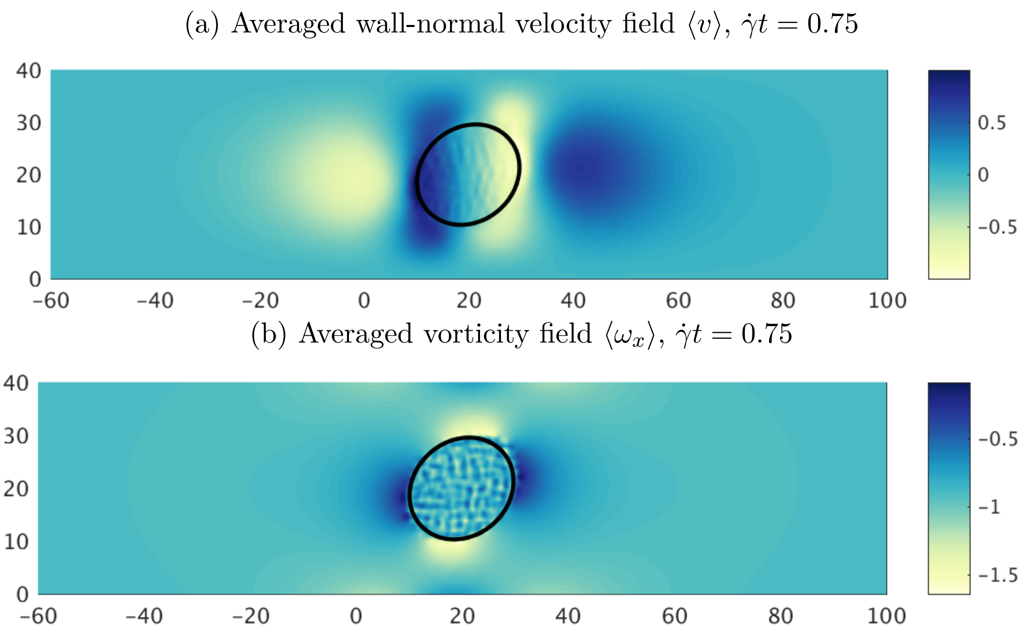

Figure 4.7: (a) Wall-normal velocity field at $\dot{\gamma}t = 0.75$ induced by the presence of the particle cloud in the Couette flow. The flow field is averaged in the spanwise direction. The location of the particle cloud is represented by the solid ellipse. (b) Average vorticity field in the spanwise direction. $H/a = 40$.

come into contact with another particle, they do interact through lubrication forces with particles that are displaced due to the particle contact force.

The displacement due to the contact force increases with the strain amplitude, and contributes significantly to the displacement towards the channel walls at higher strain amplitude. This is seen in the example trajectories of two particles that come into contact during an oscillation in fig. 4.9. During the forward half period the overtaking particle is displaced closer to the channel wall, and then moves back past its initial position on the reverse half period. When R_{ref} is increased the overtaking particle has a larger displacement in the cross-stream direction, and thus a higher velocity during the rest of the cycle causing a larger backward extension of the cloud.

Fig. 4.10 shows the particle averaged contact pressure over one period for strain amplitudes $\gamma_0 = 5$ and $\gamma_0 = 10$, scaled by the average wall shear stress, $\tau_w = \eta\dot{\gamma}$.

(a) Averaged wall-normal velocity field $\langle v \rangle$, $\dot{\gamma}t = 2.5$

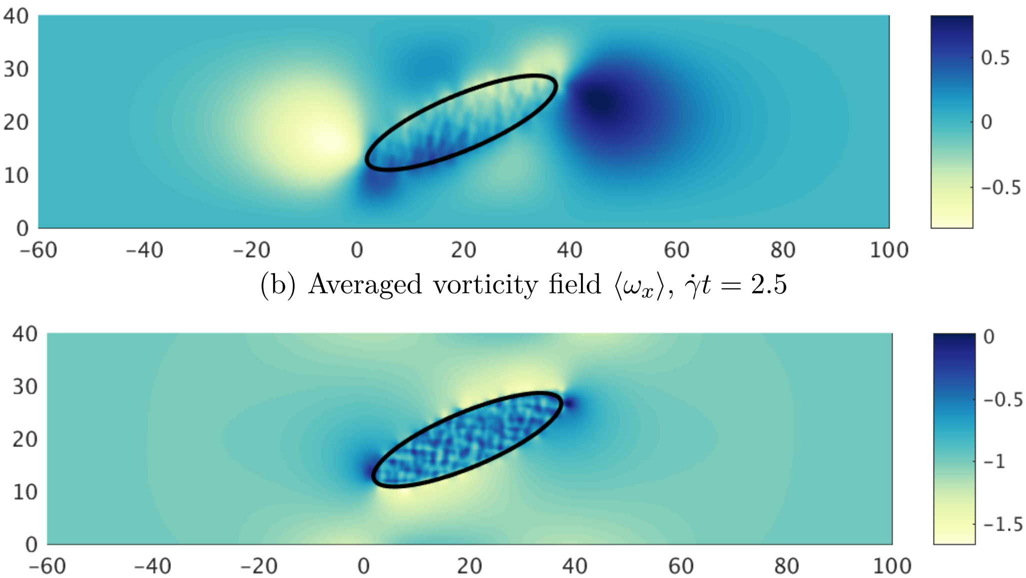

Figure 4.8: (a) Wall-normal velocity field at $\dot{\gamma}t = 2.5$ induced by the presence of the particle cloud in the Couette flow. The flow field is averaged in the spanwise direction. The location of the particle cloud is represented by the solid ellipse. (b) Average vorticity field in the spanwise direction. $H/a = 40$.

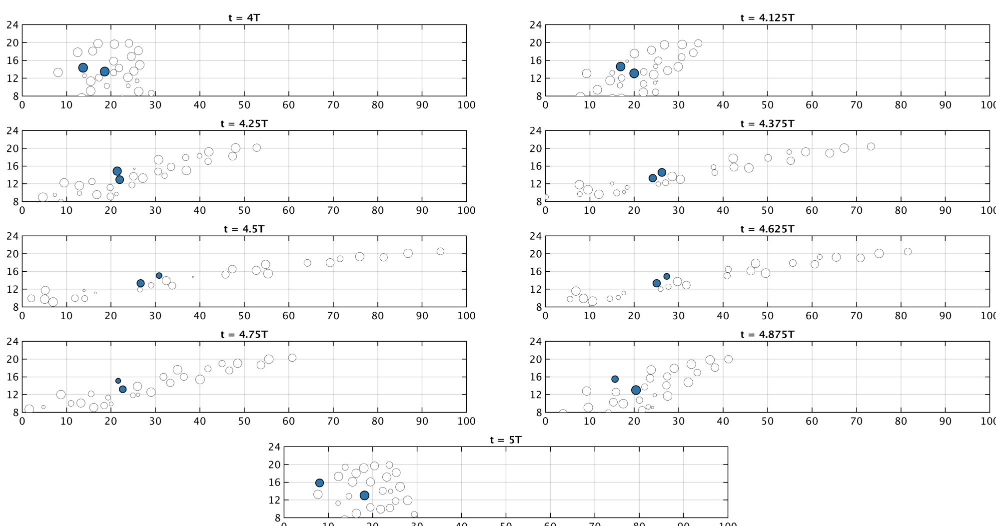

Figure 4.9: Example of particle locations over one period in one planar slice in the spanwise direction. Here, $H = 24a$, $\gamma_0 = 10$, and $\phi = 40\%$. The two shaded particles interact through the contact force at $\dot{\gamma}t = 4.25T$, with the overtaking particle being displaced towards the upper wall by $\dot{\gamma}t = 4.5T$. The particles are displaced from their original positions at the end of the period, with the overtaking particle having a greater displacement in the stream-wise direction.

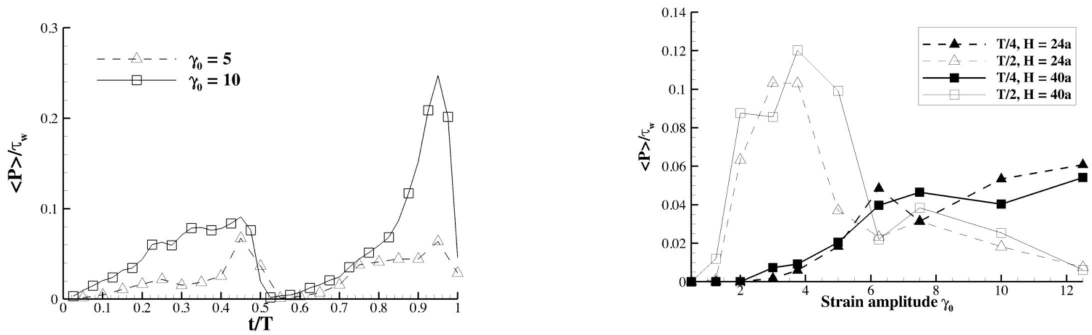

Figure 4.10: (a): Average contact pressure over one period for $\gamma_0 = 5$ and $\gamma_0 = 10$, averaged over 4T-12T. (b): Average contact pressure at $T/4$ and $T/2$, averaged 4T-12T. The pressure is still developing for $\gamma_0 < 5$.

Because the contact force has a very short range relative to the size of the particles, the particles must be squeezed tightly together before a significant contact pressure develops. When the flow reverses at $\dot{\gamma}t = T/2$ the particle contacts are able to relax and the contact pressure instantaneously drops to zero. It takes a few strain units for the contact force to develop again (Peters et al., 2016). When $\gamma_0 = 5$, the contact pressure reaches its maximum value only at the end of each half period. In contrast, for $\gamma_0 = 10$, the maximum on the first half cycle is only slightly higher than the value at $\dot{\gamma}t = T/4$. The asymmetry between the first half cycle and the second half cycle in fig. 4.10 is because the shearing of the cloud in the first half cycle results in a long, thin profile, increasing cross-sectional area of the cloud and reducing the volume fraction and the number of particles in contact. At the end of the second half cycle the cloud returns to close to its initial shape, where the cross-sectional area is at a minimum and the volume fraction is at a maximum.

To examine when the contact pressure is significant in the particle irreversibility, we consider the average contact pressure, $\langle P \rangle/\tau_w$, defined as in eq. 2.1.20 and 2.1.21. Fig. 4.10 shows the contact pressure at times $\dot{\gamma}t = T/4$ and just before reversal at $\dot{\gamma}t \approx T/2$ for channel heights $H = 24$ and $H = 40$. The pressure is still developing for $\gamma_0 \leq 6$ at $\dot{\gamma}t = T/4$, and reaches a maximum at $\dot{\gamma}t = T/2$. For very low strain amplitude, $\gamma_0 < 2$, the contact pressure is still very low at $\dot{\gamma}t = T/2$, corresponding to the cases that are reversible on the macroscopic scale. At high strain amplitude, $\gamma_0 > 8$, the contact pressure drops significantly at $\dot{\gamma}t = T/2$ due to the elongation of the cloud.

Fig. 4.11 shows scatter plots of the maximum contact pressure and cross-stream displacement experienced by each particle during one oscillation. Particles that do not have any contact interactions with other particles are indicated by points on the y-axis. Some of these particles do experience a cross-stream displacement, indicating that a particle may not need to come into contact with another particle to experience an irreversible displacement. However, these particles must be near other particles that do experience a contact force. In these cases, the two particles that do come into contact are irreversibly displaced, and their displacements result in the displacement of the third particle. In other words, had a contact not occurred, the particle trajectory would be reversible, but the particle does not have to itself come into contact with another particle. The maximum contact pressure is typically not associated with the largest displacements because particles that are being squeezed between multiple other particles will experience a large contact pressure but their mobility will be limited by the presence of neighboring particles. In addition, fig. 4.11 shows the conditional probabilities of cross-stream displacement values given that the particle did or did not experience a contact event during that oscillation. Particles that undergo contact with another particle are statistically more likely to have a larger cross-stream displacement. For $\gamma_0 = 5$, only 0.35% of particles that do not experience a contact event have a displacement greater than $0.33a$, versus 6.9% of particles that experience a contact event. For $\gamma_0 = 10$, 13.44% of particles with no contact event have $\Delta y \geq 0.33a$, compared to 40.7% of particles with a contact event.

Here, the irreversible particle contact force contributes to the most significant particle displacements in a single oscillation, however, the particle interactions through lubrication forces also cause small migrations of the particles if those lubrication neighbors are displaced through a contact force with another particle. These small lubrication force displacements accumulate over many oscillations to create a larger net displacement.

4.3.2 Spherical clouds

Previous experiments have used clouds with an initial spherical shape instead of a circular cylinder (Metzger and Butler, 2012). In order to provide a direct comparison with experiments, as well as to give additional insight into the cylindrical clouds, in this section we consider spherical clouds of densely packed particles in an oscillating flow. The clouds are seeded using the procedure described in sec. 4.2 with an initial radius of $R/a = 10$ and volume fraction $\phi = 40\%$, and contain 401 particles.

The particle positions after sixteen oscillations are shown in fig. 4.12. In comparison to the cylindrical clouds in fig. 4.3, the spherical clouds show greater particle dispersion. The parallelogram shape that appears for high strain amplitude with cylindrical clouds is less obvious in spherical clouds. This could be due to differences in geometry, as cylindrical clouds have a higher proportion of particles towards the upper and lower edges of the clouds, creating more contacts between particles during each oscillation. Moderate strain amplitude clouds, $\gamma_0 = 5$ and $\gamma_0 = 7.5$, predominately extend along the channel centerline.

Fig. 4.13 shows the change in the cloud volume fraction over many oscillations, and provides a direct comparison to fig. 3 in Metzger and Butler (2012). The

(a) $\gamma_0 = 5$

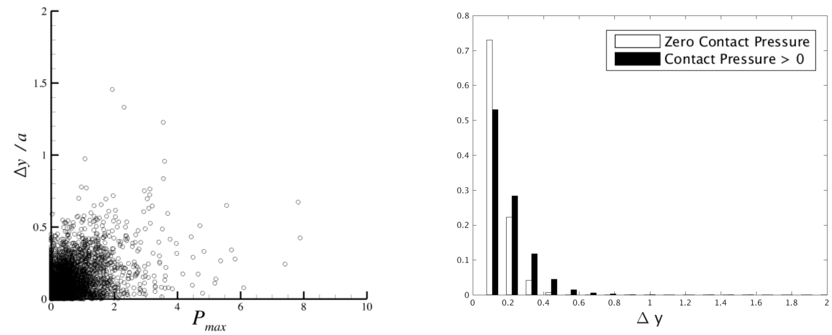

(b) $\gamma_0 = 10$

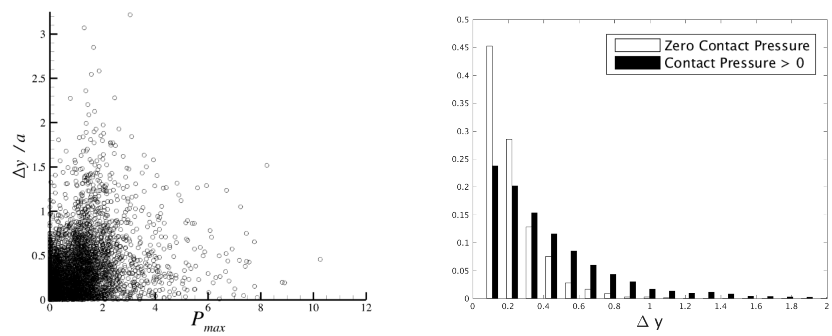

Figure 4.11: (a): $\gamma_0 = 5$. (b): $\gamma_0 = 10$. Left: Scatter plots of all particle displacements in the cross-stream direction over one period ($|\Delta y|$) with respect to the maximum contact pressure experienced during that period. Right: Probabilities of particle displacements. The white bars are particles where the maximum contact pressure for that period is zeros, so the particles have no contact with another particle. Solid black bars are non-zero contact pressure at some point during one oscillation. While non-linear hydrodynamic interactions can cause a displacement in the cross-stream direction, larger displacements are almost always accompanied by a non-zero contact pressure. The higher strain amplitude is associated with higher displacements and larger maximum contact pressures.

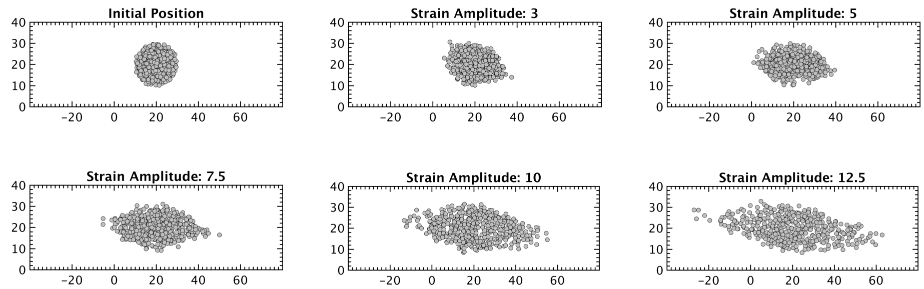

Figure 4.12: Initial particle positions (top left) and positions after twenty oscillations for spherical clouds with varying strain amplitudes for channel height $H = 40a$. Particles are actual size and are projected onto the yz-plane.

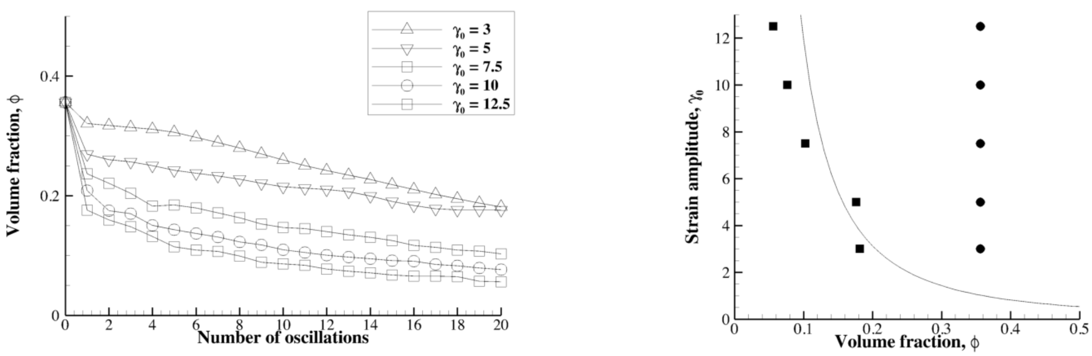

Figure 4.13: (a) Volume fraction of the spherical cloud after each oscillation, with various values of strain amplitude γ_0. The cloud is assumed to be an ellipsoid. (b) Comparison of the initial spherical cloud volume fractions (◯) and cloud volume fractions after twenty oscillations (□). The solid line is the critical curve from Pine et al. (2005) for irreversibility in a homogenous shear flow, given by $\gamma_0 = C\phi^{-\alpha}$, where $C = 0.14$ and $\alpha = -1.93$.

volume fraction is calculated at the end of each oscillation by assuming the cloud is a perfect ellipsoid with major axis oriented parallel to the stream-wise direction, z. The lengths of the axes are found by the minimum and maximum particle locations in each direction. Visual inspection of fig. 4.12 shows that this is a reasonable approximation for $\gamma_0 < 7.5$, but may over estimate the volume fraction for higher strain amplitude clouds when there are loose particles at the front and tail of the cloud. In addition, it should be noted that the initial volume fraction, when calculated in this manner, is lower than the initial seeding of $\phi = 40\%$, because the particles are not constrained during the seeding expansion step resulting in a slightly larger initial cloud radius. In fig. 4.13 the volume fraction shows a large initial drop during the first oscillation, then smaller decreases after each subsequent cycle. Increasing the strain amplitude decreases the final volume fraction, with the largest difference during the initial oscillation. Fig. 4.13 shows the initial and final volume fractions from fig. 4.13 at each oscillation, along with the critical volume fraction curve for self-diffusivity in a homogeneously seeded channel for a given strain amplitude from Pine et al. (2005). Below this curve, a homogeneous oscillating suspension flow is reversible. As found by Metzger and Butler (2012), the spherical cloud elongates over multiple oscillations in the velocity direction, decreasing in volume fraction until it drops below the critical volume fraction for the strain amplitude.

Both the spherical and cylindrical clouds with $\phi = 40\%$ display similar trends that are dependent on the strain amplitude. Below the critical strain amplitude in Pine et al. (2005), the clouds are macroscopically reversible, with no changes in their size or position over many oscillations. When the strain amplitude is above the critical strain amplitude, and below $\gamma_0 \approx 7.5$, the cloud extends along the channel centerline, creating an ellipsoid cloud in the spherical case and an elliptic cylinder in the cylindrical case, and undergoes a slight compression towards the channel centerline. With strain amplitude above $\gamma_0 \approx 7.5$, the cloud shows a backward extension of the upper and lower edges of the initial cross section, creating a parallelogram shape. This backward extension is more evident for the cylindrical clouds, which have a greater number of particles in the edges of the cloud closest to the channel walls. The particle contact force drives the backward extension, and a strain amplitude of $\gamma_0 \approx 7.5$ corresponds to the time that the contact pressure needs to develop its maximum value during each half cycle.

4.4 Higher volume fraction clouds, $\phi = 55\%$

Distinctive behavior emerges for large particle clouds in experiments with higher volume fraction, as noted by Metzger and Butler (2012). When $\frac{R}{a} \approx 20$ and ϕ is large, the particles form a galaxy shape with the center of the cloud rotating as if it was a rigid body and shedding particles in the front and back to form the galaxy arms. The galaxy shape does not form at the same volume fraction when $\frac{R}{a} \approx 12$. In this section we will fix the volume fraction at $\phi = 55\%$, while varying the radius R of the cylindrical cloud. The channel height is set as $H/R = 4$, except for cloud radius $R/a = 5$ where $H/R = 4.8$. In all cases, the strain amplitude is chosen as $\gamma_0 = 10$ to be high enough to allow time for the galaxy arms to develop.

Results similar to those in the experiments are seen in the present simulations, where the galaxy formation depends on the size of the particle cloud, as shown in Fig. 4.14. For $R/a < 10$, the normal elongation behavior is present, while for $R/a > 15$, galaxies are formed, consistent with the experimental results. The critical radius for formation of a galaxies depends on the volume fraction of the cloud. If the particles are seeded in a hexagonal pattern, so that the volume fraction is close to

(a) $\dot{\gamma}t = 30$ ($\dot{\gamma}t = 1.5T$)

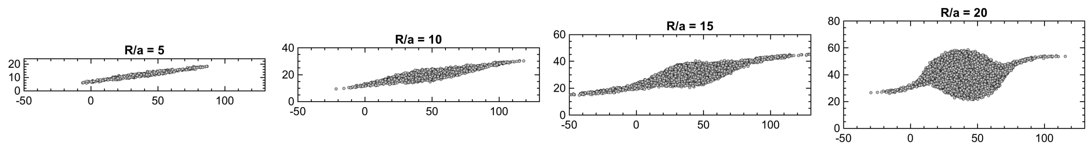

(b) $\dot{\gamma}t = 40$ ($\dot{\gamma}t = 2T$)

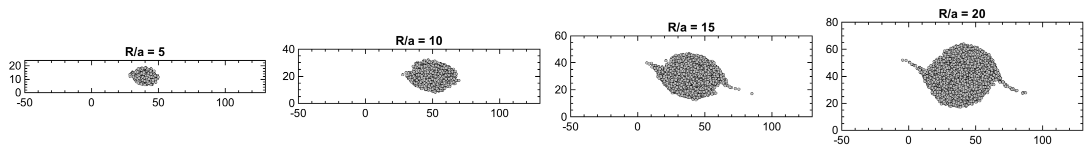

Figure 4.14: Particle positions after $\dot{\gamma}t = 30$ (top) and $\dot{\gamma}t = 40$ (bottom), for various values of R/a with initial volume fraction $\phi = 55\%$. When $R/a \leq 10$, the clouds extend with the imposed shear and return to their original positions after each oscillation. For $R/a > 10$, the clouds form a galaxy-like shape both on their extension and at the end of the oscillation. Particles are actual size.

the maximum packing limit for spheres, galaxy formation can be seen at $R/a = 8$. In contrast, clouds with lower volume fraction, $\phi = 40\%$, were not observed to rotate at $R/a = 20$, 30, or 80.

When the particles are forming the galaxy the center of the cloud appears to rotate as a solid cylinder with a small elongation in the stream-wise direction. This can be seen by looking at the wall-normal velocity field, $\langle v \rangle$, around the cloud, shown in fig. 4.15 at $\dot{\gamma}t = 30$ ($\dot{\gamma}t = 1.5T$). In comparison with figs. 4.7a and 4.8a for $\phi = 40\%$, the blockage caused by the presence of the cloud induces a stronger wall-normal velocity when $\phi = 55\%$, with a peak blockage of 25% of the shear flow compared with 10% for $\phi = 44\%$. Here, the effect is strong enough that the cloud continues to rotate over the entire period instead of shearing with the flow.

Greater insight into the movement of the particles is found by color-coding and tracking the particles that form the galaxy arms. In fig. 4.16 the particles in the arms are color-coded at $\dot{\gamma}t = 30$ (red and blue particles) and $\dot{\gamma}t = 40$ (green particles.) The particles are then tracked back to their original positions at $\dot{\gamma}t = 0$. Particles

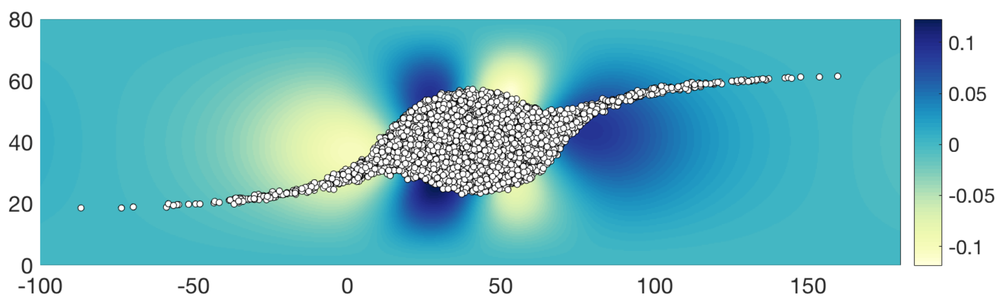

Figure 4.15: Plot of particle locations relative to the averaged wall-normal velocity $\langle v \rangle$ at $\dot{\gamma}t = 30$ ($\dot{\gamma}t = 1.5T$) for $R/a = 20$, $H/a = 80$. The particle arms form in the locations where the wall-normal velocity field induced by the cloud rotation switches direction. As for lower volume fraction clouds, the stresslet of the bulk cloud causes the cloud to rotate. A video illustrating the particle migration is available in the supplementary material.

forming the arms come from the cylinder edge, and are localized within the cloud. The movie available on the Brown Digital Repository (Howard, 2018) shows that during the first half period the cloud rotates as well as extends until the extension of the edge of the cloud, represented by the blue particles, is large enough that some particles reach the area outside the cloud where the wall-normal velocity changes sign. At this stage the blue particles break off from the cloud, forming the arm of the galaxy during the first half cycle. The particles closer to the edge of the cloud have final positions closer to the tips of the arms. The process reverses during the second half of the oscillation, with the blue and red particles rejoining the cloud and the green particles forming the arms. The shape and length of the cloud arms therefore depend on the flow field outside the cloud, caused by the blockage effect and the modified stresslet of the particle cloud. In test cases changing the channel length affects the length and number of particles in the galaxy arms, but not the onset of rotation in the cloud.

In extensional clouds, particles are displaced by discrete particle contact forces and continuous long-range hydrodynamic and lubrication forces, as discussed in fig.

(a) $\dot{\gamma}t = 0$ ($\dot{\gamma}t = 0T$)

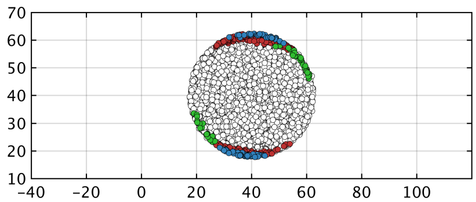

(b) $\dot{\gamma}t = 30$ ($\dot{\gamma}t = 1.5T$)

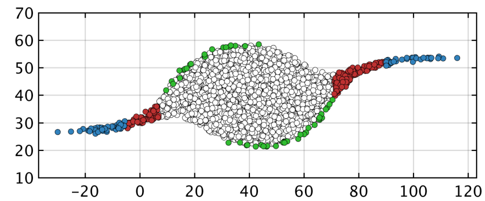

(c) $\dot{\gamma}t = 40$ ($\dot{\gamma}t = 2T$)

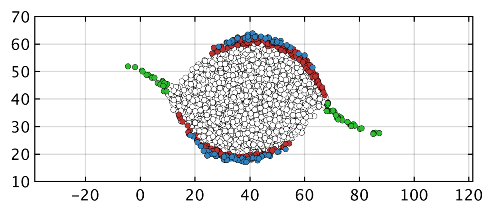

Figure 4.16: $R/a = 20$. Particles color-coded based on their positions at $\dot{\gamma}t = 40$ (green) and $\dot{\gamma}t = 30$ (blue and red.) The particles that end up in the galaxy arms outside of the cloud at $\dot{\gamma}t = 30$ and $\dot{\gamma}t = 40$ originate in the outside of the cloud. The particles that are in the arms at $\dot{\gamma}t = 30$ are in the bottom and top of the cloud at $\dot{\gamma}t = 0$, with particles further out in the arm closer to the top and bottom of the cloud. The particles that are in the arms at $\dot{\gamma}t = 40$ are in the edge of the cloud, but rotated by about 45°. During the first half period the cloud rotates approximately 90° in the clockwise direction, shown by the rotation of the green particles. See movie in supplementary material (Howard, 2018).

4.11. Fig. 4.17 shows the analogous scatter plots and probabilities for rotational clouds. Here, the particles that form the galaxy arms have a significant displacement in the y-direction without a particle contact force. Because of the high volume fraction, almost all particles have contact with another particle at some point during an oscillation, and the particles in the body of the cloud can experience extremely large contact pressures due to the tight packing of the particles. To achieve a meaningful average, we compare particles with a maximum pressure $P/\tau_w < 2$ and 10 instead of $P/\tau_w = 0$ in fig. 4.11. In comparison to the extensional cloud with $R = 10a$, the rotating cloud with $R = 20a$ has a large population of particles that have a low maximum pressure but a large cross-stream displacement, representing the particles that end up outside the initial footprint of the rotating cloud. This is due to two factors: the induced wall-normal flow outside the cloud, and the tight constraints on particles within the cloud body, limiting two particle interactions in the shear flow. Because the particles that form the galaxy arms are not displaced out of the cloud solely due to contact forces on those particles, varying the cutoff distance of the contact force, R_{ref}, does not change the qualitative behavior of the cloud, shown in fig. 4.18, as long as the particles still come into contact.

In fig. 4.19 we consider the average area fraction profile, contact pressure, and angular velocity of the cloud taken just before $\dot{\gamma}t = 20$ or $\dot{\gamma}t = T$. The averaged area fraction, $\phi(r)$, is defined as

$$\phi(r) = \frac{1}{2\pi r L_x} \sum_{i=1}^{N_p} \int_0^{L_x} \int_0^{2\pi} \chi_p^i(x, r, \theta)\, d\theta dx,$$

where $\chi_p^i(x, r, \theta)$ is the indicator function for the i^{th} particle, N_p is the number of particles, and r is the distance from the center of mass of the cloud in the $yz-$plane, denoted $\mathbf{r}^m = (y_{cm}, z_{cm})$. The phasic average of a variable $\mathbf{g}$ is defined as in Drew

(a) $R/a = 10$

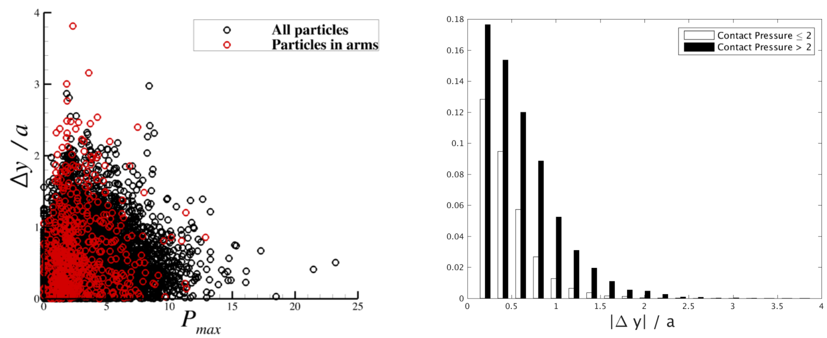

(b) $R/a = 20$

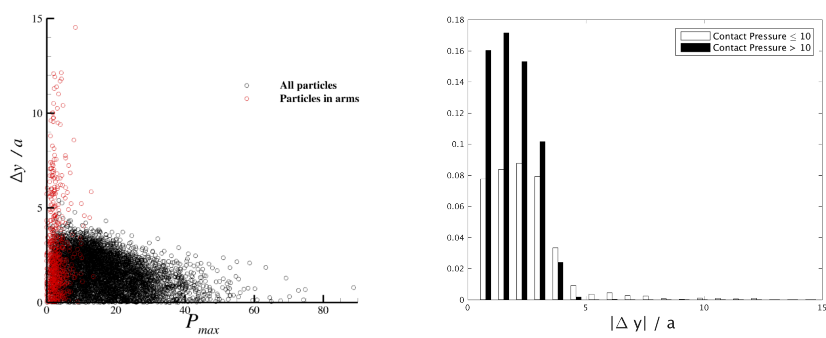

Figure 4.17: (a): $R/a = 10$ (extensional). (b): $R/a = 20$ (rotational). Left: Scatter plots of all particle displacements in the cross-stream direction over one period ($|\Delta y|$) with respect to the maximum contact pressure experienced during that period. Particles that end up outside the initial footprint of the cloud, defined as $r > R + 2a$ to account for the initial transient expansion of the cloud, are colored red. Right: Probabilities of particle displacements.

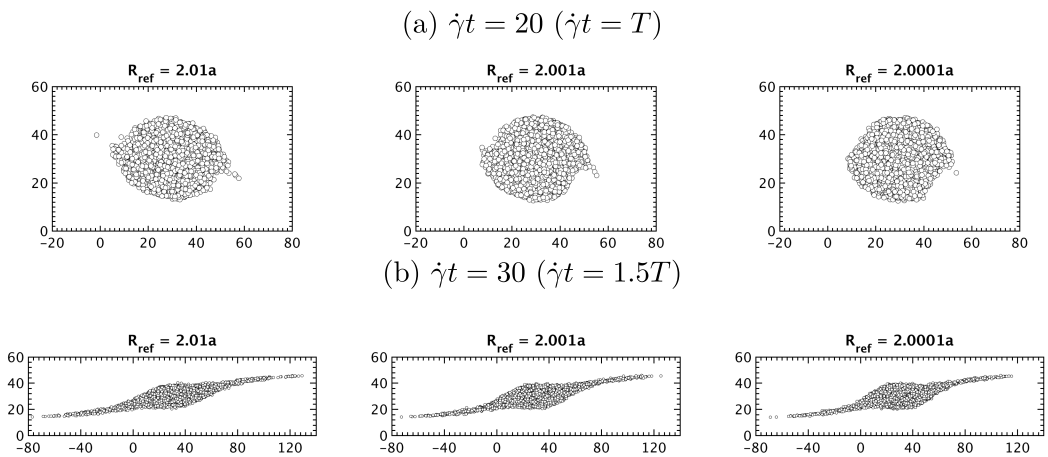

Figure 4.18: Particle positions after $\dot{\gamma}t = 20$ (top) and $\dot{\gamma}t = 30$ (bottom), for various values of R_{ref} with $R/a = 15$ and initial volume fraction $\phi = 55\%$. Changing R_{ref} has only small changes in the length of the maximum extension, and reduces the number of particles in the arms at the end of each period so that the cloud returns closer to its initial positions. Particles are actual size.

(1983):

$$\langle \mathbf{g}\chi_p \rangle(r) = \frac{1}{2\pi r L_x} \sum_{i=1}^{N_p} \int_0^{L_x} \int_0^{2\pi} \mathbf{g}^i(x, r, \theta)\chi_p^i(x, r, \theta)\, d\theta dx.$$

The angular velocity of the i^{th} particle, Ω^i, is found from the moment of momentum scaled by $m(r^i)^2$,

$$\Omega^i = \frac{\mathbf{x}^i \times m\mathbf{v}^i}{m(r^i)^2},$$

where $\mathbf{x}^i = (y^i, z^i)$ and $\mathbf{v}^i = (v^i, w^i)$ are the y and z components of the position and velocity, respectively. Here, $r^i = ||\mathbf{x}^i - \mathbf{r}^m||$, the distance between the center of particle i and the center of mass of the cloud.

For the non-rotating clouds, $R/a \leq 10$, the volume fraction drops significantly from $\phi_i = 55\%$ after one period, while when $R/a > 10$, the volume fraction remains high or increases in the center of cloud. The volume fraction decreases at the edges of the cloud, as the cloud is free to expand under the influence of the particle pressure stemming from the tightly packed particles.

The contact pressure, shown in fig. 4.19b, is highest in the center of the cloud, with the maximum value increasing with the cloud radius R. At $\dot{\gamma}t = 20$ the cloud has undergone one oscillation cycle, and the particles have expanded outside the initial footprint of the cloud, creating a significant volume fraction at distances greater than the initial cloud radius. However, the contact pressure quickly drops to zero for particles further from the center of mass of the cloud than the initial cloud radius, $r/a > R/a$, because the particles are not constrained. The differential rotation of the cloud in fig. 4.19c is highest at the outside edge of the cloud, and goes to zero in the center of the cloud, demonstrating that the cloud is not rotating as solid cylinder, but instead the outer layers are shearing in comparison to the cylinder core. Outside the tightly packed cylinder body, the angular velocity of the particles drops close to zero. The particles that form the arms of the galaxy are primarily advected by the shear flow, with some wall-normal migration due to the velocity field induced by the stresslet and bulk hydrodynamic effect of the cloud, and do not have a significant angular velocity.

4.5 Conclusions

In this chapter, we have considered cylindrical and spherical clouds of densely packed neutrally buoyant particles suspended in an oscillating Couette flow. The system illustrates two distinct regimes of irreversible particle migration. When the particle volume fraction is lower, close to $\phi = 40\%$, the particle contacts generate an irreversible stresslet, allowing particles to progressively escape the cloud. The contact interactions between particles in the system drive an irreversible fluid disturbance, and in turn drives the net motion of particles, which may not experience a contact force, out of the cloud. At high strain amplitude, the addition of two particle discrete

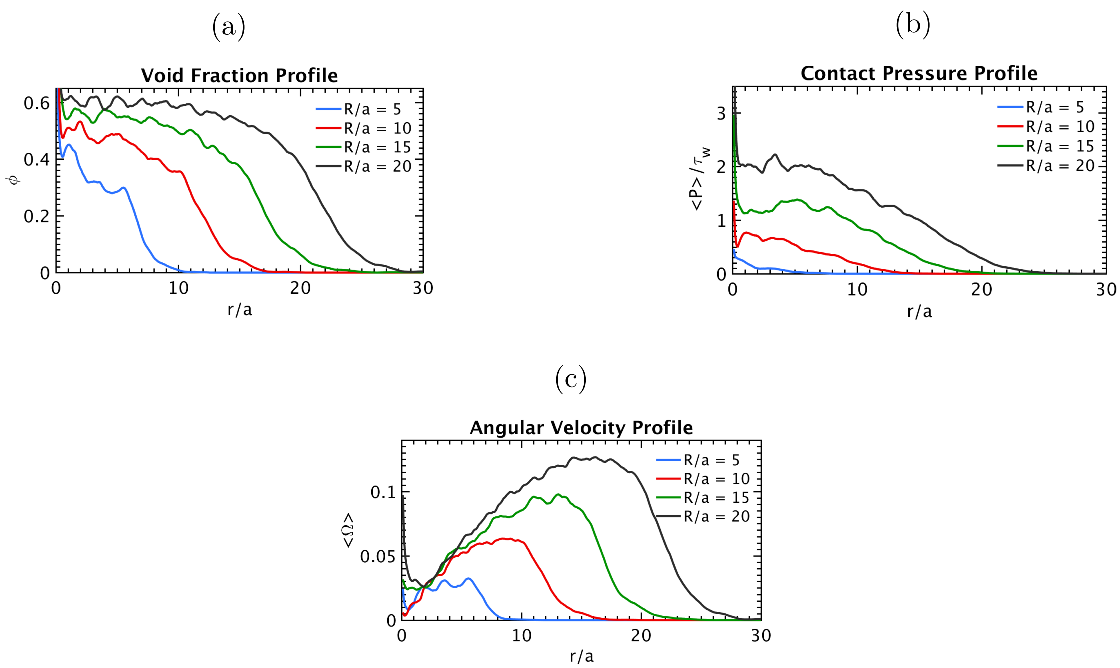

Figure 4.19: Volume fraction profiles (a), average contact pressure profiles (b), and average angular velocity profiles relative to the center of mass of the cloud (c) taken just before $\dot{\gamma}t = 20$. The contact pressure increases with the size of the cloud. The angular velocity of the particles is largest at the outside of the cloud, where the particles can be advected by the surrounding fluid flow.

particle contact events creates an additional mechanism for particles to extend out of the cloud.

When the cloud is in a compact state it represents a dense, porous body that significantly blocks the flow. This induced bulk flow from the presence of the cloud generates a wall-normal flow causing the cloud to rotate. The bulk stresslet generated by the particles can squeeze and stretch the cloud, which may enhance the rotation. At low volume fraction, $\phi = 40\%$, the cloud shears after this initial rotation, causing an elongation of the cloud in the streamwise direction. For large, dense clouds with $\phi = 55\%$, the rotation caused by the presence of the cloud is strong enough that the cloud does not shear with the flow, causing particles along the edges of the cloud to be advected away from the cloud to form galaxy-like arms.In this case, the rotation of the cloud is determined by the ratio of the cloud radius to particle radius. Clouds with $R/a \leq 10$ shear in the same manner as the lower volume fraction clouds with $\phi = 40\%$. A ratio $R/a > 10$ is needed for the cloud to begin to rotate.

When two particles come into contact the particles are irreversibly displaced across streamlines. This cross-stream displacement increases with particle roughness, represented by the size of the cutoff barrier for the particle contact force. This changes the macroscopic shape of the cloud at $\phi = 40\%$ as the particles are advected by the flow during the remaining portion of the cycle. This migration is significant at high strain amplitudes, where the particle contact pressure has a significant amount of time to develop.

This study demonstrates that the particle contact forces contribute to the irreversible particle displacements in suspension systems, both directly through two particle contacts and indirectly through particle displacements of nearby neighbors. At lower volume fractions, $\phi = 40\%$, the particle contact force is key in determining the particle migration, and as the strain amplitude increases the macroscopic state of the cloud after many oscillations corresponds to the maximum contact pressure the cloud has reached over each half oscillation. The contact pressure is shown to instantaneously drop to zero after each oscillation, so a sufficiently large strain amplitude is needed for the contact pressure to have time to develop in each half cycle. In contrast, at high volume fraction, $\phi = 55\%$, almost all the particles are in contact with other particles, and the role of the contact force in the development of galaxy arms becomes limited to the edges. Instead, the particles are advected by the wall-normal flow that develops in response to rotation of the cylindrical cloud.

Chapter Five

Developing Poiseuille flow with monodisperse particles

In this chapter, we consider the case of a developing Poiseuille flow. In contrast to previous studies, which looked at a final steady state Poiseuille flow once the stress and volume fraction profiles have reached a steady state (Yeo and Maxey, 2011), the developing Poiseuille flow data can help elucidate questions as to the primary factors driving particle migration in a channel.

Nott and Brady (1994) show that, assuming the particles are driven purely by hydrodynamics, the characteristic timescale for a suspension Poiseuille flow to reach steady state is

$$t_s \sim \left(\frac{H_y}{a}\right)^3 \frac{a}{12d(\phi)\langle u\rangle}, \tag{5.0.1}$$

where H_y is the channel height, a is the particle radius, $\langle u\rangle$ is the average velocity across the channel, and $d(\phi)$ is a non-dimensional function of ϕ due to the self-diffusivity of the particles, which can be estimated from experiments. Estimating the value of $d(\phi) \approx 1/12$ gives

$$t_s \sim \left(\frac{H_y}{a}\right)^3 \frac{a}{\langle u\rangle}. \tag{5.0.2}$$

Nott and Brady (1994) note that using this scaling it is unlikely that many early Poiseuille flow experiments, including those of Koh et al. (1994), were in steady-state when the final values were reported. Thus, in section 5.1 we discuss the dynamics of a developing suspension Poiseuille flow, which may provide a better comparison to experiments before reaching steady state. Simulations of developing Poiseuille flows also provide comparisons to experiments where data is available throughout the the experiment, as in Snook et al. (2016) discussed in sec. 5.2.

5.1 Steady pressure driven suspension flows

5.1.1 Simulation parameters and definitions

A channel half height of $h = 20a$ is used in the simulations, resulting in a channel height $H_y = 40a$. The channel length is $L_z = 60a$ and the channel depth is $L_x = 30a$, and the volume fraction is fixed at $\phi = 0.4$, which gives $N_p = 6876$ particles.

The simulations are started from a random configuration of particles. Particles with a radius $0.85a$ are placed in a channel with random coordinates. Then, a molecular dynamics simulation is run as the particle size is slowly increased to a over 1,000 time steps. At high volume fraction, randomly placing full size particles in a channel without the inflation step is time prohibitive, as it can take many, many iterations to find an empty location for each particle. This two step process allows for a uniform volume fraction across the channel, although some layering does occur at the channel walls due to the inflation procedure.

The accumulated strain is defined as

$$\gamma = \frac{\langle u_z \rangle t}{h},$$

where $\langle u_z \rangle$ is the particle bulk velocity in the streamwise direction.

A constant pressure gradient of $f^D = \frac{\partial p}{\partial z} = 0.0288$ is imposed on the flow, which sets the streamwise fluid velocity in the absence of embedded particles. The streamwise bulk particle velocity varies in response to the imposed pressure gradient depending on the local volume fraction, as shown in fig. 5.1. The bulk particle velocity increases to a steady value of $\langle u_z \rangle = 1.28$ over about 250–300 strain units.

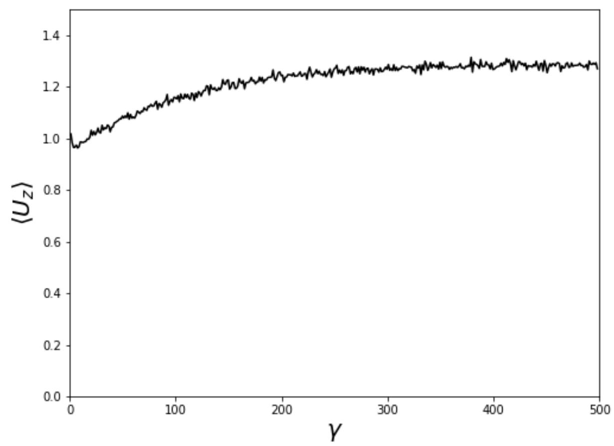

Figure 5.1: Development of the bulk particle velocity as a function of the accumulated strain, γ, for $\phi = 0.4$.

Using the scaling in eq. 5.0.2, and solving for the characteristic number of strain units needed to reach steady-state in this simulation gives $\gamma_s = \frac{2H_y^2}{a^2}$. Given the parameters from above, $\gamma_s \sim 1600$. In this section, we will be considering accumulated strains $\gamma \ll 1600$ to study the initial development of the suspension.

The phase-averaged, mean velocity profile for the particles as defined in 2.1.23 is shown in fig. 5.2 to flatten over time. The streamwise velocity is scaled by the centerline velocity of a parabolic flow of pure fluid that has the same bulk velocity of the suspension, denoted by U_c, and is averaged over the channel centerline. The velocity profile is blunted in the center of the channel, consistent with the experiments by Lyon and Leal (1998). The blunting of the profile initially occurs in the first 120 strain units, with very few changes after. The velocity profiles at $y/a = 1$ show the effects of particles "rolling" along the wall through the almost step-function increase in the velocity. While the no-slip condition is enforced at the channel walls, the weak tangential lubrication forces due to the wall does allow some sliding. Mostly, the particles move with the fluid velocity at their center and roll to match the shear

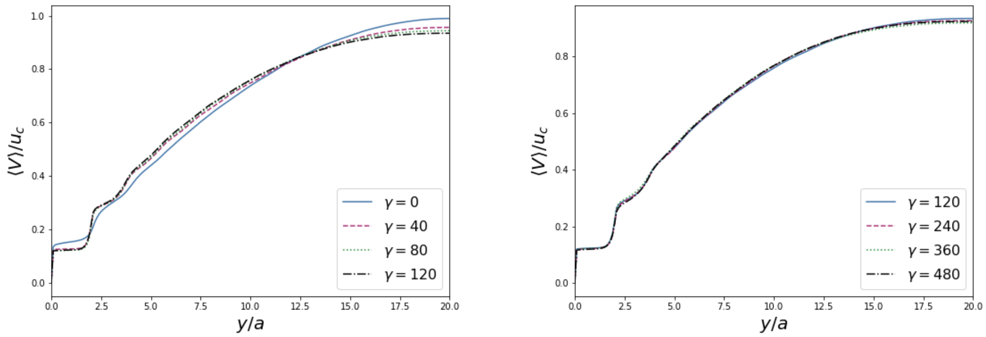

Figure 5.2: Phase-averaged, mean streamwise velocity profile for the particles. $\phi = 0.4$.

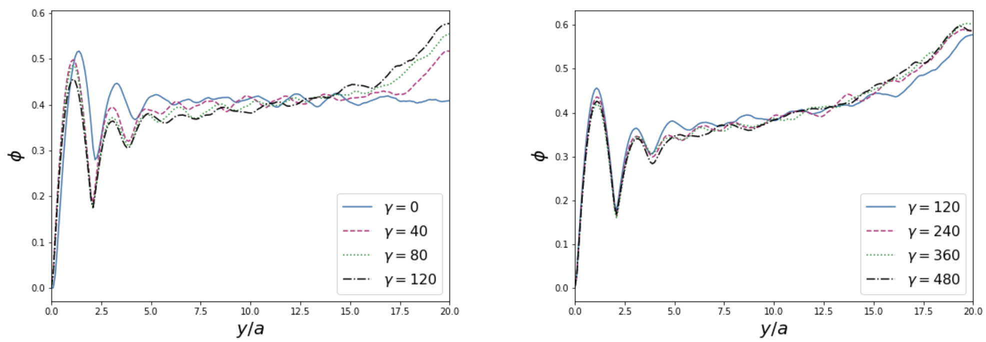

Figure 5.3: Volume fraction profiles at accumulated strain $\gamma = 0 - 500$ for $\phi = 0.4$.

rate. This particle rolling has been seen in experiments where dye is placed on the outer wall of the channel to coat the particles as they roll (Souzy et al., 2015).

The volume fraction is computed by the averaged area fraction, defined as

$$\phi(y) = \frac{1}{L_x L_z} \left\langle \int \int \chi_p(x, y, z) \; dx dz \right\rangle . \tag{5.1.1}$$

Once the flow is started, the particles begin to migrate towards the channel centerline, located at $y/a = 20.0$ in fig. 5.3. Some particles do migrate into the wall layer, away from the centerline, during the first few strain units. The volume fraction in fig. 5.3 shows clear particle layering at the channel walls at $y = a$, with an additional

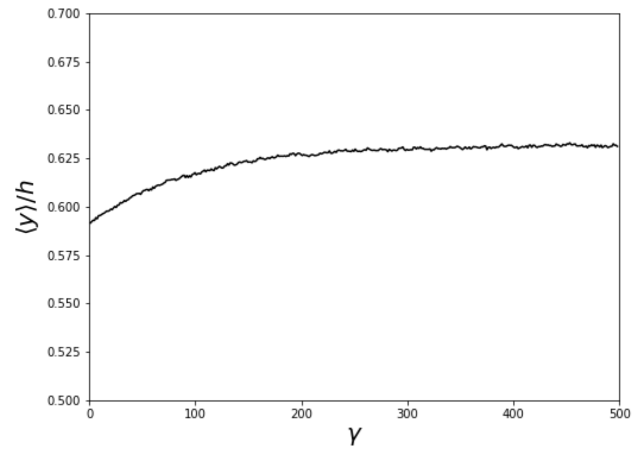

Figure 5.4: Particle location averaged over the channel centerline and scaled by the channel halfwidth for $\phi = 0.4$.

layer of particles forming on top of the initial layer at $y = 3a$. The development and formation of the wall layering will be discussed in detail in sec. 6.4.5. As the accumulated strain increases, the particles migrate towards the center of the channel and the volume fraction in the mid-shear region, defined as $6 \leq y/a \leq 13$, decreases slightly. This trend continues until around $\phi = 240$, when the volume fraction in the center of the channel reaches a constant value of $\phi = 0.587$. From that point, the volume fraction profile remains qualitatively the same across the channel, with small variations as particles rearrange slightly within the flow.

The migration to the channel centerline can also be seen in the average particle location plotted in fig. 5.4. The particle location is averaged over the channel centerline and scaled by the channel halfwidth, so a value of 0 is at the channel wall and 1 is on the centerline. The average location increases with the strain amplitude, which means particles are migrating towards the centerline. This is a quite small migration on average.

The particle contact pressure profile is shown in fig. 5.5 as defined in eq. 2.1.21,

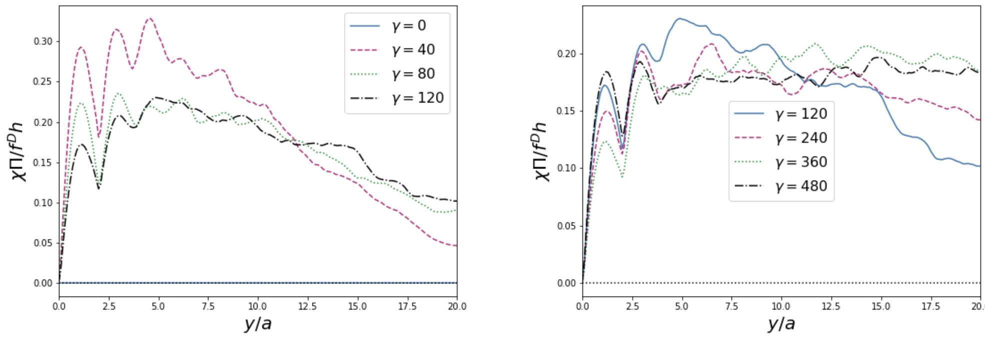

Figure 5.5: Particle contact stress profiles as defined by eq. 2.1.21 at accumulated strain $\gamma = 0 - 500$ for $\phi = 0.4$.

scaled by the wall shear stress, $\sigma_w = f^D h$. . Gradients in the contact pressure are indicative of particle movements, with particles moving from areas of high contact pressure to low contact pressure. The actual migration is probably driven by the S_{22} contact stress, as discussed in sec. 5.1.2. Thus, these profiles are consistent with an average particle migration to the centerline, especially when $\gamma < 240$. The contact pressure is initially zero across the channel, as no particles are in contact when the flow begins. The contact pressure quickly develops to be highest in the midshear region and wall region and lowest in the channel center. As particles migrate the particle pressure increases at the centerline while decreasing in the mid-shear region. At long time, strain amplitude $\gamma > 360$, the contact pressure reaches an equilibrium across the channel, where the value is almost constant outside of the region near the wall. Interestingly, this equilibrium is reached well after the volume fraction profile ceases to evolve, suggesting that once the steady-state volume fraction profile is reached the particles continue to rearrange into a more stable state.

Fig. 5.6 shows the developing stress profiles, which contains the contributions from the FCM longer range hydrodynamic stresslet, lubrication stresslet, and contact stresses. These stresses follow a similar trend to the particle contact pressure, where

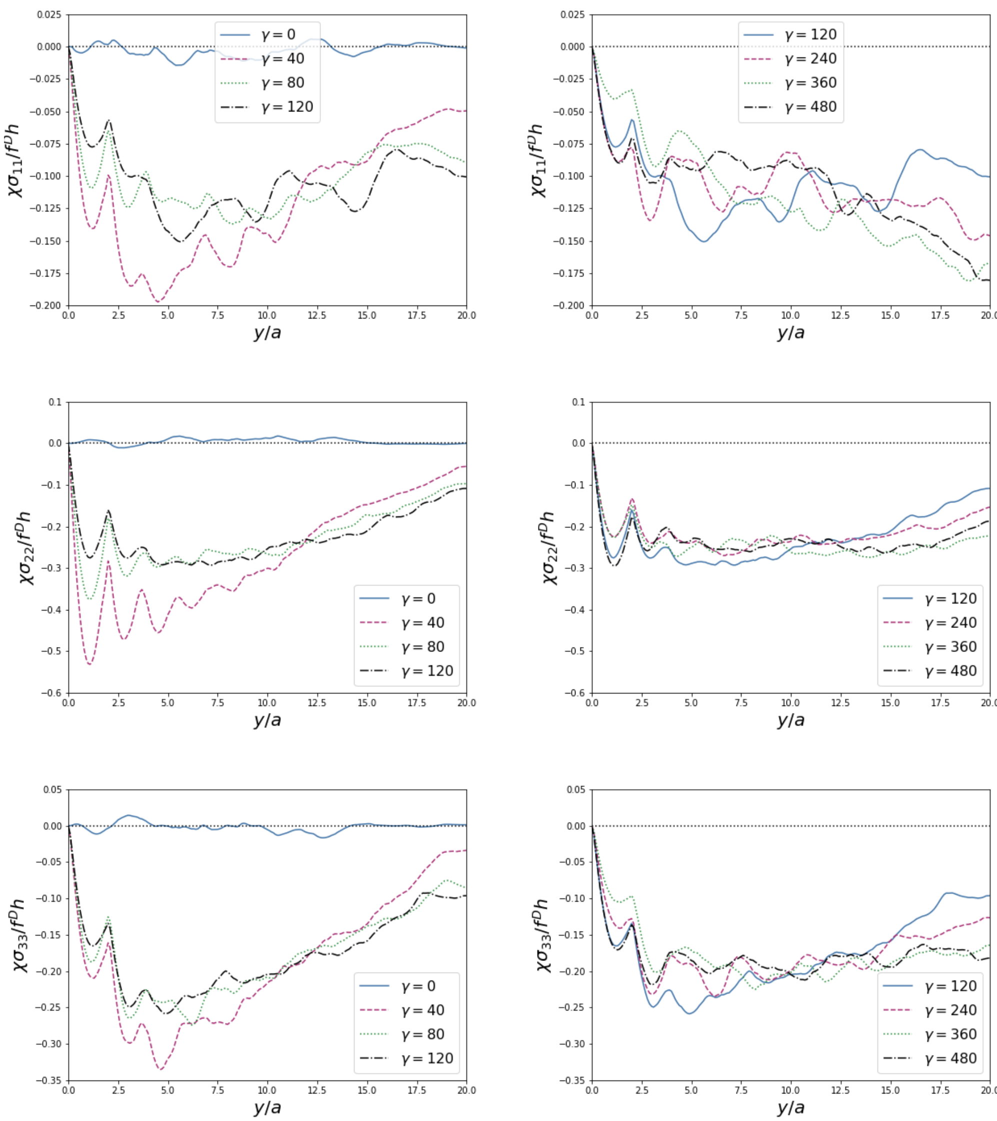

Figure 5.6: Stress profiles σ_{11} (top), σ_{22} (middle), and σ_{33} (bottom) for monodisperse steady flows of particles for $\phi = 0.4$ for $\gamma = 0 - 480$.

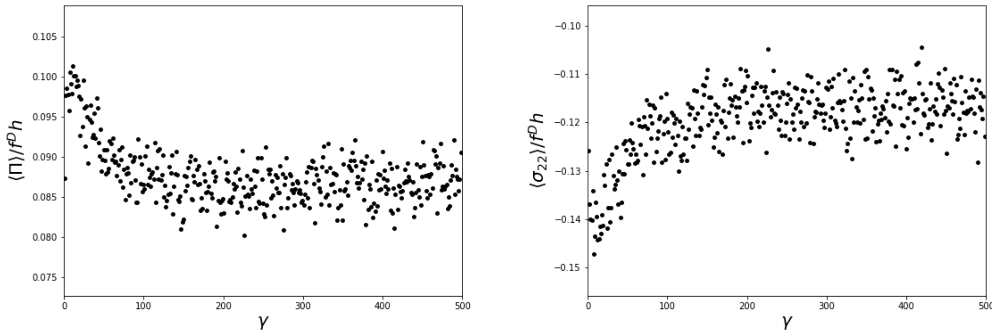

Figure 5.7: Averaged particle contact pressure $\langle P\rangle$ and stress $\langle\sigma_{22}\rangle$ for $\phi = 0.4$.

the largest values are found at short times, then the stresses relax to an equilibrium value across the channel.

The change in the stress and contact pressure profiles over time can be seen in fig. 5.7, which shows the bulk, particle-averaged pressure $\langle\Pi\rangle$ and 22-stress $\langle\sigma_{22}^P\rangle$. Both quantities have the largest absolute value at the start of the simulation, then the average value decreases to a stable value after an accumulated strain of $\gamma \approx 150$. In fig. 5.7 each symbol represents a individual time step. Cleary, there is some variation in both the contact pressure and σ_{22}, which is due to the fact that particle contacts are discrete events instead of continuum values. As particles move past each other into contact, the contact pressure spikes and then decreases. This variation is about 5% of the equilibrium value for the contact pressure and 15% of the equilibrium value for σ_{22}.

The coordination number, defined as

$$C = \frac{1}{N_P}\sum_{i=1}^{N_P} \#\{j : ||x_i - x_j|| < R_{ref}\},$$

gives another way to measure the contacts between particles. Here, instead of looking at the net pressure developed by those contacts, the mean number of contacts is

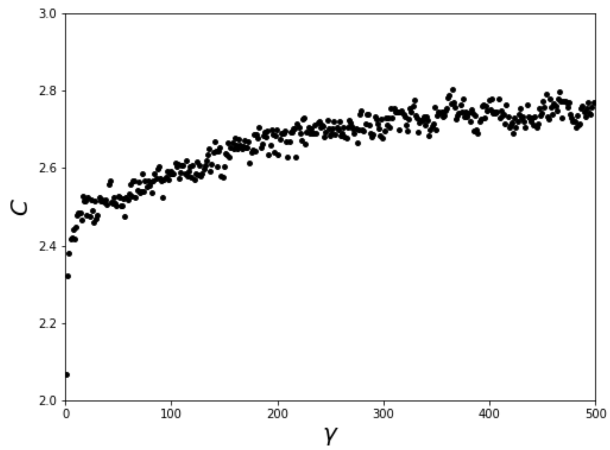

Figure 5.8: Particle coordination number, C, for $\phi = 0.4$.

considered. Combined with the contact pressure, the coordination number can be used to determine whether there is a large contact pressure between a small number of particle contacts or a small contact pressure between a large number of neighbors per particle. Shown in fig. 5.8, the coordination number increases with the strain amplitude. It is unclear if the coordination number has reached a constant value by the end of the simulation at $\gamma = 500$. In either case, the timescale for the coordination value to reach a steady equilibrium is certainly much longer than for the particle stresses in fig. 5.7. This lends additional evidence to the fact that while the volume fraction profile has reached a steady value, at the strain amplitudes considered here the particles are continuing to rearrange. Since the contact pressure remains approximately constant after $\gamma_c \approx 150$, the increasing coordination number in this range suggests that particles begin having more contacts with neighbors, but with a lower pressure per contact.

Sample particle trajectories are shown in fig. 5.9 for three randomly selected particles. Each particle has a net migration towards the channel centerline at $y/h = 1.0$, but the particle migration is not uniform over time. The trajectories are color-

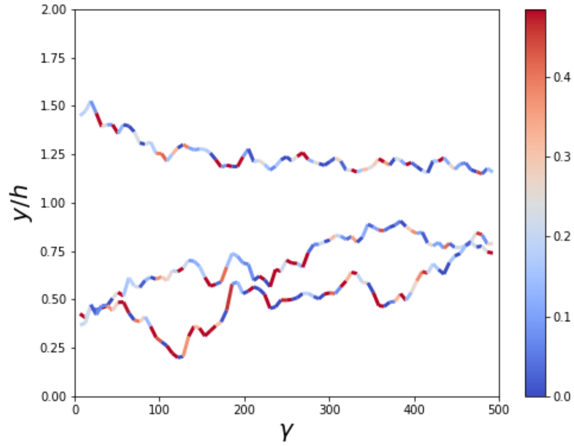

Figure 5.9: Sample particle trajectories for three randomly selected particles. The particle position in the y direction is plotted for 500 strain units, colored by the net contact pressure on that particle.

coded by the net contact pressure on the particle due to all neighboring particles. In section 2.2.2.2 we showed that an irreversible particle displacement is possible without the particle experiencing a contact force if nearby particles are displaced by contact. However, the largest displacements do occur when contact takes place. In fig. 5.9 the largest contact pressures occur when the particles have the largest displacement, however, the particles do have some displacements even when they have a zero contact pressure.

The normal stress differences are given in fig. 5.10. With the notation used in this work, $N_1 = \sigma_{33} - \sigma_{22}$, and $N_2 = \sigma_{22} - \sigma_{11}$. Here, N_1 is shown to be positive, and N_2 negative, with $|N_2| > |N_1|$. A positive value of N_1 means that $|\sigma_{22}| > |\sigma_{33}|$, and a negative value of N_2 implies $|\sigma_{22}| > |\sigma_{11}|$, consistent with fig. 5.6.

The shear stress is shown in fig. 5.11. It is compared the total shear stress in a Poiseuille flow,

$$\frac{\langle \sigma_{23}^{tot} \rangle}{f^D h} = 1 - \frac{y}{h}. \tag{5.1.2}$$

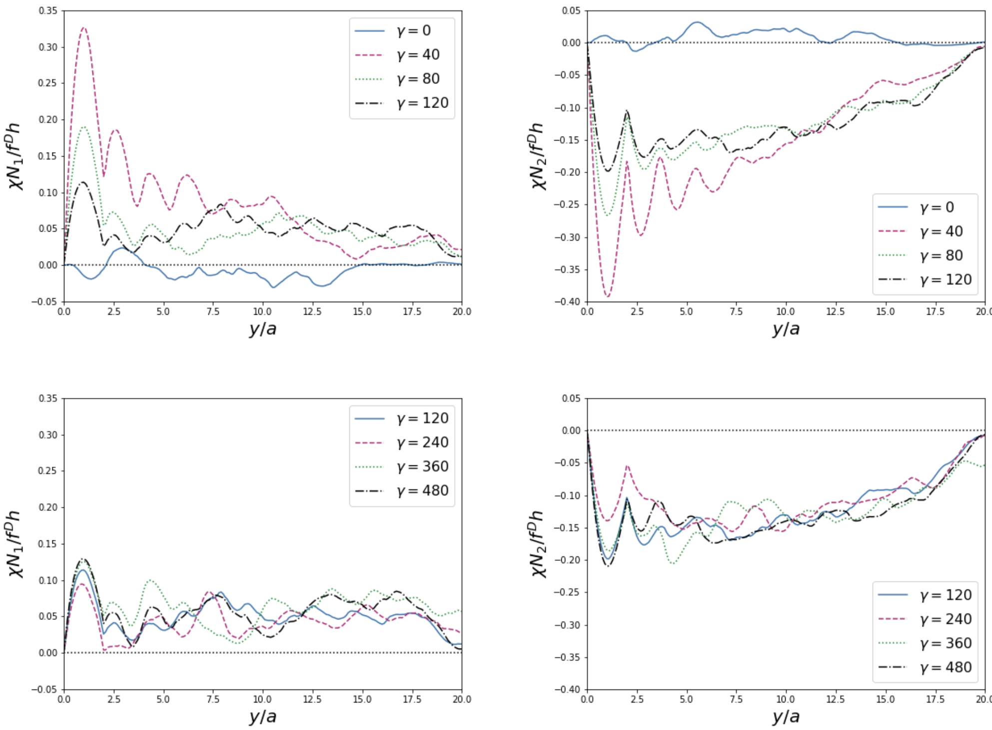

Figure 5.10: Normal stress difference profiles for monodisperse steady flows of particles for $\phi = 0.4$.

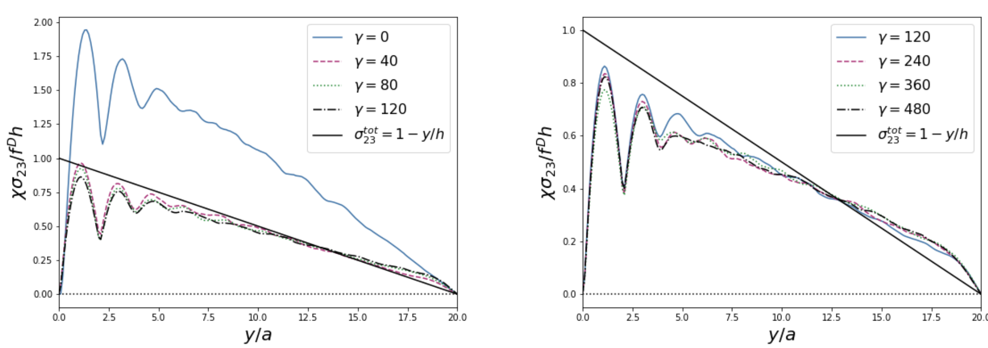

Figure 5.11: Particle shear stress profiles at accumulated strain $\gamma = 0 - 500$ for $\phi = 0.4$.

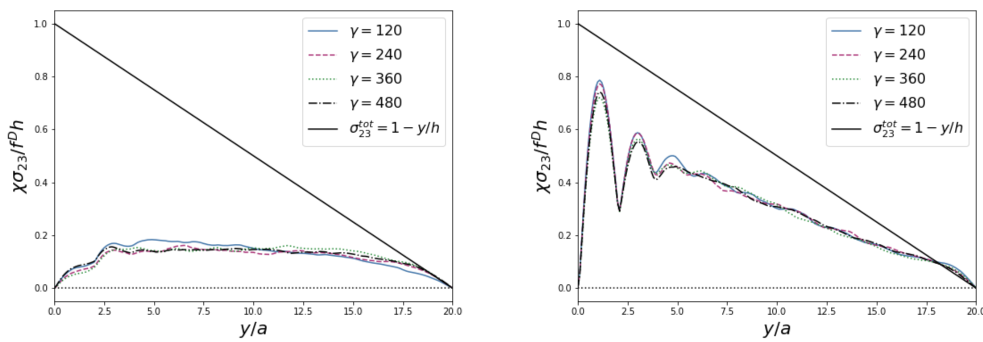

Figure 5.12: Particle shear stress profiles from contact forces (left) and all other terms (right).

The shear stress is slightly larger than the comparison in the center of the channel, and less at the channel wall. In fig. 5.12 the shear stress is broken down into the component from the contact forces and from all other terms. The contact stress is uniform across the channel, aside from deviations at the wall and at the center of the channel where the shear rate goes to zero. The overshoot at the channel centerline is possible due to the finite particle size and the approximate nature of the stress dipole moments as compared to the continuous body force density of eq. 2.1.1.

5.1.2 Particle fluxes

The SBM from Morris and Boulay (1999) gives the particle migration flux, or the flux of particles relative to the suspension mean flow as:

$$\mathbf{j}_{\perp} = \phi\mathbf{U} - \phi\langle\mathbf{u}\rangle = \frac{2a^2}{9\eta_f} f(\phi)\nabla\cdot\Sigma_p. \qquad (5.1.3)$$

Here, $\mathbf{U}$ is the local average velocity of the particles phase, $\langle\mathbf{u}\rangle$ is the average particle phase velocity, η_f is the viscosity of the suspending fluid, and Σ_P is the particle phase stress. The hinderance function, $f(\phi)$, is taken from Richardson and Zaki (1954)

$$f(\phi) = (1-\phi)^{\alpha}.$$

We take $\alpha = 5$ as in Boyer et al. (2011).

In the simulations, the particle Σ_P can be approximated by the σ_{22} component of the stress tensor, giving

$$\mathbf{j}_{\perp}^{FCM} \approx \frac{2a^2}{9\eta_f} f(\phi) \frac{\partial \sigma_{22}}{\partial y} \tag{5.1.4}$$

A comparison of the particle fluxes computed directly from the FCM simulations and from the SBM is given in fig. 5.13. The two quantities agree in magnitude, and both go to zero at the channel centerline, as is expected due to the symmetry of the flow. The SBM does not take into account layering at the channel walls, so the approximations are clearly not valid in a region near the wall where the stress tensor has a large gradient. Because of the subsequent layering that builds atop the wall layering, the fluxes calculated from the stress tensor are not valid within a region of $\sim 10a$ from the channel wall. Overall, the SBM using the FCM stress tensor captures the general features of the particle flux profile for $0.5 < y/h < 1$, but the result is noisy due to the fact that the stress tensor has contributions from the particle contact force, which consists of intermittent discrete contact events instead of a continuous force.

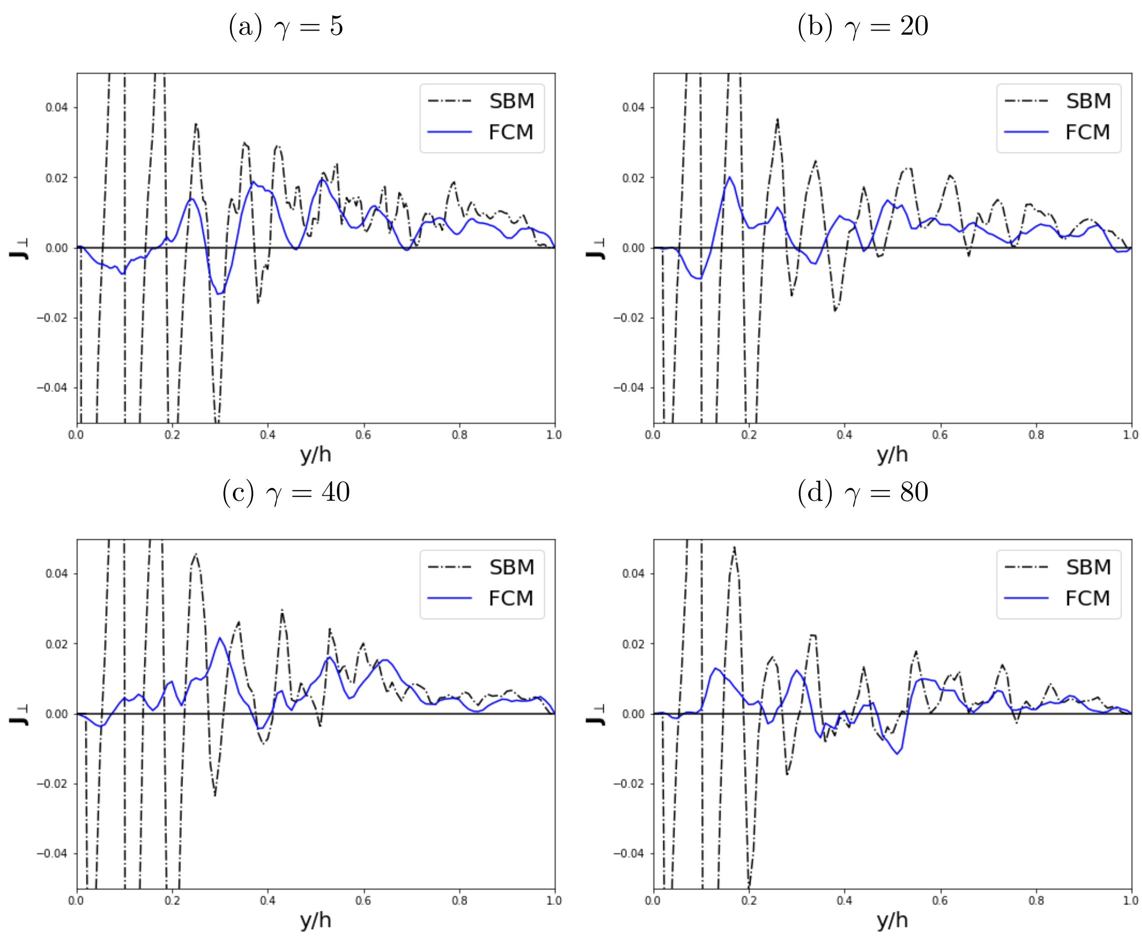

Figure 5.13: Particle fluxes from the FCM simulations (solid blue lines) and from the SBM with $\Sigma_P = \sigma_{22}$ (dash-dotted black lines.)

5.2 Oscillating suspension flows

Eq. 5.0.2 for the characteristic timescale to steady state for a suspension flow can be also used to find the length of the channel needed for the suspension to reach steady state:

$$\frac{L}{H} \sim \left(\frac{H}{a}\right)^2 \frac{1}{12d(\phi)} \sim \left(\frac{H}{a}\right)^2. \tag{5.2.1}$$

This long channel length scaling means that experiments require extremely large channels if they are going to reach steady state flows, a situation that is highly impractical in many laboratories. To compensate, many experiments consider oscillating flows, where the channel can be much shorter

In this section, experimental results by Snook et al. (2016) are compared with FCM results for an oscillating Poiseuille flow. Fundamental questions include how the development of an oscillating flow compares to that of a steady flow, and how the time scale of development depends on the particle volume fraction.

5.2.1 Simulation parameters

The experiments were done in a pipe with a circular geometry, as opposed to a planar channel in the simulations. To achieve a meaningful comparison between the simulations and experiments, the particle-averaged strain rate is matched. The particle averaged strain amplitude for a channel is $3\langle \Delta Z \rangle_P / H$, compared to $8\langle \Delta Z \rangle_P / 3R$ for a pipe, where R is the pipe radius. The strain amplitude in a channel is scaled by $\gamma_0^{channel} = 8/4.5\gamma_0^{pipe}$, resulting in a strain amplitude $\gamma_0^{channel} = 9.6$.

To match the pipe radius of $8.21a$ in the experiments, a channel half height of

$h = 8a$ is used in the simulations, resulting in a channel height $H_y = 16a$. The channel length is $L_z = 80a$ and the channel depth is $L_x = 30a$. This results in 1834, 2751, or 3667 particles when $\phi = 0.2$, 0.3, or 0.4, respectively.

5.2.2 Simulation results

In figures 5.14 (a-c), the volume fraction profiles after each oscillation are plotted along with the steady state volume fraction profiles from Snook et al. (2016). The volume fraction profiles from the experiments are substantially higher across the channel, except occasionally in the wall layer. This is due to limitations with the experimental image analysis used to detect the particle locations when calculating the volume fraction. Areas that appear darker in the images can be mislabeled as particles, resulting in a higher particle volume fraction (Snook et al., 2016). The largest differences between the FCM results and the experimental results occur in the mid-shear region, around $-0.5 \leq y/h \leq 0.1$. These differences could both be because of errors in the experimental image processing and because of the differences in the channel versus pipe geometry. The final volume fraction profiles for all volume fractions considered are shown in fig. 5.15.

Also shown in figures 5.14 (a-c) are the steady-state results of the suspension balance models by Morris and Boulay (1999) (Morris in legend) and Boyer et al. (2011) (Boyer in legend), using MATLAB code from Snook et al. (2016).

One interesting result from Snook et al. (2016) is the that the final volume fraction profiles clearly show the development of a wall layer near $y/h = -1$, which was not possible to visualize in some earlier experiments. This wall layering is visible in fig. 5.14, and is comparable between the FCM simulations and the experimental

(a) $\phi = 20\%$

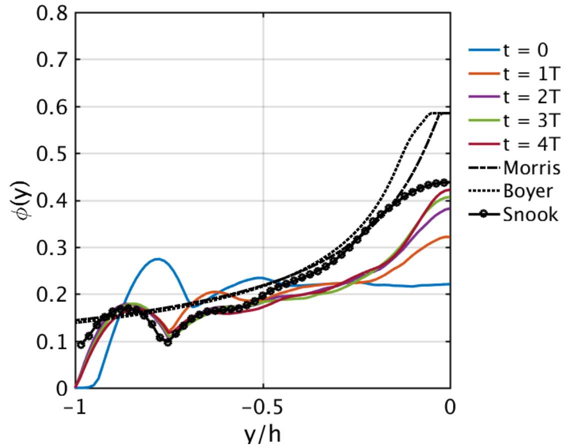

(b) $\phi = 30\%$

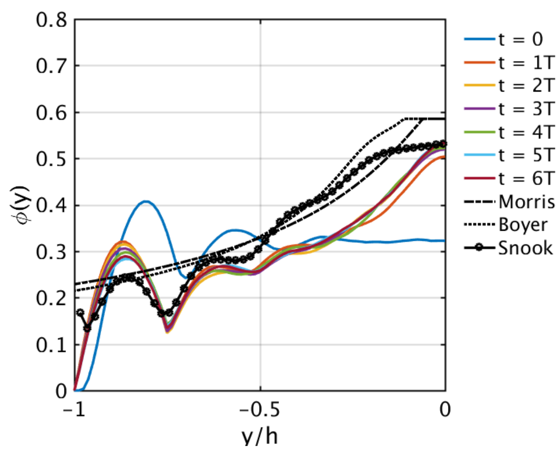

(c) $\phi = 40\%$

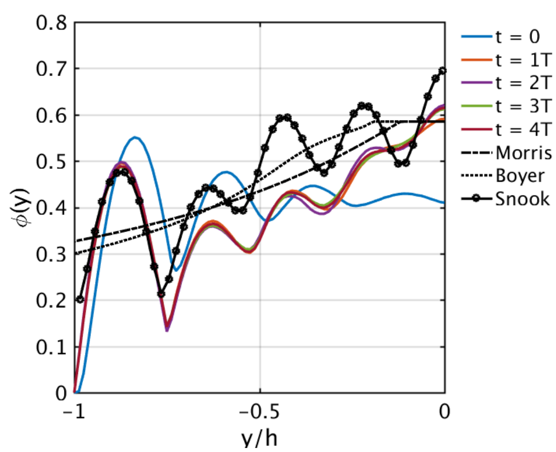

Figure 5.14: Volume fraction profiles for monodisperse oscillating flows of particles for $\phi = 0.2, 0.3$, and 0.4. Solid lines: FCM. Dashed, dotted lines: Suspension Balance Models. Circles: experimental results from Snook et al. (2016). h is the channel half height, $h = H_y/2$.

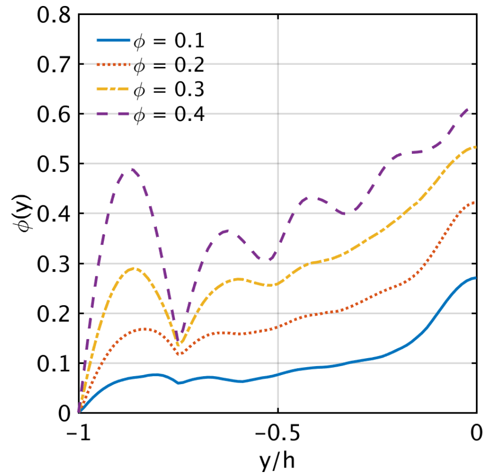

Figure 5.15: Final volume fraction profiles.

results. Although an exact comparison is not possible due to over-predictions in the experimental volume fraction profiles, there is qualitative agreement between the locations of the wall layers and volume fraction in the wall layer. When the volume fraction is high enough, as in $\phi = 0.4$, additional layers from across the channel on top of the wall layer.

ϕ	Experimental oscillation number
0.2	13 ± 4
0.3	5 ± 1
0.4	3 ± 1

Table 5.1: Number of oscillations to steady state from Snook et al. (2016).

The number of oscillations to steady state is given in table 5.1. Visually, the volume fraction profiles in fig. 5.14 show similar results for $\phi = 0.3$ and $\phi = 0.4$. After a large initial transient from the initial particle seeding, the volume fraction profiles evolve very slowly. At $\phi = 0.3$, the volume fraction in the wall layer does continue to drop after six oscillations, but the centerline volume fraction does not change significantly after the first two oscillations. When $\phi = 0.4$, the volume fraction profile is relatively constant after the first two oscillations.

(a) $\phi = 20\%$

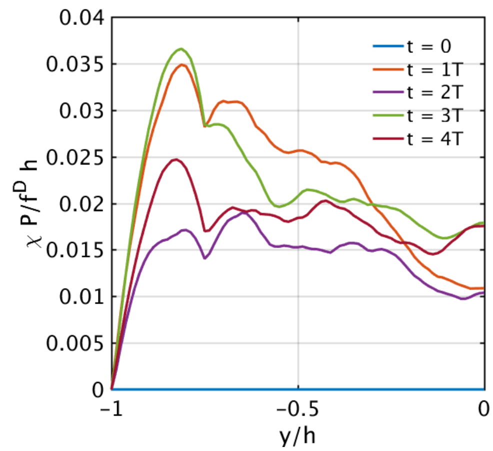

(b) $\phi = 30\%$

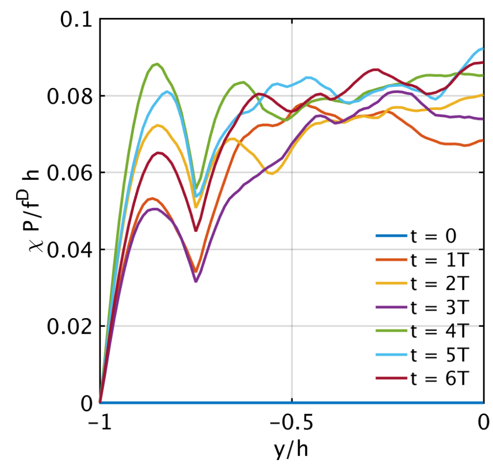

(c) $\phi = 40\%$

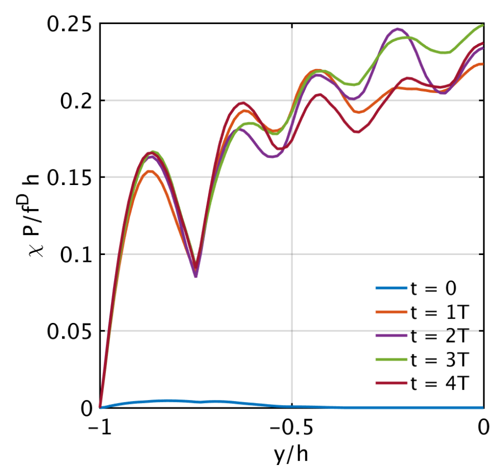

Figure 5.16: Particle contact pressure profiles for monodisperse oscillating flows of particles for $\phi = 0.2, 0.3$, and 0.4. Profiles are taken just before the end of each oscillation.

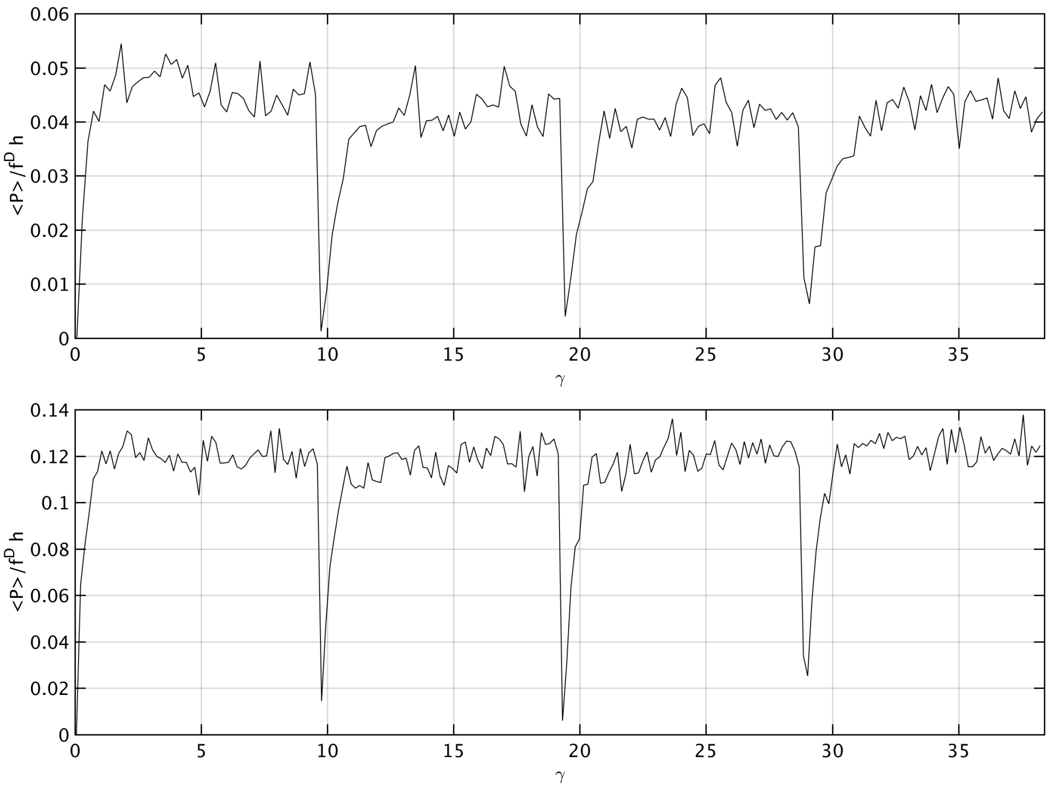

Figure 5.17: Average particle pressure $\langle P\rangle$ scaled by the wall shear stress σ_0 for $\phi = 0.3$ (top) and $\phi = 0.4$ (bottom). The average particle pressure drops instantaneously to zero each time the flow reverses. The contact pressure then rebuilds over $1-2$ strain units, reaching steady value for the remainder of the period.

Fig. 5.16 shows that while the volume fraction profiles may reach steady values, the particle contact pressure profiles continue to evolve. For example, when $\phi = 40\%$, the volume fraction does not change significantly after $t = 2T$, but the contact pressure decreases in the channel centerline from $2T$ to $4T$. While the particles are remaining in similar positions relative to the distance from the channel walls, they are rearranging within these layers to minimize the particle contact pressure.

The average particle pressure is shown in fig. 5.17 for volume fractions $\phi = 0.3$ and $\phi = 0.4$. As in the oscillating clouds in sec. 4.3.1, the contact pressure drops to zero almost instantaneous after each half oscillation because the contact pressure needs forcing from the imposed fluid flow on the particles in order to develop.

Without this, the particles relax, and the particle contacts are lost.

Pine et al. (2005) found that the critical strain amplitude for irreversibility in a homogeneous shear flow follows a power law fit

$$\gamma_c = 2C\phi^{-\alpha} \tag{5.2.2}$$

where the factor of 2 is added because Pine et al. (2005) defined the strain amplitude in terms of a quarter period instead of a half period in this work. The value of the parameters are given as $C = 0.14 \pm 0.03$ and $\alpha = -1.93 \pm 0.14$. For the cases considered here, this gives a critical strain amplitude of $\gamma_c = 2.85$ when $\phi = 0.3$ and $\gamma_c = 1.64$ when $\phi = 0.4$. Interestingly, this is approximately the accumulated strain needed for the contact pressure profile to rebuild after each half oscillation. Pham et al. (2016) showed that the critical strain amplitude does depend on the exact form of the particle contact force model for the particle surface roughness, giving a critical strain amplitude of:

$$\gamma_c = \frac{0.22}{\epsilon^{0.5}}\left(\frac{0.58}{\phi} - 1\right) \tag{5.2.3}$$

where ϵ the dimensionless gap width between two particles in contact, $h = 2\epsilon a$. Using this model with the minimum separation of two particles in contact in the simulation gives $\gamma_c = 4.377$ for $\phi = 0.3$ ($\epsilon = 0.0024$) and $\gamma_c = 2.11$ for $\phi = 0.4$ ($\epsilon = 0.0022$). The value for $\phi = 0.4$ again corresponds to the development time for the average particle pressure.

Chapter Six

Bidisperse suspensions

6.1 Introduction

The preceding chapters have discussed suspensions of monodispersed particles, that is, particles that have identical properties including equal sizes and weights. However, most experimental data relies on experiments with substantial variations in the particle sizes due to limitations in particle manufacturing. In some cases, this size variation can be up to 10%, as in Lyon and Leal (1998). In addition, many industrial and food products are represented by bidisperse or polydisperse suspensions, including popular beverages such as dairy milk (Kromkamp et al., 2006), soy milk (Bodenstab et al., 2003), and beer (Morris, 1987). Flow-induced segregation of particles by size has strong promises for microfiltration (van Dinther et al., 2013). Motivated by the goal of quantifying the rheological differences between polydisperse experiments and monodisperse simulations, in this chapter we consider the case where the particles have one of two sizes.

Two important quantities when considering bidispersed suspensions is the ratio of the particle radii and the fraction of small particles in the suspension. We denote the particle size ratio as $\lambda = \frac{a_s}{a_l}$, where a_s is the radius of a small particle and a_l the radius of a large particle. The total volume fraction of the suspension is denoted by ϕ_t, and the volume fractions of small and large particles are ϕ_s and ϕ_l, so that $\phi_t = \phi_s + \phi_l$. There are several notation conventions for the fraction of small particles. Here, we will use the notation $\beta = \frac{\phi_s}{\phi_t}$, the ratio of the volume fractions of the two species. The volume fraction of large particles is then $\phi_l = (1-\beta)\phi_t$. This notation means that when $\beta = 0$ or 1 the suspension is monodispersed. The subscript on ϕ_t may be dropped for simplicity.

Early experiments by Graham et al. (1991) used nuclear magnetic resonance

(NMR) images to find the volume fraction of particles in an annular Couette flow with particle size ratio $\lambda = 0.245$ and total volume fraction $\phi_t = 0.6$. They found that overall the particles migrate to the lower shear rate regions just as in shear-induced migration in monodisperse systems. While they could not directly distinguish between the small and large particles, the particle layering at the outer wall of the device suggests that layers consist only of large particles, and further suggests the particles may segregate by size (Graham et al., 1991). Subsequent studies found the first quantitative evidence for size segregation of particles by showing that when particles in a suspension migrate to areas of lower shear the large particles migrate faster (Husband et al., 1994). These findings were confirmed for a Poiseuille flow by Lyon and Leal (1998). At a size ratio of $\lambda = 0.29$ and total volume fraction of $\phi_t = 0.3 - 0.4$, Lyon and Leal (1998) found that the large particles enriched the center of the channel when the volume fraction of suspended large particles was equal to or greater than the volume fraction of small particles ($\phi_l \geq \phi_s$). The work by Lyon and Leal (1998) demonstrates that bidisperse suspensions in a Poiseuille flow undergo enrichment of large particles at the channel centerline, rather than segregation, with the difference being that the small particles do not migrate out of the center of the channel leaving only large particles. Instead, there is a higher volume fraction of large particles in the center of the channel than of small particles but the two species remain mixed. When measuring the particle velocity profiles, Lyon and Leal (1998) found that the velocity profiles are flattened more than monodisperse suspension flows, but there is no dependence on the relative volume fractions of small and large particles in the suspension.

Several more recent experiments and numerical simulations have considered suspensions of colloidal particles in Poiseuille flow and found similar large particle enrichment at the channel centerline. Semwogerere and Weeks (2008) showed through experiments that with a size ratio of $\lambda = 0.46$ and Péclet number $Pe = 47 - 480$ the primary factor for large particle enrichment is the shorter development length, or shorter time to steady state, for the larger particles. The large particles migrate to the center of the channel first, blocking the smaller particles as they try to migrate to the centerline. In order for this enrichment to occur, the volume fraction of large particles must be sufficiently high so that the large particles can fully block the small particle migration, giving the requirement that initially $\phi_s \leq \phi_l$ for enrichment. These results have been confirmed through multi-particle collision dynamics (MPCD) simulations by Kanehl and Stark (2015) with a size ratio of $\lambda = 0.5$, $Pe = 1 - 16$, and up to 1000 suspended particles.

Other experimental results have highlighted additional features of enrichment, segregation, and particle self-diffusion in bidisperse suspension flows. In experiments with varying channel geometries, Gao et al. (2009) showed that microchannels with special shapes, such as herringbone geometries, can enhance particle segregation. Work by Zarraga and Leighton (2001) considered the self-diffusivity of dilute bidisperse suspensions through two particle collisions in a shear flow, in a similar manner to work by Da Cunha and Hinch (1996). When a large and a small sphere with non-zero surface roughnesses come into contact, both spheres are displaced from their original trajectories, with the small sphere having a larger displacement.

Much work has been done to develop and extend monodisperse phenomenological models for the particle migration to bidisperse and polydisperse suspensions. Pesche et al. (1998) extended the diffusive flux model by Phillips et al. (1992) to bidisperse suspensions where $\lambda \ll 1$ by assuming that the large particles did not interact with the small particles. This was further extended by Kanehl and Stark (2015) for general bidisperse suspensions, removing the restriction on λ. Other approaches include using an effective temperature (mean square velocity fluctuations) to provide closure relations to the monodisperse suspension balance model (SBM) (Vollebregt et al., 2012, van der Sman and Vollebregt, 2012). These SBM results agree well with experimental results from Semwogerere and Weeks (2008). The SBM has also been extended to model bidisperse suspensions where the particles also have different weights to predict particle segregation in a pipe (Norman et al., 2005).

Few numerical results are available for non-Brownian bidisperse suspensions. The earliest simulations for modeling bidisperse suspensions were done in three-dimensions with Stokesian Dynamics for a monolayer of particles confined in the plane of shear (Chang and Powell, 1993, 1994,). These simulations found that bidisperse suspensions had lower effective shear viscosities than monodisperse suspensions because the presence of small particles reduces the average cluster size in the suspension (Chang and Powell, 1993). Further work with Stokesian Dynamics by Meunier and Bossis (2008) considered the self-diffusion of two-particle collisions, finding that the self-diffusion decreases as λ decreases. More recently, Spectral Ewald Accelerated Stokesian Dynamics has been used to investigate short-time dynamics of bidisperse colloidal particles in a steady shear flow (Wang et al., 2015, Wang and Brady, 2015, 2016). Pednekar et al. (2018) simulated frictional bidisperse and polydisperse suspensions in a three-dimensional periodic domain at high volume fraction for size ratios $\lambda = 0.25 - 0.5$ to quantify the relative viscosity and normal stress differences.

Work with the Force Coupling Method for bidisperse suspensions has been limited to low volume fractions, $\phi_t \leq 0.2$ (Abbas et al., 2006). To the best of our knowledge, no previous numerical studies exist for non-colloidal particles with different particle sizes at higher volume fractions for flows confined to a channel. In this chapter, we will discuss how to extend FCM to bidisperse suspensions with higher volume fractions and show results for bidisperse Couette and Poiseuille flows.

6.2 Numerical method

6.2.1 Lubrication forces

In FCM the lubrication forces are computed exactly using the analytical forms of forces between two particles. To calculate the total lubrication force on a particle the force due to each of its neighbors is computed, then added in a pairwise manner to the grand resistance matrix, see section 2.1. This method has also been used in Stokesian Dynamics (Sierou and Brady, 2002) and lattice-Boltzmann simulations (Nguyen and Ladd, 2002).

To calculate the lubrication resistance matrix we begin by considering the lubrication resistance formulae for two particles isolated in an infinite domain, with radii a_1 and a_2, size ratio $\lambda = \frac{a_2}{a_1}$, separation $s = 2r/(a_1 + a_2)$, and nondimensional gap width $\xi = s - 2 = (r - a_1 - a_2)/(\frac{1}{2}(a_1 + a_2))$.

The resistance matrix for lubrication forces relates the lubrication forces, torques, and stresses with the particle translational and angular velocities, and is given by Kim and Karilla (1991):

$$\begin{bmatrix} F_1 \\ F_2 \\ T_1 \\ T_2 \\ S_1 \\ S_2 \end{bmatrix} = \mu \begin{bmatrix} A_{11} & A_{12} & \tilde{B}_{11} & \tilde{B}_{12} & \tilde{G}_{11} & \tilde{G}_{12} \\ A_{21} & A_{22} & \tilde{B}_{21} & \tilde{B}_{22} & \tilde{G}_{21} & \tilde{G}_{22} \\ B_{11} & B_{12} & C_{11} & C_{12} & \tilde{H}_{11} & \tilde{H}_{12} \\ B_{21} & B_{22} & C_{21} & C_{22} & \tilde{H}_{21} & \tilde{H}_{22} \\ G_{11} & G_{12} & H_{11} & H_{12} & M_{11} & M_{12} \\ G_{21} & G_{22} & H_{21} & H_{22} & M_{21} & M_{22} \end{bmatrix} \begin{bmatrix} U_1 - U^\infty(x_1) \\ U_2 - U^\infty(x_2) \\ \Omega_1 - \Omega^\infty(x_1) \\ \Omega_1 - \Omega^\infty(x_1) \\ E^\infty \\ E^\infty \end{bmatrix} \tag{6.2.1}$$

Each element of the submatrices A_{ij}, B_{ij}, C_{ij}, G_{ij}, H_{ij}, and M_{ij} is found through the composition of the resistance functions, denoted X^A, Y^A, Y^B, X^C, Y^C, X^G, Y^G, Y^H, X^M, and Y^M. Following the work of Jeffrey and Onishi (1984), Jeffrey (1992), we non-dimensionalize the resistance matrices by the sum of the particle radii:

$$\hat{A}_{ij} = \frac{A_{ij}}{3\pi(a_1+a_2)},\ \hat{B}_{ij} = \frac{B_{ij}}{\pi(a_1+a_2)^2},\ \hat{C}_{ij} = \frac{C_{ij}}{\pi(a_1+a_2)^3},$$

$$\hat{G}_{ij} = \frac{G_{ij}}{\pi(a_1+a_2)^2},\ \hat{H}_{ij} = \frac{H_{ij}}{\pi(a_1+a_2)^3},\ \hat{M}_{ij} = \frac{5M_{ij}}{6\pi(a_1+a_2)^3}.$$

While other choices for non-dimensionalization exist, the choice above leads to symmetry between the components of the resistance functions. This symmetry greatly reduces the number of independent components which need to be computed, as:

$$\begin{aligned}
X^A_{ij}(s,\lambda) &= X^A_{(3-i)(3-j)}(s,\lambda^{-1}) = X^A_{ji}(s,\lambda)\\
Y^A_{ij}(s,\lambda) &= Y^A_{(3-i)(3-j)}(s,\lambda^{-1}) = Y^A_{ji}(s,\lambda)\\
Y^B_{ij}(s,\lambda) &= -Y^B_{(3-i)(3-j)}(s,\lambda^{-1})\\
X^C_{ij}(s,\lambda) &= X^C_{(3-i)(3-j)}(s,\lambda^{-1}) = X^C_{ji}(s,\lambda)\\
Y^C_{ij}(s,\lambda) &= Y^C_{(3-i)(3-j)}(s,\lambda^{-1}) = Y^C_{ji}(s,\lambda)\\
X^G_{ij}(s,\lambda) &= -X^G_{(3-i)(3-j)}(s,\lambda^{-1})\\
Y^G_{ij}(s,\lambda) &= -Y^G_{(3-i)(3-j)}(s,\lambda^{-1})\\
Y^H_{ij}(s,\lambda) &= Y^H_{(3-i)(3-j)}(s,\lambda^{-1})\\
X^M_{ij}(s,\lambda) &= X^M_{(3-i)(3-j)}(s,\lambda^{-1}) = X^M_{ji}(s,\lambda)\\
Y^M_{ij}(s,\lambda) &= Y^M_{(3-i)(3-j)}(s,\lambda^{-1}) = Y^M_{ji}(s,\lambda)
\end{aligned}$$

From here forward we will drop the hat notation when referring to the non-dimensionalized resistance functions.

The entries of the resistance matrix in eq. 6.2.1 are given by Kim and Karilla (1991):

$$
\begin{aligned}
A_{ij}^{\alpha\beta} &= X_{\alpha\beta}^{A} d_i d_j + Y_{\alpha\beta}^{A}(\delta_{ij} - d_i d_j) && (6.2.2)\\
B_{ij}^{\alpha\beta} &= \tilde{B}_{ij}^{\alpha\beta} = Y_{\alpha\beta}^{B}\epsilon_{ijk} d_k && (6.2.3)\\
C_{ij}^{\alpha\beta} &= X_{\alpha\beta}^{C} d_i d_j + Y_{\alpha\beta}^{C}(\delta_{ij} - d_i d_j) && (6.2.4)\\
G_{ij}^{\alpha\beta} &= X_{\alpha\beta}^{G}(d_i d_j - \frac{1}{3}\delta_{ij}) d_k + Y_{\alpha\beta}^{G}(d_i \delta_{jk} - d_i \delta_{ijk} - 2 d_i d_j d_k) && (6.2.5)\\
H_{ij}^{\alpha\beta} &= Y_{\alpha\beta}^{H}(d_i \epsilon_{jkm} d_m + d_j \epsilon_{ikm} d_m) && (6.2.6)
\end{aligned}
$$

In the FCM algorithm, we consider the FCM resistance matrix with the lubrication resistance matrix correction:

$$
\begin{bmatrix} F_1 \\ F_2 \\ T_1 \\ T_2 \end{bmatrix} = \Big((M^{FCM})^{-1}(\lambda) + \mathcal{L}(\lambda) \Big) \begin{bmatrix} U_1 - U^{\infty}(x_1) \\ U_2 - U^{\infty}(x_2) \\ \Omega_1 - \Omega^{\infty}(x_1) \\ \Omega_1 - \Omega^{\infty}(x_1) \end{bmatrix}
$$

Here, M^{FCM} is the FCM mobility matrix, which is inverted to get the FCM resistance matrix. The lubrication correction matrix is denoted $\mathcal{L}(\lambda)$ and consists of the difference between the analytical resistance functions and the FCM resistance functions,

$$
\mathcal{L}(\lambda) = \mathcal{R}^{L} = \mathcal{R}_{2B}(\lambda) - \mathcal{R}_{2B}^{FCM}(\lambda),
$$

where $\mathcal{R}_{2B}(\lambda)$ is the exact two-body resistance matrix. The FCM resistance matrix $\mathcal{R}_{2B}^{FCM}(\lambda)$ is found by constructing the two-body FCM mobility matrix for two particles with size ratio λ with varying separation distances, then inverting the matrix. The polynomial fit tool in MATLAB is used to construct a fifth degree polynomial fit for each of the resistance functions. Lubrication forces stem from relative motion of two particles, so we use the relative velocity formula of the resistance matrices (Nguyen and Ladd, 2002, Cichocki et al., 1999).

The exact two-body resistance matrices, $\mathcal{R}_{2B}$ are taken from Jeffrey and Onishi (1984) for the coefficients for A, B, and C, and Jeffrey (1992) for G, H, M, and are also available in Kim and Karilla (1991). The analytical forms of the resistance functions each have a near-field and far-field form, where the appropriate form depends on the particle separations. For widely separated particles, $\mathcal{R}_{2B}$ uses the twin multiple expansions. For small separations, $\mathcal{R}_{2B}$ uses asymptotic expansions in terms of ϵ. The resistance functions from Jeffrey and Onishi (1984), Jeffrey (1992) do contain some typographical mistakes. A number of corrections are available, including an errata online posted by Ichiki (2008). Corrections to the first five resistance functions are available in papers by Dance and Maxey (2003) and Yeo and Maxey (2010) for equal size particles. Rosa et al. (2011) contains a list of the first five resistance functions for particles with unequal sizes. A complete listing of all the near-field resistance functions is available in Townsend (2018). For completeness, a list of the near-field and far-field forms of the resistance functions, along with the order one corrections, for a range of λ are available in Appendix A, and corresponding MATLAB code to generate all the resistance function coefficients is available through the Brown Digital Repository (Howard, 2018).

The two-body FCM, far-field, and near-field forms of the resistance function X_{11}^{A} are shown in fig. 6.1 for $\lambda = 1$ and $\lambda = 0.5$. It is necessary to choose a cutoff distance for the resistance functions, which represents the separation at which two particles in the simulation are considered to no longer be coupled by lubrication forces. In practice, the cutoff distance is chosen at the point that $\mathcal{R}_{2B}^{FCM}(\lambda) \approx \mathcal{R}_{2B}(\lambda)$ so the difference between the two terms goes to zero. In the example shown in fig. 6.1, the FCM and exact resistance functions for widely separated spheres are

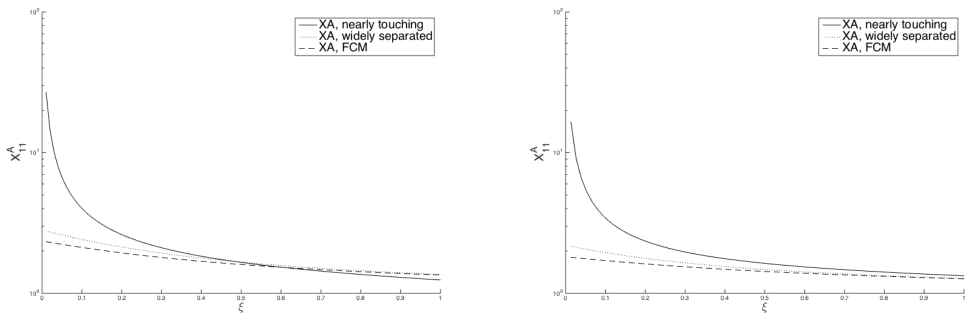

Figure 6.1: Exact resistance functions for nearly touching and widely separated spheres and FCM resistance function in terms of non-dimensional gap width ξ. (Left) $\lambda = 1$ (right) $\lambda = 0.5$.

indistinguishable for $\xi > 0.8$, so the cutoff for the lubrication forces is chosen to be $\xi = 0.8$.

Bidisperse suspensions add additional complications in calculating the lubrication cut-off distance. If the cut-off distance is too large, greater than 2λ, it is possible for a small particle to be in the gap between two large particles that are considered lubrication neighbors. The resistance functions assume only empty fluid between to lubrication neighbors, so in this case the analytical functions will be no longer valid. To avoid this, the lubrication cut-off distance must be less than the diameter of the smallest particle in the simulation. For very small values of λ, this can mean that $\mathcal{R}_{2B}^{FCM}(\lambda) \neq \mathcal{R}_{2B}(\lambda)$ at the cut-off distance, so the lubrication force term will have a jump discontinuity. This is a case that we are still investigating, but have had success in using a smoothing term to avoid the discontinuity:

$$\mathcal{R}\xi = \begin{cases} \mathcal{R}_{2B}(\xi) - \mathcal{R}_{2B}^{FCM}(\xi) & |\xi| \leq 0.9\xi_c \\ ((1 - f(\xi))\mathcal{R}_{2B}(\xi) + f(\xi)\mathcal{R}_{2B}^{FCM}(\xi)) - \mathcal{R}_{2B}^{FCM}(\xi) & |\xi| > 0.9\xi_c \end{cases} \tag{6.2.7}$$

Here, ξ_c is the lubrication cut-off distance and $f(\xi)$ is a smooth function that varies from 0 at $\xi = 0.9\xi_c$ to 1 at $\xi = \xi_c$. This transitions the difference in the resistance functions to zero over 10% of the lubrication range preventing sudden jumps in the lubrication force. For size ratios of $\lambda \geq 0.5$, this correction is not necessary as we can take the cutoff to be $\xi_c = 0.8 < 2a_s$, but can arise for smaller values of λ.

The above procedure for constructing the resistance matrix is only exact for two isolated particles in pure fluid in an infinite domain. In dense suspensions, almost all particles will have more than one neighboring particle within the lubrication cut-off distance. In this cases, the individual two-body resistance matrices are added in a pairwise manner to generate the net lubrication resistance matrix (Yeo and Maxey, 2010).

Once the lubrication forces and torques torques are found, the particle velocities and angular velocities can be found by solving

$$V = \mathcal{R}^{-1} F^{lub},$$

where $V = [U_i,\ \Omega_i]^T$ is a $6N_p$ vector containing the particle angular and translational velocities and $F^{lub} = [F_i,\ T_i]^T$ is a $6N_p$ vector containing the particle forces and torques. To do so, it is necessary to invert the resistance matrix $\mathcal{R}$. This can be done efficiently with a preconditioned conjugate gradient method, using $P = diag(\mathcal{R})$ as a preconditioner. The preconditioner improves the time to convergence, as seen in Fig. 6.2.

To solve the flow problem, we need to determine the stresslet coefficients, S, given the particle forces, F, and torques, T. This means solving

$$-\tilde{E}^{\infty} - M_{FE}F - M_{TE}T = M_{SE}S,$$

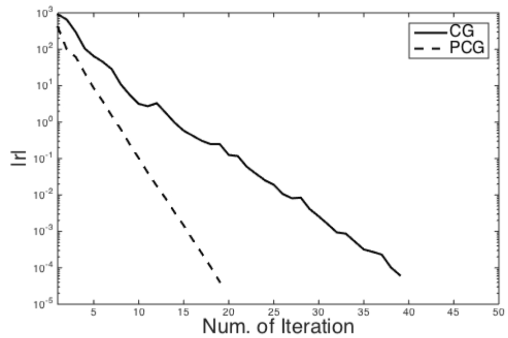

Figure 6.2: Residual history for CG and PCG solvers for a bidisperse suspension with $\lambda = 0.5$, $\phi_t = 0.3$.

which requires inverting the M_{SE} mobility matrix. In a dilute suspension,

$$S_{ij}^n = \frac{20}{3}\pi\mu a_n^3 E_{ij}^n$$

where a_n is the radius of particle n. Thus, the condition number of M_{SE} will increase approximately as $\kappa(M_{SE}) \approx (a_l/a_s)^3$. We then choose Jacobi preconditioner with diagonal matrices $3/20\pi\mu a_n^3$ and use a preconditioned conjugate gradient method to invert the mobility matrix M_{SE}.

6.2.2 Contact forces

A short range repulsion force between the particles acts to prevent particle overlap and physically represents the roughness of the particles, as discussed in sec. 2.2. As in previous studies, the contact force between particles α and β, with centers $\mathbf{r}^\alpha$ and $\mathbf{r}^\beta$, acts along the line of centers of the particles and is given by

$$\mathbf{F}_P^{\alpha\beta} = \begin{cases} -6\pi\bar{a}^2\dot{\gamma}F_{ref}\left(\dfrac{R_{ref}^2 - |\mathbf{r}|^2}{R_{ref}^2 - 4\langle a\rangle^2}\right)^6 \dfrac{\mathbf{r}}{|\mathbf{r}|} & \text{if} \quad |\mathbf{r}| < R_{ref}, \\ 0 \quad \text{otherwise} & \end{cases} \tag{6.2.8}$$

in which $\mathbf{r} = \mathbf{r}^\beta - \mathbf{r}^\alpha$, R_{ref} is the cut-off distance and $\bar{a}$ is the reduced radius,

$$\bar{a} = \frac{a_\alpha + a_\beta}{2}. \tag{6.2.9}$$

F_{ref} is a constant chosen so that the minimum gap between the particles is $0.005a$ when $R_{ref} = 2.01a$ (Yeo and Maxey, 2010).

6.2.3 Validation tests

Exact results for the relative velocities for two particles in a shear flow can be obtained from Batchelor and Green (1972) in terms of three non-dimensional functions and the particle separation distance r,

$$\mathbf{V}(r) = -\dot{\gamma}\begin{cases} r_2(B/2 - r_1^2/r^2(A-B)) \\ r_1(B/2 - r_2^2/r^2(A-B)) \\ r_1 r_2 r_3/r^2(A-B) \end{cases} \tag{6.2.10}$$

Here, $\mathbf{r} = (r_1, r_2, r_3)$ is the separation between the particles in the stream-wise, velocity gradient, and vorticity directions, respectively. The values of A, B, and C are given by Batchelor and Green for the far-field case of widely separated spheres for all size ratios λ, and in the near-field case for $\lambda = 1$. The near-field values of A and B for $\lambda = 0.5$ can be found in Pesche (1998). The results of the FCM simulations and the near- and far-field values are shown in figure 6.3 for $\lambda = 1.0$ and $\lambda = 0.5$, where $\xi = r/a_l$. Good agreement is shown between the values, even when the particles are very close together.

The trajectories of two particles in a Couette flow with size ratio $\lambda = 0.5$ are

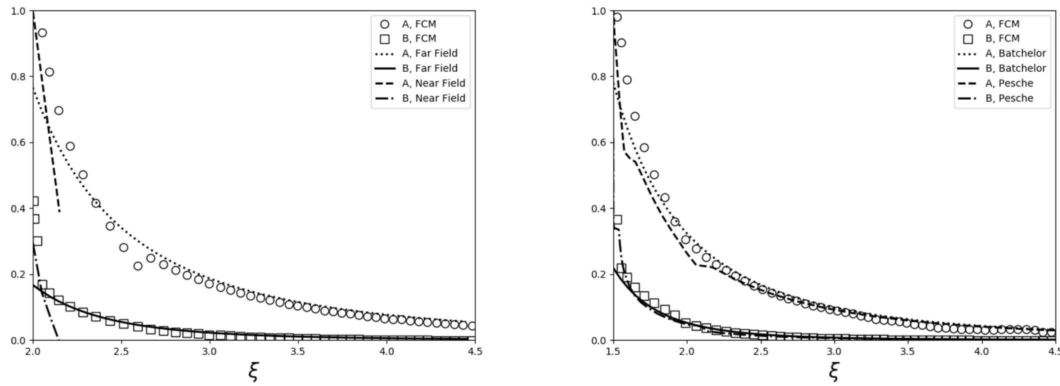

Figure 6.3: Values of A and B for two particles in a shear flow. Left: $\lambda = 1.0$. Right: $\lambda = 0.5$

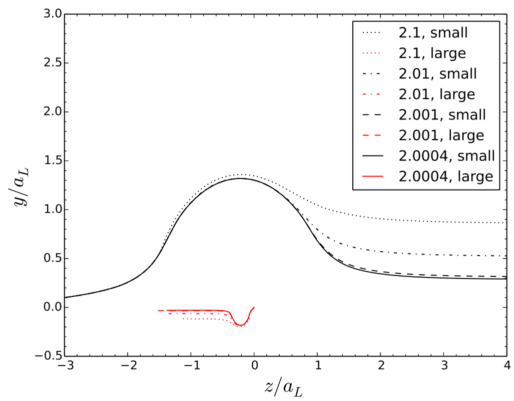

Figure 6.4: Trajectories of two particles with $\lambda = 0.5$ in a shear flow, $\dot{\gamma} = 1$ for varying values of R_{ref}. As R_{ref} is increased the particles are further displaced across streamlines.

shown in figure 6.4. The trajectories depend on the contact force cutoff parameter R_{ref}, which determines the minimum separation between the spheres, as in the case of two monodisperse spheres. These results are consistent with Zarraga and Leighton (2001). As noted by Zarraga and Leighton (2001), the small sphere undergoes much larger displacement than the large sphere, on the order of one particle radius for $R_{ref} = 2.01$. The corresponding values for ϵ_{min} are shown in table 6.1.

R_{ref}	ϵ_{min}/a_l
2.1	0.0488
2.01	0.00462
2.001	0.000358
2.0004	0.0001158

Table 6.1: Values of R_{ref} and corresponding minimum distance between particles

6.2.4 Simulation parameters

The bidisperse simulations are completed in a planar channel with channel width $H_y = 40$ and vorticity dimension $L_x = 30$. The large particle size is kept fixed at $a_l = 1$ and the small particle size is varied. The large particle radius a_l is used as a scaling parameter. The channel length in the streamwise direction L_z is adjusted depending on the particle size ratio to control the total number of particle is in the simulation, which is of the order of 10^4. A simulation with monodisperse particles is also run to provide a comparison.

	λ	L_z	ϕ_t	β	$\langle a \rangle$	N_p	f_s
L60_1	0.6	30	0.4	0.25	0.757	6558	0.607
L60_2	0.6	30	0.4	0.50	0.671	9677	0.822
L60_3	0.6	30	0.4	0.75	0.627	12797	0.933
L72_1	0.72	40	0.4	0.25	0.868	6509	0.472
L72_2	0.72	40	0.4	0.50	0.796	8433	0.728
L72_3	0.72	40	0.4	0.75	0.751	10357	0.889
L80_1	0.8	60	0.4	0.25	0.921	8515	0.394
L80_2	0.8	60	0.4	0.50	0.868	10216	0.657
L80_3	0.8	60	0.4	0.75	0.829	11791	0.854
Monodisperse	–	60	0.4	–	1.0	6878	–

Table 6.2: List of bidisperse simulation parameters. The last column is the fraction of small particles, $f_s = N_s/N_p$, where N_s is the number of small particles and N_p is the total number of particles, provided as a comparison to other works. $\langle a \rangle$ is the average particle radius, $\langle a \rangle = \frac{N_s a_s + N_l a_l}{N_s + N_l}$, and $\beta = \phi_s/\phi_t$ is the ratio of the small particle volume fraction to the total volume fraction.

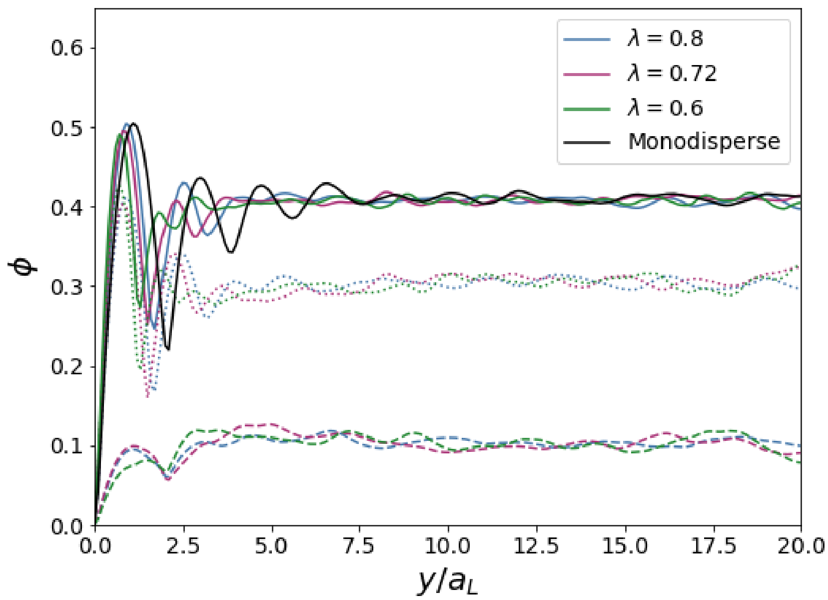

Figure 6.5: Total volume fraction profile (solid lines), large particle volume fraction profile (dashed lines), and small particle volume fraction profile (dotted lines) for $\lambda = 0.8, 0.72$, and 0.6 with $\beta = 0.75$, compared to a monodisperse simulations.

6.3 Couette flows

For each of the Couette flows, each simulation is run for 20 strain units, then results are averaged over the subsequent 5 strain units.

The total volume fraction profile and the volume fraction profiles of the small and large particles are shown in figs. 6.5 and 6.6. In both cases there are some variations at the channel walls due to the differences in the particle sizes, with the first peak appearing at $y/a_l = a_s$. The volume fraction profiles in the center of the channel do not change significantly due to the bidispersity of the simulations. The velocity profile is shown in fig. 6.7, in comparison to a linear fit. Again, there is little difference between the different values for λ. There is some variation at the channel wall, representing the layer that forms at the wall.

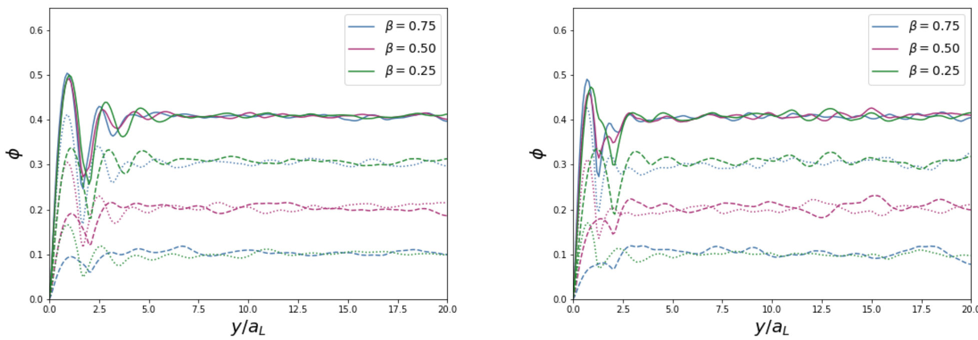

Figure 6.6: Total volume fraction profile (solid lines), large particle volume fraction profile (dashed lines), and small particle volume fraction profile (dotted lines) for $\lambda = 0.8$ (left) and $\lambda = 0.6$ (right).

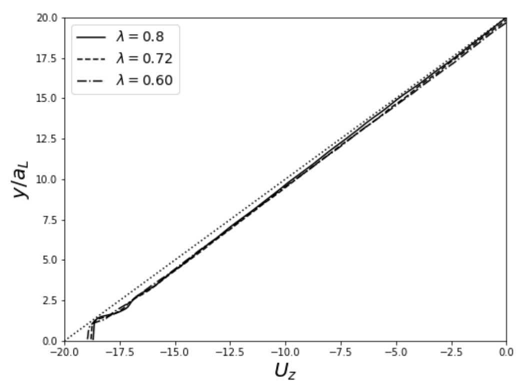

Figure 6.7: Particle velocity profiles U for $\lambda = 0.8$ (solid), $\lambda = 0.72$ (dashed), and $\lambda = 0.6$ (dash-dotted), $\beta = 0.75$. The dotted line is a linear profile. There is no significant difference between the velocity profiles.

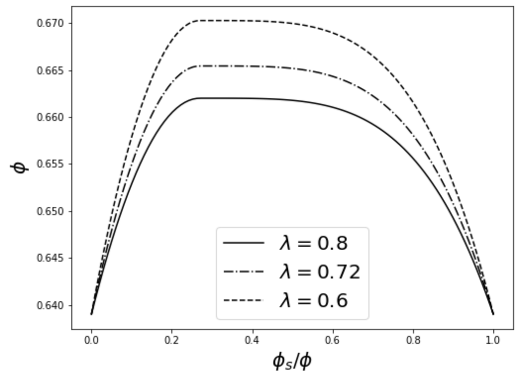

Figure 6.8: Maximum volume fraction $\phi_{bi,max}$ from Qi and Tanner (2011)

6.3.1 Maximum volume fraction and relative viscosity

One important question is how particle bidispersity changes rheological properties such as the maximum volume fraction and suspension viscosity. Bidisperse and polydisperse particles can form more optimal packings, with smaller particles filling in the gaps between large particles. Several attempts have been make to theoretically predict the maximum volume fraction (Ouchiyama and Tanaka, 1984, Sudduth, 1993, Gondret and Petit, 1997, Mwasame et al., 2016, Shapiro and Probstein, 1991, Probstein et al., 1994). An overview of these approaches is available in Pednekar et al. (2018). Here, we use the work of Qi and Tanner (2011), which provides a good fit to experiments by Chong et al. (1971), and gives

$$\phi_{bi,max} = \phi_{max} + \zeta_k \zeta_\lambda \phi_{max}(1 - \phi_{max}), \tag{6.3.1}$$

where ϕ_{max} is the random close packing volume fraction for a monodispersed suspension. This formula reduces to $\phi_{bi,max} = \phi_{max}$ in the case that $\phi_s/\phi_t = 0$ or 1, i.e., in the case that the suspension is monodispersed. Qi and Tanner (2011) take $\phi_{max} = 0.639$ for monodisperse suspensions.

Fitting to experimental data, $\zeta_\lambda = 1 - e^{-\frac{(1/\lambda - 1)^{1/3}}{6}}$ and $\zeta_k = 1 - \frac{1}{0.0729}\left(\frac{\phi_s}{\phi_t} - 0.27\right)^2$ when $\frac{\phi_s}{\phi_t} < 0.27$ and $\xi_k = 1 - \frac{1}{0.284}\left(\frac{\phi_s}{\phi_t} - 0.27\right)^2$ when $\frac{\phi_s}{\phi_t} > 0.27$.

The maximum volume fraction from eq. 6.3.1 is shown in fig. 6.8 for $\lambda = 0.6, 0.72$, and 0.8. The change in the maximum volume fraction is quite small for the cases considered here, with an increase of at most 3%. While that is not insignificant, it is equivalent to the typical variation in the maximum packing volume fraction from different references. In light of such a small change, Kanehl and Stark (2015) kept ϕ_{max} fixed at 0.64 for all bidispersed suspensions they considered, which they note is sufficient for their simulations. The model from Qi and Tanner (2011) has been fitted to experimental data from Chong et al. (1971), but they are considering much smaller values of $\lambda \ll 0.2$, where larger variations occur in $\phi_{bi,max}$.

Using this the maximum volume fraction formula in eq. 6.3.1 allows for calculation of the relative viscosity of the bidispersed suspension Qi and Tanner (2011):

$$\eta_r = \left[\left(1 - \frac{\phi_l}{1 - c_l\phi_l}\right)\left(1 - \frac{\phi_s}{1 - c_s\phi_s}\right)\right]^{-5/2} \tag{6.3.2}$$

where $c_s = \frac{1 - \phi_{bi,max} + \phi_{max}}{\phi_{bi,max} - \phi_l}$ and $c_l = \frac{1 - \phi_{max}}{\phi_{max}}$.

The relative viscosity of the suspension from the FCM simulations in a Couette flow can be found by

$$\mu_r = 1 + \frac{1}{\mu\dot{\gamma}}\langle\sigma_{23}^P\rangle, \tag{6.3.3}$$

where $\langle\sigma_{23}^P\rangle$ is the particle phase average of the shear stress. The relative viscosity from the FCM data is shown in comparison to the fits from eq. 6.3.2 in fig. 6.9. Because the maximum volume fraction does not change significantly and the particle packing is similar to that of a monodisperse suspension at maximum volume fraction,

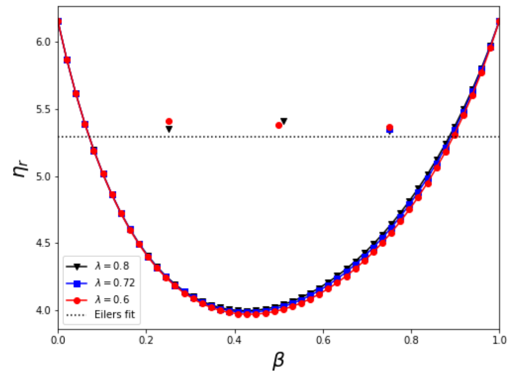

Figure 6.9: Relative viscosity data for bidisperese Couette flow (symbols) and fits from Qi and Tanner (2011) (lines) and (Stickel and Powell, 2005) (dotted line).

we have also compared to the Eilers' fit (Stickel and Powell, 2005),

$$\mu_r = \left(1 + \frac{\frac{1}{2}[\eta]\phi_t}{1 - \phi_t/\phi_{max}}\right)^2. \tag{6.3.4}$$

$[\eta] = 2.5$ is a fitting parameter. Stickel and Powell (2005) showed that experimental data can be well represented by the Eilers' fit with $\phi_{max} = 0.65$.

6.3.2 Normal stress differences

The normal stress differences are given by

$$\langle N_1 \rangle = \langle \sigma_{33}^P \rangle - \langle \sigma_{22}^P \rangle \tag{6.3.5}$$

$$\langle N_2 \rangle = \langle \sigma_{22}^P \rangle - \langle \sigma_{11}^P \rangle \tag{6.3.6}$$

The particle averaged normal stress differences scaled by the wall shear stress, $\tau = \mu_r \mu \dot{\gamma}$,are shown in fig. 6.10. As in simulations for monodisperse suspensions, we find that N_2 and N_1 are negative (Sierou and Brady, 2002, Yeo and Maxey, 2010). Experiments with bidisperse suspensions have again shown that both N_2 and N_1

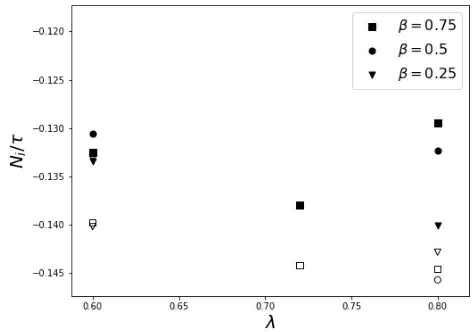

Figure 6.10: Average normal stress differences for bidisperse suspensions at a range of particle size ratios and small particle volume fractions. Filled symbols: N_1. Empty symbols: N_2.

are negative, and similar in magnitude (Gamonpilas et al., 2016, 2018). Zarraga et al. (2000) showed that for monodisperse spheres in a shear flow $|N_2| > |N_1|$, and $|N_2| \approx 3.6|N_1|$, while Stokesian Dynamics simulations by Sierou and Brady (2002) found that $|N_2| \approx |N_1|$. Here we find that the two normal stress differences are approximately equal in magnitude, with $|N_1| < |N_2|$, but the difference is quite small. Fig. 6.11 contains profiles of the normal stress differences across the channel. Both N_1 and N_2 are negative and approximately uniform away from the wall layer. The behavior near the wall layer varies, with N_1 becoming positive immediately adjacent to the wall. N_2 becomes more negative in the wall layer.

An understanding of this behavior of the normal stress differences can be found from looking at the particle stress profiles at the channel wall in fig. 6.12, which shows that σ_{33} becomes less negative at the channel wall, while σ_{22} becomes more negative, resulting in a positive value for N_1. The value of σ_{11} becomes slightly less negative at the channel wall, so N_2 becomes more negative. Fig. 6.12 also shows the relative contributions to the stress profiles from the small and large particles. The

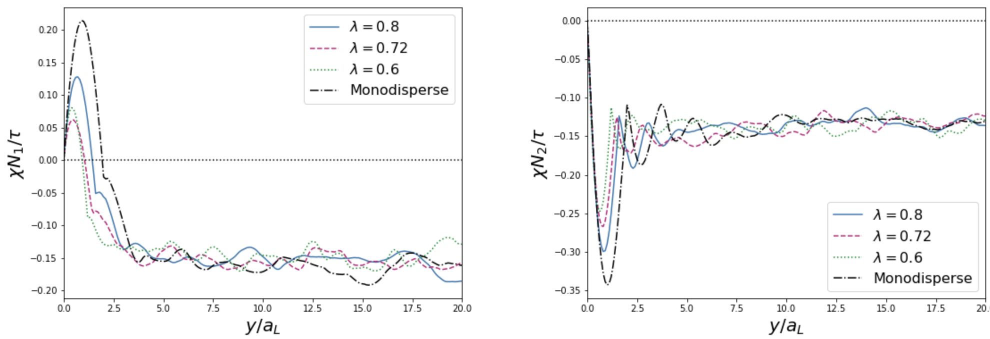

Figure 6.11: Normal stress difference profiles N_1 (left) and N_2 (right) for varying λ. Both N_1 and N_2 are negative on average across the channel, however N_1 is positive in the wall layer.

stresses are divided relative to the volume fraction of each species, with

$$\frac{\langle \sigma_{ij}^S \rangle}{\langle \sigma_{ij}^L \rangle} \approx \frac{\phi_s}{\phi_l}.$$

This is demonstrated in fig. 6.13, where the relative volume fractions of the small and large particles are compared to the average contributions to the total stress from the small and large particles. The data fits very well to a linear fit.

Finally, we can consider the contact pressure profile for bidisperse Couette flows in fig. 6.14. These profiles are unsurprising in that they are constant across the channel, with an exception near the wall. There are no significat gradients in the contact pressure.

In all the quantities considered in this section, including the maximum volume fraction, the relative viscosity, the stresses, and the volume fraction, the bidisperse suspensions behavior in a very similar manner as a monodisperse suspension. This is partly because there is not a significant variation in the maximum volume fraction at the particle size ratios considered. In addition, segregation of bidisperse suspension flows has been shown to occur when there is a gradient in the shear rate, as the

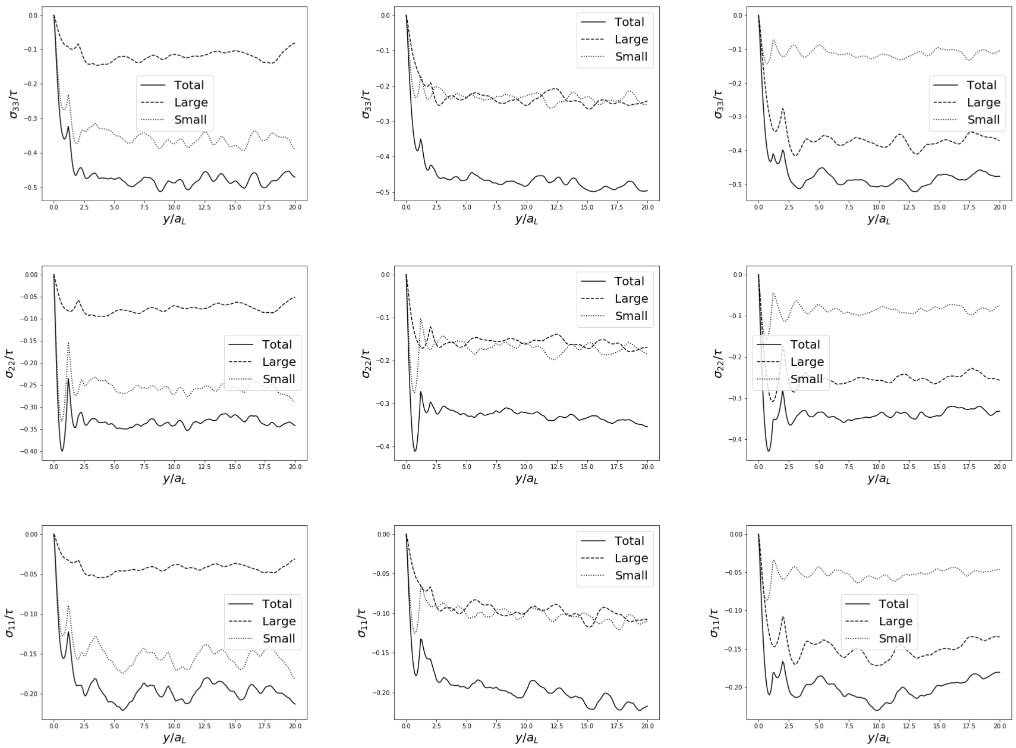

Figure 6.12: Stress profiles σ_{33} (top row), σ_{22} (middle row), σ_{11} (bottom row) for $\lambda = 0.6$ for $\beta = 0.25$ (left column), $\beta = 0.5$ (middle column), and $\beta = 0.75$ (right column). The stress for each size particle is distributed by the relative volume fraction of each species.

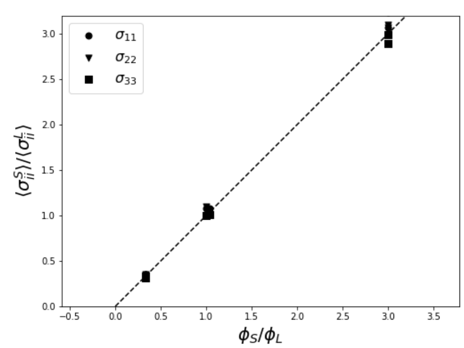

Figure 6.13: Ratio of particle stresses for small and large particles compared to a linear fit (dashed line). The relative contribution to the total stress from the small and large particles is directly proportional to the relative volume fractions of the small and large particles.

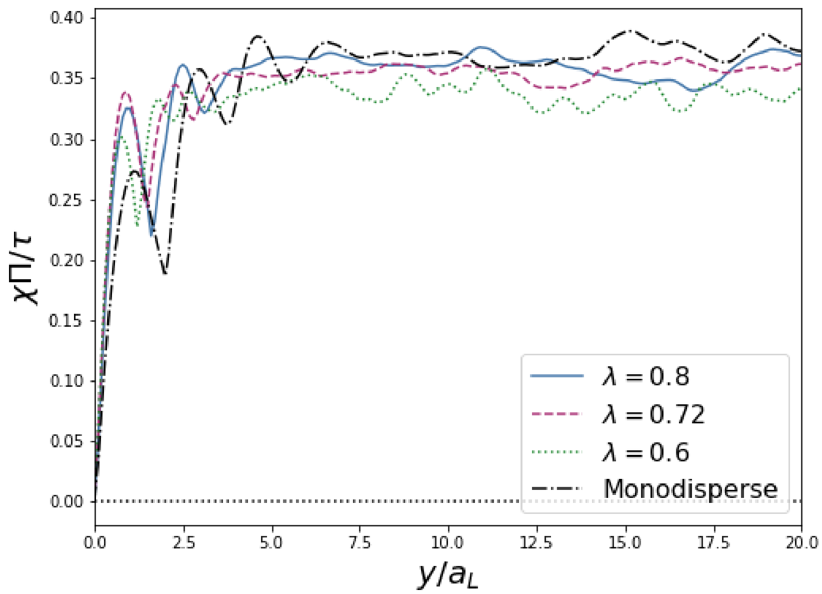

Figure 6.14: Particle contact pressure. The pressure is constant across the channel.

induced particle velocity then depends on the particle size. In the case of a Couette flow, there is no particle migration flux, and thus no mechanism for size-induced segregation.

6.4 Bidisperse Poiseuille flows

Previous experiments with bidisperse particle sizes in a Poiseuille flow have been completed by Lyon and Leal (1998) and Semwogerere and Weeks (2008). We will first consider the work of Semwogerere and Weeks (2008), which considered particles with small Péclet numbers in the range $Pe = 47 - 480$ where the effects of Brownian motion are significant, in contrast to the current simulations where the particles are non-Brownian with $Pe \gg 1$. Nevertheless, comparisons can be made to the experiments.

To compare as closely as possible with Semwogerere and Weeks (2008), which used values of $\lambda = 0.47$ and $H_y = 33.3a_l$, FCM simulations were completed with $\lambda = 0.5$ and channel height $H_y = 32a_l$, with $L_x = 20a_l$ and $L_z = 30a_l$, shown in figure 6.15. In fig. 6.15a, the total volume fraction is $\phi_t = 20\%$, with equal volume fractions of large and small particles. Here, the large particles migrate to the center of the channel faster than the small particles, creating a region enriched with large particles. In experiments, the volume fraction of small particles drops in the center of the channel (Semwogerere and Weeks, 2008). In the FCM simulations we see the enrichment area of large particles, however, the drop of the small particle volume fraction in the center of the channel is not evident. This is possibly because of the difference in Pe. At low Pe, the particles experience significant forces due to Brownian motion, which disrupts the shear-induced migration in a Poiseuille flow. Without Brownian motion, there is no mechanism for the small particles to be removed from the center of the channel. In the second case in fig. 6.15b, the volume fraction of small particles is more than double the volume fraction of large particles. Here, there is a significant migration of small particles towards the channel centerline. The large particles are excluded from the wall layer, but outside of the near-wall region the large particle volume fraction does not change significantly from its initial profile.

6.4.1 Volume fraction and mean velocity profiles

One motivation for this study is considering bidisperse suspensions with λ close to unity. This represents the case where the particles are close to a uniform size, with some variation possibly due to manufacturing constraints, as typically seen in experiments. Here, we consider how varying the size ratio λ changes the particle

(a) $\phi_l = 10\%, \phi_s = 10\%$ (b) $\phi_l = 10\%, \phi_s = 25\%$

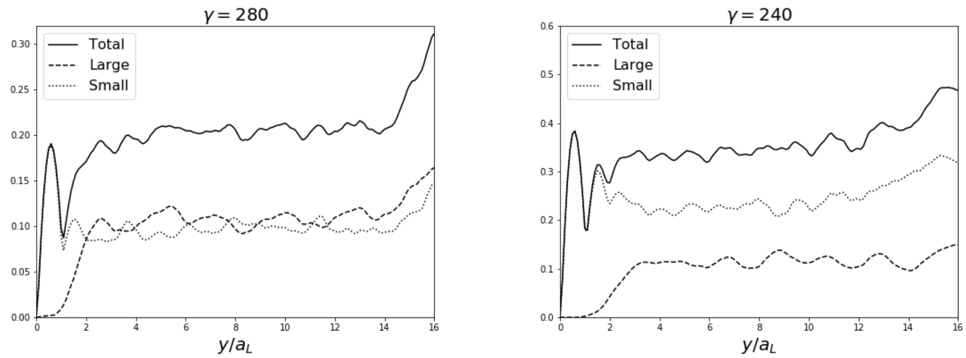

Figure 6.15: Volume fraction profiles from FCM. Left: with equal volume fractions of large and small particles, the large particles migrate to the center of the channel faster. Right: with a larger volume fraction of small particles than large particles, this migration is not evident.

migrations and stresses in comparison to a monodisperse suspension where all particles have radius a_l. By quantifying the differences that may be present between the monodisperse and bidisperse suspensions, we can begin to understand the effect varying particle size has on experiments in comparison to simulations.

The volume fraction of a particle phase α, where α is either large or small particles, is defined as

$$\phi_\alpha(y) = \frac{1}{H_x \times H_z} \left\langle \sum_{i=1}^{N_p} \chi_p^\alpha(\mathbf{x})\, dx\, dz \right\rangle,$$

where $\chi_p^\alpha(\mathbf{x})$ is an indicator function for the particle phase α. Fig. 6.16 compares the volume fraction profiles for $\lambda = 0.8, 0.72$, and 0.6 with the volume fraction from a monodisperse suspension. In all cases, the large particle radius is fixed as $a_l = 1$, and the small particle radius is varied as $a_s = \lambda$.

One way to understand the features in the volume fraction profile is to divide the channel into three regions: the near-wall region, $0 \leq y \leq 6a_l$, the mid-shear zone, $6 \leq y \leq 12a_l$, and the center region, $12 \leq y \leq 20a_l$, and consider changes in the volume fraction in each of these regions. In the near-wall region the particles form a monolayer, which peaks slightly more than one small particle radius away from the wall. The volume fraction profile in the near-wall region depends significantly on λ and on the ratio of small and large particle volume fractions, $\beta = \frac{\phi_s}{\phi_t}$. For bidisperse suspensions, the wall layer consists almost entirely of small particles, shown by the spike in the volume fraction profile for $\lambda = 0.6$ and $\lambda = 0.72$ at $y/a_l = a_s$. A second layer forms on top of the wall monolayer at $y/a_l = 3a_s$. If β is small enough, large particles can enter that second layer. The wall layer is discussed in more detail in sec. 6.4.5.

The second area of interest is the center region, where large particle enrichment occurs. For $\lambda = 0.8$, there is no significant difference between the monodisperse and bidisperse volume fractions at the centerline. In contrast, the volume fraction profile for the monodisperse suspension is $\sim 5\%$ higher in the center of the channel than when $\lambda = 0.6$ and $\beta \geq 0.5$. Here, the significant size difference of the particles leads to a substantially higher migration flux for the large particles than the small particles. Suspensions with a higher proportion of large particles will have a higher volume fraction at the channel centerline at a given time step, as the large particles can migrate to the channel centerline faster until the volume fraction reaches a steady state.

In fig. 6.17, we compare the volume fractions of the large and small particles. In the cases with equal volume fractions of large and small particles, the large particles have a higher volume fraction in the mid-shear region. This is because they are excluded from the wall region, so the large particles initially in the wall region migrate away from the wall into the mid-shear region. When $\beta = 0.5$ the large particle volume fraction is consistently higher than the small particle volume fraction, as the large particles are depleted entirely or partly from the wall layer, and are forced to migrate into the mid-shear region.

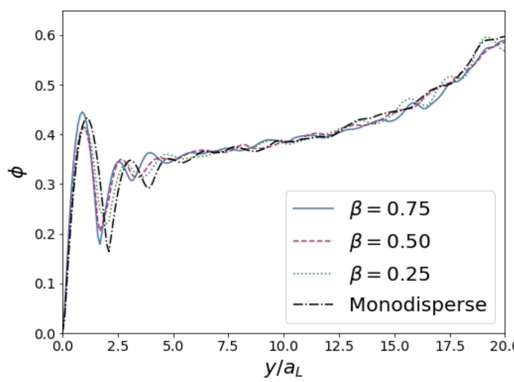

(a) $\lambda = 0.80$

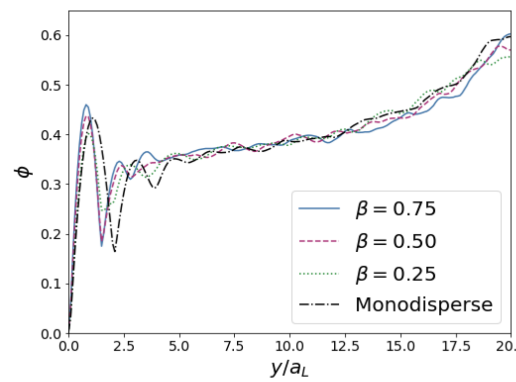

(b) $\lambda = 0.72$

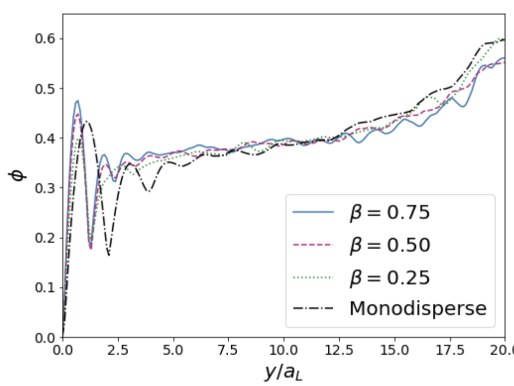

(c) $\lambda = 0.60$

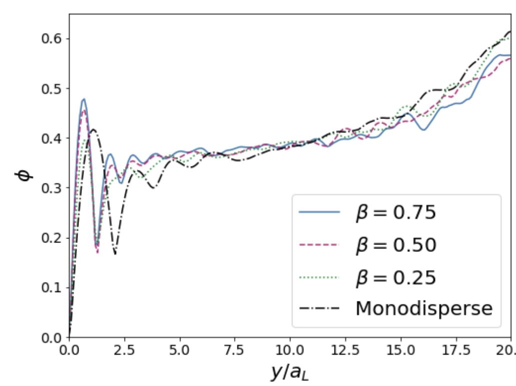

(d) $\lambda = 0.60$, $\gamma = 325 - 350$

Figure 6.16: Volume fraction profiles for bidisperse suspensions in comparison to a monodisperse suspension for size ratios $\lambda = 0.8, 0.72$, and 0.6. When $\lambda = 0.8$, there is no significant difference between the monodisperse suspensions and bidisperse suspensions in the center of the channel. When $\lambda = 0.6$, there is a significant difference in the center of the channel and in the wall layer. Each profile is averaged over $\gamma = 250 - 255$ in (a), (b), and (c). An additional volume fraction profile is shown for $\lambda = 0.6$ where the average is over $\gamma = 325 - 330$ (d).

(a) $\lambda = 0.8$

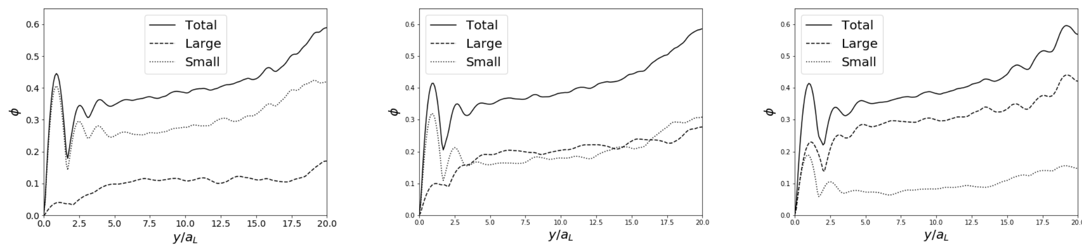

(b) $\lambda = 0.72$

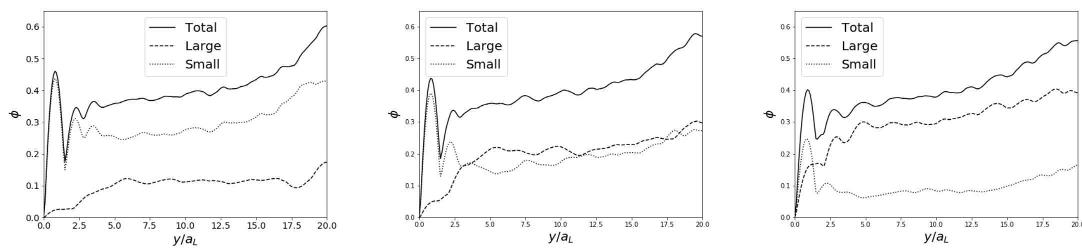

(c) $\lambda = 0.6$

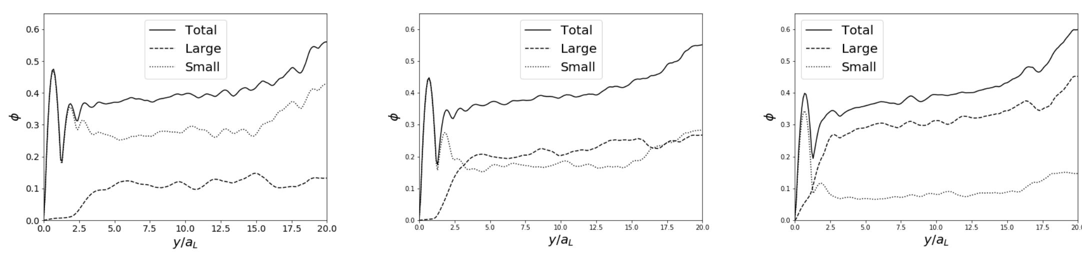

Figure 6.17: Volume fraction profiles of small and large particles for $\beta = 0.75$ (left), $\beta = 0.5$ (center), and $\beta = 0.25$ (right). Each profile is averaged over $\gamma = 250 - 255$.

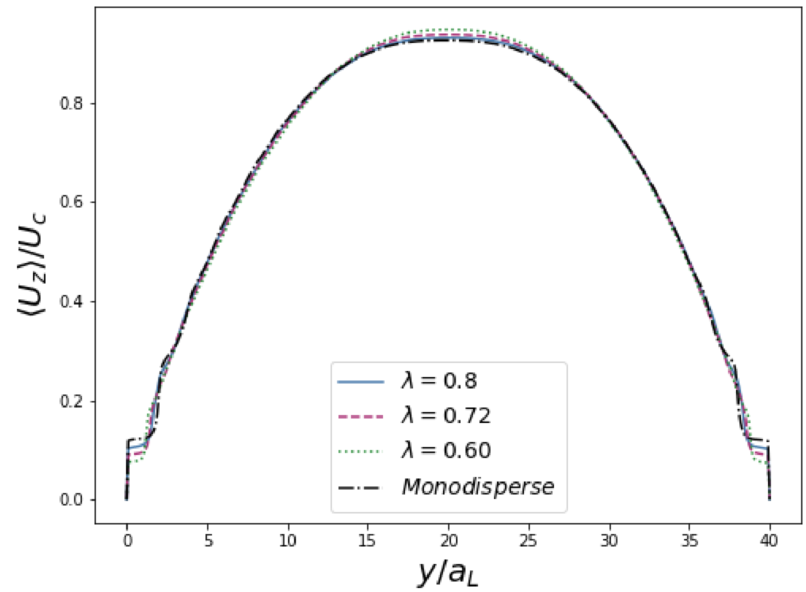

Figure 6.18: Averaged particle phase velocity for $\lambda = 0.8, 0.72$, and 0.6 and a monodisperse suspension. β is fixed at $\beta = 0.5$ for all bidispersed suspensions. Each profile is averaged over $\gamma = 250 - 255$.

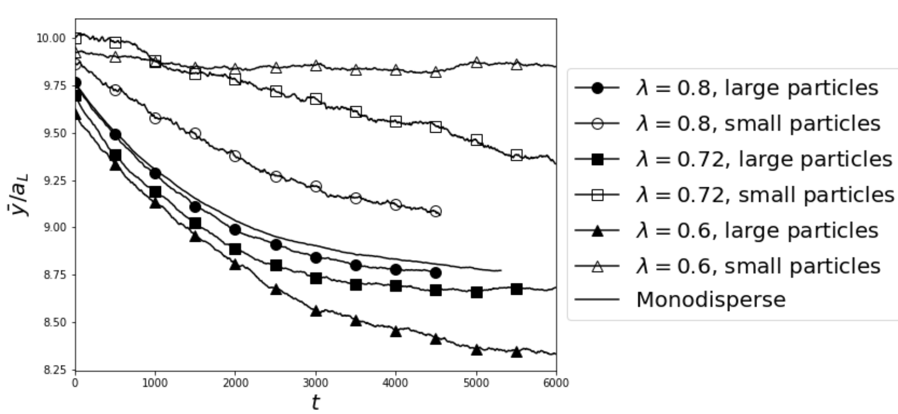

Figure 6.19: Averaged particle distance from the channel centerline for $\beta = 0.25$.

Fig. 6.18 shows the averaged particle phase velocity. Consistent with Lyon and Leal (1998), the particle phase velocity is scaled by the centerline velocity of a parabolic flow with the same bulk velocity as that of the particle phase. The particle phase velocity is blunted from a parabolic profile in the center of the channel, as the volume fraction is higher near the channel centerline. In addition, the velocity at the channel walls increases with the average particle size. The particles move in a quasi-rolling motion at the walls with the velocity at the center of the particle matching the shear rate. This velocity increases with respect to the distance from the wall to the particle center, resulting in a higher velocity for larger particles.

The average particle distance from the channel centerline is given by

$$\bar{y} = \langle y^i - H_y/2 \rangle.$$

When plotted over time as in fig. 6.19, the average particle distance from the centerline decreases, showing that the particles migrate closer to the centerline. The velocity of the initial migration depends on the particle size. In a bidispersed suspension, the large particles migrate much further towards the centerline so $\bar{y}$ decreases much faster for larger particles. Interestingly, $\bar{y}$ decreases faster for the large particles each of the bidisperse suspensions than for the monodisperse suspension, even though the particle radius is the same in each case. This may be because the large particles in the bidisperse suspensions are depleted from the wall layer, forcing more large particles into the mid-shear region. The migration is much slower for small particles, with very little change from the initial value when $a_s = 0.6$.

(a) N_1 (b) N_2

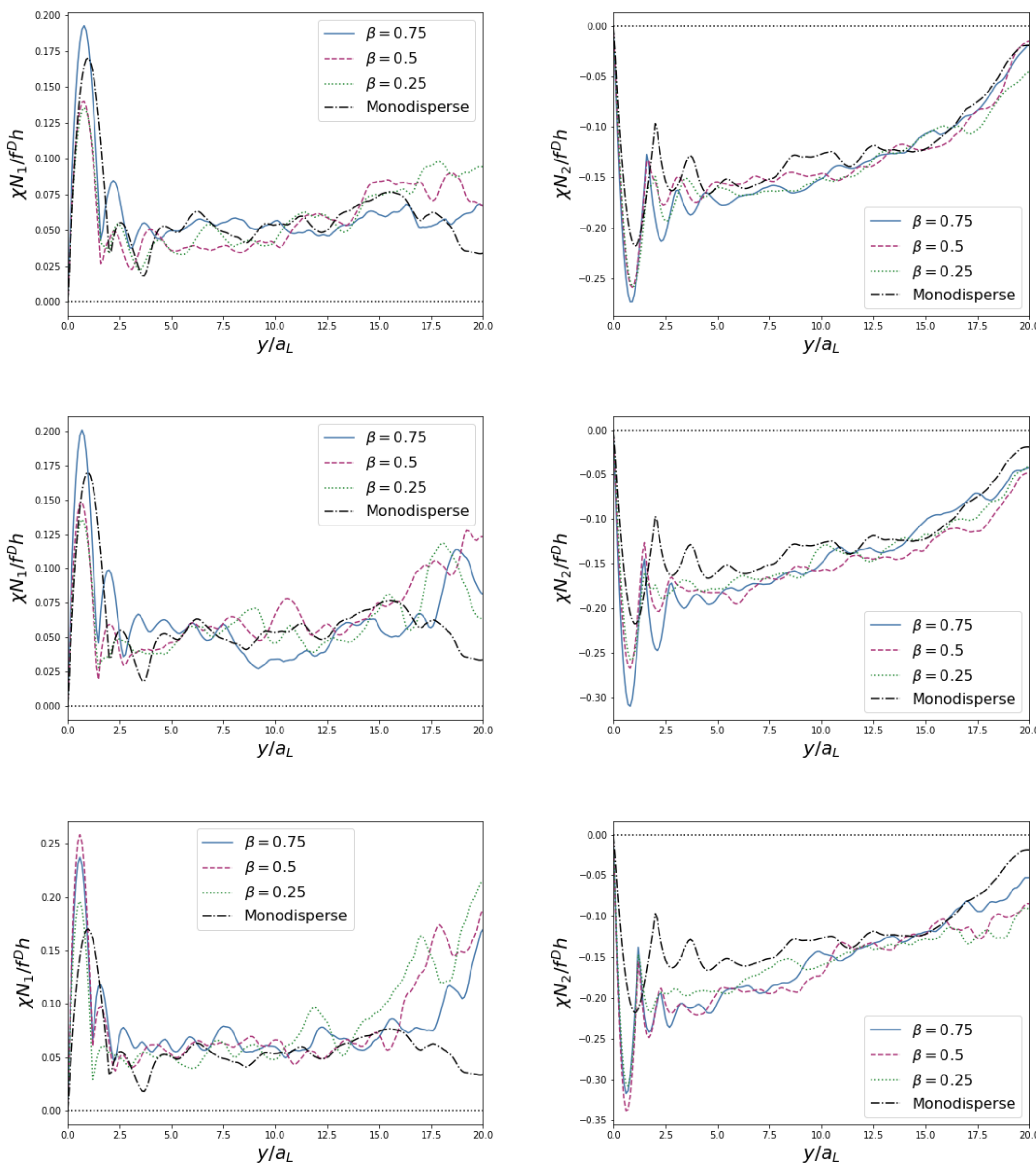

Figure 6.20: Normal stress difference profiles for $\lambda = 0.8$ (top), $\lambda = 0.72$ (middle), and $\lambda = 0.6$ (bottom). N_1 is positive and N_2 is negative. Each profile is averaged over $\gamma = 250 - 255$.

6.4.2 Rheology

The first and second normal stress difference profiles are given in fig. 6.20. In all cases, the normal stress differences for bidisperse suspensions have larger absolute value at the channel centerline than the monodisperse suspension. This difference is small for $\lambda = 0.8$, but for $\lambda = 0.6$ the first normal stress difference is almost four times larger at the centerline. In the midshear region, the normal stress difference profiles agree well between the bidisperse and monodisperse suspensions.

The particle averaged 22 stress profile, $\chi\sigma_{22}$ is plotted in fig. 6.21a. Here again the profiles for bidisperse suspensions have a larger absolute value at the centerline, with the largest difference for $\lambda = 0.6$. In contrast, the shear stress profiles shown in fig. 6.21a agree quite well at the centerline with the monodisperse profiles. Differences occur nearest the walls, where the bidisperse suspension with $\lambda = 0.6$ has the highest values. Fig. 6.22 is included as a comparison of how the σ_{22} profile evolves over time for $\lambda = 0.6$ The stress in the center of the channel is continuing to increase at $\gamma = 300$, which slightly decreasing in the mid-shear region and near the wall.

Fig. 6.23 has the particle contact pressure profiles. For $\lambda = 0.8$, the contact pressure profile for the bidisperse suspensions and the monodisperse suspension are quite similar. Although the bidisperse suspensions have a slightly higher value, this could be due to noise in the profiles. At $\lambda = 0.72$, the contact pressure of the bidisperse suspensions is higher in the near-wall region, and slightly higher along the channel centerline. For $\lambda = 0.6$, the particle contact pressure is significantly higher in the center of the channel for the bidisperse suspensions. The stress profile forms local maximums, with spacing $y = 2a_s$. From 6.24, this large particle contact pressure is almost entirely due to the small particles. This could be due to caging of the small particles. The small particles are mobile and can fit between the gaps

(a) Σ_{22} (b) Σ_{23}

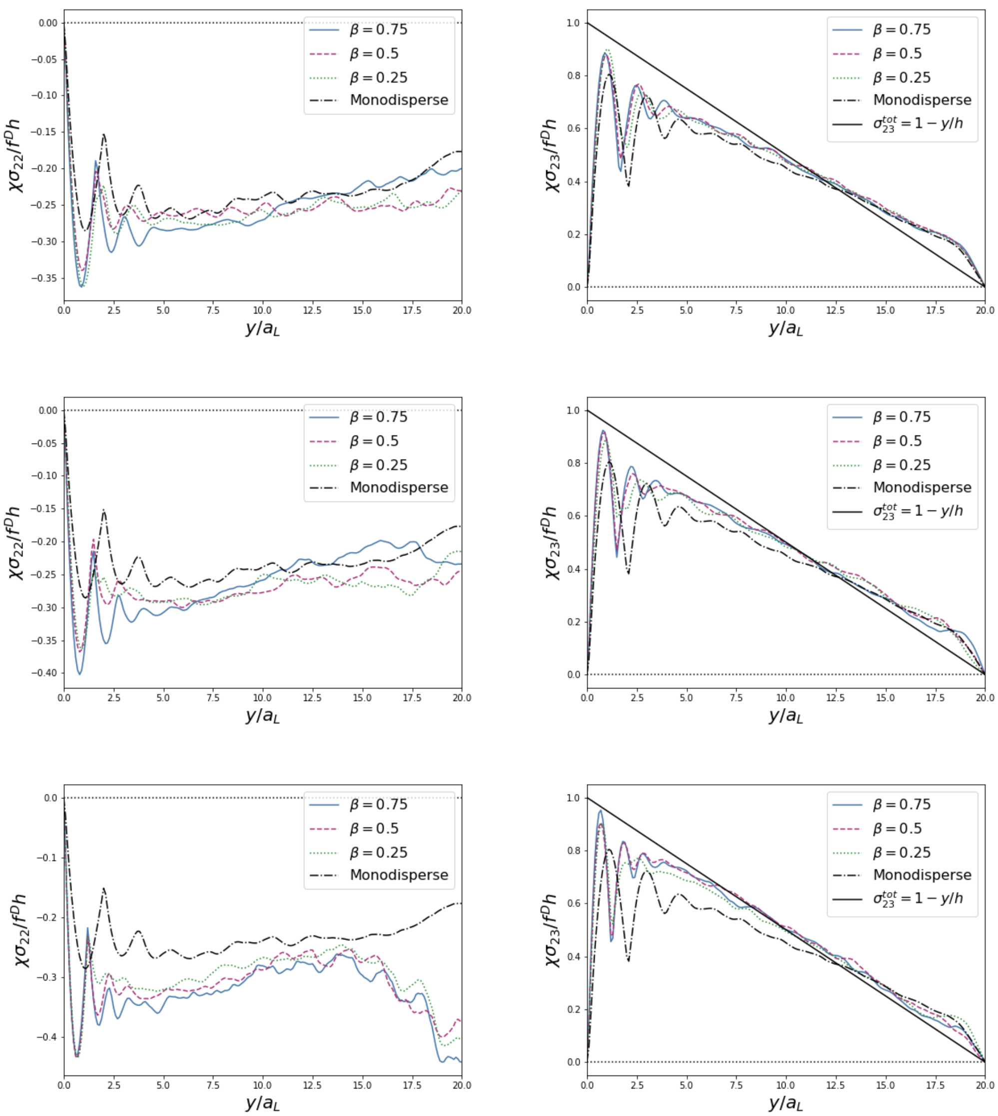

Figure 6.21: Stress profiles for $\lambda = 0.8$ (top), $\lambda = 0.72$ (middle), and $\lambda = 0.6$ (bottom). Each profile is averaged over $\gamma = 250 - 255$.

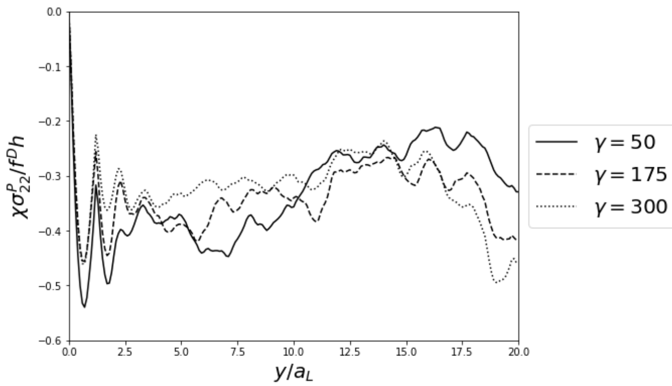

Figure 6.22: Development of the averaged particle stress σ_{22} over time. $\lambda = 0.6$ and $\beta = 0.5$.

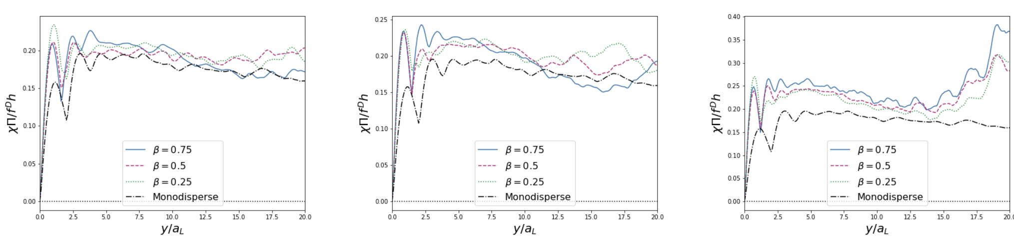

Figure 6.23: Contact pressure profiles for $\lambda = 0.8$ (left), $\lambda = 0.72$ (center), and $\lambda = 0.6$ (right). Each profile is averaged over $\gamma = 250 - 255$.

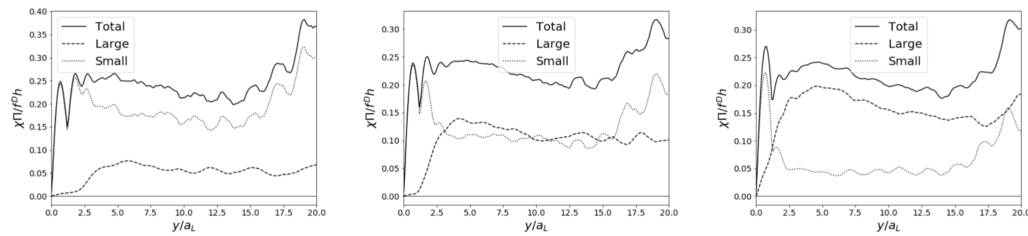

Figure 6.24: Contact pressure profiles for $\lambda = 0.6$ for $\beta = 0.25$ (left), $\beta = 0.5$ (center), and $\beta = 0.75$ (right).

between large particles, however they then may get stuck and tightly confined by multiple large particles.

In the simulations presented above, we see that a suspension with $\lambda = 0.8$ or $\lambda = 0.72$ develops in a similar manner as a monodisperse suspension. While there are differences in the wall layering due to the particle sizes, the stress profiles in the midshear and center regions are very close. This suggests that a small variation in particle size, up to 30%, does not change the final development of the suspension, and that monodisperse simulations are a good approximation to experiments.

6.4.3 Quantifying enrichment

In simulations where $\beta \neq 0.5$ it can be difficult to visually tell if enrichment occurs by looking at the particle volume fraction profiles. To quantify particle enrichment we introduce the index of dissimilarity. The channel is divided into k equal bins in the velocity gradient direction y. The index of dissimilarity I is given by:

$$I = \frac{1}{2} \sum_{i=1}^{k} \left| \frac{n_s^i}{N_s} - \frac{n_l^i}{N_l} \right|,$$

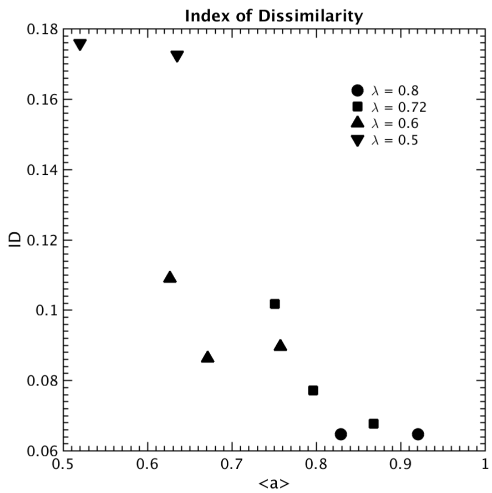

Figure 6.25: Index of dissimilarity plotted versus the average particle radius.

where N_s and N_l are the total number of small and large particles and n_s^i and n_l^i are the number of small and large particles in bin i (Sakoda, 1981). I gives a measure of the percentage of particles that would have to move from an area of high concentration of one particle size to an area of low concentration of particles of that size to give a homogeneously mixed suspension. The particle layer closest to each wall is excluded.

The index of dissimilarity is plotted in fig. 6.25 versus the average particle radius and in fig. 6.26 versus the particle size ratio. The index of dissimilarity increases with decreasing λ and decreasing $\langle a \rangle$. Typically, a suspension with a higher value of λ will have a lower index of dissimilarity for a given average particle radius than a suspension with a lower value of λ, because there will be a greater differential in the particle migration fluxes.

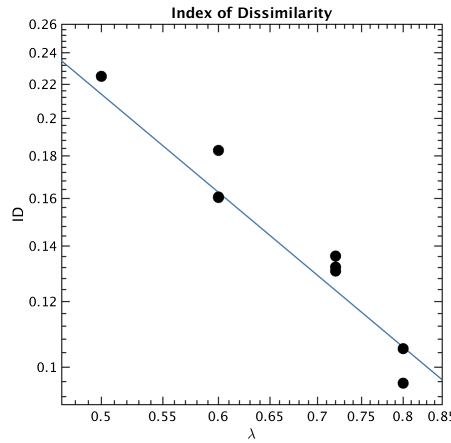

Figure 6.26: Index of dissimilarity plotted versus the particle size ratio. Fit: $\lambda^{-3/2}$.

6.4.4 Pair distribution functions

The pair distribution functions give insight to the microstructure of the suspension by describing the conditional probability of finding another particle of size β at a given distance from a particle of size α. We take the definitions of the partial pair distribution functions from Wang and Brady (2016):

$$g_{\alpha\beta}(\mathbf{r}) = \frac{1}{n_{\alpha\beta}} \left\langle \sum_{i\in\alpha, j\in\beta} \frac{1}{V} \delta(\mathbf{r} - \mathbf{r}_i + \mathbf{r}_j) \right\rangle, \tag{6.4.1}$$

where n_α and n_β are the number of particles of size α and $beta$, $\mathbf{r}_k$ is the center of particle k, and V is the volume of the average box size considered. The pair distribution function for the entire suspension is found from the partial pair distribution functions by

$$g(\mathbf{r}) = \sum_{\alpha,\beta} \frac{n_\alpha n_\beta}{(n_\alpha + n_\beta)} g_{\alpha\beta}(\mathbf{r}). \tag{6.4.2}$$

Figure 6.27a shows a plane at $y/a_l = H_y/2$. Solid black lines are marked between any two particles that are in contact, defined as the distance between the particle centers is less than the contact force cutoff distance. One feature of interest is that

(a)

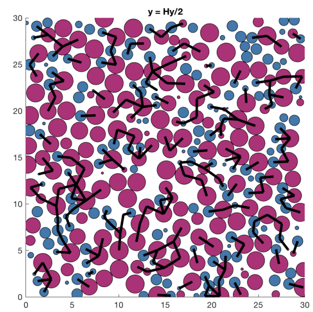

(b)

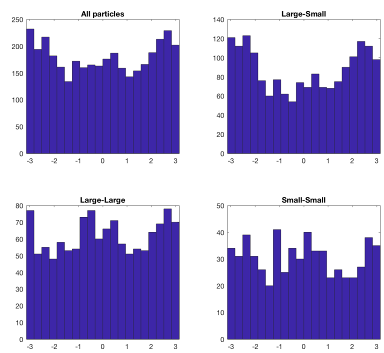

Figure 6.27: (a) Plane at $y/a_l = H_y/2$. Large particles are red and small particles are blue. Black lines indicate particle contact forces. The direction of mean fluid velocity is left to right. (b) Histogram of the angle of a vector connecting the centers of two particles in contact and a vector parallel to the channel wall. $\lambda = 0.6$.

the small particles in blue appear to, on average, trail the large particles in red. This can be further seen in fig. 6.27b, which shows a histogram of the angle the contact force makes with a vector parallel to the channel wall for all particle contacts. Here, an angle of $n\pi$, $n \in \mathbb{Z}$, corresponds to a contact force parallel to the flow. For the large-small particle contacts, the most common angles are clustered around $\pm\pi$, indicating that the large and small particles are aligned in the stream-wise direction, with the small particle following behind the large particle. The large-large particle contacts are similarly aligned in the stream-wise direction. The small-small particle contacts do not show a distinct alignment with the flow.

Figs. 6.28 and 6.29 show the pair distribution functions $g(z, x)$ and $g(z, y)$ projected into the $z - x$ and $z - y$ planes, respectively. The pair distribution function in the plane of the velocity direction and mean vorticity direction in fig. 6.28 (right) shows the asymmetry in the large-small particle contacts. There is a higher probability of a small particle being located behind a large particle relative to the streamwise direction, as shown by the bottom left and top right figures. Fig. 6.28 (left) shows the total pair distribution function between all particles. There are shells of high probability at $\mathbf{r} = 2a_s, a_s + a_l$, and $2a_l$, denoting the possible combinations of particle contacts. Wang and Brady (2016), in studies for a bidisperse suspension in a shear flow in a periodic cell noticed an enrichment of small-large particle contacts along the direction of flow at high Péclet number. Here we are seeing that small-large contacts are preferred, with the small particle trailing the large particle.

Fig. 6.29 shows the structure that forms due to the shear flow in the half channel. There is a depletion of particle pairs near the angle $\theta = 5\pi/4$, consistent with the results of Yeo and Maxey (2010), Gao et al. (2009), Wang and Brady (2016), Pednekar et al. (2018) for the pair distribution functions of particles in a shear flow.

6.4.5 Particle wall layering

In the volume fraction profiles from simulations of bidisperse suspensions in Poisuille flow in sec. 6.4.1 the initial peak in the volume fraction occurs at $y/a_l = a_s$. By examining fig. 6.17 it is clear that the large particles are excluded from the wall layer unless the volume fraction of large particles in the suspension is quite large, corresponding to smaller values of β. In this section, we show that this exclusion of large particles in the wall layer can easily arise though very small changes to particle properties, due to inter-particle contacts in the wall layer.

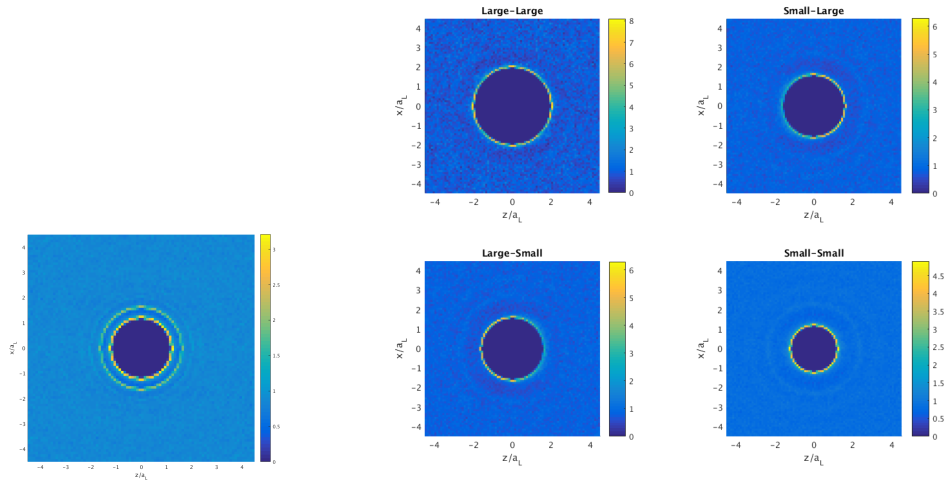

Figure 6.28: Pair distribution in the velocity-vorticity (zx) plane between all particles (left) and separated by species (right). The wall layer, $|y - H_y/2| > H_y - 3$, is excluded. Here, $\lambda = 0.6$ and $\beta = 0.5$.

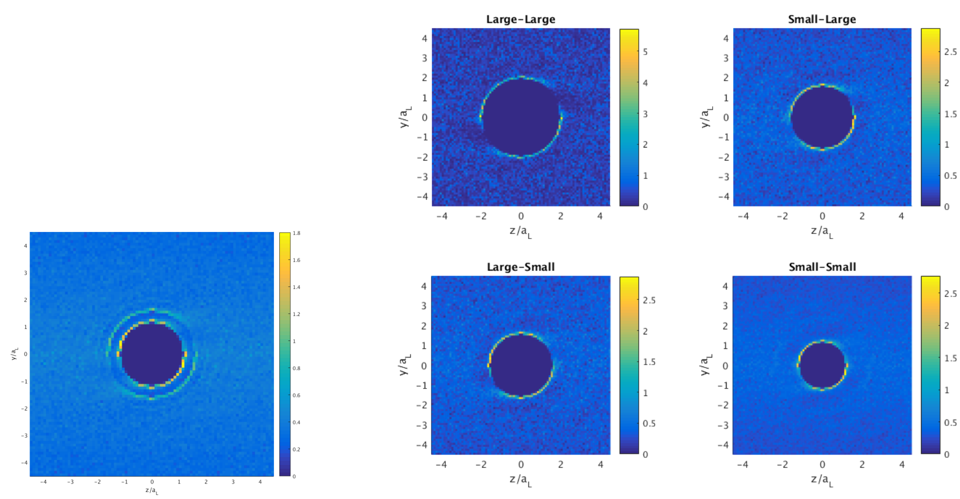

Figure 6.29: Pair distribution in the velocity-velocity gradient (zy) plane between all particles (left) and separated by species (right) for $3a_l \leq y \leq H_y/2$. Here, $\lambda = 0.6$ and $\beta = 0.5$.

Simulations with FCM clearly show strong particle layers forming on the walls of the channel in both Couette and Poseuille flow, with additional layers forming on the wall layer if the volume fraction is high enough (Yeo and Maxey, 2010, 2011). Simulations of wall-bounded Couette and Poiseuille flow suspensions have shown similar wall-layering (Kulkarni and Morris, 2008, Kanehl and Stark, 2015). Some early experimental results do show evidence of wall layering (Hampton et al., 1998), however, limitations of experimental techniques can often obscure regions near channel walls, including the wall layer. More recent experiments of a suspension in a Poiseuille flow show strong evidence of a wall layer and the additional layers that can form across the channel at high volume fraction (Snook et al., 2016). While FCM does enforce the no-slip condition at the channel wall, the particles are free to move along the wall in a quasi-rolling motion and thus the particles in the wall layer do have a nonzero velocity. When a particle is near the wall, there is a strong lubrication force that forms between the particle and the wall, preventing the particle from being displaced from the wall. In addition, if all wall layer particles are equal sized and equidistant from the channel wall, all interactions between the particles will act along the line of centers of the particles, which will be parallel to the wall and incapable of bumping a particle from the channel wall. Additional interactions with particles above the wall layer act as a force to push wall layer particles closer to the channel wall. This results in a coherent monolayer forming at the channel wall, from which it is very difficult for particles to escape.

Fig. 6.30 shows the volume fraction profile for a monodisperse suspension with total volume fraction $\phi = 0.4$. The volume fraction in the wall layer at $y/a = 1$ increases quickly in the first 20-40 strain units. The initial shift in the wall layer from $\gamma = 0$ to $\gamma = 20$ is due to an initial transient from the particle seeding. After accumulated strain $\gamma = 40$, the volume fraction increases only slightly in the wall

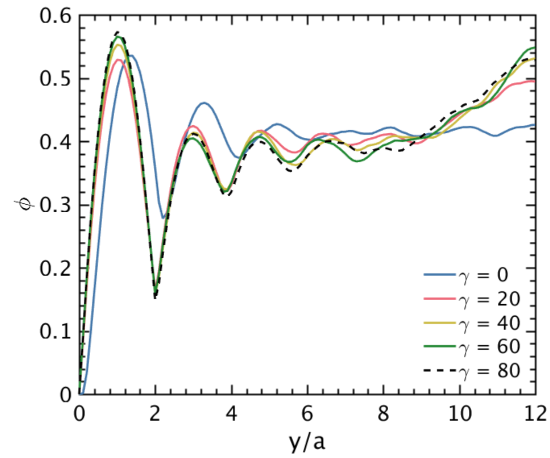

Figure 6.30: Volume fraction profile for a monodispersed suspension at accumulated strain $\gamma = \frac{U_B t}{H/2} = 0, 20, 40, 60$, and 80. Total volume fraction $\phi = 40\%$ and channel height $H = 24a$.

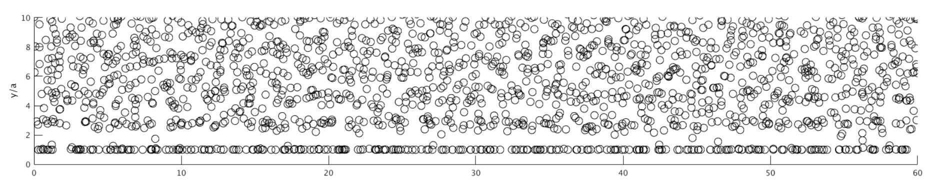

Figure 6.31: Plot of all particle locations flattened onto a plane in the vorticity direction for a monodisperse suspension with $\phi = 0.4$ and $\gamma = 80$. The wall layer is clearly visible by the particles centered at $y/a = 1$. A less coherent layer forms at $y/a = 3$ above the wall layer. Particles are shown at 25% of their actual size.

Mode	R_{ref}
Monodisperse	$R_{ref} = 1.05$
Bidisperse A	$R_{ref} = 1.05$ or 1.10
Bidisperse B	$R_{ref} = 1.05$ or 1.575
Random A	$R_{ref} \in [1.05, 1.10]$
Random B	$R_{ref} \in [1.05, 1.15]$

Table 6.3: Values of R_{ref} for the simulations considered in sec. 6.4.5.

layer. A second layer forms on top of the wall layer at $y/a = 3$. At high enough volume fraction, additional layers can form at $y/a = 2n + 1$. For this example, at $\gamma = 10$ the there is $N_p = 577$ particles in the wall layer. At $\gamma = 80$, $N_p = 654$. Between $\gamma = 10$ and $\gamma = 80$, 134 particles enter the wall layer while only 57 enter. The wall layer is clearly visible in fig. 6.31, which shows the particle locations at $\gamma = 80$ plotted on a plane at 25% of the particle actual size. There is a strong layer of particles located at $y/a = 1$. The next layer of particles at $y/a = 3$ is less coherent, but still visible.

In this section we consider suspensions where the particles are all the same size ($\lambda = 1.0$), but have different particle surface roughness parameters given in table 6.3. For simulations labeled “Bidisperse”, half of the particles have each of the two values of R_{ref}. In simulations labeled “Random”, the particles are randomly assigned a value of R_{ref} in the given range.

The final volume fraction profiles at $\gamma = 80$ are shown for each case in fig. 6.32. The volume fraction in the wall layer of both the bidisperse and random simulations is lower than that of the monodisperse simulation, which is not surprising as in those cases there is a mechanism for particles to be removed from the wall layer through the inter-particle contact force. The rest of the volume fraction profile is qualitatively similar across the simulations, so changing the wall layer properties does not result in changes across the channel.

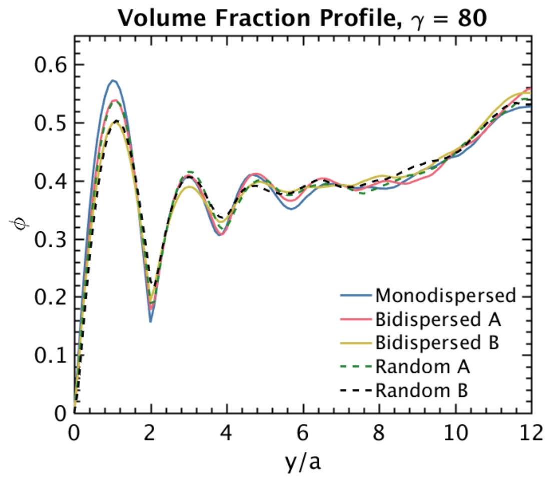

Figure 6.32: Volume fraction profile for the four cases varying R_{ref} and a monodispersed suspension at $\gamma = 80$. The volume fraction in the wall layer decreases when R_{ref} is varied, with a larger decrease corresponding to a higher variation in R_{ref}.

Fig. 6.33 has the number of particles in the wall layer after each ten strain units for each of the simulations. In each case, the particles with the largest values of R_{ref} are beginning to be depleted from the wall layer. When there is a large variation in R_{ref}, as in Bidisperse B, almost all particles with the larger value of R_{ref} are depleted from the wall layer by $\gamma = 10$, and have been replaced by particles with smaller values of R_{ref}. Fig. 6.33 also shows the final particle positions of particles are initially in the wall layer at the beginning of the simulation. Particles that are removed from the wall layer are most likely to be in the midshear region, although some do migrate into the center of the channel. The large bars at either side of the domain indicate that most particles that begin in the wall layer remain in the wall layer after accumulated strain $\gamma = 80$.

(a) Bidisperse A

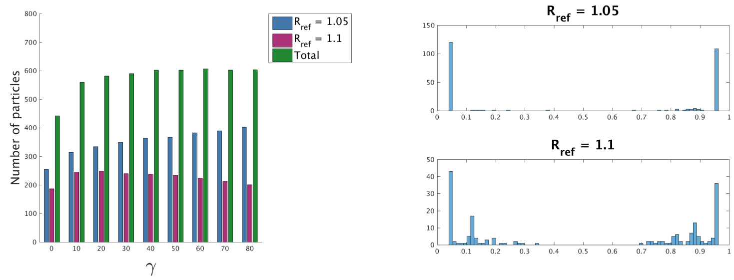

(b) Bidisperse B

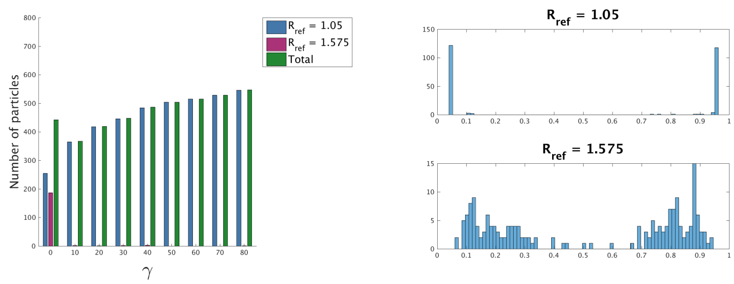

(c) Random A

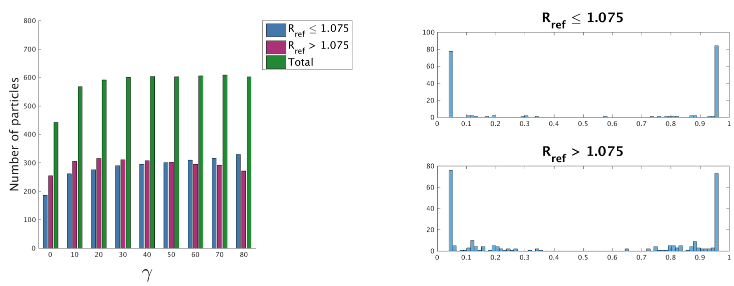

(d) Random B

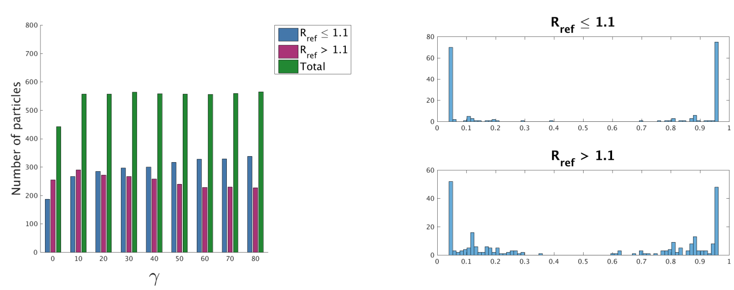

Figure 6.33: (Left) Number of particles in the wall layer for $\gamma = 0 - -80$. Green: total particles. Blue: Smaller value of R_{ref}. Purple: Larger value of R_{ref}. The particles with a larger value of R_{ref} are more likely to migrate away from the wall, with the number of particles leaving the wall layer corresponding to larger values of R_{ref}. (Right) Final locations of particles initially in the wall layer after $\gamma = 80$. The particles with larger values of R_{ref} migrate significantly further away from the channel walls.

Chapter Seven

Beyond FCM: Generalized Moving Least Squares

Numerical modeling of a fluid containing suspended particles is crucial, as simulations give a much greater amount of information than state-of-the-art experiments, including data on the forces and stresses on all of the suspended particles at each time step (Gao et al., 2009, Blanc et al., 2011, Metzger and Butler, 2012, Guasto et al., 2010). Current simulation methods are constrained by the complexities of handling the suspended particles, including the multiscale challenge of resolving both the short range forces that occur between nearly touching particles and the long range hydrodynamic forces on the scale of the system. In addition, the inherent stiffness of these systems leads to numerical challenges. Fully resolved simulations, such as Arbitrary Lagrangian Eulerian (ALE) require generating a mesh fitted to the particles, which must then be regenerated as the particles are advected with the flow (Prosperetti and Tryggvason, 2009, Hu, 1996, Maxey, 2017). While effective for high-resolution studies of a small number of particles, scaling ALE methods to a large number of particles poses further challenges (Swaminathan et al., 2006, Prosperetti and Tryggvason, 2009). Other methods avoid generating a body fitted mesh by using Lagrangian particles, as in Stokesian Dynamics (SD), or by using a fixed mesh for the entire domain, as in the Immersed Boundary Method (IBM) or the Force Coupling Method (FCM). In SD, a mobility matrix for the particle motion is obtained by a low-order multiple representation of the fluid flow induced by the particles (Bossis and Brady, 1984, Brady, 1988, 2001, Maxey, 2017). The method can handle systems with a large number of densely packed particles; however, it is restricted to simple, zero-Reynolds number flows. In IBM, a fixed mesh fills the entire domain, and particles are represented by a forces on a diffuse interface representing the surface (Peskin, 2002, Breugem, 2012). IBM is at most first-order accurate. FCM is like IBM in that the fluid fills the entire domain. Similarly to SD, the particles are represented by low-order finite force multiples, however, FCM can also be used in the low Reynolds number regime (Maxey and Patel, 2001, Liu et al., 2002, Lomholt and Maxey, 2003). The Navier-Stokes equations are solved in the entire domain, allowing for use of efficient Navier-Stokes solvers without the difficulties of remeshing. In both FCM and SD, lubrication viscous forces due to the pressure driven flow that develops between two moving particles are incorporated in a pairwise manner from analytical lubrication formulae for spherical particles (Dance and Maxey, 2003, Kim and Karilla, 1991, Jeffrey and Onishi, 1984, Jeffrey, 1992). Each of these methods can have significant limitations. In FCM, lattice-Boltzmann, and SD, the lubrication forces are added in a pairwise manner, which is an approximation that can break down if the particles have large size variations. In addition, FCM and SD are valid for spherical particles, and cannot be used for particles with arbitrary shapes.

Here, we present work on a novel meshless particle method using Generalized Moving Least Squares (GMLS) for high-order simulations of suspension Stokes flows with arbitrary particle shapes and complex, deforming domain boundaries (Trask et al., 2018, 2017, Mirzaei et al., 2012). These problems cannot be solved efficiently with existing suspension flow codes. Using a meshless method avoids the issues inherent to meshes, including interpolating between meshes when the domain changes or particles move. Efficient meshless methods have applications across the field of fluid dynamics. GMLS offers many large advantages over other existing methods for colloids. The first is that the method does not depend on the domain, allowing for handling of arbitrarily complex domains or moving domain boundaries. In addition, there are no restrictions made on the size or shape of the particles. Other methods, such as the FCM, are only valid for spherical or elliptical particles. Finally, in GMLS the particles suspended in the flow have a distinct boundary, represented by GMLS particles placed at the edge of the colloid. Thus, GMLS avoids the issues with methods such as the Immersed Boundary Method (IBM) and FCM, where the body forces on the particles are represented by compact smooth kernel functions leading to errors at the particle surface (Maxey, 2017, Peskin, 2002, Breugem, 2012).

7.1 Numerical Method

In Generalized Moving Least Squares (GMLS) we approximate the value of a function near a given location by seeking solutions to an ℓ^2 optimization problem, which gives a stencil similar to those found in finite-difference methods Trask et al. (2018). This form allows for systems of partial differential equations to be formulated easily as a global matrix equation, with blocks for each of the equations. The value of an operator $\mathcal{D}^\alpha$ applied a function u is found by applying the operator to the solution of the ℓ^2 optimization:

$$\mathcal{D}^\alpha u \approx \mathcal{D}^\alpha u_h(x;\ x_i) := \mathcal{D}^\alpha q^*(x_i), \text{ where } q^* = \arg\min_{q\in\pi_m} \sum_j \left[u(x_j) - q(x_j)\right]^2 W_{ij}.$$

Here, π^m is the space of polynomials of degree m and W_{ij} is a radially symmetric weighting function, $W_{ij} := W(x_i - x_j)$. While formulated above for scalar functions, GMLS can be generalized to $\mathbb{R}^n$ by minimizing over the space of polynomials of degree m in $\mathbb{R}^n$.

7.1.1 Staggered GMLS

Many problems of interest, including those in electro-statics and fluid flows, can be written in the form of an elliptic boundary valued problem:

$$\begin{cases} -\nabla \cdot \kappa \nabla \phi = f & \in \Omega \\ \phi = 0 & \in \partial\Omega, \end{cases} \tag{7.1.1}$$

where Ω is a bounded domain in $\mathbb{R}^3$ with boundary $\partial\Omega$ and κ is a symmetric positive definite tensor that denotes some material property.

Taking $\mathbf{u} = -\kappa\nabla\phi$, eqn. 7.1.1 can be rewritten as a system of coupled equations:

$$\begin{cases} \nabla \cdot \mathbf{u} = f & \in \Omega \\ \mathbf{u} + \kappa\nabla\phi = 0 & \in \Omega \\ \phi = 0 & \in \partial\Omega. \end{cases} \tag{7.1.2}$$

Traditionally, two methods have been used to solve eqn. 7.1.2. The first uses a single grid. One operator is approximated on that grid, and the adjoint is used for the other operator. The other method uses a primal-dual grid, such as in finite volume schemes, two approximate the two operators separately on two topologically dual grids. This second approach was developed for GMLS by Nathanial Trask, where results were presented in two-dimensions (Trask, 2015, Trask et al., 2018, 2017). Here, we show scalable three-dimensional results.

Staggered GMLS relies only on the graph of neighbor connectivity between GMLS collocation points, so there is no need to build a full mesh. Denote the set of N_p

collocation points as $N = \{\mathbf{x}_i\}_{i=1,\ldots,N_p}$. For each GMLS collocation point $\mathbf{x}_i$, identify the edge between the collocation point and each of its neighbors as $E_i = \{e_{ij} : ||\mathbf{x}_i - \mathbf{x}_j|| < \epsilon_i\}$, where ϵ_i is the radius of support of the MLS weighting function W at $\mathbf{x}_i$. The set of all edges is denoted by $E = \{E_i\}_{i=1,\ldots,N_p}$.

Next, we identify a virtual dual face with each edge and a virtual cell with each node, creating an analogy to a primal-dual mesh, such as in staggered finite difference schemes. However, the construction relies only on the graph of neighbor connectivity, and no mesh is physically constructed.

The virtual face is located at the midpoint of each edge, $\mathbf{F}_{ij} = \frac{\mathbf{x}_i + \mathbf{x}_j}{2}$, with the associated normal $\hat{n}_{ij} = \frac{\mathbf{x}_j - \mathbf{x}_i}{||\mathbf{x}_j - \mathbf{x}_i||}$. The set of faces is then denoted by $\mathbf{F}$. In addition, a virtual cell $\mathbf{C}_i$ is identified with each node $N_i \in N$. Then, we can construct the graph $\Omega_h = G(N, E) = \cup C_i$.

We then seek discrete operators

$$
\begin{aligned}
div_h &: F \to C \\
grad_h &: C \to F
\end{aligned}
$$

in a similar manner as compatible mixed methods in $H(div)$[1] for finite element problems (Braess, 2007).

The technical proofs of the convergence of this method are given in detail in Trask (2015). Here, we will consider only the implementation.

[1] $H(div, \Omega) := \{\tau \in L_2(\Omega)^d; div(\tau) \in L_2(\Omega)\}$.

The gradient operator is found by a centered difference formula long the edges:

$$grad_h(p)_{ij} \cdot \hat{n}_{ij} = \frac{p_j - p_i}{||\mathbf{x}_j - \mathbf{x}_i||} \tag{7.1.3}$$

To reconstruct variables at faces, define the flux variable $f_{ij} = \mathbf{u} \cdot \hat{n}_{ij}$. Then, the reconstructed value, $\mathbf{p}^*$, can be found through the standard MLS approximation:

$$\min_{\mathbf{p} \in (\pi_m(\mathbb{R}^3))^3} \left[\sum_{j=1}^{N_p} (f_{ij} - \mathbf{p}_{ij} \cdot \hat{n}_{ij})^2 W(||\mathbf{x}_i - \mathbf{x}_{ij}||) \right]. \tag{7.1.4}$$

The divergence operator is then $div_h(\mathbf{u}) = \nabla \cdot \mathbf{p}^*$.

7.1.2 Staggered GMLS for Stokes' equations

Representation of Stokes flow using finite-differences typically requires the pressure and velocity terms to be considered on separate, staggered meshes (McKee et al., 2008). GMLS has been applied colloids in Stokes flow by using a staggered mesh as proposed by Trask et al. (2018). He proposed introducing a primal/dual basis by identifying a virtual dual face with each edge between collocation points and a virtual cell with each collocation point (Nicolaides and Trapp, 2006, Bochev et al., 2013, Trask et al., 2018). In addition, to enforce the divergence-free condition for the velocity of the fluid, Trask et al. (2018) proposed choosing $\mathbf{u}$ to be in the space of divergence-free polynomials in $\mathbb{R}^3$ of degree m, denoted π^m_{div}. The Stokes equations in a domain Ω along with a set of force-free and torque-free colloids with positions X_i, orientations Ω_i, and boundaries ∂X_i, then become a set of coupled equations for the fluid and the motions of the colloids:

$$\begin{cases} \nu\nabla \times \nabla \times \mathbf{u} + \nabla p = \mathbf{f} & \mathbf{x} \in \Omega \\ \mathbf{u} = \mathbf{w} & \mathbf{x} \in \partial\Omega \end{cases} \tag{7.1.5}$$

$$\begin{cases} \nabla^2 p = \nabla \cdot \mathbf{f} & \mathbf{x} \in \Omega \\ \partial_n p + \nu\hat{\mathbf{n}} \cdot \nabla \times \nabla \times \mathbf{u} = \hat{\mathbf{n}} \cdot \mathbf{f} & \mathbf{x} \in \partial\Omega \end{cases} \tag{7.1.6}$$

$$\begin{cases} \mathbf{u} = \dot{\mathbf{X}}_i + \dot{\Theta}_i \times (\mathbf{x} - \mathbf{X}_i) & \mathbf{x} \in \partial\Omega_i \\ m_i\ddot{\mathbf{X}}_i = \int_{\partial\Omega_i} \sigma_v \cdot \ dA \\ I_i\ddot{\Theta}_i = \int_{\partial\Omega_i} (\mathbf{x} - \mathbf{X}_i) \times \sigma_v \cdot \ dA \end{cases} \tag{7.1.7}$$

Each of the operators in equations 1-3 can be expressed as the form of ℓ^2 optimization problem. For example, from equation 7.1.5, we take the viscous curl-curl operator as: $\nabla \times \nabla \times \mathbf{u}(\mathbf{x}_i) \approx \nabla \times \nabla \times_h \mathbf{u}(\mathbf{x}_i) := \nabla \times \nabla \times \mathbf{v}^*(\mathbf{x}_i)$ where $\mathbf{v}^*$ is the standard GMLS approximant over the divergence-free basis: $\mathbf{v}^* = \arg\min_{v \in \pi_m^{div}} \left\{ \sum_{j=1}^{N_P} [\mathbf{u}(\mathbf{x}_j) - \mathbf{v}(\mathbf{x}_j)]^2 W_{ij} \right\}$. Similar formulas can be found for the gradient, divergence, and Laplacian operators, so that the global matrix can be formed to solve for the function values at each point in the domain Ω.

7.1.3 Results for a single particle

Due to computational limitations in our GMLS code for three-dimensions, in what follows we present work for a single particle in Stokes flow.

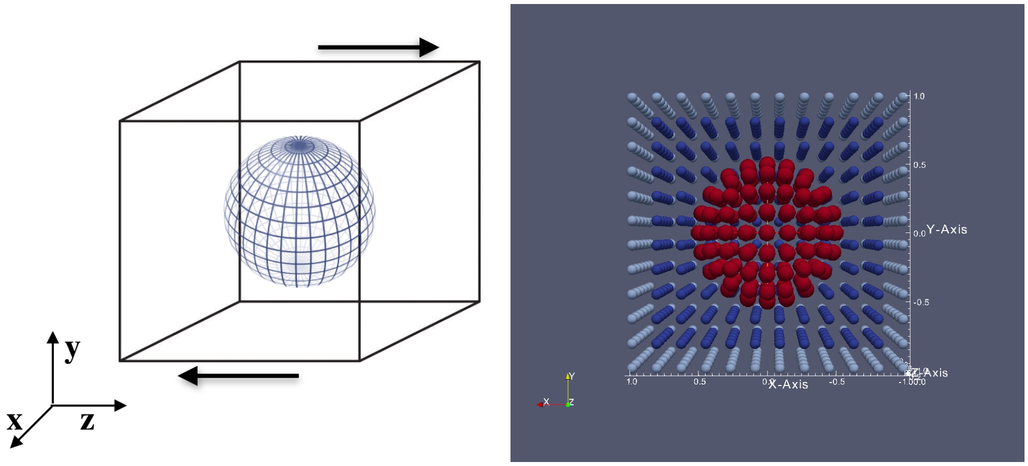

Figure 7.1: Configuration for a GMLS simulation of a sphere in Stokes flow. Dirichlet boundary conditions are imposed on the particles on the edges of the domain (light blue) to enforce the shear flow. The edge of the sphere is represented by red particles.

7.1.3.1 Sphere in shear flow

First, we consider a sphere with radius 1/2 in a box with side length 1 where the top and bottom walls have a given velocity to represent a shear flow. The Dirichlet boundary conditions

$$\mathbf{u} = (0, 0, y)$$

are enforced on the boundary of the domain $\partial\Omega$. In this case, the exact angular velocity of the sphere is $\omega_x = 0.5$.

The GMLS results are shown in fig. 7.2 and table 7.1. In fig. 7.2 the GMLS collocation points are color coded by their velocity in the streamwise direction, $\mathbf{u}_z$. The GMLS simulations are able to very accurately solve for the particle angular velocity with even only 12^3 GMLS collocation points.

(a) $N = 12$ (b) $N = 24$

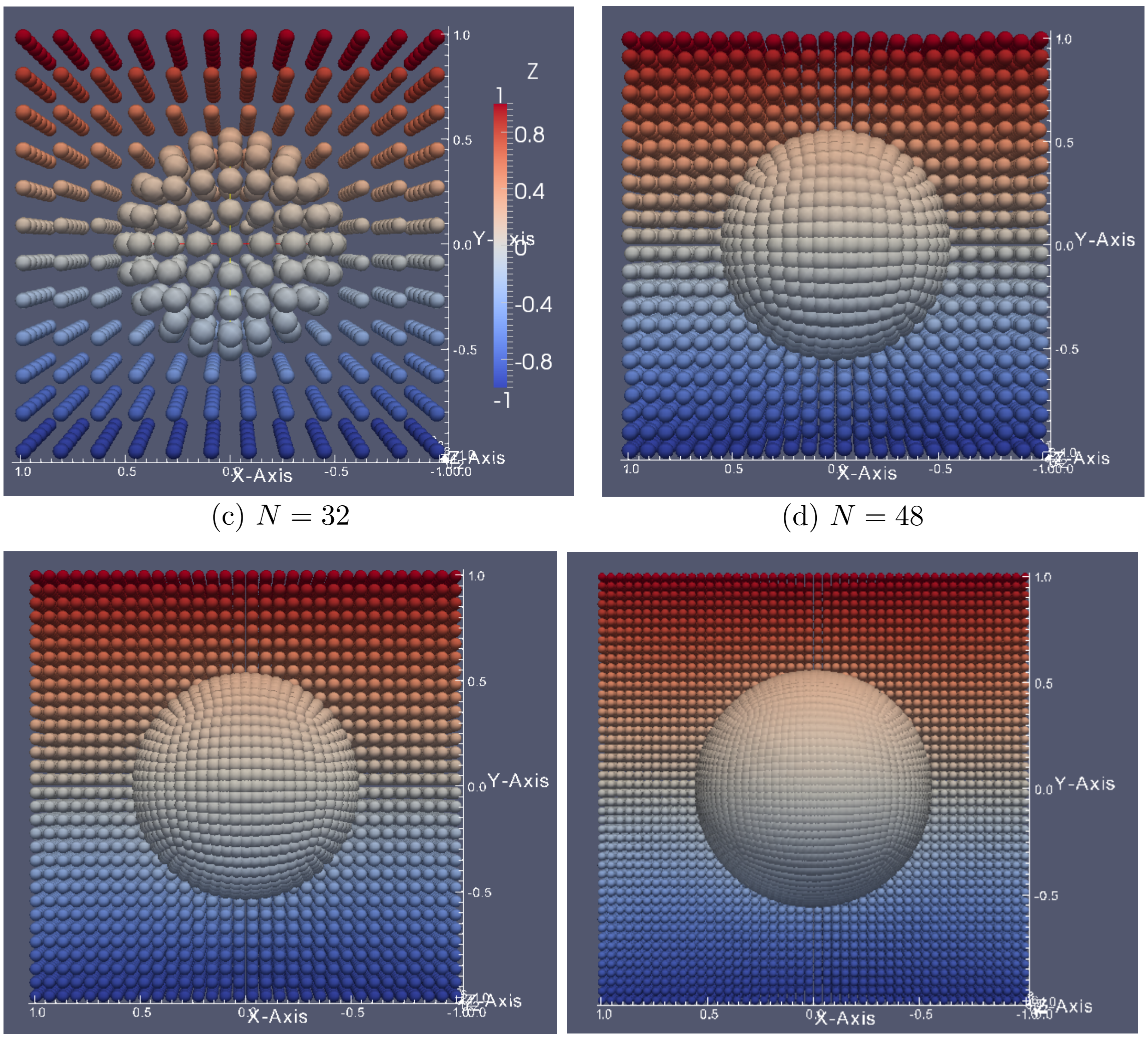

(c) $N = 32$ (d) $N = 48$

Figure 7.2: GMLS results for a sphere in a shear flow.

N	Ω_x
12	0.500684
24	0.496785
32	0.500149
48	0.499069

Table 7.1: GMLS angular particle velocity for a sphere in shear flow. The number of GMLS collocation points in the simulation is N^3. The exact solution is $\omega_x = 0.5$.

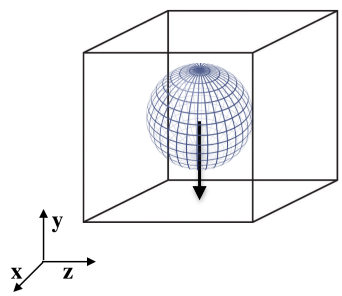

Figure 7.3: Configuration for a GMLS simulation of a sphere settling in Stokes flow.

7.1.3.2 Sphere settling in a box

We consider a sphere with radius $a = 0.25$ settling in a box with side length 1 by imposing a body force on the sphere,

$$\mathbf{F} = (0, -6\pi\mu a U_0, 0),$$

shown in fig. 7.3. In this case, it requires $N = 48^3$ GMLS collocation points to capture the recirculation in the fluid that occurs due to the movement of the sphere. With fewer GMLS collocation points, there is not enough resolution between the sphere and the edge of the domain to capture the dynamics of the fluid. The results are shown in fig. 7.4.

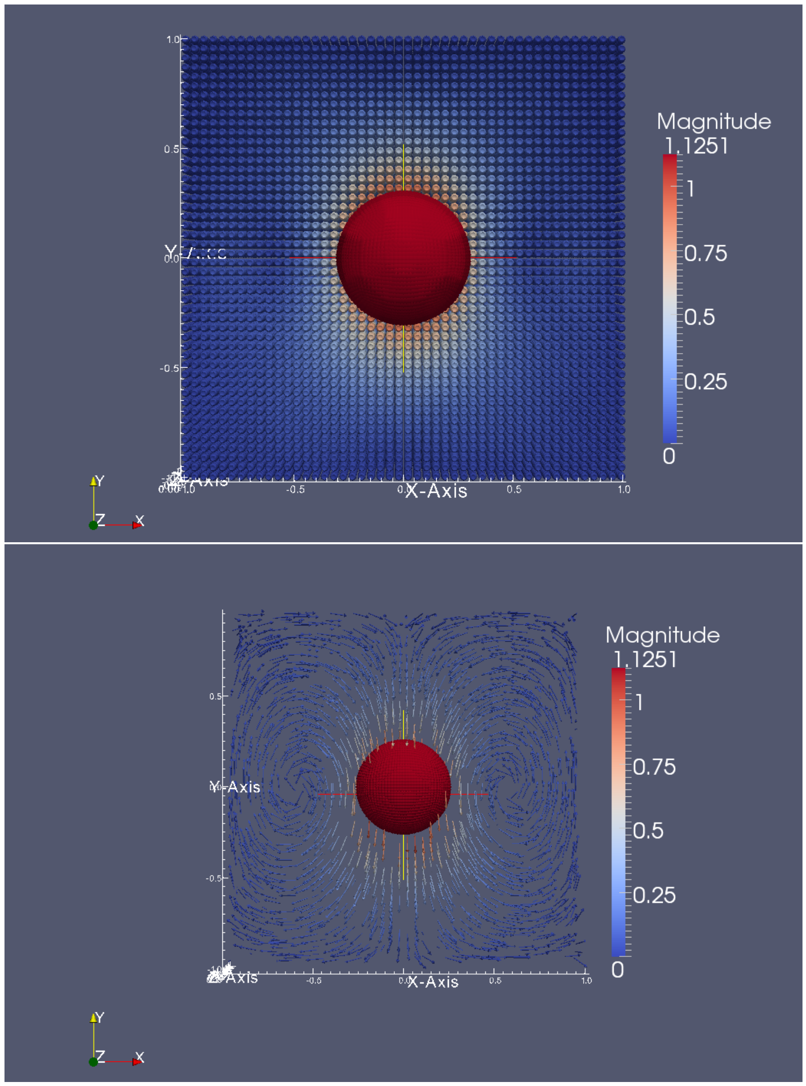

Figure 7.4: GMLS results for a sphere in settling in a box a shear flow. (Left) GMLS collocation points color-coded by the magnitude of their velocities. (Right) Vectors plotted at each GMLS collocation points showing the direction of the velocity, color indicates the magnitude of the velocity at the point.

Chapter Eight

Conclusion

8.1 Summary and discussion

The main objective of this thesis is to investigate irreversible particle motions in suspension shear flows. To that goal, we have used simulations of a number of inhomogenous systems, where particles have either different properties or are not distributed evenly in the domain. Each of these systems gives insight into the particle dynamics.

A great body of literature over the past seventy years has been devoted to homogeneous suspensions both through simulations and experiments. However, these idealized systems do not correspond to industrial and physical applications, where suspended particles may have very diverse properties. We will summarize the major results of each chapter below.

In chapter 2, we discussed the particle contact force as implemented in FCM. There is strong evidence that particle self-diffusivity in homogenous systems can be attributed to particle surface asperities in experiments (Pham et al., 2015, 2016). In FCM, this surface roughness is represented by a short-range contact force between the particles, which causes two particles interacting in a shear flow to be displaced across streamlines after they come into contact. We also investigated the force chains that develop in a wall bounded Couette flow due to the contact force. In the case of high volume fractions, half the particles are members of a large force chain which spans the channel.

Chapters 3 and 4 considered cases where the particles were inhomogeneously distributed in the channel, surrounded by a region of pure fluid. In chapter 3, the particles are seeded a plug in half the channel in the spanwise direction and subjected to an oscillating pressure gradient. Particles at the leading edge of the plug are free to move into the pure fluid, resulting in particles advancing along the walls while the core of the plug remains in the same streamwise position after many oscillations. Particle motion in the cross-stream direction at the front of the plug occurs when particles come into contact, due to the effects of the contact force. This leads to discrete particle motion after contact instead of a continuous migration. In chapter 4 the particles are seeded in a cylinder or sphere, with pure fluid on all sides. The FCM simulations agree quite well with experiments by Metzger and Butler (2012). At high enough strain amplitude the particles extend out of the initial footprint of the cloud through two different effects. The first is through interparticle contacts, which force particles towards the channel walls. The second is that the cloud acts as a dense porous body, which partially blocks the fluid flow. This creates a circular flow that rotates the cloud as a solid body. At very high volume fraction this effect is strong enough to cause "arms" to extend off the body of the cloud. The clouds also demonstrate the importance of three-body irreversibility, where two particles that come into contact may displace a third particle through lubrication forces only. In both these studies, a key parameter is the particle contact pressure. It is shown that the strain amplitude must be high enough that the contact pressure can develop fully during each half oscillation in order for irreversible particle dynamics to occur.

Chapter 5 considers the dynamics of a developing homogeneous suspension in both steady and oscillating Poiseuille flows. It is shown that while the volume fraction may reach a steady profile, the contacts between the particles continue to evolve on a longer time scale as the contact pressure between the particles relaxes. Results are compared to the Suspension Balance Model (Nott and Brady, 1994, Morris and Boulay, 1999, Nott et al., 2011, Miller and Morris, 2006).

In chapter 6, we look at bidisperse suspensions with the motivating question of at which size ratio the rheology of a bidisperse suspension is significantly different from that of a monodisperse suspension. In Couette flows, the bidisperse suspensions are indistinguishable from monodisperse suspensions, possibly because the maximum volume fraction does not change substantially as the particle size ratio is varied for the particle sizes considered in this study. For Poiseuille flow a significant difference is seen as shear-induced migration causes large particle enrichment at the channel centerline line, as previously seen in experiments (Lyon and Leal, 1998, Semwogerere and Weeks, 2008). This is the first set of three-dimensional simulations for non-Brownian bidisperse particles suspended in a channel flow.

Chapter 7 discusses Generalized Moving Least Squares as a new simulation tool for suspension flows. GMLS is a meshless method that can provide high-fidelity simulations of the full dynamics without having to explicitly incorporate terms such as the lubrication forces. The meshless method allows for simulations of complex, changing domains without the method being adapted to account for the boundaries.

8.2 Future directions

A number of future directions for study arise from this work. The first is to investigate adding a friction model to the FCM code. Many currently simulation methods do incorporate frictional forces between the particles (Townsend and Wilson, 2017, Gallier et al., 2014, Peters et al., 2016, Singh et al., 2018, Pednekar et al., 2018). These forces have been shown to change the rheology of the system, including increasing the relative viscosity, especially at very high volume fractions.

Many of the applications of bidisperse suspensions consider particles where the size ratios are much smaller than those considered here. It would be interesting to complete a similar study with $\lambda \leq 0.5$. In addition, many real-life systems are polydisperse. Because of the way the lubrication forces are calculated in FCM as presented here, it is necessary to compute some terms of the FCM corrections as a preprocessing step for each possible particle size ratio in the simulation because the terms are too time consuming to compute during the simulation, which resists the method to a finite number of particle sizes that must be known in advance. However, it may be possible that the exact size ratio could be approximated by binning the particles according to size to create a finite number of terms to precompute. As the lubrication resistance formulae vary smoothly with respect to λ, this would introduce a small error that may not be appreciable.

Developing GMLS into a tool for full-scale simulations continues to be an ongoing project in collaboration with Sandia National Laboratories through a Laboratory Directed Research and Development grant. The goal of the project is to build and release a complete package for multi-physics simulations with meshfree methods by providing C++ interfaces to external libraries in the Trilinos software library. Compadre provides a flexible structure for new computing architectures, as well as a stand-alone GMLS implementation with minimal dependencies. Remaining open questions include the most efficient pre-conditioners for each term of the GMLS Stokes flow implementation.

Appendix A

Analytical resistance functions

The resistance functions used in the simulations in chapter 6 use the analytical, theoretical forms of the resistance functions given in (Jeffrey and Onishi, 1984, Jeffrey, 1992, Kim and Karilla, 1991). Some references to these functions contain typographical errors, and the asymptotic values are not available for all particle size ratios. Here, we give the near-field, far-field, and FCM forms of the two-particle resistance functions for $\lambda = \frac{a_S}{a_L} = 0.5, 0.6, 0.72, 0.8, 0.9$, and 1.0.

MATLAB code to generate the FCM resistance functions and the order one corrections to the near-field resistance functions is available on the Brown Digital Repository (Howard, 2018).

A.1 FCM resistance functions

The FCM resistance functions are in the form

$$R = C_0 + C_1\epsilon + C_2\epsilon^2 + C_3\epsilon^3 + C_4\epsilon^4$$

where the coefficients C_i are found by inverting the FCM mobility matrix at a range of particle separations and finding the polynomial best fit to the resulting resistance functions.

A.2 Near-field resistance functions

The near-field resistance functions are of the form:

$$R = F(\epsilon) + \mathcal{O}(1)$$

where $\mathcal{O}(1)$ is an order one correction and $F(\epsilon)$ is an a function of the gap between the two particles.

X_A terms

$$\begin{aligned}
g_1(\lambda) &= 2\lambda^2/(1+\lambda)^3 \\
g_2(\lambda) &= \frac{\lambda}{5}\frac{(1+7\lambda+\lambda^2)}{(1+\lambda)^3} \\
g_3(\lambda) &= \frac{1}{42}\frac{(1+18\lambda-29\lambda^2+18\lambda^3+\lambda^4)}{(1+\lambda)^3}
\end{aligned}$$

$$\begin{aligned}
X_{11}^A &= g_1(\lambda)\frac{1}{\epsilon} + g_2(\lambda)\log(\epsilon^{-1}) + g_3(\lambda)\epsilon\log(\epsilon^{-1}) + \mathcal{O}(1) \\
X_{12}^A &= \frac{-2}{1+\lambda}\left[g_1(\lambda)\frac{1}{\epsilon} + g_2(\lambda)\log(\epsilon^{-1}) + g_3(\lambda)\epsilon\log(\epsilon^{-1})\right] + \mathcal{O}(1) \\
X_{22}^A &= g_1(1/\lambda)\frac{1}{\epsilon} + g_2(1/\lambda)\log(\epsilon^{-1}) + g_3(1/\lambda)\epsilon\log(\epsilon^{-1}) + \mathcal{O}(1) \\
X_{21}^A &= X_{12}^A
\end{aligned}$$

Y_A terms

$$\begin{aligned}
g_2(\lambda) &= 4\lambda/15(2+\lambda+2\lambda^2)/(1+\lambda)^3 \\
g_3(\lambda) &= 2/375(16-45\lambda+58\lambda^2-45\lambda^3+16\lambda^4)/(1+\lambda)^3 \\
Y_{11}^A &= g_2(\lambda)\log(\epsilon^{-1}) + g_3(\lambda)\epsilon\log(\epsilon^{-1}) + \mathcal{O}(1) \\
Y_{12}^A &= -\frac{2}{1+\lambda}\left[g_2(\lambda)\log(\epsilon^{-1}) + g_3(\lambda)\epsilon\log(\epsilon^{-1})\right] + \mathcal{O}(1) \\
Y_{11}^A &= g_2(1/\lambda)\log(\epsilon^{-1}) + g_3(1/\lambda)\epsilon\log(\epsilon^{-1}) + \mathcal{O}(1) \\
Y_{21}^A &= Y_{12}^A
\end{aligned}$$

Y_B terms

$$
\begin{aligned}
g_2(\lambda) &= -1/5\lambda(4+\lambda)/(1+\lambda)^2 \\
g_3(\lambda) &= -1/250(32-33\lambda+83\lambda^2+43\lambda^3)/(1+\lambda)^2
\end{aligned}
$$

$$
\begin{aligned}
Y_{11}^B &= \frac{2}{3}\left[g_2(\lambda)\log(\epsilon^{-1}) + g_3(\lambda)\epsilon\log(\epsilon^{-1})\right] + \mathcal{O}(1) \\
Y_{12}^B &= \frac{-4}{(1+\lambda)^2}\frac{2}{3}\left[g_2(\lambda)\log(\epsilon^{-1}) + g_3(\lambda)\epsilon\log(\epsilon^{-1})\right] + \mathcal{O}(1) \\
Y_{22}^B &= \frac{2}{3}\left[g_2(1/\lambda)\log(\epsilon^{-1}) + g_3(1/\lambda)\epsilon\log(\epsilon^{-1})\right] + \mathcal{O}(1) \\
Y_{21}^B &= \frac{-4}{(1+(1/\lambda))^2}\frac{2}{3}\left[g_2(1/\lambda)\log(\epsilon^{-1}) + g_3(1/\lambda)\epsilon\log(\epsilon^{-1})\right] + \mathcal{O}(1)
\end{aligned}
$$

X_C terms

$$
\begin{aligned}
X_{11}^C &= -\frac{\lambda^2}{4(1+\lambda)}\epsilon\log(\epsilon^{-1}) + \mathcal{O}(1) \\
X_{12}^C &= \frac{2\lambda^2}{(1+\lambda)^4}\epsilon\log(\epsilon^{-1}) + \mathcal{O}(1) \\
X_{22}^C &= -\frac{(1/\lambda)^2}{4(1+1/\lambda)}\epsilon\log(\epsilon^{-1}) + \mathcal{O}(1) \\
X_{21}^C &= X_{12}^C
\end{aligned}
$$

Y_C terms

$$
\begin{aligned}
g_2(\lambda) &= \frac{2\lambda}{5(1+\lambda)} \\
g_3(\lambda) &= \frac{(8+6\lambda+33\lambda^2)}{125(1+\lambda)} \\
g_4(\lambda) &= \frac{4\lambda^2}{5(1+\lambda)^4} \\
g_5(\lambda) &= \frac{2\lambda(43-24\lambda+43\lambda^2)}{125(1+\lambda)^4}
\end{aligned}
$$

$$
\begin{aligned}
Y_{11}^C &= g_2(\lambda)\log(\epsilon^{-1}) + g_3(\lambda)\epsilon\log(\epsilon^{-1}) + \mathcal{O}(1) \\
Y_{12}^C &= g_4(\lambda)\log(\epsilon^{-1}) + g_5(\lambda)\epsilon\log(\epsilon^{-1}) + \mathcal{O}(1) \\
Y_{22}^C &= g_2(1/\lambda)\log(\epsilon^{-1}) + g_3(1/\lambda)\epsilon\log(\epsilon^{-1}) + \mathcal{O}(1) \\
Y_{21}^C &= Y_{12}^C
\end{aligned}
$$

The correction to g_5 comes from Ladd (1990).

X_G terms

$$
\begin{aligned}
g_1(\lambda) &= \frac{3\lambda^2}{(1+\lambda)^3} \\
g_2(\lambda) &= \frac{3\lambda(1+12\lambda-4\lambda^2)}{10(1+\lambda)^3} \\
g_3(\lambda) &= \frac{(5+181\lambda-453\lambda^2+566\lambda^3-65\lambda^4)}{140(1+\lambda)^3}
\end{aligned}
$$

$$
\begin{aligned}
X_{11}^G &= \frac{2}{3}\left[g_1(\lambda)\frac{1}{\epsilon} + g_2(\lambda)\log(\epsilon^{-1}) + g_3(\lambda)\epsilon\log(\epsilon^{-1})\right] + \mathcal{O}(1) \\
X_{12}^G &= \frac{-8}{3(1+\lambda)^2}\left[g_1(\lambda)\frac{1}{\epsilon} + g_2(\lambda)\log(\epsilon^{-1}) + g_3(\lambda)\epsilon\log(\epsilon^{-1})\right] + \mathcal{O}(1) \\
X_{22}^G &= \frac{2}{3}\left[g_1(1/\lambda)\frac{1}{\epsilon} + g_2(1/\lambda)\log(\epsilon^{-1}) + g_3(1/\lambda)\epsilon\log(\epsilon^{-1})\right] + \mathcal{O}(1) \\
X_{21}^G &= \frac{-8}{3(1+1/\lambda)^2}\left[g_1(1/\lambda)\frac{1}{\epsilon} + g_2(1/\lambda)\log(\epsilon^{-1}) + g_3(1/\lambda)\epsilon\log(\epsilon^{-1})\right] + \mathcal{O}(1)
\end{aligned}
$$

Y_G terms

$$
\begin{aligned}
g_2(\lambda) &= \frac{\lambda(4-\lambda+7\lambda^2)}{10(1+\lambda)^3} \\
g_3(\lambda) &= \frac{(32-179\lambda+532\lambda^2-356\lambda^3+221\lambda^4)}{500(1+\lambda)^3}
\end{aligned}
$$

$$
\begin{aligned}
Y_{11}^{G} &= \frac{2}{3}\left[g_2(\lambda)\log(\epsilon^{-1}) + g_3(\lambda)\epsilon\log(\epsilon^{-1})\right] + \mathcal{O}(1) \\
Y_{12}^{G} &= \frac{-8}{3(1+\lambda)^2}\left[g_2(\lambda)\log(\epsilon^{-1}) + g_3(\lambda)\epsilon\log(\epsilon^{-1})\right] + \mathcal{O}(1) \\
Y_{22}^{G} &= \frac{2}{3}\left[g_2(1/\lambda)\log(\epsilon^{-1}) + g_3(1/\lambda)\epsilon\log(\epsilon^{-1})\right] + \mathcal{O}(1) \\
Y_{21}^{G} &= \frac{-8}{3(1+1/\lambda)^2}\left[g_2(1/\lambda)\log(\epsilon^{-1}) + g_3(1/\lambda)\epsilon\log(\epsilon^{-1})\right] + \mathcal{O}(1)
\end{aligned}
$$

Y_H terms

$$
\begin{aligned}
g_2(\lambda) &= \frac{\lambda(2-\lambda)}{10(1+\lambda)^2} \\
g_3(\lambda) &= \frac{(16 - 61\lambda + 180\lambda^2 + 2\lambda^3)}{500(1+\lambda)^2} \\
g_4(\lambda) &= \frac{\lambda^2(1+7\lambda)}{20(1+\lambda)^2} \\
g_5(\lambda) &= \frac{\lambda(43 + 147\lambda - 185\lambda^2 + 221\lambda^3)}{1000(1+\lambda)^2}
\end{aligned}
$$

$$
\begin{aligned}
Y_{11}^{H} &= g_2(\lambda)\log(\epsilon^{-1}) + g_3(\lambda)\epsilon\log(\epsilon^{-1}) + \mathcal{O}(1) \\
Y_{12}^{H} &= \frac{8}{(1+\lambda)^3}\left[g_4(\lambda)\log(\epsilon^{-1}) + g_5(\lambda)\epsilon\log(\epsilon^{-1})\right] + \mathcal{O}(1) \\
Y_{22}^{H} &= g_2(1/\lambda)\log(\epsilon^{-1}) + g_3(1/\lambda)\epsilon\log(\epsilon^{-1}) + \mathcal{O}(1) \\
Y_{21}^{H} &= \frac{8}{(1+1/\lambda)^3}\left[g_4(1/\lambda)\log(\epsilon^{-1}) + g_5(1/\lambda)\epsilon\log(\epsilon^{-1})\right] + \mathcal{O}(1)
\end{aligned}
$$

X_M terms

$$
\begin{aligned}
g_1(\lambda) &= \frac{6\lambda^2}{5(1+\lambda)^3} \\
g_2(\lambda) &= \frac{3\lambda(1+17\lambda-9\lambda^2)}{25(1+\lambda)^3} \\
g_3(\lambda) &= \frac{(5+272\lambda-831\lambda^2+1322\lambda^3-415\lambda^4)}{350(1+\lambda)^3} \\
g_4(\lambda) &= \frac{6\lambda^3}{5(1+\lambda)^3} \\
g_5(\lambda) &= -\frac{3\lambda(4-17\lambda+4\lambda^2)}{25(1+\lambda)^3} \\
g_6(\lambda) &= -\frac{\lambda(65-832\lambda+1041\lambda^2-832\lambda^3+65\lambda^4)}{350(1+\lambda)^3}
\end{aligned}
$$

$$
\begin{aligned}
X_{11}^M &= g_1(\lambda)\frac{1}{\epsilon} + g_2(\lambda)\log(\epsilon^{-1}) + g_3(\lambda)\epsilon\log(\epsilon^{-1}) + \mathcal{O}(1) \\
X_{12}^M &= \frac{8}{(1+\lambda)^3}\left[g_4(\lambda)\frac{1}{\epsilon} + g_5(\lambda)\log(\epsilon^{-1}) + g_6(\lambda)\epsilon\log(\epsilon^{-1})\right] + \mathcal{O}(1) \\
X_{22}^M &= g_1(1/\lambda)\frac{1}{\epsilon} + g_2(1/\lambda)\log(\epsilon^{-1}) + g_3(1/\lambda)\epsilon\log(\epsilon^{-1}) + \mathcal{O}(1) \\
X_{21}^M &= X_{12}^M
\end{aligned}
$$

Y_M terms

$$
\begin{aligned}
g_2(\lambda) &= \frac{6\lambda(1-\lambda+4\lambda^2)}{25(1+\lambda)^3} \\
g_3(\lambda) &= \frac{3(8-67\lambda+294\lambda^2-394\lambda^3+197\lambda^4)}{625(1+\lambda)^3} \\
g_4(\lambda) &= \frac{3\lambda^2(7-10\lambda+7\lambda^2)}{50(1+\lambda)^3} \\
g_5(\lambda) &= \frac{3\lambda(221-728\lambda+1902\lambda^2-728\lambda^3+221\lambda^4)}{2500(1+\lambda)^3}
\end{aligned}
$$

The coefficients from g_5 come from Jeffrey (1992), note the correction to Kim and Karilla (1991).

$$
\begin{aligned}
Y_{11}^M &= g_2(\lambda)\log(\epsilon^{-1}) + g_3(\lambda)\epsilon\log(\epsilon^{-1}) + \mathcal{O}(1) \\
Y_{12}^M &= \frac{8}{(1+\lambda)^3}\left[g_4(\lambda)\log(\epsilon^{-1}) + g_5(\lambda)\epsilon\log(\epsilon^{-1})\right] + \mathcal{O}(1) \\
Y_{22}^M &= g_2(1/\lambda)\log(\epsilon^{-1}) + g_3(1/\lambda)\epsilon\log(\epsilon^{-1}) + \mathcal{O}(1) \\
Y_{21}^M &= Y_{12}^M
\end{aligned}
$$

A.3 Far-field resistance functions

The far-field resistance functions are of the form

$$R_{jk} = \sum_{i=0}^{11} C_i R_j^i$$

where $R_j = \frac{a_i}{2(\epsilon+a_1+a_2)}$. The coefficients are given below. For the sake of succinctness, only non-zero coefficients are given. The far-field forms for X^G, X^M, and Y^M are not used, but can be represented in a similar manner using the formulae in Kim and Karilla (1991).

X_A terms

$$
\begin{aligned}
X_{11}^A &= C_0(\lambda) + C_2(\lambda)R_1^2 + C_4(\lambda)R_1^4 + C_6(\lambda)R_1^6 + C_8(\lambda)R_1^8 + C_{10}(\lambda)R_1^{10} \\
X_{12}^A &= \frac{-2}{1+\lambda}\left[C_1(\lambda)R_1 + C_3(\lambda)R_1^3 + C_5(\lambda)R_1^5 + C_7(\lambda)R_1^7 + C_9(\lambda)R_1^9 + C_{11}(\lambda)R_1^{11}\right] \\
X_{22}^A &= C_0(1/\lambda) + C_2(1/\lambda)R_2^2 + C_4(1/\lambda)R_2^4 + C_6(1/\lambda)R_2^6 + C_8(1/\lambda)R_2^8 + C_{10}(1/\lambda)R_2^{10} \\
X_{21}^A &= X_{12}^A
\end{aligned}
$$

$$
\begin{aligned}
C_0 &= 1 \\
C_2 &= 9\lambda \\
C_4 &= -24\lambda + 81\lambda^2 + 36\lambda^3 \\
C_6 &= 16\lambda + 108\lambda^2 + 281\lambda^3 + 648\lambda^4 + 144\lambda^5 \\
C_8 &= 576\lambda^2 + 4848\lambda^3 + 5409\lambda^4 + 4524\lambda^5 + 3888\lambda^6 + 576\lambda^7 \\
C_{10} &= 2304\lambda^2 + 20736\lambda^3 + 42804\lambda^4 + 115849\lambda^5 + 76176\lambda^6 + 39264\lambda^7 \\
&\quad +20736\lambda^8 + 2304\lambda^9 \\
C_1 &= 3.0\lambda \\
C_3 &= -4.0\lambda + 27\lambda^2 - 4\lambda^3 \\
C_5 &= 72\lambda^2 + 243\lambda^3 + 72\lambda^4 \\
C_7 &= 288\lambda^2 + 1620\lambda^3 + 1515\lambda^4 + 1620\lambda^5 + 288\lambda^6 \\
C_9 &= 1152\lambda^2 + 9072\lambda^3 + 14752\lambda^4 + 26163\lambda^5 + 14752\lambda^6 + 9072\lambda^7 + 1152\lambda^8) \\
C_{11} &= 4608\lambda^2 + 46656\lambda^3 + 108912\lambda^4 + 269100\lambda^5 + 319899\lambda^6 + 269100\lambda^7 \\
&\quad +108912\lambda^8 + 46656\lambda^9 + 4608\lambda^{10}
\end{aligned}
$$

Y_A **terms**

$$
\begin{aligned}
Y_{11}^A &= C_0(\lambda) + C_2(\lambda)R_1^2 + C_4(\lambda)R_1^4 + C_6(\lambda)R_1^6 + C_8(\lambda)R_1^8 + C_{10}(\lambda)R_1^{10} \\
Y_{12}^A &= \frac{-2}{1+\lambda}\left[C_1(\lambda)R_1 + C_3(\lambda)R_1^3 + C_5(\lambda)R_1^5 + C_7(\lambda)R_1^7 + C_9(\lambda)R_1^9 + C_{11}(\lambda)R_1^{11}\right] \\
Y_{22}^A &= C_0(1/\lambda) + C_2(1/\lambda)R_2^2 + C_4(1/\lambda)R_2^4 + C_6(1/\lambda)R_2^6 + C_8(1/\lambda)R_2^8 + C_{10}(1/\lambda)R_2^{10} \\
Y_{21}^A &= Y_{12}^A
\end{aligned}
$$

$$
\begin{aligned}
C_0 &= 1 \\
C_2 &= 9/4\lambda \\
C_4 &= 1/16(96\lambda + 81\lambda^2 + 288\lambda^3) \\
C_6 &= 1/64(256\lambda + 3456\lambda^2 + 1241\lambda^3 + 5184\lambda^4 + 4608\lambda^5) \\
C_8 &= 1/256(71424 + 136352\lambda + 126369\lambda^2 - 3744\lambda^3 + 165888\lambda^4 + 73728\lambda^5)\lambda^2 \\
C_{10} &= 1/1024(1179648 + 2011392\lambda + 6303168\lambda^2 + 10548393\lambda^3 + 8654976\lambda^4 \\
&\quad -179712\lambda^5 + 3981312\lambda^6 + 1179648\lambda^7)\lambda^2 \\
C_1 &= 3/2\lambda \\
C_3 &= 1/8(16 + 27\lambda + 16\lambda^2)\lambda \\
C_5 &= 1/32(1008 + 243\lambda + 1008\lambda^2)\lambda^2 \\
C_7 &= 1/128(18432 + 16848\lambda + 19083\lambda^2 + 16848\lambda^3 + 18432\lambda^4)\lambda^2 \\
C_9 &= 1/512(294912 + 580608\lambda + 967088\lambda^2 + 766179\lambda^3 + 967088\lambda^4 + 580608\lambda^5 \\
&\quad +294912\lambda^6)\lambda^2 \\
C_{11} &= 1/2048(4718592 + 14598144\lambda + 22600704\lambda^2 + 43912080\lambda^3 + 95203835\lambda^4 \\
&\quad +43912080\lambda^5 + 22600704\lambda^6 + 14598144\lambda^7 + 4718592\lambda^8)\lambda^2
\end{aligned}
$$

Y_B **terms**

$$
\begin{aligned}
Y^B_{11} &= \frac{2}{3}\left[C_3(\lambda)R_1^3 + C_5(\lambda)R_1^5 + C_7(\lambda)R_1^7 + C_9(\lambda)R_1^9 + C_{11}(\lambda)R_1^{11}\right] \\
Y^B_{12} &= \frac{8}{3(1+\lambda)^2}\left[C_2(\lambda)R_1^2 + C_4(\lambda)R_1^4 + C_6(\lambda)R_1^6 + C_8(\lambda)R_1^8 + C_{10}(\lambda)R_1^{10}\right] \\
Y^B_{22} &= \frac{2}{3}\left[C_3(1/\lambda)R_2^3 + C_5(1/\lambda)R_2^5 + C_7(1/\lambda)R_2^7 + C_9(1/\lambda)R_2^9 + C_{11}(1/\lambda)R_2^{11}\right] \\
Y^B_{21} &= \frac{8}{3(1+1/\lambda)^2}[C_2(1/\lambda)R_2^2 + C_4(1/\lambda)R_2^4 + C_6(1/\lambda)R_2^6 + C_8(1/\lambda)R_2^8 \\
&\quad +C_{10}(1/\lambda)R_2^{10}]
\end{aligned}
$$

$$
\begin{aligned}
C_2 &= -6\lambda \\
C_4 &= -27/2\lambda^2 \\
C_6 &= 1/8(-864\lambda^2 - 243\lambda^3 - 576\lambda^4) \\
C_8 &= 1/32(-13824 - 15552\lambda - 77451\lambda^2 - 12960\lambda^3 - 9216\lambda^4)\lambda^2 \\
C_{10} &= 1/128(-221184 - 497664\lambda - 1905696\lambda^2 - 1125603\lambda^3 - 2816256\lambda^4 \\
&\quad -373248\lambda^5 - 147456\lambda^6)\lambda^2 \\
C_3 &= -9\lambda \\
C_5 &= 1/4(-48 - 81\lambda - 144\lambda^2)\lambda \\
C_7 &= 1/16(-3024 - 8409\lambda - 3888\lambda^2 - 2304\lambda^3)\lambda^2 \\
C_9 &= 1/64(-55296 - 50544\lambda - 283041\lambda^2 - 488400\lambda^3 - 103680\lambda^4 - 36864\lambda^5)\lambda^2 \\
C_{11} &= 1/256(-884736 - 1741824\lambda - 9831696\lambda^2 - 4579497\lambda^3 - 8586864\lambda^4 \\
&\quad -18941184\lambda^5 - 2322432\lambda^6 - 589824\lambda^6)\lambda^2
\end{aligned}
$$

X_C terms

$$
\begin{aligned}
X_{11}^C &= C_0(\lambda) + C_6(\lambda)R_1^6 + C_8(\lambda)R_1^8 + C_{10}(\lambda)R_1^{10} \\
X_{12}^C &= \frac{8}{(1+\lambda)^3}\left[C_3(\lambda)R_1^3 + C_9(\lambda)R_1^9 + C_{11}(\lambda)R_1^{11}\right] \\
X_{22}^C &= C_0(1/\lambda) + C_6(1/\lambda)R_2^6 + C_8(1/\lambda)R_2^8 + C_{10}(1/\lambda)R_2^{10} \\
X_{21}^C &= X_{12}^C
\end{aligned}
$$

$$
\begin{aligned}
C_0 &= 1.0 \\
C_6 &= 64\lambda^3 \\
C_8 &= 768\lambda^5 \\
C_{10} &= 6144\lambda^7 \\
C_3 &= 8\lambda^3 \\
C_9 &= 512\lambda^6 \\
C_{11} &= (6144 + 6144\lambda^2)\lambda^6
\end{aligned}
$$

Y_C terms

$$
\begin{aligned}
Y_{11}^C &= C_0(\lambda) + C_4(\lambda)R_1^4 + C_6(\lambda)R_1^6 + C_8(\lambda)R_1^8 + C_{10}(\lambda)R_1^{10} \\
Y_{12}^C &= \frac{-8}{(1+\lambda)^3}\left[C_3(\lambda)R_1^3 + C_5(\lambda)R_1^5 + C_7(\lambda)R_1^7 + C_9(\lambda)R_1^9 + C_{11}(\lambda)R_1^{11}\right] \\
Y_{22}^C &= C_0(1/\lambda) + C_4(1/\lambda)R_2^4 + C_6(1/\lambda)R_2^6 + C_8(1/\lambda)R_2^8 + C_{10}(1/\lambda)R_2^{10} \\
Y_{21}^C &= Y_{12}^C
\end{aligned}
$$

$$
\begin{aligned}
C_0 &= 1 \\
C_4 &= 12\lambda \\
C_6 &= (27 + 256\lambda)\lambda^2 \\
C_8 &= 1/4(864 + 243\lambda + 864\lambda^2 + 9984\lambda^3)\lambda^2 \\
C_{10} &= 1/16(13824 + 15552\lambda + 151179\lambda^2 + 15552\lambda^3 + 20736\lambda^4 + 294912\lambda^5)\lambda^2 \\
C_3 &= 4\lambda^3 \\
C_5 &= 18\lambda^4 \\
C_7 &= 1/2(144 + 81\lambda + 144\lambda^2)\lambda^4 \\
C_9 &= 1/8(2304 + 3888\lambda - 6439\lambda^2 + 3888\lambda^3 + 2304\lambda^4)\lambda^4 \\
C_{11} &= 1/32(36864 + 103680\lambda - 175152\lambda^2 + 518049\lambda^3 - 175152\lambda^4 + 103680\lambda^5 \\
&\quad +36864\lambda^6)\lambda^4
\end{aligned}
$$

Y_G terms

$$
\begin{aligned}
Y_{11}^G &= \frac{2}{3}\left[C_5(\lambda)R_1^5 + C_7(\lambda)R_1^7 + C_9(\lambda)R_1^9 + C_{11}(\lambda)R_1^{11}\right] \\
Y_{12}^G &= \frac{-8}{3(1+\lambda)^2}\left[C_4(\lambda)R_1^4 + C_6(\lambda)R_1^6 + C_8(\lambda)R_1^8 + C_{10}(\lambda)R_1^{10}\right] \\
Y_{22}^G &= \frac{2}{3}\left[C_5(1/\lambda)R_2^5 + C_7(1/\lambda)R_2^7 + C_9(1/\lambda)R_2^9 + C_{11}(1/\lambda)R_1^{11}\right] \\
Y_{21}^G &= \frac{-8}{3(1+1/\lambda)^2}\left[C_4(1/\lambda)R_2^4 + C_6(1/\lambda)R_2^6 + C_8(1/\lambda)R_2^8 + C_{10}(1/\lambda)R_1^{10}\right]
\end{aligned}
$$

$$
\begin{aligned}
C_4 &= 12\lambda + 20\lambda^3 \\
C_6 &= 27\lambda^2 + 135\lambda^4 \\
C_8 &= (216 + 243/4\lambda - 1008\lambda^2 + 1215/4\lambda^3 + 1080\lambda^4)\lambda^2 \\
C_{10} &= (864 + 972\lambda + 42123/16\lambda^2 + 648\lambda^3 - 96073/16\lambda^4 + 4860\lambda^5 + 6240\lambda^6)\lambda^2 \\
C_5 &= (18 + 90\lambda^2)\lambda \\
C_7 &= (24 + 81/2\lambda - 336\lambda^2 + 405/2\lambda^3 + 600\lambda^4)\lambda \\
C_9 &= (378 + 21209/8\lambda - 972\lambda^2 - 62147/8\lambda^3 + 2970\lambda^4 + 3360\lambda^5)\lambda^2 \\
C_{11} &= (1728 + 3158/2\lambda + 103329/32\lambda^2 + 69387\lambda^3 + 763173/32\lambda^4 - 166737/2\lambda^5 \\
&\quad +24840\lambda^6 + 17280\lambda^7)\lambda^2
\end{aligned}
$$

Y_H terms

$$
\begin{aligned}
Y_{11}^H &= C_6(\lambda)R_1^6 + C_8(\lambda)R_1^8 + C_{10}(\lambda)R_1^{10} \\
Y_{12}^H &= \frac{8}{(1+\lambda)^3}\left[C_3(\lambda)R_1^3 + C_7(\lambda)R_1^7 + C_9(\lambda)R_1^9 + C_{11}(\lambda)R_1^{11}\right] \\
Y_{22}^H &= C_6(1/\lambda)R_2^6 + C_8(1/\lambda)R_2^8 + C_{10}(1/\lambda)R_2^{10} \\
Y_{21}^H &= \frac{8}{(1+1/\lambda)^3}\left[C_3(1/\lambda)R_2^3 + C_7(1/\lambda)R_2^7 + C_9(1/\lambda)R_2^9 + C_{11}(1/\lambda)R_2^{11}\right]
\end{aligned}
$$

$$
\begin{aligned}
C_6 &= 24\lambda - 120\lambda^3 \\
C_8 &= 54\lambda^2 + 1280\lambda^3 + 270\lambda^4 - 1280\lambda^5 \\
C_{10} &= 432\lambda^2 + 243/2\lambda^3 + -1872\lambda^4 + 46015/2\lambda^5 + 2880\lambda^6 - 9600\lambda^7 \\
C_3 &= 10\lambda^3 \\
C_7 &= (36 + 180\lambda^2)\lambda^4 \\
C_9 &= 144\lambda^4 + 81\lambda^5 + 5248\lambda^6 + 405\lambda^7 + 1200\lambda^8 \\
C_{11} &= (576 + 972\lambda + 153049/4\lambda^2 - 864\lambda^3 + 186173/4\lambda^4 + 5940\lambda^5 \\
&\quad +6720\lambda^6)\lambda^4
\end{aligned}
$$

	C_0	C_1	C_2	C_3	C_4
X_{11}^A	2.3556	-2.655	3.3299	-2.4352	0.75645
X_{12}^A	-1.7151	2.7145	-3.3332	2.4342	-0.75624
X_{22}^A	2.3556	-2.655	3.3299	-2.4352	0.75645
X_{21}^A	-1.7151	2.7145	-3.3332	2.4342	-0.75624
Y_{11}^A	1.3344	-0.62106	0.74206	-0.52562	0.16026
Y_{12}^A	-0.61067	0.70759	-0.75616	0.52256	-0.15862
Y_{22}^A	1.3344	-0.62106	0.74206	-0.52562	0.16026
Y_{21}^A	-0.61067	0.70759	-0.75616	0.52256	-0.15862
Y_{11}^B	-0.19933	0.4374	-0.54382	0.38414	-0.11572
Y_{12}^B	0.35272	-0.52404	0.55739	-0.37465	0.11153
Y_{22}^B	-0.19933	0.4374	-0.54382	0.38414	-0.11572
Y_{21}^B	0.35272	-0.52404	0.55739	-0.37465	0.11153
X_{11}^C	1.0151	-0.041369	0.055947	-0.040527	0.01225
X_{12}^C	-0.12408	0.17789	-0.15103	0.079858	-0.019737
X_{22}^C	1.0151	-0.041369	0.055947	-0.040527	0.01225
X_{21}^C	-0.12408	0.17789	-0.15103	0.079858	-0.019737
Y_{11}^C	1.1251	-0.30608	0.38482	-0.26563	0.077822
Y_{12}^C	0.096307	-0.18097	0.19931	-0.13043	0.037692
Y_{22}^C	1.1251	-0.30608	0.38482	-0.26563	0.077822
Y_{21}^C	0.096307	-0.18097	0.19931	-0.13043	0.037692
X_{11}^G	0.96486	-2.0037	2.4164	-1.691	0.50937
X_{12}^G	-1.1629	2.0657	-2.4205	1.6918	-0.5107
X_{22}^G	0.96486	-2.0037	2.4164	-1.691	0.50937
X_{21}^G	-1.1629	2.0657	-2.4205	1.6918	-0.5107
Y_{11}^G	0.081377	-0.21063	0.27965	-0.20247	0.061548
Y_{12}^G	-0.11086	0.23958	-0.28461	0.1949	-0.057877
Y_{22}^G	0.081377	-0.21063	0.27965	-0.20247	0.061548
Y_{21}^G	-0.11086	0.23958	-0.28461	0.1949	-0.057877
Y_{11}^H	0.016363	-0.065683	0.10778	-0.085874	0.027182
Y_{12}^H	0.16935	-0.25935	0.23489	-0.13141	0.034041
Y_{22}^H	0.016363	-0.065683	0.10778	-0.085874	0.027182
Y_{21}^H	0.16935	-0.25935	0.23489	-0.13141	0.034041
X_{11}^M	-1.4228	0.90554	-1.0411	0.68645	-0.19748
X_{11}^M	-0.59044	0.93806	-0.94627	0.59988	-0.17176
X_{22}^M	-1.4228	0.90554	-1.0411	0.68645	-0.19748
X_{21}^M	-0.59044	0.93806	-0.94627	0.59988	-0.17176
Y_{11}^M	-1.0785	0.19696	-0.25443	0.18091	-0.054354
Y_{12}^M	0.080677	0.036141	-0.12664	0.095514	-0.026815
Y_{22}^M	-1.0785	0.19696	-0.25443	0.18091	-0.054354
Y_{21}^M	0.080677	0.036141	-0.12664	0.095514	-0.026815

Table A.1: FCM resistance functions for $\lambda = 1.0$

	C_0	C_1	C_2	C_3	C_4
X_{11}^A	2.3097	-2.6526	3.4166	-2.5425	0.79818
X_{12}^A	-1.698	2.7886	-3.5188	2.6147	-0.82085
X_{22}^A	2.3738	-2.8096	3.6267	-2.6989	0.84701
X_{21}^A	-1.698	2.7886	-3.5188	2.6147	-0.82085
Y_{11}^A	1.3251	-0.62502	0.76744	-0.55349	0.17063
Y_{12}^A	-0.60816	0.7361	-0.81192	0.57229	-0.17576
Y_{22}^A	1.3411	-0.66789	0.82854	-0.60059	0.18559
Y_{21}^A	-0.60816	0.7361	-0.81192	0.57229	-0.17576
Y_{11}^B	-0.20412	0.46533	-0.59692	0.43088	-0.13159
Y_{12}^B	0.31381	-0.48457	0.53018	-0.36295	0.10927
Y_{22}^B	-0.19208	0.44274	-0.57046	0.41214	-0.12581
Y_{21}^B	0.39018	-0.60867	0.67156	-0.46168	0.13922
X_{11}^C	1.0149	-0.042843	0.060063	-0.044616	0.013707
X_{12}^C	-0.12299	0.18518	-0.16421	0.089794	-0.022706
X_{22}^C	1.0149	-0.042843	0.060063	-0.044616	0.013707
X_{21}^C	-0.12299	0.18518	-0.16421	0.089794	-0.022706
Y_{11}^C	1.1315	-0.33626	0.43964	-0.3125	0.093383
Y_{12}^C	0.09511	-0.18649	0.2121	-0.14161	0.041379
Y_{22}^C	1.1169	-0.29905	0.38833	-0.27369	0.081184
Y_{21}^C	0.09511	-0.18649	0.2121	-0.14161	0.041379
X_{11}^G	0.97843	-2.1153	2.6354	-1.8847	0.57529
X_{12}^G	-1.0287	1.8927	-2.2736	1.6137	-0.49144
X_{22}^G	0.92663	-1.9994	2.4729	-1.7561	0.53333
X_{21}^G	-1.2776	2.3646	-2.8596	2.0406	-0.62381
Y_{11}^G	0.080116	-0.21705	0.2984	-0.22111	0.068177
Y_{12}^G	-0.10119	0.22733	-0.2782	0.19432	-0.058412
Y_{22}^G	0.081575	-0.22014	0.30191	-0.22345	0.068863
Y_{21}^G	-0.11975	0.27166	-0.33492	0.2347	-0.070592
Y_{11}^H	0.018006	-0.073508	0.12369	-0.10067	0.032359
Y_{12}^H	0.16837	-0.27132	0.2568	-0.14835	0.039201
Y_{22}^H	0.014643	-0.062677	0.10697	-0.087362	0.02808
Y_{21}^H	0.16687	-0.26642	0.24922	-0.14232	0.03726
X_{11}^M	-1.4494	1.0096	-1.2095	0.82139	-0.24075
X_{12}^M	-0.58026	0.95754	-0.99223	0.63916	-0.18462
X_{22}^M	-1.3853	0.85261	-0.99939	0.66496	-0.19192
X_{21}^M	-0.58026	0.95754	-0.99223	0.63916	-0.18462
Y_{11}^M	-1.0783	0.20657	-0.27755	0.20276	-0.061976
Y_{12}^M	0.079629	0.037467	-0.13628	0.10592	-0.030342
Y_{22}^M	-1.0769	0.20091	-0.26777	0.19447	-0.059213
Y_{21}^M	0.079629	0.037467	-0.13628	0.10592	-0.030342

Table A.2: FCM resistance functions for $\lambda = 0.9$

	C_0	C_1	C_2	C_3	C_4
X_{11}^A	2.2333	-2.5477	3.3304	-2.5013	0.78949
X_{12}^A	-1.6437	2.7547	-3.5282	2.6457	-0.83493
X_{22}^A	2.3632	-2.8751	3.7764	-2.8366	0.89465
X_{21}^A	-1.6437	2.7547	-3.5282	2.6457	-0.83493
Y_{11}^A	1.3125	-0.62006	0.77929	-0.57043	0.17742
Y_{12}^A	-0.60014	0.75589	-0.85651	0.61364	-0.19027
Y_{22}^A	1.3458	-0.71279	0.9153	-0.6772	0.21171
Y_{21}^A	-0.60014	0.75589	-0.85651	0.61364	-0.19027
Y_{11}^B	-0.20685	0.48803	-0.64295	0.47244	-0.14587
Y_{12}^B	0.27056	-0.43173	0.48259	-0.33475	0.10159
Y_{22}^B	-0.18174	0.43883	-0.58353	0.42962	-0.13256
Y_{21}^B	0.4292	-0.69993	0.79662	-0.55772	0.16989
X_{11}^C	1.0145	-0.043401	0.063034	-0.047968	0.014967
X_{12}^C	-0.11929	0.18875	-0.17457	0.098457	-0.025405
X_{22}^C	1.0145	-0.043401	0.063034	-0.047968	0.014967
X_{21}^C	-0.11929	0.18875	-0.17457	0.098457	-0.025405
Y_{11}^C	1.1364	-0.36336	0.49166	-0.35823	0.1088
Y_{12}^C	0.091192	-0.18497	0.21478	-0.14485	0.042496
Y_{22}^C	1.1063	-0.28323	0.37802	-0.27079	0.08103
Y_{21}^C	0.091192	-0.18497	0.21478	-0.14485	0.042496
X_{11}^G	0.96656	-2.1464	2.7256	-1.9715	0.60557
X_{12}^G	-0.86883	1.6276	-1.9727	1.4051	-0.42835
X_{22}^G	0.86009	-1.9015	2.3763	-1.6922	0.51387
X_{21}^G	-1.3757	2.6112	-3.212	2.3154	-0.71185
Y_{11}^G	0.077847	-0.22026	0.31254	-0.23629	0.073735
Y_{12}^G	-0.089914	0.20897	-0.2619	0.18569	-0.056322
Y_{22}^G	0.080641	-0.22627	0.31934	-0.24077	0.075041
Y_{21}^G	-0.12875	0.30552	-0.38914	0.278	-0.084472
Y_{11}^H	0.019796	-0.081541	0.13982	-0.11568	0.037627
Y_{12}^H	0.16333	-0.27577	0.27059	-0.15997	0.042803
Y_{22}^H	0.012769	-0.058005	0.10243	-0.08537	0.02777
Y_{21}^H	0.16034	-0.26562	0.25446	-0.14691	0.038555
X_{11}^M	-1.465	1.0811	-1.329	0.91698	-0.2711
X_{12}^M	-0.54709	0.91833	-0.9531	0.61068	-0.17534
X_{22}^M	-1.3351	0.75369	-0.88298	0.58173	-0.16593
X_{21}^M	-0.54709	0.91833	-0.9531	0.61068	-0.17534
Y_{11}^M	-1.0764	0.21174	-0.29542	0.22126	-0.068681
Y_{12}^M	0.076048	0.038553	-0.14219	0.11281	-0.032715
Y_{22}^M	-1.0733	0.19914	-0.27304	0.20193	-0.062164
Y_{21}^M	0.076048	0.038553	-0.14219	0.11281	-0.032715

Table A.3: FCM resistance functions for $\lambda = 0.8$

	C_0	C_1	C_2	C_3	C_4
X_{11}^A	2.1487	-2.3815	3.1179	-2.3425	0.73923
X_{12}^A	-1.569	2.6328	-3.3754	2.5316	-0.79862
X_{22}^A	2.3284	-2.8402	3.7453	-2.8143	0.88707
X_{21}^A	-1.569	2.6328	-3.3754	2.5316	-0.79862
Y_{11}^A	1.2998	-0.60798	0.77573	-0.57301	0.17917
Y_{12}^A	-0.58854	0.76241	-0.87891	0.63601	-0.19835
Y_{22}^A	1.3473	-0.74484	0.98057	-0.73579	0.23182
Y_{21}^A	-0.58854	0.76241	-0.87891	0.63601	-0.19835
Y_{11}^B	-0.20695	0.50015	-0.67045	0.49809	-0.1548
Y_{12}^B	0.23329	-0.38002	0.42931	-0.2995	0.091207
Y_{22}^B	-0.17083	0.42686	-0.57989	0.43201	-0.13412
Y_{21}^B	0.4603	-0.77456	0.8992	-0.63635	0.19493
X_{11}^C	1.0138	-0.042905	0.064059	-0.04966	0.015678
X_{12}^C	-0.11398	0.18767	-0.17925	0.1034	-0.027054
X_{22}^C	1.0138	-0.042905	0.064059	-0.04966	0.015678
X_{21}^C	-0.11398	0.18767	-0.17925	0.1034	-0.027054
Y_{11}^C	1.1388	-0.38057	0.52707	-0.39027	0.11976
Y_{12}^C	0.085668	-0.17698	0.20663	-0.13908	0.040623
Y_{22}^C	1.0959	-0.26311	0.35735	-0.25822	0.077547
Y_{21}^C	0.085668	-0.17698	0.20663	-0.13908	0.040623
X_{11}^G	0.93489	-2.0965	2.6725	-1.9338	0.59348
X_{12}^G	-0.72713	1.3602	-1.6357	1.1552	-0.34971
X_{22}^G	0.78473	-1.7463	2.17	-1.5308	0.46093
X_{21}^G	-1.4324	2.736	-3.3687	2.4261	-0.74476
Y_{11}^G	0.075225	-0.21991	0.31911	-0.24455	0.076905
Y_{12}^G	-0.079683	0.18935	-0.24056	0.17187	-0.052348
Y_{22}^G	0.078736	-0.22729	0.32708	-0.24953	0.078298
Y_{21}^G	-0.13584	0.33303	-0.43361	0.31353	-0.095827
Y_{11}^H	0.021308	-0.087873	0.15219	-0.12709	0.041623
Y_{12}^H	0.15561	-0.27152	0.27217	-0.16257	0.043635
Y_{22}^H	0.011162	-0.052888	0.095488	-0.080553	0.026371
Y_{21}^H	0.15158	-0.25746	0.2494	-0.14393	0.037535
X_{11}^M	-1.4664	1.1019	-1.3655	0.94393	-0.27877
X_{12}^M	-0.50198	0.83766	-0.84884	0.52923	-0.14867
X_{22}^M	-1.2866	0.64325	-0.73802	0.47216	-0.13092
X_{21}^M	-0.50198	0.83766	-0.84884	0.52923	-0.14867
Y_{11}^M	-1.0733	0.21152	-0.30384	0.23181	-0.072757
Y_{12}^M	0.071021	0.039022	-0.14267	0.11409	-0.033169
Y_{22}^M	-1.0687	0.19213	-0.26871	0.20108	-0.062312
Y_{21}^M	0.071021	0.039022	-0.14267	0.11409	-0.03317

Table A.4: FCM resistance functions for $\lambda = 0.72$

	C_0	C_1	C_2	C_3	C_4
X_{11}^A	1.9846	-2.0024	2.5722	-1.9053	0.59539
X_{12}^A	-1.4009	2.2836	-2.8657	2.1176	-0.66118
X_{22}^A	2.2246	-2.614	3.3975	-2.5161	0.78437
X_{21}^A	-1.4009	2.2836	-2.8657	2.1176	-0.66118
Y_{11}^A	1.2752	-0.57312	0.74239	-0.55271	0.17352
Y_{12}^A	-0.55971	0.74971	-0.87851	0.64107	-0.20084
Y_{22}^A	1.344	-0.77961	1.0593	-0.808	0.25673
Y_{21}^A	-0.55971	0.74971	-0.87851	0.64107	-0.20084
Y_{11}^B	-0.20235	0.50319	-0.68664	0.51517	-0.16094
Y_{12}^B	0.17456	-0.28938	0.32708	-0.2275	0.069134
Y_{22}^B	-0.14935	0.3901	-0.5425	0.4083	-0.12722
Y_{21}^B	0.50284	-0.87865	1.0394	-0.74136	0.22776
X_{11}^C	1.0122	-0.0409	0.062168	-0.049468	0.015873
X_{12}^C	-0.10123	0.17685	-0.17667	0.1049	-0.0279
X_{22}^C	1.0122	-0.0409	0.062168	-0.049468	0.015873
X_{21}^C	-0.10123	0.17685	-0.17667	0.1049	-0.027902
Y_{11}^C	1.1385	-0.39369	0.55987	-0.42166	0.1307
Y_{12}^C	0.072832	-0.15133	0.17297	-0.11271	0.031931
Y_{22}^C	1.0772	-0.21936	0.3027	-0.21943	0.065704
Y_{21}^C	0.072832	-0.15133	0.17297	-0.11272	0.031936
X_{11}^G	0.84693	-1.8833	2.3596	-1.6777	0.50771
X_{12}^G	-0.50657	0.91311	-1.0473	0.70921	-0.2079
X_{22}^G	0.63691	-1.3919	1.6591	-1.1191	0.32468
X_{21}^G	-1.462	2.7405	-3.291	2.3203	-0.70125
Y_{11}^G	0.069843	-0.2134	0.31837	-0.24774	0.078522
Y_{12}^G	-0.06242	0.15159	-0.19411	0.13886	-0.042269
Y_{22}^G	0.073171	-0.21895	0.32191	-0.24831	0.078318
Y_{21}^G	-0.14574	0.37236	-0.49669	0.36306	-0.11137
Y_{11}^H	0.023586	-0.096455	0.16801	-0.14127	0.046511
Y_{12}^H	0.13663	-0.24777	0.25198	-0.14992	0.039739
Y_{22}^H	0.008586	-0.042728	0.078791	-0.067003	0.021971
Y_{21}^H	0.13162	-0.22972	0.22215	-0.12523	0.031618
X_{11}^M	-1.4452	1.0544	-1.2906	0.87528	-0.2537
X_{12}^M	-0.40443	0.63993	-0.58391	0.32277	-0.081641
X_{22}^M	-1.2053	0.44284	-0.46532	0.2644	-0.064715
X_{21}^M	-0.40442	0.63992	-0.5839	0.32276	-0.081639
Y_{11}^M	-1.0659	0.20203	-0.30282	0.23704	-0.075495
Y_{12}^M	0.05963	0.038085	-0.13279	0.10536	-0.030177
Y_{22}^M	-1.0584	0.16988	-0.24312	0.18399	-0.057285
Y_{21}^M	0.05963	0.038088	-0.1328	0.10538	-0.030187

Table A.5: FCM resistance functions for $\lambda = 0.6$

	C_0	C_1	C_2	C_3	C_4
X_{11}^A	1.8203	-1.5985	1.9721	-1.4179	0.43426
X_{12}^A	-1.2116	1.8621	-2.2338	1.5998	-0.48906
X_{22}^A	2.0876	-2.2642	2.8394	-2.0386	0.62124
X_{21}^A	-1.2116	1.8621	-2.2338	1.5998	-0.48906
Y_{11}^A	1.2488	-0.52566	0.68348	-0.50867	0.15949
Y_{12}^A	-0.52189	0.71072	-0.83422	0.60794	-0.19021
Y_{22}^A	1.3335	-0.78691	1.0901	-0.83824	0.26716
Y_{21}^A	-0.52189	0.71071	-0.83422	0.60793	-0.1902
Y_{11}^B	-0.19266	0.48642	-0.66733	0.50096	-0.15631
Y_{12}^B	0.12549	-0.20736	0.22956	-0.15665	0.04701
Y_{22}^B	-0.12628	0.33897	-0.47524	0.35711	-0.11074
Y_{21}^B	0.5285	-0.94199	1.1168	-0.79324	0.24253
X_{11}^C	1.0102	-0.035114	0.056286	-0.045677	0.014833
X_{12}^C	-0.085619	0.15693	-0.16199	0.097944	-0.026266
X_{22}^C	1.0102	-0.035114	0.056286	-0.045677	0.014833
X_{21}^C	-0.085623	0.15695	-0.16204	0.097983	-0.02628
Y_{11}^C	1.1336	-0.38738	0.55777	-0.42264	0.13132
Y_{12}^C	0.057955	-0.11711	0.12502	-0.074595	0.019393
Y_{22}^C	1.0591	-0.17132	0.23628	-0.16935	0.04996
Y_{21}^C	0.057951	-0.11711	0.12504	-0.07466	0.019429
X_{11}^G	0.73799	-1.5901	1.9126	-1.3101	0.38524
X_{12}^G	-0.33368	0.55867	-0.58485	0.36335	-0.099247
X_{22}^G	0.49022	-1.0198	1.1186	-0.68774	0.18355
X_{21}^G	-1.4188	2.5383	-2.8909	1.9505	-0.57082
Y_{11}^G	0.063953	-0.20152	0.30557	-0.23942	0.076061
Y_{12}^G	-0.046752	0.11387	-0.14435	0.10194	-0.030718
Y_{22}^G	0.065262	-0.19945	0.29557	-0.22809	0.071764
Y_{21}^G	-0.15236	0.39912	-0.53743	0.3928	-0.12005
Y_{11}^H	0.025241	-0.10161	0.17621	-0.14795	0.048663
Y_{12}^H	0.11341	-0.20931	0.21036	-0.12116	0.030868
Y_{22}^H	0.0063226	-0.032152	0.059309	-0.0503	0.016207
Y_{21}^H	0.10843	-0.19103	0.17994	-0.09596	0.022592
X_{11}^M	-1.4045	0.93821	-1.1064	0.71874	-0.20033
X_{12}^M	-0.30294	0.43224	-0.31592	0.12185	-0.018205
X_{22}^M	-1.1371	0.27246	-0.23903	0.098078	-0.013351
X_{21}^M	-0.30293	0.43218	-0.31582	0.12178	-0.018186
Y_{11}^M	-1.0571	0.18472	-0.28678	0.22897	-0.073692
Y_{12}^M	0.046998	0.034309	-0.11163	0.08548	-0.023399
Y_{22}^M	-1.0468	0.13954	-0.20165	0.15269	-0.047383
Y_{21}^M	0.047001	0.034313	-0.1117	0.085603	-0.023463

Table A.6: FCM resistance functions for $\lambda = 0.5$

λ	X_{11}^A	X_{12}^A	X_{22}^A	X_{21}^A
1.0	0.99538	-0.3502	0.99538	-0.3502
0.9	1.0172	-0.34879	0.97114	-0.34879
0.8	1.0384	-0.34394	0.94154	-0.34394
0.72	1.0544	-0.33683	0.91324	-0.33683
0.6	1.0753	-0.31906	0.86151	-0.31906
0.5	1.0881	-0.29574	0.80828	-0.29574

Table A.7: Order one corrections for X_A

λ	Y_{11}^A	Y_{12}^A	Y_{22}^A	Y_{21}^A
1.0	0.99832	-0.27366	0.99832	-0.27366
0.9	1.0052	-0.27243	0.98967	-0.27243
0.8	1.011	-0.26819	0.9777	-0.26819
0.72	1.0148	-0.26192	0.96472	-0.26192
0.6	1.0185	-0.246	0.93668	-0.246
0.5	1.0193	-0.22456	0.90088	-0.22456

Table A.8: Order one corrections for Y_A

λ	Y_{11}^B	Y_{12}^B	Y_{22}^B	Y_{21}^B
1.0	0.15931	-0.0011131	0.15931	-0.0011131
0.9	0.14476	0.0091301	0.17458	-0.010956
0.8	0.12945	0.02055	0.19236	-0.021043
0.72	0.11669	0.030261	0.20878	-0.028927
0.6	0.096864	0.044676	0.238	-0.039453
0.5	0.080032	0.0545	0.26774	-0.045709

Table A.9: Order one corrections for Y_B

λ	X_{11}^C	X_{12}^C	X_{22}^C	X_{21}^C
1.0	1.0518	-0.15026	1.0518	-0.15026
0.9	1.0461	-0.14901	1.0578	-0.14901
0.8	1.0401	-0.14476	1.0648	-0.14476
0.72	1.0351	-0.13863	1.0712	-0.13863
0.6	1.0273	-0.12381	1.0826	-0.12381
0.5	1.0208	-0.10553	1.094	-0.10553

Table A.10: Order one corrections for X_C

λ	Y_{11}^C	Y_{12}^C	Y_{22}^C	Y_{21}^C
1.0	0.70281	-0.027455	0.70281	-0.027455
0.9	0.72944	-0.027663	0.67449	-0.027751
0.8	0.75717	-0.028457	0.64085	-0.028644
0.72	0.78015	-0.029582	0.60905	-0.029858
0.6	0.81589	-0.032072	0.55041	-0.032505
0.5	0.84668	-0.034579	0.48757	-0.035169

Table A.11: Order one corrections for Y_C

λ	X_{11}^G	X_{12}^G	X_{22}^G	X_{21}^G
1.0	-0.31287	0.13026	-0.31287	0.13026
0.9	-0.26701	0.10286	-0.35792	0.15183
0.8	-0.21654	0.066786	-0.40537	0.16807
0.72	-0.17348	0.03131	-0.4434	0.17524
0.6	-0.10651	-0.032171	-0.49439	0.17202
0.5	-0.051763	-0.091151	-0.52012	0.15255

Table A.12: Order one corrections for X_G

λ	Y_{11}^G	Y_{12}^G	Y_{22}^G	Y_{21}^G
1.0	-0.094061	0.068296	-0.094061	0.068296
0.9	-0.083933	0.065163	-0.10597	0.071283
0.8	-0.074358	0.061495	-0.1218	0.074415
0.72	-0.067058	0.058066	-0.13854	0.076974
0.6	-0.056574	0.05182	-0.17423	0.080614
0.5	-0.048069	0.045319	-0.21958	0.08281

Table A.13: Order one corrections for Y_G

λ	Y_{11}^H	Y_{12}^H	Y_{22}^H	Y_{21}^H
1.0	-0.074056	-0.029336	-0.074056	-0.029336
0.9	-0.072737	-0.022997	-0.074513	-0.036874
0.8	-0.070397	-0.017497	-0.073863	-0.046411
0.72	-0.067675	-0.014015	-0.072133	-0.055552
0.6	-0.061959	-0.010883	-0.06635	-0.07145
0.5	-0.055509	-0.010531	-0.056825	-0.085501

Table A.14: Order one corrections for Y_H

λ	X_{11}^M	X_{12}^M	X_{22}^M	X_{21}^M
1.0	-0.71716	0.14581	-0.71716	0.14581
0.9	-0.74085	0.14581	-0.69877	0.14581
0.8	-0.77154	0.14566	-0.68667	0.14566
0.72	-0.80101	0.14502	-0.68528	0.14502
0.6	-0.85241	0.14137	-0.70859	0.14137
0.5	-0.89971	0.13255	-0.76977	0.13255

Table A.15: Order one corrections for X_M

λ	Y_{11}^M	Y_{12}^M	Y_{22}^M	Y_{21}^M
1.0	-0.90142	0.22481	-0.90142	0.22481
0.9	-0.91705	0.22267	-0.87985	0.22267
0.8	-0.92915	0.2155	-0.84708	0.2155
0.72	-0.93649	0.20552	-0.80867	0.20552
0.6	-0.94452	0.18341	-0.71938	0.18341
0.5	-0.94995	0.16041	-0.60185	0.16041

Table A.16: Order one corrections for Y_M

Bibliography

[1] M. Abbas, E. Climent, O. Simonin, and M. R. Maxey. Dynamics of bidisperse suspensions under Stokes flows: Linear shear flow and sedimentation. *Phys. Fluids*, 18:1–20, 2006. doi: 10.1063/1.2396916.

[2] P. A. Arp and S. G. Mason. The kinetics of flowing dispersions. *J. Colloid Interface Sci.*, 61:44–61, 1977. doi: 10.1016/0021-9797(77)90414-3.

[3] G. K. Batchelor. The stress system in a suspension of force-free particles. *J. Fluid Mech.*, 41(03):545, 1970. doi: 10.1017/S0022112070000745. URL http://www.journals.cambridge.org/abstract_S0022112070000745.

[4] G. K. Batchelor and J. T. Green. The hydrodynamic interaction of two small freely-moving spheres in a linear flow field. *J. Fluid Mech.*, 56(02):375, 1972. doi: 10.1017/S0022112072002927. URL http://www.journals.cambridge.org/abstract_S0022112072002927.

[5] G. K. Batchelor and J. Van Rensburg. Structure formation in bidisperse sedimentation. *J. Fluid Mech.*, 166:379–407, 1986. doi: 10.1017/S0022112086000204.

[6] F. Blanc, F. Peters, and E. Lemaire. Experimental signature of the pair trajectories of rough spheres in the shear-induced microstructure in noncolloidal suspensions. *Phys. Rev. Lett.*, 107(20):208302, 2011. doi: 10.1103/PhysRevLett.107.208302.

[7] P. Bochev, K. Peterson, and X. Gao. A new Control Volume Finite Element Method for the stable and accurate solution of the drift-diffusion equations on general unstructured grids. *Comput. Methods Appl. Mech. Eng.*, 254:126–145, 2013. doi: 10.1016/J.CMA.2012.10.009. URL http://www.sciencedirect.com/science/article/pii/S0045782512003179.

[8] S. Bodenstab, M. Juillerat, W. Bauer, and K. Sommer. Separating the Role of Particles and the Suspending Fluid for the Flow of Soy Milks. *J. Food Sci.*, 68(5):1722–1730, 2003. doi: 10.1111/j.1365-2621.2003.tb12319.x. URL http://doi.wiley.com/10.1111/j.1365-2621.2003.tb12319.x.

[9] G. Bossis and J. F. Brady. Dynamic simulation of sheared suspensions. I. General method. *J. Chem. Phys.*, 80:5141, 1984. doi: 10.1063/1.446585. URL http://link.aip.org/link/JCPSA6/v80/i10/p5141/s1&Agg=doi.

[10] F. Boyer, O. Pouliquen, and É. Guazzelli. Dense suspensions in rotating-rod flows: normal stresses and particle migration. *J. Fluid Mech.*, 686:5–25, 2011. doi: 10.1017/jfm.2011.272. URL http://www.journals.cambridge.org/abstract_S0022112011002722.

[11] J. Brady. Stokesian Dynamics. *Annu. Rev. Fluid Mech.*, 20:111–157, 1988. doi: 10.1146/annurev.fluid.20.1.111.

[12] J. F. Brady. Computer simulation of viscous suspensions. *Chem. Eng. Sci.*, 56:2921–2926, 2001. doi: 10.1016/S0009-2509(00)00475-9.

[13] D. Braess. *Finite Elements: Theory, Fast Solvers, and Applications in Solid Mechanics*. Cambridge University Press, 2007. ISBN 9780511618635.

[14] W.-P. Breugem. A second-order accurate immersed boundary method for fully resolved simulations of particle-laden flows. *J. Comput. Phys.*, 231 (13):4469–4498, 2012. doi: 10.1016/J.JCP.2012.02.026. URL http://www.sciencedirect.com/science/article/pii/S0021999112001374.

[15] J. E. Butler, P. D. Majors, and R. T. Bonnecaze. Observations of shear-induced particle migration for oscillatory flow of a suspension within a tube. *Phys. Fluids*, 11(10):2865–2877, 1999. doi: 10.1063/1.870145.

[16] C. Chang. Effect of particle size distributions on the rheology of concentrated bimodal suspensions. *J. Rheol.*, 38(1):85, 1994. doi: 10.1122/1.550497.

[17] C. Chang and R. L Powell. Dynamic Simulation of Bimodal Suspensions of Hydrodynamically Interacting Spherical-Particles. *J. Fluid Mech.*, 253(1993): 1–25, 1993. doi: 10.1017/S0022112093001697.

[18] C. Chang and R. L. Powell. The rheology of bimodal hard-sphere dispersions. *Phys. Fluids*, 6(5):1628–1636, 1994. doi: doi:10.1063/1.868226.

[19] C. Chang and R. L Powell. Self-diffusion of bimodal suspensions of hydrodynamically interacting spherical particles in shearing flow. *J. Fluid Mech.*, 281: 51–80, 1994. doi: 10.1017/S0022112094003034. URL http://www.journals.cambridge.org/abstract_S0022112094003034.

[20] J. S. Chong, E. B. Christiansen, and A. D. Baer. Rheology of concentrated suspensions. *J. Appl. Polym. Sci.*, 15(8):2007–2021, 1971. doi: 10.1002/app.1971.070150818. URL http://doi.wiley.com/10.1002/app.1971.070150818.

[21] B. Chun, I. Kwon, H. W. Jung, and H. C. Hyun. Lattice Boltzmann simulation of shear-induced particle migration in plane Couette- Poiseuille flow: Local ordering of suspension. *Phys. Fluids*, 29(29):121605–121605, 2017. doi: 10.1063/1.4991428. URL https://doi.org/10.1063/1.4991428.

[22] B. Cichocki, M. L. Ekiel-Jeżewska, and E. Wajnryb. Lubrication corrections for three-particle contribution to short-time self-diffusion coefficients in colloidal dispersions. *J. Chem. Phys.*, 111(7):3265, 1999. doi: 10.1063/1.479605. URL https://aip.scitation.org/doi/abs/10.1063/1.479605.

[23] L. Corté, P. M. Chaikin, J. P. Gollub, and D. J. Pine. Random organization in periodically driven systems. *Nature Physics*, 4(5):420–424, 2008. doi: 10.1038/nphys891.

[24] F. R. Cui, A. A. Howard, M. R. Maxey, and A. Tripathi. Dispersion of a suspension plug in oscillatory pressure-driven flow. *Phys. Rev. Fluids*, 2(9):094303, 2017. doi: 10.1103/PhysRevFluids.2.094303. URL https://link.aps.org/doi/10.1103/PhysRevFluids.2.094303.

[25] F. R. Da Cunha and E. J. Hinch. Shear-induced dispersion in a dilute suspension of rough spheres. *J. Fluid Mech.*, 309:211–223, 1996.

[26] S. L. Dance and M. R. Maxey. Incorporation of lubrication effects into the force-coupling method for particulate two-phase flow. *J. Comput. Phys.*, 189:212–238, 2003. doi: 10.1016/S0021-9991(03)00209-2.

[27] P. G. De Gennes. Conjectures on the transition from Poiseuille to plug flow in suspensions. *J. Phys.*, 40:783–787, 1979. doi: 10.1051/jphys:01979004008078300. URL https://hal.archives-ouvertes.fr/file/index/docid/209163/filename/ajp-jphys_1979_40_8_783_0.pdf.

[28] M. M. Denn and J. F. Morris. Rheology of non-Brownian suspensions. *Annu. Rev. Chem. Biomol. Eng.*, 5:203–228, 2014. doi: 10.1146/annurev-chembioeng-060713-040221.

[29] D. Di Carlo. Inertial microfluidics. *Lab Chip*, 9:3038–3046, 2009. doi: 10.1039/b912547g.

[30] G. Drazer, J. Koplik, B. Khusid, and A. Acrivos. Deterministic and stochastic behaviour of non-Brownian spheres in sheared suspensions. *J. Fluid Mech.*, 460:307–335, 2002. doi: 10.1017/S0022112002008261.

[31] D. A. Drew. Mathematical Modeling of Two-Phase Flow. *Annual Review of Fluid Mechanics*, 15:261–291, 1983. doi: 10.1146/annurev.fl.15.010183.001401.

[32] A. Gadala-Maria and A. Acrivos. Shear-induced structure in a concentrated suspension of solid spheres. *J. Rheol.*, 24(6):799–814, 1980.

[33] S. Gallier, E. Lemaire, F. Peters, and L. Lobry. Rheology of sheared suspensions of rough frictional particles. *J. Fluid Mech.*, 757:514–549, 2014. doi: 10.1017/jfm.2014.507.

[34] S. Gallier, E. Lemaire, F. Peters, and L. Lobry. Percolation in suspensions and De Gennes conjectures. *Phys. Rev. E*, 92:020301, 2015. URL https://hal.archives-ouvertes.fr/hal-01213898/document.

[35] C. Gamonpilas, J. F. Morris, and M. M. Denn. Shear and normal stress measurements in non-Brownian monodisperse and bidisperse suspensions. *J. Rheol.*, 60(2):289–296, 2016. doi: 10.1122/1.4942230. URL http://sor.scitation.org/doi/10.1122/1.4942230.

[36] C. Gamonpilas, J. F. Morris, and M. M. Denn. Erratum: “Shear and normal stress measurements in non-Brownian monodisperse and bidisperse suspensions”. *J. Rheol.*, 62(2):665–667, 2018. doi: 10.1122/1.5003086. URL http://sor.scitation.org/doi/10.1122/1.5003086.

[37] C. Gao, B. Xu, and J. F. Gilchrist. Mixing and segregation of microspheres in microchannel flows of mono- and bidispersed suspensions. *Phys. Rev. E*, 79(3): 036311, 2009. doi: 10.1103/PhysRevE.79.036311. URL https://link.aps.org/doi/10.1103/PhysRevE.79.036311.

[38] P. Gondret and L. Petit. Dynamic viscosity of macroscopic suspensions of bimodal sized solid spheres. *J. Rheol*, 41(6):1261–1274, 1997.

[39] A. L. Graham, S. A. Altobelli, Eiichi Fukushima, L. A. Mondy, and T. S. Stephens. Note: NMR imaging of shearâĂŘinduced diffusion and structure in concentrated suspensions undergoing Couette flow. *J. Rheol.*, 35(1):191–201, 1991. doi: 10.1122/1.550227. URL http://sor.scitation.org/doi/10.1122/1.550227.

[40] I. M. Griffiths and H. A. Stone. Axial dispersion via shear-enhanced diffusion in colloidal suspensions. *Europhys. Lett.*, 97:58005, 2012. doi: 10.1209/0295-5075/97/58005.

[41] J. S. Guasto, A. S. Ross, and J. P. Gollub. Hydrodynamic irreversibility in particle suspensions with nonuniform strain. *Phys. Rev. E*, 81(6):061401, 2010. doi: 10.1103/PhysRevE.81.061401.

[42] R. E. Hampton, A. A. Mammoli, A. L. Graham, and N. Tetlow. Migration of particles undergoing pressure-driven flow in a circular conduit. *J. Rheol.*, 41: 621–640, 1997. doi: 10.1122/1.550863.

[43] R. E. Hampton, A. A. Mammoli, A. L. Graham, N. Tetlow, and S. A. Altobelli. Migration of particles undergoing pressure-driven flow in a circular conduit. *J. Rheol.*, 41(3):621, 1998. doi: 10.1122/1.550863. URL https://sor.scitation.org/doi/abs/10.1122/1.550863.

[44] A. A. Howard. Source code for generating lubrication resistance functions, 2018. URL https://doi.org/10.7301/Z05B00ZM.

[45] A. A. Howard. Rotating cloud simulation, 2018. URL https://doi.org/10.7301/Z01N7ZM7.

[46] H. H. Hu. Direct simulation of flows of solid-liquid mixtures. *Int. J. Multiph. Flow*, 22(2):335–352, 1996. doi: 10.1016/0301-9322(95)00068-2.

[47] D. M. Husband, L. A. Mondy, E. Ganani, and A. L. Graham. Direct measurements of shear-induced particle migration in suspensions of bimodal spheres. *Rheol. Acta*, 33(3):185–192, 1994. doi: 10.1007/BF00437303. URL http://link.springer.com/10.1007/BF00437303.

[48] K. Ichiki. Errata on the papers for two-body exact solutions in Stokes flows, 2008. URL http://ryuon.sourceforge.net/twobody/errata.html.

[49] M. S. Ingber, A. A. Mammoli, P. Vorobieff, R. McCollam, and A. L. Graham. Experimental and numerical analysis of irreversibilities among particles suspended in a Couette device. *J. Rheol.*, 50(2):99, 2006. doi: 10.1122/1.2169806. URL http://scitation.aip.org/content/sor/journal/jor2/50/2/10.1122/1.2169806.

[50] I. Jánosi, T. Tél, D. Wolf, and J. Gallas. Chaotic particle dynamics in viscous flows: The three-particle stokeslet problem. *Phys. Rev. E*, 56(3):2858–2868, 1997. doi: 10.1103/PhysRevE.56.2858.

[51] D. J. Jeffrey. The calculation of the low Reynolds number resistance functions for two unequal spheres. *Phys. Fluids A Fluid Dyn.*, 4(1):16–29, 1992. doi: 10.1063/1.858494. URL http://scitation.aip.org/content/aip/journal/pofa/4/1/10.1063/1.858494.

[52] D. J. Jeffrey and Y. Onishi. Calculation of the resistance and mobility functions for two unequal rigid spheres in low-Reynolds-number flow. *J. Fluid Mech.*, 139:261, 1984. doi: 10.1017/S0022112084000355. URL http://www.journals.cambridge.org/abstract_S0022112084000355.

[53] P. Kanehl and H. Stark. Hydrodynamic segregation in a bidisperse colloidal suspension in microchannel flow: A theoretical study. *J. Chem. Phys.*, 142(21):214901, 2015. doi: 10.1063/1.4921800. URL http://scitation.aip.org/content/aip/journal/jcp/142/21/10.1063/1.4921800.

[54] A. Karnis, H.L. Goldsmith, and S.G. Mason. The kinetics of flowing dispersions: I. Concentrated suspensions of rigid particles. *J. Colloid Interface Sci.*, 22(6):531–553, 1966. doi: 10.1016/0021-9797(66)90048-8. URL https://www.sciencedirect.com/science/article/pii/0021979766900488.

[55] S. Kim and S. J. Karilla. *Microhydrodynamics : Principles and Selected Applications*. Dover Publications, Inc., 1991. doi: 10.1002/cite.330641004.

[56] C. J. Koh, P. Hookham, and L. G. Leal. An experimental investigation of concentrated suspension flows in a rectangular channel. *J. Fluid Mech.*, 266, 1994. URL http://journals.cambridge.org/abstract_S0022112094000911.

[57] J. Kromkamp, F. Faber, K. Schroen, and R. Boom. Effects of particle size segregation on crossflow microfiltration performance: Control mechanism for concentration polarisation and particle fractionation. *J. Memb. Sci.*, 268(2):189–197, 2006. doi: 10.1016/J.MEMSCI.2005.06.012. URL https://www.sciencedirect.com/science/article/pii/S0376738805004679.

[58] P. M. Kulkarni and J. F. Morris. Suspension properties at finite Reynolds number from simulated shear flow. *Phys. Fluids*, 20(4):040602, 2008. doi: 10.1063/1.2911017. URL http://aip.scitation.org/doi/10.1063/1.2911017.

[59] A. J. C. Ladd. Hydrodynamic transport coefficients of random dispersions of hard spheres. *J. Chem. Phys.*, 93(5):3484–3494, 1990. doi: 10.1063/1.458830. URL http://aip.scitation.org/doi/10.1063/1.458830.

[60] D. Leighton and A. Acrivos. The shear-induced migration of particles in concentrated suspensions. *J. Fluid Mech.*, 181:415–439, 1987.

[61] D. Lhuillier. Migration of rigid particles in non-Brownian viscous suspensions. *Phys. Fluids*, 21(2):023302, 2009. doi: 10.1063/1.3079672. URL http://scitation.aip.org/content/aip/journal/pof2/21/2/10.1063/1.3079672.

[62] D. Liu, M. Maxey, and G. E. Karniadakis. A fast method for particulate microflows. *J. Microelectromechanical Syst.*, 11(6):691–702, 2002. doi: 10.1109/JMEMS.2002.805209.

[63] S. Lomholt and M. R. Maxey. Force-coupling method for particulate two-phase flow: Stokes flow. *J. Comput. Phys.*, 184(2):381–405, 2003. doi: 10.1016/S0021-9991(02)00021-9. URL http://linkinghub.elsevier.com/retrieve/pii/S0021999102000219.

[64] M. K. Lyon and L. G. Leal. An experimental study of the motion of concentrated suspensions in two-dimensional channel flow. Part 2. Bidisperse systems. *J. Fluid Mech.*, 363, 1998. doi: 10.1017/S0022112098008829. URL http://www.journals.cambridge.org/abstract_S0022112098008829.

[65] M. K. Lyon and L. G. Leal. An experimental study of the motion of concentrated suspensions in two-dimensional channel flow. Part 1. Monodisperse systems. *J. Fluid Mech.*, 363, 1998. doi: 10.1017/S0022112098008817. URL http://www.journals.cambridge.org/abstract_S0022112098008817.

[66] M. Maxey. Simulation Methods for Particulate Flows and Concentrated Suspensions. *Annu. Rev. Fluid Mech.*, 49(1):171–193, 2017. doi: 10.1146/annurev-fluid-122414-034408. URL http://www.annualreviews.org/doi/10.1146/annurev-fluid-122414-034408.

[67] M. R. Maxey and B. K. Patel. Localized force representations for particles sedimenting in Stokes Flow. *Int. J. Muliphase Flow*, 27:1603–1626, 2001.

[68] S. McKee, M. F. Tomé, V. G. Ferreira, J. A. Cuminato, A. Castelo, F. S. Sousa, and N. Mangiavacchi. The MAC method. *Comput. Fluids*, 37(8):907–930, 2008. doi: 10.1016/j.compfluid.2007.10.006. URL http://linkinghub.elsevier.com/retrieve/pii/S0045793007001909.

[69] B. Metzger and J. E. Butler. Irreversibility and chaos: Role of long-range hydrodynamic interactions in sheared suspensions. *Phys. Rev. E*, 82(5):51406, 2010.

[70] B. Metzger and J. E. Butler. Clouds of particles in a periodic shear flow. *Phys. Fluids*, 24(2):021703, 2012. doi: 10.1063/1.3685537. URL http://scitation.aip.org/content/aip/journal/pof2/24/2/10.1063/1.3685537.

[71] B. Metzger, P. Pham, and J. E. Butler. Irreversibility and chaos: Role of lubrication interactions in sheared suspensions. *Physical Review E*, 87(5):052304, 2013. doi: 10.1103/PhysRevE.87.052304. URL http://link.aps.org/doi/10.1103/PhysRevE.87.052304.

[72] A. Meunier and G. Bossis. The influence of surface forces on shear-induced tracer diffusion in mono and bidisperse suspensions. *Eur. Phys. J. E*, 25

(2):187–199, 2008. doi: 10.1140/epje/i2007-10279-y. URL http://link.springer.com/10.1140/epje/i2007-10279-y.

[73] R. M. Miller and J. F. Morris. Normal stress-driven migration and axial development in pressure-driven flow of concentrated suspensions. *J. Nonnewton. Fluid Mech.*, 135(2-3):149–165, 2006. doi: 10.1016/j.jnnfm.2005.11.009. URL http://linkinghub.elsevier.com/retrieve/pii/S0377025706000127.

[74] D. Mirzaei, R. Schaback, and M. Dehghan. On generalized moving least squares and diffuse derivatives. *IMA J. Numer. Anal.*, 32(3):983–1000, 2012. doi: 10.1093/imanum/drr030. URL https://academic.oup.com/imajna/article-lookup/doi/10.1093/imanum/drr030.

[75] J. F. Morris. Anomalous migration in simulated oscillatory pressure-driven flow of a concentrated suspension. *Phys. Fluids*, 13(9):2457–2462, 2001. doi: 10.1063/1.1390363.

[76] J. F. Morris. A review of microstructure in concentrated suspensions and its implications for rheology and bulk flow. *Rheol. Acta*, 48(8):909–923, 2009. doi: 10.1007/s00397-009-0352-1. URL http://link.springer.com/10.1007/s00397-009-0352-1.

[77] J. F. Morris and F. Boulay. Curvilinear flows of noncolloidal suspensions :. *J. Rheol.*, 43:1213–1237, 1999.

[78] T. M. Morris. The Relationship Between Haze and the Size of Particles in Beer. *J. Inst. Brew.*, 93(1):13–17, 1987. doi: 10.1002/j.2050-0416.1987.tb04468.x. URL http://doi.wiley.com/10.1002/j.2050-0416.1987.tb04468.x.

[79] P. M. Mwasame, N. J. Wagner, and A. N. Beris. Modeling the effects of polydispersity on the viscosity of noncolloidal hard sphere suspensions. *J. Rheol.*, 60(2):225–240, 2016. doi: 10.1122/1.4938048. URL http://sor.scitation.org/doi/10.1122/1.4938048.

[80] N.-Q. Nguyen and A. J. C. Ladd. Lubrication corrections for lattice-Boltzmann simulations of particle suspensions. *Phys. Rev. E*, 66(4):046708, 2002. doi: 10.1103/PhysRevE.66.046708. URL https://link.aps.org/doi/10.1103/PhysRevE.66.046708.

[81] R. A. Nicolaides and K. A. Trapp. Covolume Discretization of Differential Forms. In *Compat. Spat. Discret.*, pages 161–171. Springer New York, New York, NY, 2006. doi: 10.1007/0-387-38034-5_8. URL http://link.springer.com/10.1007/0-387-38034-5_8.

[82] J. T. Norman, H. V. Nayak, and R. T. Bonnecaze. Migration of buoyant particles in low-Reynolds-number pressure-driven flows. *J. Fluid Mech.*, 523:1–35, 2005. doi: 10.1017/S0022112004000886.

[83] P. R. Nott and J. F. Brady. Pressure-driven flow of suspensions: simulation and theory. *J. Fluid Mech.*, 275:157, 1994. doi: 10.1017/S0022112094002326. URL http://www.journals.cambridge.org/abstract_S0022112094002326.

[84] P. R. Nott, É. Guazzelli, and O. Pouliquen. The suspension balance model revisited. *Phys. Fluids*, 23(4):043304, 2011. doi: 10.1063/1.3570921.

[85] N. Ouchiyama and T. Tanaka. Porosity estimation for random packings of spherical particles. *Ind. Eng. Chem. Fundam.*, 23(4):490–493, 1984. doi: 10.1021/i100016a019. URL http://pubs.acs.org/doi/abs/10.1021/i100016a019.

[86] S. Pednekar, J. Chun, and J. Morris. Bidisperse and polydisperse suspension rheology at large solid fraction. *J. Rheol.*, 62(2):513–526, 2018. URL https://arxiv.org/pdf/1711.03136.pdf.

[87] R. Pesche, G. Bossis, and A. Meunier. Numerical simulation of particle segregation in a bidisperse suspension. 1998. URL https://hal.archives-ouvertes.fr/hal-00694958.

[88] Raphael Pesche. *Etude par simulation numerique de la segregation de particules dans une suspension bidisperse*. PhD thesis, 1998.

[89] C. Peskin. The immersed boundary method. *Acta Numer.*, 11:479–517, 2002. doi: 10.1017/S0962492902000077.

[90] F. Peters, G. Ghigliotti, S. Gallier, F. Blanc, E. Lemaire, and L. Lobry. Rheology of non-Brownian suspensions of rough frictional particles under shear reversal: A numerical study. *J. Rheol.*, 60(4):715–732, 2016. doi: 10.1122/1.4954250. URL http://sor.scitation.org/doi/10.1122/1.4954250.

[91] P. Pham, B. Metzger, and J. E. Butler. Particle dispersion in sheared suspensions: Crucial role of solid-solid contacts. *Phys. Fluids*, 27(5):051701, 2015. doi: 10.1063/1.4919728.

[92] P. Pham, J. E. Butler, and B. Metzger. Origin of critical strain amplitude in periodically sheared suspensions. *Physical Review Fluids*, 1(2):022201, 2016. doi: 10.1103/PhysRevFluids.1.022201. URL http://link.aps.org/doi/10.1103/PhysRevFluids.1.022201.

[93] R. J. Phillips, R. C. Armstrong, R. A. Brown, A. L. Graham, and J. R. Abbott. A constitutive equation for concentrated suspensions that accounts for shear-induced particle migration. *Phys. Fluids A*, 4(1):30–40, 1992. doi: 10.1063/1.858498.

[94] D. J. Pine, J. P. Gollub, J. F. Brady, and A. M. Leshanksy. Chaos and threshold for irreversibility in sheared suspensions. *Nature*, 438:997–1000, 2005. doi: 10.1038/nature04380.

[95] I. V. Pivkin, P. D. Richardson, and G. Karniadakis. Blood flow velocity effects and role of activation delay time on growth and form of platelet thrombi. *Proc. Natl. Acad. Sci. U. S. A.*, 103(46):17164–9, 2006. doi: 10.1073/pnas.0608546103.

[96] M. Popova, P. Vorobieff, M. Ingber, and A. Graham. Interaction of two particles in a shear flow. *Phys. Rev. E*, 75:066309, 2007. doi: 10.1103/PhysRevE.75.066309.

[97] R. F. Probstein, M. Z. Sengun, and T-C. Tseng. Bimodal model of concentrated suspension viscosity for distributed particle sizes. *J. Rheol.*, 38(4):811–829, 1994. doi: 10.1122/1.550594. URL http://sor.scitation.org/doi/10.1122/1.550594.

[98] A. Prosperetti and G. Tryggvason. *Computational methods for multiphase flow*. Cambridge University Press, 2009.

[99] F. Qi and R. I. Tanner. Relative viscosity of bimodal suspensions. *Korea-Australia Rheol. J.*, 23(2):105–111, 2011. doi: 10.1007/s13367-011-0013-7. URL http://link.springer.com/10.1007/s13367-011-0013-7.

[100] A. Ramachandran. A macrotransport equation for the particle distribution in the flow of a concentrated, non-colloidal suspension through a circular tube. *J. Fluid Mech.*, 734:219–252, 2013. doi: 10.1017/jfm.2013.455.

[101] A. Ramachandran and D. T. Leighton. The influence of secondary flows induced by normal stress differences on the shear-induced migration of particles in concentrated suspensions. *J. Fluid Mech.*, 603:207–243, 2008. doi: 10.1017/S0022112008000980.

[102] I. Rampall, J. R. Smart, and D. T. Leighton. The influence of surface roughness on the particle-pair distribution function of dilute suspensions of non-colloidal spheres in simple shear flow. *J. Fluid Mech.*, 339:1–24, 1997. doi: 10.1017/S002211209600479X.

[103] J. F. Richardson and W. N. Zaki. The sedimentation of a suspension of uniform spheres under conditions of viscous flow. *Chem. Eng. Sci.*, 3(2):65–73, 1954. doi: 10.1016/0009-2509(54)85015-9. URL https://www.sciencedirect.com/science/article/pii/0009250954850159.

[104] B. Rosa, L.-P. Wang, M. R. Maxey, and W. W. Grabowski. An accurate and efficient method for treating aerodynamic interactions of cloud droplets. *J. Comput. Phys.*, 230(22):8109–8133, 2011. doi: 10.1016/J.JCP.2011.07.012. URL https://www.sciencedirect.com/science/article/pii/S0021999111004311.

[105] J. M. Sakoda. A Generalized Index of Dissimilarity. *Demography*, 18(2):245, 1981. doi: 10.2307/2061096. URL http://link.springer.com/10.2307/2061096.

[106] D. Semwogerere and E. R. Weeks. Shear-induced particle migration in binary colloidal suspensions. *Phys. Fluids*, 20(4):043306, 2008. doi: 10.1063/1.2907378. URL http://aip.scitation.org/doi/10.1063/1.2907378.

[107] D. Semwogerere, J. F. Morris, and E. R. Weeks. Development of particle migration in pressure-driven flow of a Brownian suspension. *J. Fluid Mech.*, 581:437, 2007. doi: 10.1017/S0022112007006088. URL http://www.journals.cambridge.org/abstract_S0022112007006088.

[108] A. P. Shapiro and R. F. Probstein. Random Packings of Spheres and Fluidity Limits of Monodisperse and Bidisperse Suspensions. *Phys. Rev. Lett.*, 68

(9):1422–1425, 1991. URL https://journals.aps.org/prl/pdf/10.1103/PhysRevLett.68.1422.

[109] A. Sierou and J. F. Brady. Rheology and microstructure in concentrated noncolloidal suspensions. *J. Rheol.*, 46(5):1031–1056, 2002. doi: 10.1122/1.1501925. URL http://sor.scitation.org/doi/10.1122/1.1501925.

[110] A. Singh, R. Mari, M. M. Denn, and J. F. Morris. A constitutive model for simple shear of dense frictional suspensions. *J. Rheol.*, 62(2):457–468, 2018. doi: 10.1122/1.4999237. URL http://sor.scitation.org/doi/10.1122/1.4999237.

[111] J. R. Smart and D. T. Leighton. Measurement of the hydrodynamic surface roughness of noncolloidal spheres. *Phys. Fluids A*, 1(1):52–60, 1989. doi: 10.1063/1.857523. URL http://aip.scitation.org/doi/10.1063/1.857523.

[112] B. Snook, J. E. Butler, and É. Guazzelli. Dynamics of shear-induced migration of spherical particles in oscillatory pipe flow. *J. Fluid Mech*, 786(5):128–153, 2016. doi: 10.1017/jfm.2015.645. URL http://www.journals.cambridge.org/abstract_S002211201500645X.

[113] M. Souzy, X. Yin, E. Villermaux, C. Abid, and B. Metzger. Super-diffusion in sheared suspensions. *Phys. Fluids*, 27(4):041705, 2015. doi: 10.1063/1.4918613. URL http://aip.scitation.org/doi/10.1063/1.4918613.

[114] J. J. Stickel and R. L. Powell. Fluid Mechanics and Rheology of Dense Suspensions. *Annu. Rev. Fluid Mech.*, 37(1):129–149, 2005. doi: 10.1146/annurev.fluid.36.050802.122132. URL http://www.annualreviews.org/doi/10.1146/annurev.fluid.36.050802.122132.

[115] R. D. Sudduth. A generalized model to predict the viscosity of solutions with suspended particles. I. *J. Appl. Polym. Sci.*, 48(1):25–36, 1993. doi: 10.1002/app.1993.070480104. URL http://doi.wiley.com/10.1002/app.1993.070480104.

[116] T. N. Swaminathan, K. Mukundakrishnan, H. H. Hu, and H. U. Howard. Sedimentation of an ellipsoid inside an infinitely long tube at low and intermediate Reynolds numbers. *J. Fluid Mech.*, 551:357–385, 2006. doi: 10.1017/S0022112005008402.

[117] R. I. Tanner and S. Dai. Particle roughness and rheology in noncolloidal suspensions. *J. Rheol.*, 60(4):809–818, 2016. doi: 10.1122/1.4954643. URL http://sor.scitation.org/doi/10.1122/1.4954643.

[118] G. I. Taylor and J. Friedman. National Committee for Fluid Mechanics Films, 1966. URL http://web.mit.edu/hml/ncfmf.html.

[119] J. Towns, T. Cockerill, M. Dahan, I. Foster, K. Gaither, A. Grimshaw, V. Hazlewood, S. Lathrop, D. Lifka, G. D. Peterson, R. Roskies, J. R. Scott, and N. Wilkins-Diehr. Xsede: Accelerating scientific discovery. *Computing in Science & Engineering*, 16(5):62–74, 2014. doi: 10.1109/MCSE.2014.80. URL doi.ieeecomputersociety.org/10.1109/MCSE.2014.80.

[120] A. K. Townsend. Generating, from scratch, the near-field asymptotic forms of scalar resistance functions for two unequal rigid spheres in low-Reynolds-number flow. 2018. URL http://arxiv.org/abs/1802.08226.

[121] A. K. Townsend and H. J. Wilson. Frictional shear thickening in suspensions: The effect of rigid asperities. *Phys. Fluids*, 29(12):121607, 2017. doi: 10.1063/1.4989929. URL http://aip.scitation.org/doi/10.1063/1.4989929.

[122] N. Trask. *Compatible high-order meshless schemes for viscous fluid flows through l2 optimization*. PhD thesis, Brown University, 2015.

[123] N. Trask, M. Perego, and P. Bochev. A High-Order Staggered Meshless Method for Elliptic Problems. *SIAM J. Sci. Comput.*, 39(2):A479–A502, 2017. doi: 10.1137/16M1055992. URL http://epubs.siam.org/doi/10.1137/16M1055992.

[124] N. Trask, M. Maxey, and X. Hu. A compatible high-order meshless method for the Stokes equations with applications to suspension flows. *J. Comp. Phys.*, 355:310–326, 2018.

[125] R. G. M. van der Sman and H. M. Vollebregt. Effective temperature for sheared suspensions: A route towards closures for migration in bidisperse suspension. *Adv. Colloid Interface Sci.*, 185-186:1–13, 2012. doi: 10.1016/J.CIS.2012.08.006. URL https://www.sciencedirect.com/science/article/pii/S0001868612001315.

[126] A. M. C. van Dinther, C. G. P. H. Schroën, A. Imhof, H. M. Vollebregt, and R. M. Boom. Flow-induced particle migration in microchannels for improved microfiltration processes. *Microfluid. Nanofluidics*, 15(4):451–465, 2013. doi: 10.1007/s10404-013-1158-0. URL http://link.springer.com/10.1007/s10404-013-1158-0.

[127] H. M. Vollebregt, R. G. M. van der Sman, and R. M. Boom. Model for particle migration in bidisperse suspensions by use of effective temperature. *Faraday Discussions*, 158(1):89, 2012. doi: 10.1039/c2fd20035j. URL http://xlink.rsc.org/?DOI=c2fd20035j.

[128] M. Wang and J. F. Brady. Short-time transport properties of bidisperse suspensions and porous media: A Stokesian dynamics study. *J. Chem. Phys.*, 142(9):094901, 2015. doi: 10.1063/1.4913518. URL http://aip.scitation.org/doi/10.1063/1.4913518.

[129] M. Wang and J. F. Brady. Spectral Ewald Acceleration of Stokesian Dynamics for polydisperse suspensions. *J. Comput. Phys.*, 306:443–477, 2016. doi: 10.1016/j.jcp.2015.11.042. URL http://www.sciencedirect.com/science/article/pii/S0021999115007822.

[130] M. Wang, M. Heinen, and J. F. Brady. Short-time diffusion in concentrated bidisperse hard-sphere suspensions. *J. Chem. Phys.*, 142(6):064905, 2015. doi: 10.1063/1.4907594. URL http://aip.scitation.org/doi/10.1063/1.4907594.

[131] K. Yeo. *Some aspects of suspension flows: Stokes to turbulent flows*. PhD thesis, Brown University, 2011.

[132] K. Yeo and M. R Maxey. Simulation of concentrated suspensions using the force-coupling method. *J. Comput. Phys.*, 229:2401–2421, 2010. doi: 10.1016/j.jcp.2009.11.041.

[133] K. Yeo and M. R. Maxey. Dynamics of concentrated suspensions of non-colloidal particles in Couette flow. *J. Fluid Mech.*, 649:205, 2010. doi: 10.1017/S0022112009993454. URL http://www.journals.cambridge.org/abstract_S0022112009993454.

[134] K. Yeo and M. R Maxey. Numerical simulations of concentrated suspensions of monodisperse particles in a Poiseuille flow. *J. Fluid Mech.*, 682:491–518, 2011. doi: 10.1017/jfm.2011.241.

[135] I. E. Zarraga and D. T. Leighton. Shear-induced diffusivity in a dilute bidisperse suspension of hard spheres. *J. Colloid Interface Sci.*, 243(2):503–514, 2001. doi: 10.1006/jcis.2001.7854.

[136] I. E. Zarraga and D. T. Leighton. Measurement of an unexpectedly large shear-induced self-diffusivity in a dilute suspension of spheres. *Phys. Fluids*, 14(7):2194, 2002. doi: 10.1063/1.1483304. URL http://scitation.aip.org/content/aip/journal/pof2/14/7/10.1063/1.1483304.

[137] I. E. Zarraga, D. A. Hill, and D. T. Leighton Jr. The characterization of the total stress of concentrated suspensions of noncolloidal spheres in Newtonian fluids. *J. Rheol.*, 44:671, 2000. doi: 10.1122/1.551083. URL http://sor.scitation.org/doi/abs/10.1122/1.551083.